UNIVERSITY OF
BIRMINGHAM

Bacterial Biofilms and Biomineralisation on Titanium

Anqi Wang

A thesis submitted to the University of Birmingham
for the degree of

Doctor of Philosophy

2011

School of Metallurgy and Materials
College of Engineering and Physical Sciences
The University of Birmingham
Birmingham B15 2TT
United Kingdom
2011

UNIVERSITY OF
BIRMINGHAM

University of Birmingham Research Archive

e-theses repository

This unpublished thesis/dissertation is copyright of the author and/or third parties. The intellectual property rights of the author or third parties in respect of this work are as defined by The Copyright Designs and Patents Act 1988 or as modified by any successor legislation.

Any use made of information contained in this thesis/dissertation must be in accordance with that legislation and must be properly acknowledged. Further distribution or reproduction in any format is prohibited without the permission of the copyright holder.

Abstract

This study investigated bacterial interactions with titanium, and evaluated the use of *Serratia* biomineralisation to produce a hydroxyapatite (HA) coating on titanium.

Adherence of Gram-positive *Staphylococcus epidermidis* and *Streptococcus sanguinis* and Gram-negative *Serratia* sp. NCIMB 40259 and *Escherichia coli* was compared on commercially pure titanium, Ti6Al4V alloy, pure aluminium and pure vanadium. Grain boundaries, grain orientation and alloy phase structure did not influence adhesion or early proliferation. Adherence of all four strains was equivalent on pure titanium and Ti6Al4V and inhibited on pure aluminium.

Serratia biomineralisation was used to introduce a crystalline coating on Al_2O_3 grit blasted titanium discs and a porous titanium mesh. The porous coating consisted of micro-scale spheres composed of nano-scale calcium deficient HA. Embedded alumina particles and alkali treatment did not noticeably alter precipitation of *Serratia* HA, nor the structure of the coating in comparison with non-treated substrates. Coatings were retained after sintering at 800^oC in argon, although the original curved plate-like crystals changed to nano-scale β-tricalcium phosphate particles. A phosphorous-rich diffusion zone formed at the coating-titanium interface.

This biomineralised coating may have applications for coatings of implants in non load-bearing sites, and other non-clinical applications where a high surface area is the major concern.

To my parents

Acknowledgement

I would like to pay special thanks to Dr Rachel Sammons and Prof Ian Jones for their enormous guidance and enlightening suggestions and to Dr Junfa Mei for his supervision. Dr Yau Yau Tse has shared her professional knowledge and enthusiasm over the past three years.

Many colleagues and friends in University of Birmingham have offered generous help in this project. Thanks to them all:

Dr M Chu, Mr PF Stanley, Dr R Ding, Mr X Kuo, Mrs T Morris and other colleagues in EM group, Prof X Wu, Mrs A Cabezas, Mr M Cunningham, Mr A Burbery, School of Metallurgy and Materials, University of Birmingham.

Prof GL Landini, Mr SJ Wilson, Ms M Holder, Ms S Grant, Mr M Baylis, School of Dentistry, University of Birmingham.

Prof LE Macaskie, Dr P Yong, School of Bioscience, University of Birmingham

Mr CL Yeung, Prof J Preece, School of Chemical Engineering, University of Birmingham.

Dr T Miri, School of Chemical Engineering, University of Birmingham.

Table of contents

List of abbreviations

α-TCP: α-$Ca_3(PO_4)_2$

Al: alunimium

β-CPP: β-$Ca_2P_2O_7$

β-TCP: β-$Ca_3(PO_4)_2$

bcc: body centred cubic

BF: bright field

BSE: back-scattered electron

CP Ti: commercially pure titanium

DCDP: $CaHPO_4.2H_2O$

DF: dark field

EBSD: electron backscattered diffraction

ECPA: equal channel angular pressing

EDX: energy dispersive X-ray analysis

FIB/SEM: focused ion beam scanning electron microscopy

HA: hydroxyapatite ($Ca_{10}(PO_4)_6(OH)_2$)

HAADF: high angle annular dark field detector

hcp: hexagonal close placked

Oc: osteocalcin

OCP: $Ca_8(HPO_4)_2(OH)_4.5H_2O$

Op: osteopontin

PBS: phosphate buffered saline

PLD: pulsed laser deposition

SAD: selected area diffraction

SBF: simulated body fluid

SE: secondary electron

SEM: scanning electron microscopy

Sp. Act: acid phosphatase activity

STEM: scanning transmission electron microscopy

T_β: β transus temperature

TBS: tryptone soya broth

TCP: $Ca_3(PO_4)_2$

TEM: transmission electron microscopi

Ti: titanium

Ti 64: Ti6Al4V

TTCP: $Ca_4(PO_4)_2$°

V: vanadium

W: tungstun

WDX: wavelength dispersive X-ray analysis

List of figures

List of tables

Preface

I Biofilms on titanium

Bacterial adhesion, proliferation and subsequent biofilm formation on titanium are of great interest. A thorough knowledge of the above processes is essential in the fight against medical infections associated with titanium implants, as well as in other fields such as in microbe-induced corrosion (MIC), biofouling, biomineralisation, and other potential applications such as bacteria-driven energy fuel cells.

In studies related to bacteria-substrate interactions, most researchers focus on the influence of substrate surface roughness [1], wettability [2] and chemical composition [3]. Recently, the influence of substrate microstructures, such as grain boundaries and grain orientation, has aroused much attention, not only with regard to bacterial adhesion [4, 5], but also mammalian cell behaviour [6]. Titanium and its alloys, such as Ti6Al4V, are increasingly employed as implants. In this thesis, the influence of their microstructure and chemical composition on bacterial adhesion and proliferation has been investigated, as described in Chapter 3, focusing mainly on grain boundaries and grain orientations in commercially pure titanium and the phase structure of Ti6Al4V. Their effects on the adhesion of two Gram-positive bacteria, *Staphylococcus epidermidis* and *Streptococcus sanguinis*, and two Gram-negative bacteria, *E Escherichia coli* and *Serratia* sp. NCIMB 40259, and on the proliferation of *Serratia* have been studied, mainly using a combination of backscattered electron imaging and electron backscattered diffraction.

Numerous titanium surfaces have been designed and engineered for orthopaedic and dental implants, in order to guide and promote mammalian cell adhesion, proliferation and

differentiation. However, knowledge on biofilm formation, especially mature biofilm, on these surfaces is rather limited. *Serratia* biofilm formation has been studied on titanium discs with different surface treatments, including some which are already used on commercial dental implants, as described in Chapter 4. The influence of titanium surface roughness, wettability and topography on biofilm formation in terms of the number of bacteria in the biofilm and the morphology of the biofilm has been investigated. Recently, porous titanium scaffolds have attracted much focus due to their significantly increased osteoinductivity. However, limited work has been done to understand the biofilm formation on such structures. This study offers a detailed analysis of the 3D distribution of a *Serratia* biofilm grown on a porous titanium scaffold in an air-lift fermenter with continuous culture feed, using scanning electron microscopy and micro X-ray computer tomography which is included in Chapter 4. Bacterial adhesion, proliferation and biofilm formation on titanium substrates are summarised and discussed in Chapter 5.

II Biomineralisation on titanium

Bacterial related biomineralisation is a well known phenomenon. It is responsible, for example, for the formation of some urinary stones [7], ferrous hydroxide oxidation [8], sulphide reduction [9] and precipitation of $CaCO_3$ [10]. Among the many bacterial strains that are involved in biomineralisation, *Serratia* sp. NCIMB 40259, formerly classified as a *Citrobacter* sp., has attracted attention due to its application on recycling radioactive waste (UO_2^{2+}) [11] and in the treatment of organic phosphate contaminated water [12] with the concomitant formation of metal phosphates, especially hydroxyapatite [12]. The bacteria's ability to trap heavy metal ions as phosphate salts is thought to be a self-protection mechanism against an unpleasant environment [13].

Bacteria-related deposition of calcium phosphate is very common and closely related to everyday life - for example - as mentioned above, it occurs in the precipitation of urinary stones [7] and calcium phosphate in dental calculus [14]. Previous work has shown that when *Serratia* was provided with a source of calcium ions and an organic phosphate, the calcium phosphate produced was hydroxyapatite [15], and this reaction was explored further to evaluate its feasibility to produce hydroxyapatite as a potential bone-substitute material [16-18]. This has been further studied in this work as an alternative approach for coating titanium substrates with hydroxyapatite.

The *Serratia* hydroxyapatite coating on a solid titanium disc is described in detail in Chapter 6, and the influence of heat treatment on both the coating and the substrate in Chapter 7. The morphology, chemical composition and type of the nano-scale calcium phosphate in the coating have been determined by X-ray diffractometry, scanning electron microscopy and transmission electron microscopy. The coating-substrate interface structure has also been analysed. *Serratia* biomineralisation is also used to coat a porous titanium mesh with hydroxyapatite as described in Chapter 8. The influence of biofilm thickness on the coating formation has been studied and the morphology the coating has been examined using electron microscopy. The crystal coated porous titanium matrix has been reconstructed by micro X-ray computed tomography to visualise the 3D distribution of crystals within the porous scaffold. The influence of heat treatment on the hydroxyapatite coated porous titanium system has also been analysed. These are further discussed in Chapter 9, where the coating achieved in this study is compared to other methods and its advantages and disadvantages discussed.

References

1. Emerson RJ, Bergstrom TS, Liu Y, Soto ER, Brown CA, McGimpsey WG, Camesano TA. Microscale correlation between surface chemistry, texture, and the adhesive strength of *Stephylococcus epidermidis*.

Langmuir 2006;22(26):11311-11321.
2. An YH, Friedman RJ. Concise review of mechanisms of bacterial adhesion to biomaterial surfaces. Journal of Biomedical Materials Research 1998;43(3):338-348.
3. Mabboux F, Ponsonnet L, Morrier J-J, Jaffrezic N, Barsotti O. Surface free energy and bacterial retention to saliva-coated dental implant materials -- an *in vitro* study. Colloids and Surfaces B: Biointerfaces 2004;39(4):199-205.
4. Geesey GG, Gillis RJ, Avci R, Daly D, Hamilton M, Shope P, Harkin G. The influence of surface features on bacterial colonization and subsequent substratum chemical changes of 316L stainless steel. Corrosion Science 1996;38(1):73-95.
5. Truong VK, Lapovok R, Estrin YS, Rundell S, Wang JY, Fluke CJ, Crawford RJ, Ivanova EP. The influence of nano-scale surface roughness on bacterial adhesion to ultrafine-grained titanium. Biomaterials 2010;31(13):3674-3683.
6. Faghihi S, Azari F, Li H, Bateni MR, Szpunar JA, Vali H, Tabrizian M. The significance of crystallographic texture of titanium alloy substrates on pre-osteoblast responses. Biomaterials 2006;27(19):3532-3539.
7. Clapham L, McLean RJC, Nickel JC, Downey J. The influence of bacteria on struvite crystal habit and its importance in urinary stone formation. Journal of Crystal Growth 1990;104(2):475-484.
8. Amemiya Y, Arakaki A, Staniland SS, Tanaka T, Matsunaga T. Controlled formation of magnetite crystal by partial oxidation of ferrous hydroxide in the presence of recombinant magnetotactic bacterial protein Mms6. Biomaterials 2007;28(35):5381-5389.
9. Newman D, Beveridge T, Morel F. Precipitation of arsenic trisulfide by *Desulfotomaculum auripigmentum*. Appllied Environmental Microbiology 1997;63(5):2022-2028.
10. Obst M, Wang J, Hitchcock AP. Soft X-ray spectro-tomography study of cyanobacterial biomineral nucleation. Geobiology 2009;7(5):577-591.
11. Macaskie LE, Empson RM, Cheetham AK, Grey CP, Skarnulis AJ. Uranium bioaccumulation by a *Citrobacter* sp. as a result of enzymically mediated growth of polycrystalline HUO_2PO_4. Science 1992;257(5071):782-784.
12. Yong P, Macaskie LE, Sammons RL, Marquis PM. Synthesis of nanophase hydroxyapatite by a *Serratia* sp. from waste-water containing inorganic phosphate. Biotechnology Letters 2004;26(22):1723-1730.
13. Macaskie LE, Bonthrone KM, Yong P, Goddard DT. Enzymically mediated bioprecipitation of uranium by a *Citrobacter* sp.: a concerted role for exocellular lipopolysaccharide and associated phosphatase in biomineral formation Microbiology 2000;146:1855-1867.
14. Wong L, Sissons CH, Pearce EIF, Cutress TW. Calcium phosphate deposition in human dental plaque microcosm biofilms induced by a ureolytic pH-rise procedure. Archives of Oral Biology 2002;47(11):779-790.
15. L.Sammons R, Thackray AC, Ledo HM, Marquis PM, Jones IP, Yong P, Macaskie LE. Characterisation and sintering of nanophase hydroxyapatite synthesised by a species of *Serratia*. Journal of Physics: Confrence Series 2007;93:1-7.
16. Macaskie LE, Yong P, Paterson-Beedle M, Thackray AC, Marquis PM, Sammons RL, Nott KP, Hall LD. A novel non line-of-sight method for coating hydroxyapatite onto the surfaces of support materials by biomineralization. Journal of Biotechnology 2005;118(2):187-200.
17. Thackray AC. Bacterial biosynthesis of a bone substitute material. PhD Thesis. University of Birmingham; 2005.
18. Thackray AC, Sammons RL, Macaskie LE, Yong P, Lugg H, Marquis PM. Bacterial biosynthesis of a calcium phosphate bone-substitute material. Journal of Materials Science: Materials in Medicine 2004;15(4):403-406.

Chapter 1 Literature review

1.1 Mineralised tissues: composition and structure

Bones

Bones are indispensable components of bodies, as they support, protect and move various organs [1]. They come in a variety of shapes and with a variety of structures, reflecting their functions, and are mainly composed of water, organic bone matrix and mineral phases [1].

The hierarchical bone structure is built up through combination or repetition of highly ordered mineralised collagen fibrils. Depending on the manner in which the fibrils are arranged, various superstructures can be achieved, as shown in Figure 1. 1. The woven fibre structure shown in Figure 1. 1a usually consists of loosely packed fibril bundles with varying sizes and different orientations. Sets of parallel fibril bundles may also be present in discrete layers, with different orientations in each layer, forming the plywood-like structure in Figure 1. 1b. It is believed that these complicated multi-level-hierarchical structures are closely related to the stress state and mechanical function of individual bones [2].

Teeth

Teeth are mainly composed of calcified matrix. The pattern in Figure 1. 1c is characteristic of the bulk of dentine that forms the inner layer of teeth. The fibrils in this pattern are in the plane parallel to the surface where dentin forms, but random or poorly oriented within this plane.

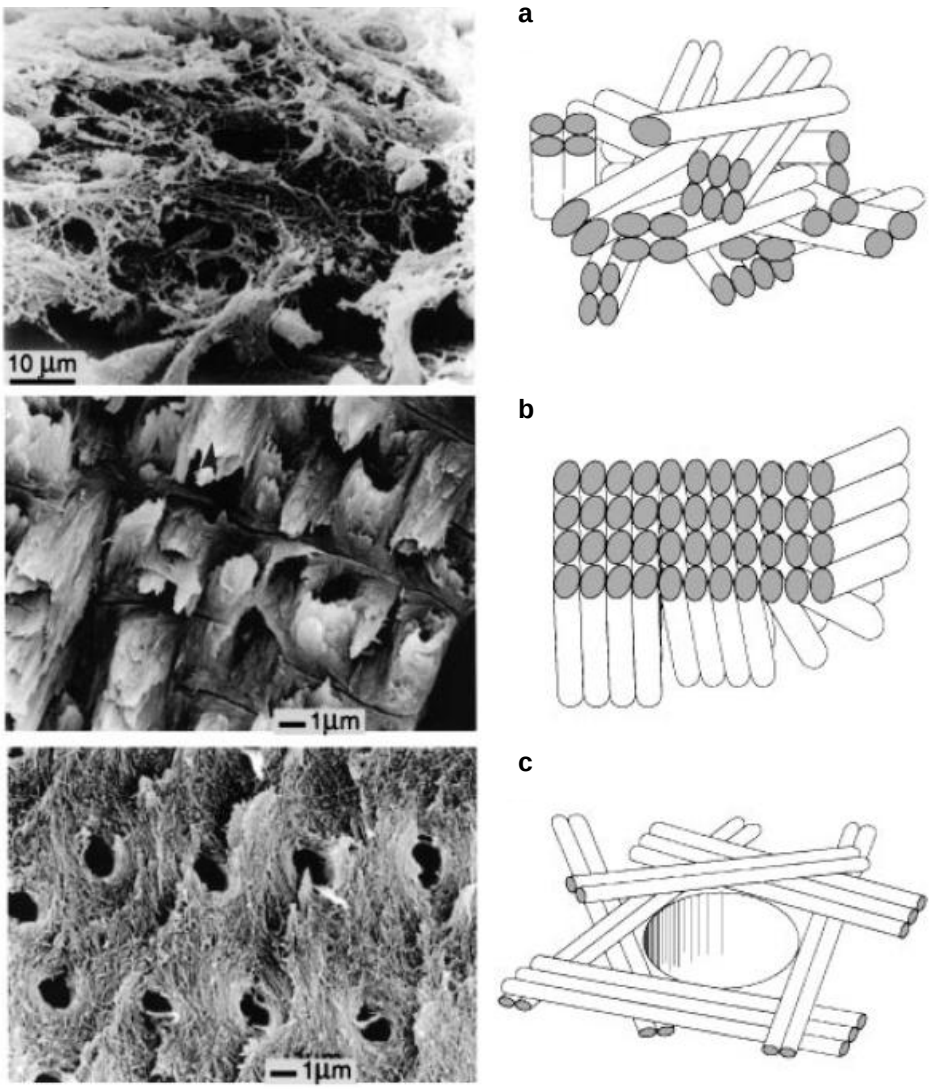

Figure 1. 1 SEM micrographs and schematic illustrations of three examples of fibril arrays in mineralised tissues (adapted from [2])

(a) Woven fibre structure (outer layer of a 19-week old human fetus femur).

(b) Plywood-like structure (baboon tibia).

(c) Radial fibril arrays (human dentin).

The major mineral in bones and teeth is calcium deficient carbonated hydroxyapatite (HA) [3]. It is different from stoichiometric HA because of the incorporation of other ions such as HPO_4^{2-}, CO_3^{2-}, Mg^{2+}, Na^{+} and F^{-}. Normally, the crystals are plate-shaped with irregular edges

[4] and preferential grown along the *c-axis* [5]. Crystal plates within the same fibril can be either arranged in such a way that they are parallel to each other and to the highly ordered collagens, such as in lamellar bones, or arranged randomly such as in trabecular bones (the cancellous bones) [5]. The formation of these plate-shaped crystals, regardless of the hexagonal symmetry of HA (hexagonal close-packed), is attributed to growth via an octacalcium phosphate (OCP) precursor phase, which forms faster than HA, and is less sensitive to crystal growth inhibitors [6]. HA, on the other hand, is much more stable than OCP *in vivo*. The transformation from OCP to HA is crystallographically possible because the (100) plane of OCP is identical to the $(10\bar{1}0)$ plane of HA [6].

Apatite formation *in vivo* is closely associated with proteins. Not only are the apatite nuclei observed accompanied by fibrious proteins, the growth of the apatite crystals is regulated via molecular recognition at the protein-mineral interface. Dentine matrix protein I is able to stabilise newly formed calcium phosphate precursors by facilitating the sequestration of calcium phosphate nuclei and thus preventing crystal aggregation and precipitation [7]. Bone Gla protein (GBP; osteocalcin) and osteonectin can inhibit hydroxyapatite crystal growth, because of their ability to bind to Ca^{2+} within the HA crystal through γ-carboxyglutamic acid and glutamic acid, aspartic acid residues, respectively [8].

1.2 Hydroxyapatite as a biomaterial

1.2.0 Preface

A biomaterial is a material, natural or synthetic, that is used ‘to replace or restore function to a body tissue and is continuously or intermittently in contact with body fluid’ [9]. According to the application, biomaterials can be roughly divided as orthopaedic implants, cardiovascular

applications, ophthalmics, dental applications, wound healing and drug delivery systems [9].

The most common synthetic biomaterials include metals, polymers, ceramics and composites. Among these materials, calcium phosphate is a popular choice for bone contacting applications because of its bioactivity. Its application as bone substitutes dates back to the 1920s [10]. Several examples of their dental applications are listed in Table 1. 1. The most commonly used calcium phosphates are hydroxyapatite (HA), octacalcium phosphate (OCP), α-tricalcium phosphate (α-TCP) and β-tricalcium phosphate (β-TCP). Their structures are compared in Table 1. 2 with that of tooth enamel.

Table 1. 1 Dental applications of calcium phosphate materials [10].

1	Restore (augment) alveolar ridge for better fit.
2	Tooth root replacement to prevent resorption of alveolar ridge.
3	Fillers for periodontal defects or bone loss.
4	As metal implant coatings to improve bone-implant adhesion
5	Repair of cleft palate
6	Repair of maxillofacial defects
7	As pulp-capping materials

Table 1. 2 Crystal structure and lattice parameters of tooth enamel and different kinds of calcium phosphate [3]

Mineral	***Chemical formula***	***Space group***	***Ca/P ratio***	***Lattice parameter***					
				a/Å	***b/Å***	***c/Å***	***α/º***	***β/º***	***γ/º***
Tooth Enamel	non-stoichiometrical	---	1.62	9.418	9.42	6.884	90	90	120
HA	$Ca_{10}(PO_4)_6(OH)_2$	$P6_3/m$	1.67	9.432	9.432	6.881	90	90	120
OCP	$Ca_8(HPO_4)_2(PO_4)_4{\cdot}5H_2O$	P1	1.33	19.69	9.52	6.835	90.2	93	109
α-TCP	α -$Ca_3(PO_4)_2$	P21/a	1.5	12.88	27.28	12.21	90	126	90
β-TCP	β-$Ca_3(PO_4)_2$	R3c	1.5	10.43	10.43	37.39	90	90	90

1.2.1 Hydroxyapatite

HA has been used for decades as a bone substitute material in orthopaedics and dentistry, capable of forming strong chemical bonds with tissues [11]. It is commonly represented as $Ca_{10}(PO_4)_6(OH)_2$ (sometimes as $Ca_5(PO_4)_3(OH)$) with a Ca/P ratio of 1.67. It is the most stable form of apatite *in vivo*, with a solubility product of around 2.63×10^{-60} [3]. Its lattice parameters are listed in Table 1. 2, and its structure is illustrated in Figure 1. 2.

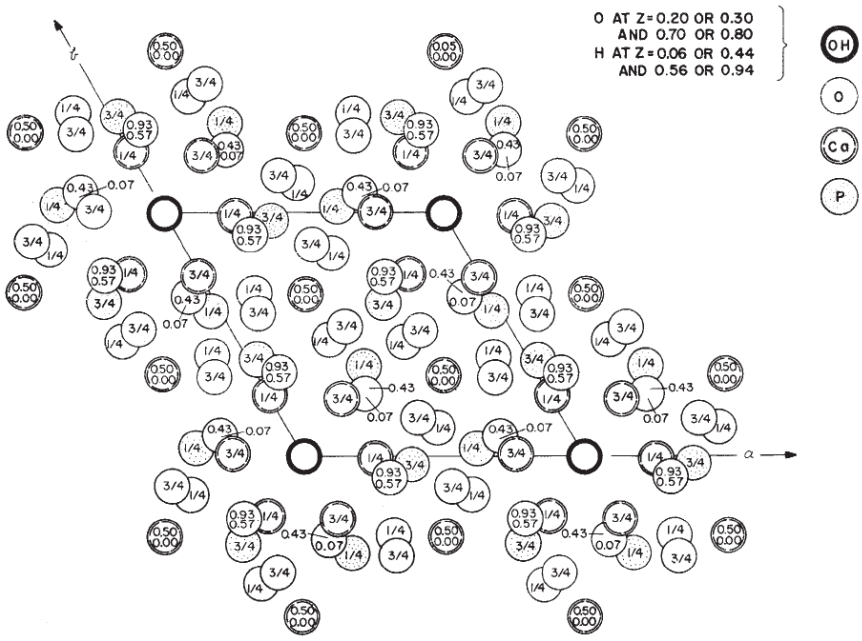

Figure 1. 2 HA structure projected onto the *xy-plane* (adapted from[12])

1.2.2 Production of HA

Synthetic HA can be achieved using dry methods such as solid state reaction and wet methods, such as sol-gel methods and precipitation from liquids.

1.2.2.1 Solid-state methods

Solid state reaction is a process during which dry ingredients such as CaO, P_2O_5, TCP and

$Ca(OH)_2$ are milled, mixed and sintered to produce crystals with the desired structure. It is a low cost process and produces stoichiometric HA with high crystallinity. However, contamination may be introduced during milling and the product can be different with different starting materials. By adjusting the composition of the starting material and the heat treatment, different calcium phosphates can be achieved. Several examples were listed in Table 1. 3.

Table 1. 3 Different phases achieved from TCP +$Ca(OH)_2$ combination after sintering (analysed used XRD) [13]

Heat treatment	***Products evolved from α-TCP and $Ca(OH)_2$ mixtures (molar ratio)***			
	3:1	***3:1.5***	***3:2***	***3:3***
600°C/8 hours	HA, βTCP, β-CPP, DCPD	---	HA, β-CPP, DCPD, CaO	HA, βTCP, β-CPP, DCPD
800°C/8 hours	HA(50%), β-TCP(50%)	---	HA(90%), β-TCP(6%), CaO(4%)	HA(94%), β-TCP(6%)
1000°C/8 hours	HA (54%), β-TCP(46%)	HA (84%), β-TCP(16%)	HA (100%)	HA(100%)
1250 °C/2 hours	HA (49%), β-TCP(26%), α-TCP(25%)	HA(74%), β-TCP(26%)	HA(100%)	HA (90%), CaO(10%)

HA=$Ca_{10}(PO_4)_6(OH)_2$; DCPD=$CaHPO_4{\cdot}2H_2O$; α-TCP=α$Ca_3(PO_4)_2$; β-TCP=β$Ca_3(PO_4)_2$; β-CPP=β$Ca_2P_2O_7$.

1.2.2.2 Sol-gel method

The sol-gel method is a wet chemical process during which calcium and phosphate sources, supplied by $Ca(NO_3)_2$ and P_2O_5 or H_3PO_4 [14, 15], are mixed in solvents and amorphous HA is thus formed. The white gel formed immediately in the solution is an amorphous precursor, which will develop to crystalline HA if sintered at above 600-700 ºC [16]. Heating to a higher

temperature can lead to a higher crystallinity but may also lead to the decomposition of HA, forming secondary phases such as β-TCP and CaO between 800 ºC and 900 ºC (Equation 1. 1) [14], TTCP ($Ca_4(PO_4)_2O$) and α-TCP at a temperature higher than 1250 ºC (Equation 1. 2) [15]. The advantage of this method is that neither a high pH value of the solution nor a high sintering temperature is needed during the reaction due to the high reactivity of the reactants. Disadvantages include the necessity for strict pH control, vigorous stirring during the reaction and a requirement of heat treatment to achieve crystalline products.

$$Ca_{10}(PO_4)_6(OH)_2 = 3Ca_3(PO_4)_2 + CaO + H_2O$$

Equation 1. 1

$$Ca_{10}(PO_4)_6(OH)_2 = Ca_4(PO_4)_2O + 2\alpha - Ca_3(PO_4)_2$$

Equation 1. 2

1.2.2.3 Precipitation

HA can be precipitated directly from supersaturated solutions containing calcium and phosphate ions following Equation 1. 3 - for example a solution made of $Ca(OH)_2$ and H_3PO_4 [17]. The precipitates can be calcified further by sintering, yielding different phases at different temperatures, similar to those described above [18]:

$$10Ca(OH)_2 + 6H_3PO_4 = Ca_{10}(PO_4)_6(OH)_2 + 13H_2O$$

Equation 1. 3

The crystal nuclei, 0.7 to 1.0 nm in size, are of OCP or amorphous calcium phosphate in undersaturated solutions and of HA in supersaturated solutions [19]. Following the nucleation, two growth mechanisms have been reported, nucleation-aggregation-agglomeration where the crystal growth was through the aggregation of the superfine nano-nuclei, driven by surface energy excess [20], and a cluster growth model where HA crystals grow by building up $Ca_9(PO_4)_6$ clusters at certain locations [19, 21]. The cluster size in the *a*- and *c*- directions is different, 0.815nm and 0.87 nm, respectively [19, 21].

While HA obtained in the sol-gel method is mainly in the form of particles, the crystals achieved by precipitation are more likely to be needles or plates of various sizes. The reaction is extremely sensitive to the environment, such as solution temperature, pH range, ion composition and concentration, rate of solution mixing and duration of precipitation [22]. Higher temperatures (>85 ºC) can result in a higher precipitation rate. HA formed in this way is usually not stoichiomechic due to the incorporation of ions, including Na^{+} Mg^{2+} and Sr^{2+}, into the HA crystal lattice, either by entering the defect sites within the structure or by substitution, causing the formation of carbonated HA or substituted apatite such as magnesium apatite and strontium apatite.

1.2.3 Biocompatibility of HA

HA is bioactive because it bonds chemically to surrounding tissues, which is desirable to achieve a firmer fixation of the implant and to avoid micromobility in the long term. After implantation, a series of complicated reactions happen at the HA surface which is exposed directly to the physiological fluids, involving the dissolution of the implanted HA (① to ③ in Figure 1. 3), protein adsorption (④ in Figure 1. 3), cell adhesion (⑤ and ⑥ in Figure 1. 3) and the formation of mineralised tissues (⑦ and ⑧ in Figure 1. 3). Bertazzo *et al.* claimed the formation of $CaHPO_4$ on the surface of the implanted HA during the process to be an equilibrium phase which could dissolve to release Ca^{2+} and HPO_4^{2-} or $H_2PO_4^{-}$ [23], as demonstrated in Equation 1. 7 and Equation 1. 8. The release of calcium and phosphate from HA can contribute to and facilitate the mineralisation *in vivo* and thus is of major significance in terms of biocompatibility [23]. The implanted HA can influence the tissue formation and *vice versa,* as the presence of osteoclasts can inhibit the dissolution process [24].

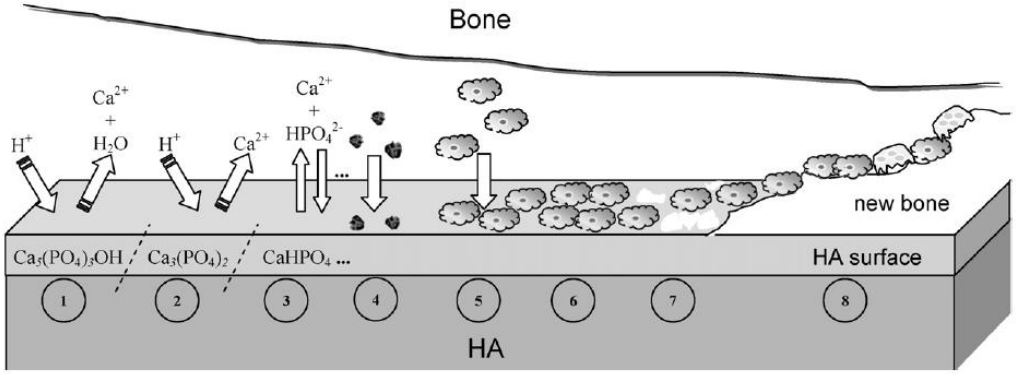

Figure 1. 3 Schematic drawing of a hypothesised mechanism for the dissolution of HA and the formation of new tissues (adapted from [23])

① Initial dissolution of HA after implantation:

$Ca_{10}(PO_4)_6(OH)_2$ (*s*)+$2H^+$ (*aq*)↔$Ca_{10}(PO_4)_6(H_2O)_2^{2+}$ (*s*) Equation 1. 4

② Further dissolution of HA:

$Ca_{10}(PO_4)_6(H_2O)_2^{2+}$ (*s*)↔$3Ca_3(PO_4)_2$ (*s*)+Ca^{2+} (*aq*)+$2H_2O$ (*aq*) Equation 1. 5

③ Equilibrium between the HA surface and the physiological solutions and the formation of $CaHPO_4$ on the modified surface:

$Ca_3(PO_4)_2$ (s)+$2H^+$ (aq)↔Ca^{2+} (aq)+$2CaHPO_4$ (s) Equation 1. 6

$CaHPO_4$ (s)+H^+ (aq)↔Ca^{2+} (aq)+$H_2PO_4^-$ (aq) Equation 1. 7

$CaHPO_4$ (s)↔Ca^{2+} (aq)+HPO_4^{2-} (aq) Equation 1. 8

④ Protein adsorption.

⑤ Cell adhesion.

⑥ Cell proliferation.

⑦ Start of mineralisation reactions.

⑧ Formation of new bone tissues.

1.2.4 Disadvantages

Although the natural similarity of HA to normal bones can accelerate the adhesion and growth of bone cells, its mechanical property is a major drawback. Compared with metals, dense HA is very brittle, with a tensile strength[1] of around 100 MPa (CP Ti, 240-550 MPa; Ti64, 895-930 MPa) and an elastic modulus[2] of less than 15 GPa (CP Ti, 102-104 GPa; Ti 64, 110-114 GPa) [25]. Therefore pure HA grafts are unfit to be used in the force-bearing sites such as hip replacements. HA is instead often used as coatings. However, the loosening of such coatings is considered as a potential cause of granulomatous inflammation and disturbance of bone remodelling which can lead to a local osteolytic process [26, 27].

1.3 Titanium and its alloys as biomaterials

1.3.0 Preface

Metals have been used as biomaterials for at least 2000 years [28]. However, it was not until the first and second World Wars that they were widely used as internal fixation devices and bone replacements. Common choices for medical devices include CrNi alloy, CoCr alloy, stainless steel, titanium and its alloys [29]. Compared with other competing metals, titanium is a relatively new engineering material. Its commercial application started in the 1940s and it was only introduced as an implantable material in the 1960s [25]. However it was not until the 1980s that researchers began to realise its superiority for medical applications. Today titanium and its alloys have become the preferred choice for bone applications because of their appropriate mechanical behaviour, superior corrosion resistance and bone acceptance [30]. Commercially pure titanium (CP Ti), Ti-6Al-4V (Ti 64), Ti-6Al-7Nb, Ti-5Al-2.5Fe, TiNi

1. Tensile strength: the maximum load that a material can support without fracture.
2. Elastic modulus: a term used to describe the ability of a material to deform elastically.

alloy, Ti-13Nb-13Zr and To-15Mo-3Zr-3Al are widely used in orthopaedic replacements and other bone contacting applications.

1.3.1 Titanium: metallurgy

Titanium (Ti) undergoes a β transition at 882ºC (T_β). Under T_β, titanium takes the hexagonal close-packed (hcp) structure, referred to as α-Ti, and above T_β, the body-centred cubic (bcc) structure (β-Ti). The addition of α or β-stabilising alloying elements to titanium gives rise to a field where both α and β phases can coexist. The incorporation of Al (α-stabiliser) and V (β-stabiliser) makes Ti 64 an α+β double-phase material with the coexistence of an hcp α phase and a bcc remanent β phase at room temprature.

1.3.2 Biocompatibility of titanium

Titanium and its alloys are notable for their osteoconductivity (the ability to allow bone growth on the surface [31, 32]. This is attributed to the surface TiO_2 oxide which forms spontaneously under atmospheric conditions due to the high reactivity of titanium with oxygen. This nanometre-scale passive layer, acting as the interface between the biological medium and the implant, is not only responsible for the superior corrosion resistance of titanium but also can attract osteogenic proteins such as osteocalcin (Oc) and osteopontin (Op), the main proteins contributing to osseointegration (close contact at the interface between the implant and bone tissue) [33]. Figure 1. 4 illustrates a possible mechanism to explain the osseointegration of titanium. At pH=7, the negatively charged TiO_2 (the implant surface) and Oc, Op are connected by the positively charged calcium ions, donated by the surrounding body fluid, the so-called calcium ion-mediated mechanism (Figure 1. 4a). (K^+ and Mg^{2+} may also contribute.) Alternatively, Oc and Op groups can be attracted and bonded to the implant through bridging by the terminal OH radicals on the TiO_2 surface (Figure 1. 4b)

[33, 34].

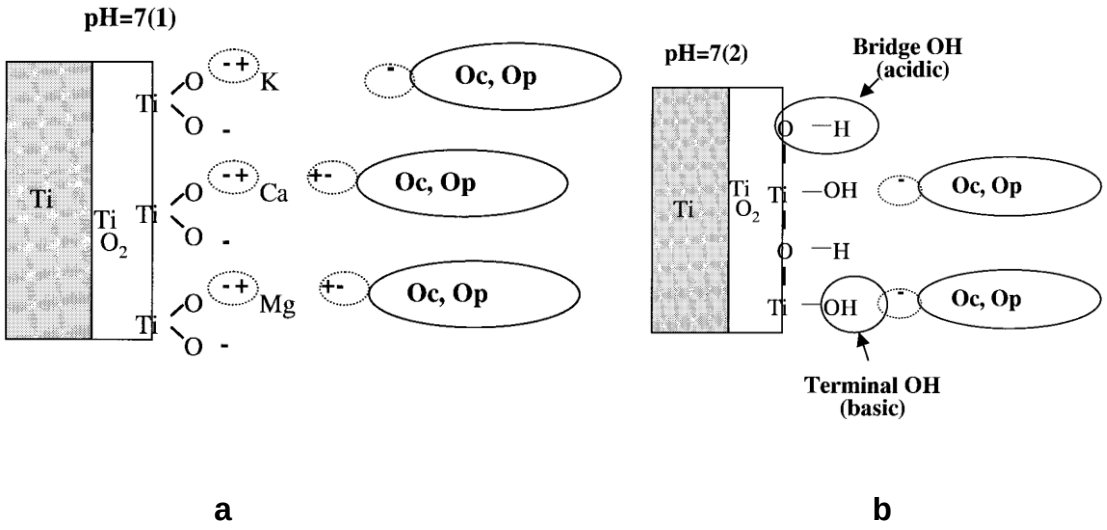

Figure 1. 4 Mechanism of adsorption of osteogenic proteins to titanium (adapted from [33])
(Oc: osteocalcin, Op: osteopontin)

a: Calcium ion-mediated mechanism.

b: Terminal OH radical-mediated mechanism.

Oc and Op are solely produced by osteoblasts. Their bonding to titanium leads to the migration of osteoblast cells toward the implants (cell adhesion). Bone formation is then triggered by Oc and Op surrounding the cells through simultaneous production of collagen which is then mineralised (Figure 1. 5) [33].

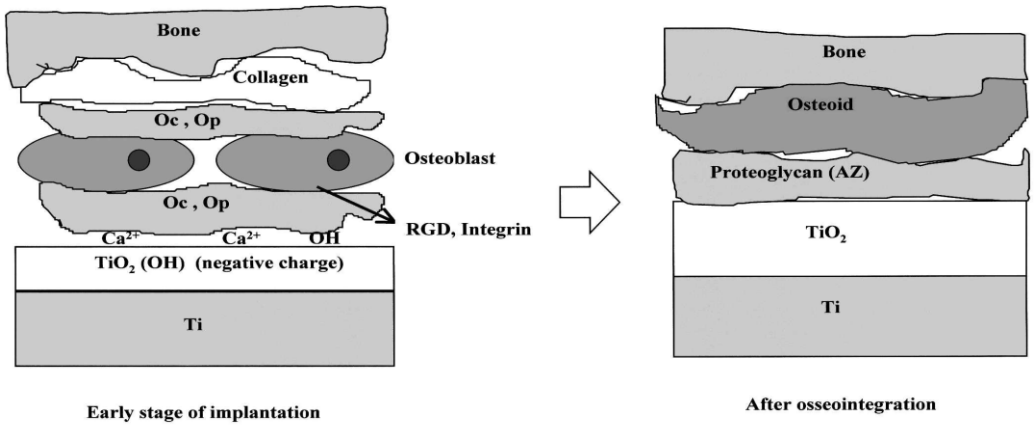

Figure 1. 5 Osseointegration of a titanium implant

(AZ: amorphous structure zones) (adapted from [33])

1.3.3 Surface treatments of implantable titanium alloys

When compared with ceramics such as calcium phosphate, titanium is considered as bioinert, due to its inability to form strong chemical bonding with the living tissue. The behaviour of cells can be much influenced by the specimen surface: either promoted or inhibited depending on properties such as roughness, topography, wettability and chemical composition. Protein adhesion, cell spreading, shapes and the organization of stress fibres can be significantly different on different titanium surfaces [35]. GM7373 cells were found to bridge deeper grooves (Ra > 0.35 μm) whilst aligning parallel to the smoother ones [32]. Last but not least, surface treatments can enhance the resistance against *in vivo* corrosion between the implant surface and the physiological environment to prevent ion release. Ion release is harmful because certain ions, such as Al and Ni, are potentially toxic to the cells [36]. With proper surface treatments, ion release from the metal substrate can be significantly reduced. A diamond-like carbon coating could reduce the nickel ion release from a nickel-titanium alloy orthodontic archwire by 80 % when it was immersed in physiological saline at 85 ^{o}C for 5 days [37]. HA coatings were also reported to reduce the metal ion release from titanium

substrates [38, 39].

1.3.3.1 Mechanical methods for modification of surface topography

Mechanical methods are treatments to control the surface morphology by cutting, turning, smoothing and particle blasting [40], to alter, roughen or to smooth the surface morphology of the implant. They are usually introduced as preparations for further treatments, but can also act as the finishing step.

Grit blasting is the most commonly employed mechanical treatment. It is a well established procedure where metal surfaces such as titanium are exposed to a flux of grits or sands under high pressure. It is well accepted that grit blasting can enhance the bone to metal contact, as blasting produces a rough surface with a high surface area and thus more bonding sites for proteins and cells [41]. Although the adhesion of human bone marrow cells was found to be unaffected by surface roughness over the range from 0.8 μm to 1.9 μm, cell proliferation in terms of total protein content and alkaline phosphate activity was quite sensitive to the roughness [42]. Al_2O_3 is the most common grit for blasting. However there are fears that the residual Al_2O_3 particles embedded within the matrix may inhibit cell growth by releasing harmful aluminium ions. Other grits, such as TiO_2, glass beads and HA granules are therefore sometimes introduced as replacements. However, there is dispute over this point, since neither torque measurements nor histomorphometric analysis showed any significant difference between Al_2O_3 and TiO_2 blasted screws after twelve weeks in adult rabbits [43]. Mouse osteoblastic cells (MC3T3-E1) were found to adhere and proliferate more poorly on Al_2O_3 grit blasted Ti6Al4V than on the untreated surface, which was attributed to an Al-rich surface layer contributed by both the embedded alumina and pressure-induced Al diffusion from the bulk material [44].

1.3.3.2 Chemical and electrical treatments

Chemical treatments, for example solvent cleaning, chemical etching and passivation, often accompany grit blasting or machining, to modify further the surface properties through chemical reactions between the titanium substrate and certain reactants. Acid etching, for example, can create a micro-textured surface on titanium that can promote cell adhesion and proliferation. The mean torque removal value of acid etched titanium screws was four times as high as that of machined-only ones after 2 months in New Zealand white rabbits [45]. As a matter of fact, in terms of endosseous integration, a machined + acid etched implant was almost comparable to plasma sprayed ones [46]. Passivation is achieved by exposing titanium to acid solutions such as nitric acid, to form a layer mainly consisting of amorphous TiO_2 as well as of Ti_2O_3 and TiO. It can prevent further oxidation of titanium during dry-heat sterilisation [47] and to minimise corrosion [48]. An anodised titanium surface can be achieved under electrochemical conditions, leading to improved corrosion and wear resistance, due to the existence of a partially crystalline oxidation film, mainly rutile (TiO_2) [49], but also trace amounts of the alloying elements from the substrate, such as Ni in TiNi alloy and Al in Ti 64 [49, 50]. Depending on the electrolytes used and the voltage and current involved, the structure of the oxidation layer is different: from a thin and compact layer to a composite of a compact layer and a columnar porous structure [51].

1.3.3.3 Coatings

A coating is introduced onto a titanium surface with various purposes: to promote cell adhesion, proliferation and differentiation, to reduce ion release, to improve corrosion resistance and to inhibit bacterial adhesion.

1. Polymer coatings

Polymer coatings can be introduced by techniques such as plasma polymerisation and electro-polymerisation. After the introduction of the coating, the surface often becomes more hydrophobic. Unlike many other methods, polymer coating can be multi-functional, via the possibility of associating various functional groups into the molecular chain [52]. Depending on the polymer itself and the functional groups involved, the cell response can be either promoted or inhibited. For example, a hexamethyldisiloxane coating is believed to be beneficial for the early adsorption of fibronectin (a high molecular weight extracelluar matrix protein that is involved in cell adhesion) [53]. A modification of titanium with biological active peptide molecules could promote cell attachment and decrease *S. aureus* adhesion [54]. Specific fibroblast attachment was enhanced if the polymer coating was functionalised by a peptide such as *N*-acetyl-GCRGYGRDGSPG through bonding covalently with an activated polymer chain [54]. Pre-treating the titanium substrates by grit blasting, acid etching and plasma or laser treatment will generally lead to stronger bonding between the substrate and the polymer coating, due to the formation of stronger mechanical interlocking, because of the increased substrate surface area and thus more irregularities to secure the polymers [55].

2. Bioglass coatings

Traditional glass contains at least 65% silicon oxide (SiO_2) and is bioinert. If this content is lowered to, for instance, 40-50%, with the addition of certain components such as sodium and calcium oxide, the glass starts to show bioactive properties [56]. Bioglass usually contains three key features which distinguish it from traditional glasses: less than 60% of SiO_2, high Na_2O and CaO contents and a high CaO/P_2O_5 ratio [57]. For example, the Biovetro GSB bioglass is composed of 7-24% Na_2O, 2-8% K_2O, 9-20% CaO, 0.1-2% MgO, 0.1-2% Al_2O_3, 46-63% SiO_2 and 4-8% P_2O_5 [56]. Common techniques to introduce a bioglass coating are

plasma-spraying [58], the sol-gel method [59] which benefits from a lower reaction temperature and a homogeneous mixture as the final composition, and pulsed laser deposition [60] which allows the formation of high-quality crystalline and stiochiometric films.

Osseointegration, the stable anchorage of an implant achieved by bone ingrowth into the discontinuities of the implant surface, of the bioglass-coated grafts can be significantly improved compared with the uncoated ones [58], however to a lesser extent than that of HA coated implants [61]. With the correct composition and appropriate crystallinity, the bioglass coating can be degraded in biological fliud. When rinsed in simulated body fliud (SBF) for 30 to 46 days a pulsed laser deposited bioactive glass thin film belonging to the SiO_2–Na_2O–K_2O–CaO–MgO–P_2O_5 system was gradually replaced by a new apatite layer through ion exchange [60].

3. Calcium phosphate coatings

Calcium phosphate coatings are so far the most promising coatings in terms of osteoconduction and osseointegration. Brushite, monetite, octacalcium phosphate, whitlockite (tricalcium phosphate), fluorapatite and HA are all in this family. Extensive studies have been made in this field, with HA attracting most attention, as will be discussed later in 1.4.

1.3.4 Porous titanium

Porous titanium can significantly reduce the implant-tissue stiffness mismatch. The Young's modulus and 0.2% proof strength of a laser-engineered net shaped porous titanium (porosity: 35-42 vol.%) are comparable to those of human cortical bones [62]. Moreover, a more stable fixation can be achieved by means of full bone ingrowth (bone formation within an irregular surface of an implant) into the porous structure [63]. Various methods have been developed to

manufacture such a matrix with different structures, including solid-state foaming [64], spark plasma sintering [65], powder sintering [66], laser fabrication [67, 68] and liquid foaming. Pore size rather than scaffold design is judged to be the more important factor for promoting bone ingrowth [69]; the optimum range of pore size ranges from 100 to 400 μm [70].

By coating the porous scaffold with calcium phosphate, the osteoconductivity of the graft can be improved and osseointegration can be accelerated. This can facilitate bone ingrowth and increase new bone formation both on the perimeter and internal surface of the implants [63, 71]. The traditional plasma/thermal spraying is no longer appropriate, as only facets facing the incoming spray can be coated. Hence wet methods such as sol-gel [72], electrochemical deposition [73] and biomimetic deposition [73] are more appropriate. In this study, bacterial biomineralisation of HA is used to coat a porous titanium web, and will be described in §1.6.

1.4 HA coated titanium as a biomaterial

1.4.0 Preface

It is well accepted that osseointegration will be improved significantly if the implant is coated with HA. The adsorption of proteins and subsequent formation of a conditioning film are of major importance in guiding cell adhesion, proliferation and differentiation; the ability of calcium phosphate to trap and adsorb bovine serum albumin almost doubles that of titanium [74]. Thus, it is not difficult to understand its superiority in accelerating tissue formation *in vivo*. Lopez-Sastre *et al.* (1998) reported that mineralised trabeculae formed in the surrounding area of plasma sprayed HA coated titanium cylinders were already mature after 4 weeks' implantation in Spanish Churra sheep [61]. Studies showed that after 12 years, although the bone loss was higher for HA-coated titanium than for pure titanium, HA-coated implants had a higher survival rate [75].

Consequently, HA coated titanium devices are considered to be a better choice as they incorporate the mechanical properties of titanium with the bioactivity of HA, maintaining the desirable mechanical strength as well as increasing the biocompatibility of the graft. The success of these coated implants, already used in orthopaedics, depends on a variety of factors, such as the interface bonding strength, coating thickness, chemical composition and the degree of crystallisation of the coating [76, 77]. It is commonly believed that a coating able to enhance osseointegration of metal implants needs to be sufficiently thick and crystallised to accommodate the bone healing process. Traditional methods to apply the coating include plasma spraying, electrophoretic deposition, the sol-gel method and biomimetic formation of HA on a bioactive titanium surface in simulated body fluid. The more important examples are described below.

1.4.1 Traditional methods

1.4.1.1 Plasma spraying

Plasma spraying is a well established commercial coating process. HA powders are injected into a plasma spray, accelerated and directed onto a target where they form a coating as they spread and solidify, as illustrated in Figure 1. 6. However, contaminants from the plasma gas can be introduced into the coating [78], and decomposition phases such as TCP, TTCP and CaO cannot be avoided [79]. Due to the thermal history of plasma-sprayed powders, which are often partially melted, the coating is not chemically homogeneous, and demonstrates a decrease in crystallinity as it gets nearer to the titanium surface with an amorphous CaP layer in direct contact with the substrate [80]. Thus, post heat treatment is applied to achieve a homogeneous composition as well as to restore the crystalline structure of the coating [81]. The coating strength can be improved by co-spraying with TiO_2 particles [82] or by making

the coating as a HA/titanium composite [83]. The main drawback of this method is the geometrical limitation of the supporting substrate: porous materials or substrates with complicated shapes cannot be evenly coated.

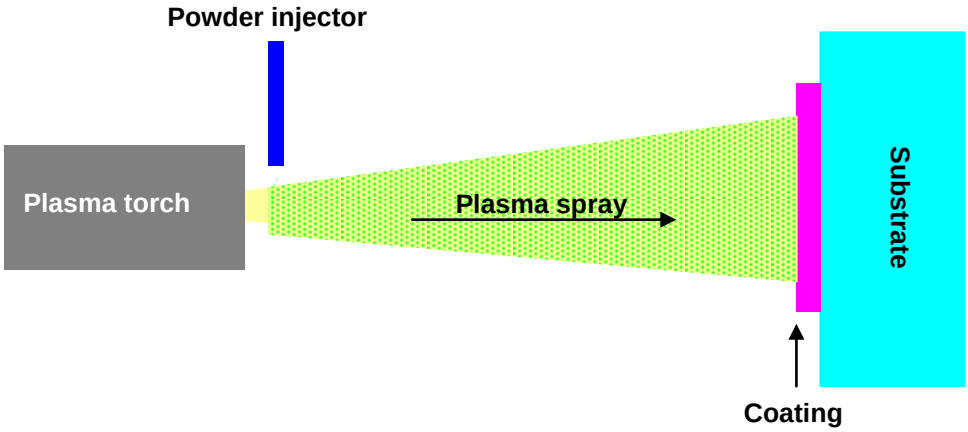

Figure 1. 6 Schematic drawing of the plasma spraying method for forming an HA coating

1.4.1.2 Pulsed laser deposition

In pulsed laser deposition, HA is irradiated by an intense laser beam and thus vaporized and directed toward a heated substrate where it recondenses and forms a thin film on the surface. Typical equipment is illustrated in Figure 1. 7. The laser parameters (intensity, wavelength, pulse width) are of major importance, as they determine the composition of the irradiated vapour [84]. Tri *et al.* showed that HA film deposited at a laser fluence at 29.3 J/cm^2 had higher crystallinity as well as a smoother surface with a lower Ca/P ratio than that achieved at 2.4 J/cm^2 [85]. By heating the substrate to different temperatures, various phases can be achieved: amorphous HA if the substrate is kept below 450 ºC [86], crystalline HA if between 400 ºC and 700 ºC and in an inert atmosphere (but α-TCP if in oxygen [87]) and β-TCP above 700 ºC [87]. The as-deposited amorphous HA film can be restored to a stoichiometrical HA crystalline phase by heat treatment at 300 ºC to 550 ºC [86, 88]. As with plasma-spraying,

pulsed later deposition is not appropriate for coating porous scaffolds.

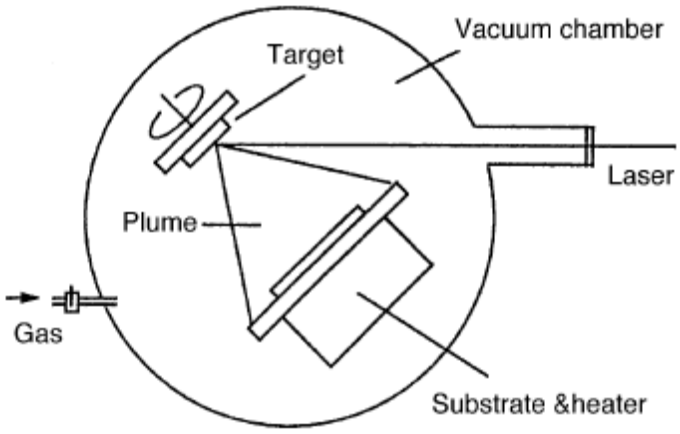

Figure 1. 7 Typical equipment for pulsed laser deposition (adapted from [87])

1.4.1.3 Electrophoretic deposition

Electrophoretic deposition is a low cost flexible process and has proved successful for producing an HA coating on metal implants [88]. HA is deposited on various substrates by electrophoresis from solutions consisting of components such as $Ca(NO_3)_2 \cdot 4H_2O$ and $NH_4H_2PO_4$ [89]. The concentration of HPO_4^{2-} in the solution is greatly influenced by the local pH and follows Equation 1. 9 or Equation 1. 10. When extra OH^- is available, with the association of Ca^{2+} and PO_4^{3-}, HA precipitates on the cathodic surface (Equation 1. 11).

$$H^+ + PO_4^{3-} \rightarrow HPO_4^{2-} \qquad \text{Equation 1. 9}$$

$$HPO_4^{2-} + OH^- \rightarrow H_2O + PO_4^{3-} \qquad \text{Equation 1. 10}$$

$$10Ca^{2+} + 6PO_4^{3-} + 2OH^- \rightarrow Ca_{10}(PO_4)_6(OH)_2 \qquad \text{Equation 1. 11}$$

The voltage and current used are important. At -0.7 V, $Ca(H_2PO_3)_2 \cdot H_2O$ was formed, but a combination of $CaHPO_4 \cdot 2H_2O$ and $Ca_{10}(PO_4)_6(OH)_2$ was formed at -1.25 V [89]. The coating

thickness is flexible, ranging from less than 1 μm to several millimetres. The main limitation is the requirement for heat treatment at high temperature to convert the as-deposited loosely held coating crystals to a more dense form.

1.4.1.4 Biomimetic method

The biomimetic method involves rinsing a NaOH-treated bioactive titanium in simulated body fluid (SBF). SBF is a well known metastable buffer solution with a composition similar to that of human plasma, as shown in Table 1. 4 [90].

Table 1. 4 Ion concentration of SBF and human plasma [90]

Ion	***Concentration (mM)***	
	SBF	***Human plasma***
Na^+	142.0	142.2
Cl^-	147.8	103.3
HCO_3^-	4.2	27.0
K^+	5.0	5.0
Mg^{2+}	1.5	1.5
Ca^{2+}	2.5	2.5
HPO_4^{2-}	1.0	1.0
SO_4^{2-}	0.5	0.5

Kokubo first reported that by soaking titanium in 5M sodium hydroxide solution, a layer of sodium titanate formed on the activated titanium surface [91]. TEM study demonstrated the close association of this sodium titanate layer with the formation of HA in the succeeding stages [92]. An XRD-XPS study revealed that the apatite formation on this bioactive surface was started by an ion-exchange mechanism [93]. The mechanism is illustrated in Figure 1. 8. After soaking in SBF, the Na^+ ions within the amorphous sodium titanate layer are released into the solution through ion exchange with H^+ to form Ti-OH groups (Figure 1. 8b), which were able to stimulate the formation of HA in SBF [91]. The Ti-OH groups react with the Ca^{2+} from the fluids to form calcium titanate (Figure 1. 8c). The calcium titanate reacts further

with PO_4^{3+} and thus HA nuclei are precipitated on the titanium surface [94]. The biomimetic HA coating on Ti was reported to grown preferentially along the *c-axis* [97, 98] and perpendicular to the titanium substrate [95]. However, there were studies indicating that the crystals precipitated on the activated titanium surface were in fact OCP rather than HA [73, 96]. At room temperature, this process is very slow, with the formation of an HA coating less than 20 μm thick after two weeks' immersion [95]. However, it can be facilitated by increasing the NaOH concentration, NaOH-treatment time and reaction temperature, and the ion strength of the SBF [97, 98]. A similar treatment was applied to titanium alloys, such as Ti-15Mo-5Zr-3Al and Ti6Al4V. The activated sodium titanate layer and the subsequent HA coatings were found to be the same as those on the pure titanium surface, indicating that this process was unaffected by the alloying elements within the substrate [93, 99].

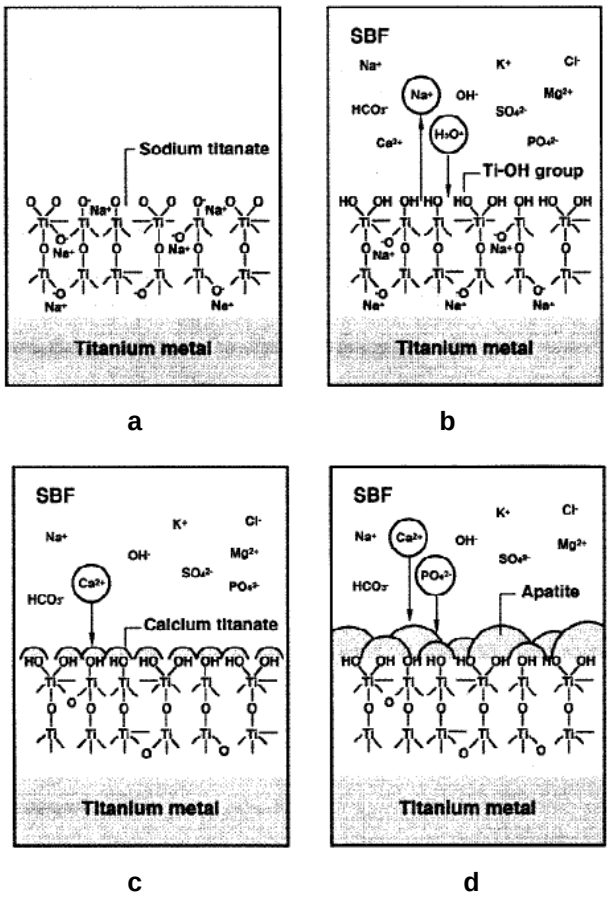

Figure 1. 8 Mechanism of apatite formation on NaOH activated titanium in SBF (adapted from [94])

a: Before soaking in SBF: the formation of sodium titanate in NaOH solution.

b: Formation of Ti-OH groups in SBF.

c: Formation of calcium titanate.

d: Formation of apatite.

1.4.2 Coating properties and their influence on cellular responses and bone formation

Coating properties such as chemical composition, particle size, crystallinity, surface structure and roughness can significantly alter the cell response, possibly through influencing protein adsorption.

1.4.2.1 The influence of chemical composition

Almost inevitably, the HA coating is not 100% pure stoichiometric. Depending on the coating method and the heat treatment route, various phases can be involved in the coating, such as TCP, OCP, CaO and amorphous HA. After implantation, the bonding between the ceramic and the cells is mainly through reactions which include dissolution of the coating, precipitation of the newly formed mineral and ion exchange between them. Thus, different cell responses are very likely on HA with or without other phases [100]. Although β-TCP is more biodegradable than HA, the latter is preferred for cell adhesion. After 24 hours' incubation, 41.5% of the cells did not adhere on β-TCP but only 4.5% on HA [101]. After implantation for 12 weeks, OCP promoted bone formation better than its hydrolyzed Ca-deficient HA form [102].

The incorporation of foreign elements into HA also matters. For an HA coating achieved in an aqueous environment, such as by precipitation, electrochemical deposition or a biomimetic method, the products are often calcium-deficient, sometimes with the incorporation of elements such as Na, F, Cl and Mg. The presence of Mg and F in the apatite can promote bone formation, although others argue that Mg has no apparent effect [103, 104]. The introduction of F into the lattice structure of apatite can be beneficial in terms of cell adhesion, proliferation and tissue formation. When comparing the attachment of human osteoblastic cells on HA blended with fluorapatite, from 0% to 100%, the best adhesion and proliferation were observed on the sample with 40% fluorapatite, which also demonstrated a higher level of mRNA and bone formation [105]. However, an inhibited cell colonial growth as well as DNA breakage was observed on fluorapatite and fluor-HA, indicating a role for cytotoxicity and genotoxity [106].

1.4.2.2 The influence of surface roughness

Cell adhesion, proliferation and detachment are sensitive to surface roughness in nano- and micro-scale [107-109]. When comparing the adhesion of human bone marrow stromal cell on HA disc polished with SiC paper 180-, 600-, and 1200-grit, Deligianni *et al.* (2000) observed that although cell differentiation was similar on all surfaces, cell adhesion, proliferation and detachment strength were increased with the increased surface roughness [108]. Human bone marrow cell differentiation evaluated by the expression of alkaline phosphatase activity was the same on HA pellets polished with 180-, 600- and 1200-grit SiC paper, but both cell adhesion and proliferation were observed to increase with HA surface roughness [111, 112].

1.4.2.3 The influence of crystal morphology and coating topography

The crystal morphology and the coating topography can be quite different depending on the coating method. Human bone marrow cells displayed a guided growing pattern on SiC-paper-ground HA surfaces, aligned along the mechanically produced grooves [108]. When compared to spherical HA particles, needle-shaped HA could stimulate a higher production of cytokines [110]. Needle-shaped HA could also stimulate a more efficient differentiation of primary human bone derived cells, demonstrating a higher osteogenic gene expression as well as alkaline phosphatase activity in comparison with spherical and rod-shaped HA [110]. Large plate-shaped (approximately 2 μm wide) biomimetic HA was reported to induce the highest expression of osteocalcin and bone sialoprotein in a 3-week MC3T3-E1 preosteoblast culture when compared to spherical-shaped and nano-plate shaped HA [111]. Plate-shaped electrochemically deposited HA coating on Ti6Al4V also appeared to be more advantageous in promoting the integration of mineralised tissues into the coating than a plasma-sprayed one, which was comparatively smoother and less textured ones [76].

1.4.2.4 The influence of crystallinity

Crystallinity of the coating influences *in vivo* mineralisation mainly through a difference in dissolution rate. Plasma-sprayed HA, for example, due to its lower crystallinity and thus higher solubility *in vivo*, contributes Ca^{2+} and PO_4^{3-} ions which assist local mineralisation and accelerate new bone formation and/or are involved in cell signalling. Thus, its effect is prominent from an early stage of implantation [76]. However, low crystallinity may lead to final failure of the implant due to its quick dissolution and thus an early exposure of the graft to the body fluid [112], while a more highly crystalline HA with lower dissolution rate is more efficient at catalysing new bone formation in the long run [113]. Increased alkaline phosphatase-specific activity, cell-surface and matrix-associated protein and osteocalcin production were found on HA with higher crystallinity [114]. Osteoblast adhesion was found to be higher on annealed pulsed laser deposited HA coated titanium with more defined cytoskeletal actin organisation as well as higher cell activity and alkaline phosphatase production than on the untreated one, attributed to a higher crystallinity of the coating [115].

1.5 Bacterial adhesion, proliferation and biofilm formation

1.5.0 Preface

Bacteria are some of the oldest living organisms on this planet. They were the dominant form of life on Earth for more than 3 billion years, and still form much of the world's biomass today.

Bacteria are closely associated with almost every aspect of human life. Bacterial infection is a major cause of human and animal diseases and even death. Microbial-induced infection is a well known cause of implant failure [116]. When a device is grafted into the body,

inflammation takes place in neighbouring areas, and surrounding tissue begins to repair itself in order to restore its functional activity. However, bacterial adhesion to the implant surfaces and the formation of a complex biofilm during this procedure can easily result in subsequent infection. There is evidence of biofilm formation *in vivo* on many devices including catheters, artificial joints and heart valves [117]. The initial adhesion of bacteria to implant surfaces is believed to be one of the major steps in the pathogenesis of foreign body infections. Hence, it is of great importance to understand the factors affecting bacterial adhesion, proliferation and the subsequent biofilm formation on implant surfaces.

On the other hand, bacteria can be beneficial: for instance, in biomineralisation, a process during which various minerals are accumulated by the microbial organisms from the environment. A range of different mechanisms are often involved [118], as discussed further later.

1.5.1 Bacteria

Bacteria can be separated into three groups using Gram staining separates: Gram-positive, Gram-negative and Gram-variable. After staining, those that are violet or dark blue are Gram-positive, red or pink Gram-negative and those that cannot be classified Gram-variable. This is because of the compositional difference of the cell walls. A network of peptidoglycan is the basic structural unit of a bacterial cell wall which offers the necessary strength and rigidity to maintain the bacterial shape and to protect them against osmotic lysis. The structures of the Gram-positive and Gram-negative bacterial cell walls are quite different. The Gram-positive cell wall is mainly composed of multilayered peptidoglycan with embedded proteins, teichoic and lipoteichoic acids (Figure 1. 9), whereas the Gram-negative cell wall is much more complicated. As well as the peptidoglycan layer, it also contains an outer

membrane with a separation layer of periplasmic space in between (Figure 1. 10). Lipopolysaccharide molecules extend from the outer membrane into the extracellular space. The outer membrane also contains porins which allow the passage across the membrane of small hydrophilic molecules [119].

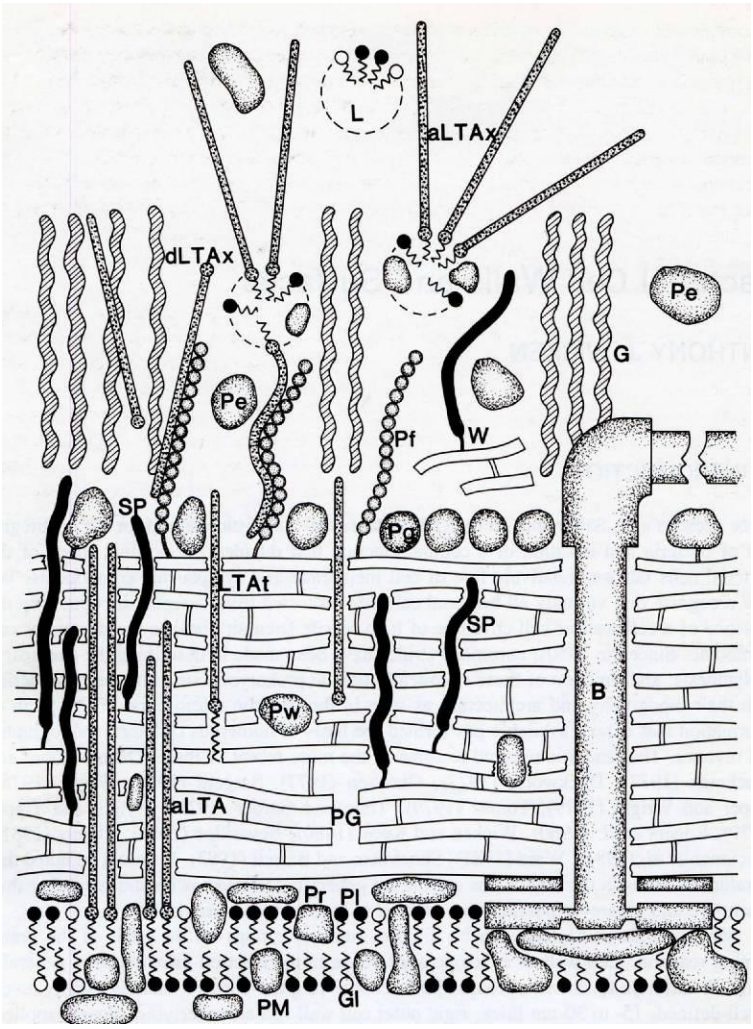

Figure 1. 9 Schematic representation of a Gram-positive bacterial cell wall (adapted from [120])

PG: cross-linked peptidoglycan. PM: plasma cell membrane composed of protein (Pr), phospholipid (Pl) and glycolipid (Gl). SP: covalently linked secondary cell wall polymers such as teichoic acids, teichuronic acids and polysaccharides. B: basal body of flagellum. Pw: noncovalently linked proteins within the peptidoglycan matrix and part of the glycocalyx region. Pg (globular) and Pf (fibrillar) are covalently associated proteins on the surface of

peptidoglycan. aLTA: acylated lipoteichoic acid. aLTAx: excreted lipoteichoic acid. dLTAx: deacylated extracellular LTA. LTAt: peptidoglycan net. L: excreted lipids. Pe: excreted proteins. W: wall turnover products. G: glycocalyx region.

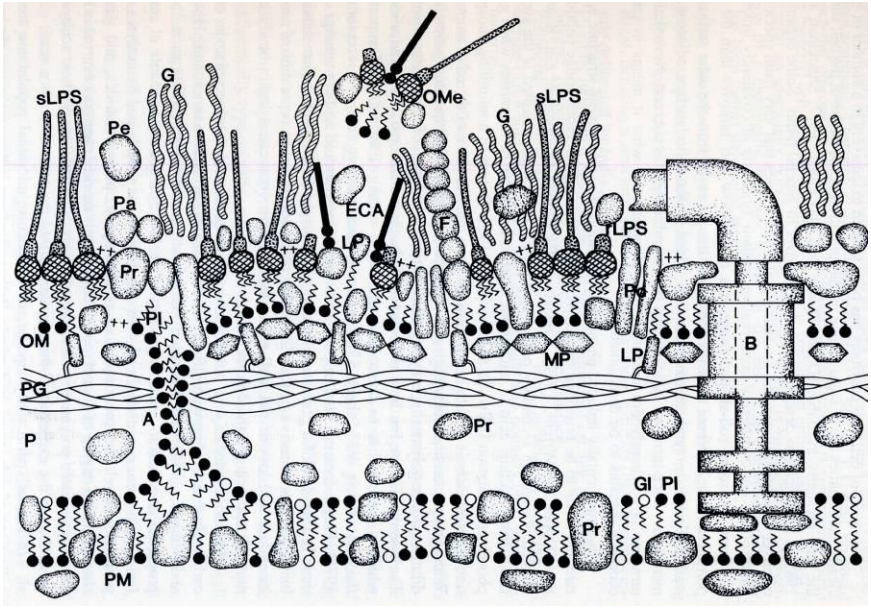

Figure 1. 10 Schematic representation of a Gram-negative bacterial cell wall (adapted from [120])

OM: outer membrane. PG: peptidoglycan monolayer. P: periplasm. PM: inner plasma membrane. A: attachment points of the outer and inner membranes. B: basal body of flagella. Pl: phospholipid. Gl: glycolipid. Pr: proteins. s/rLPS: smooth/rough lipopolysaccharide. ECA: enterobacterial common antigens (polysaccharide polymer). LP: lipoprotein. MP: matrix protein. Po: porin. F: fimbriae. Pa: outer membrane-associated protein. Pe: extracellular protein. OMe: excreted outer membrane fragments. G: extracellular capsular polysaccharide.

There are many appendages attached on the cell wall, which are essential for cell movement and important during cell attachment and biofilm formation. The flagellum enables the bacterium to move. Its rotation, driven by torque converted from electrochemical energy by the flagellar motor, confers motility to the cell [121]. Pili are the most abundant cell surface

appendages and are believed to be crucial for bacterial attachment and biofilm formation. They are usually linear, unbranched polymers, forming either thin fibrillar structures or thick helically wound rod-shape fimbriae. Curli form the major proteinaceous component of the extracellular matrix and are able to promote cell adhesion and invasion [122].

1.5.2 Bacterial adhesion

During bacterial adhesion, a planktonic bacterium swims toward or is moved near a solid surface and attaches irreversibly to the substratum after a series of physical and chemical reactions. This procedure can be divided into two stages, a reversible physical contact phase (including the initial attraction) and a time-dependent phase of irreversible chemical and molecular adherence [123].

The bacterium is attracted to a surface by physical forces such as Brownian motion, van der Waals attraction, gravitational forces, surface electrostatic charge and hydrophobic interactions. After physical contacts, the subsequent reactions at the bacterium-substratum interface lead to an irreversible adhesion, which is still far from totally understood. In general, it is believed that during this procedure, the bacterium produces substances called adhesins, which bind to proteins adsorbed onto the surface of the substrate. A firmer adhesion is achieved with the presence of capsules, flagella and pili which can fasten the bacterium to the surface and overcome the repulsive forces associated with the substratum [124].

This procedure can be affected by a number of factors, including the bacteria themselves, substrate properties and environmental contributions [123]. Hydrophobicity of both the bacteria and the substrate are of major importance [125-128]. While the hydrophobic bacteria preferentially colonise hydrophobic substrates, the hydrophilic ones like the hydrophilic surfaces better. The presence of certain bacterial structures is also important. Donlan

concluded that cell surface polymers with nonpolar sites such as fimbriae, other proteinaceous structures and components of certain Gram-positive bacteria (mycolic acids) appear to dominate attachment to hydrophobic surfaces, while EPS and LPS are more important in attachment to hydrophilic material [129]. Bacterial adhesion is also expressed as a process during which charge transfer happens between the bacterial surface proteins and the substratum. Pootinga *et al*. found that the potential of a semiconducting indium tin oxide coated glass was closely related to the amount of attached bacteria [130]. However, they also observed that the charge transfer involved in the process had only a weak effect on bacterial attachment (the initial 4 hours) [131]. Other characteristics such as chemical composition, roughness and topography can also significantly affect the adhesive behaviour. Bacterial growth can be inhibited on surfaces containing or coated with antibiotics, saliva and metal ions to which they are sensitive [125, 132]. Bacteria are generally thought to attach better on rougher surfaces with higher surface area and thus more anchoring sites [133]. However, the role of surface roughness is still quite controversial. There were reports that increased roughness at the nano-scale did not promote but weakly inhibited *Staphylococcus epidermidis* adhesion because of the reduced adhesion strength [134]. *Pseudomonas* mutants were observed to be more dependent on flow direction rather than surface roughness [135].

1.5.3 Bacterial proliferation

Bacterial proliferation is achieved by growth and division. For example, a rod shaped bacterium elongates until it doubles in length while remaining constant in width. A division then happens at approximately the midpoint of the cell and both the daughter bacteria continue similar growth modes [136]. It is hypothesised that selective synthesis of new cell walls at particular locations is responsible for maintaining the new cell morphology during

bacterial growth [119]. During the elongation of *Escherichia coli*, the peptidoglycan at the poles is inert and functions as a rigid support for the overall cell morphology. In other species, such as *Corynebacterium diphtheriae*, however, new walls are synthesised at cell pores. Division is always accomplished with the newly formed peptidoglycan (orange in Figure 1. 11) at the division sites, the middle points of the elongated cells.

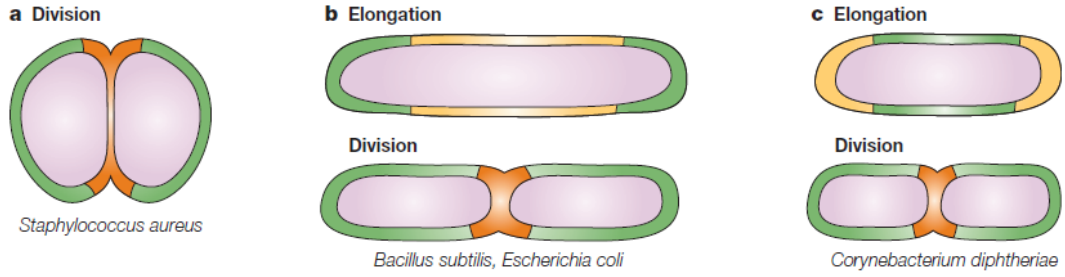

Figure 1. 11 Bacterial growth and division (adapted from [119])

Green: the original cell wall; yellow: the newly formed peptidoglycan during cell growth; orange: the newly formed peptidoglycan during cell division.

1.5.4 The formation of biofilms

During or following adhesion, the cells proliferate to form colonies which spread to form biofilm covering the surface. Figure 1. 12 is a schematic diagram of a typical biofilm development model. After the initial attachment (stage 1) and subsequent irreversible adhesion (stage 2), initial biofilm growth occurs (stage 3), mainly by colonial growth from single cell division [124]. These colonies develop further to a mature porous biofilm, forming typical colony features such as ‘mushrooms’ (stage 4) [124, 137]. Rather than being stable and steady, its structure is dynamic, driven by factors such as the redistribution of the attached bacteria via cell motility. It is believed that this heterogeneous architecture is essential as the pores and pathways form ‘water channels’ for the transport of oxygen and nutrients

throughout the biofilm [138]. When biofilm growth is not governed by nutrient transfer rate but other factors such as bacterial metabolism, a compact and homogeneous structure is more likely to form [139]. Detachment from the matured bacterial protrusions (stage 5) is common, due to reasons such as nutrient exhaustion, medium flow and surface stress condition [140] by means of twitching motility driven by pili [124], or as a simple result of physical detachment due to flow shear. As a result, the detached bacteria migrate to new sites and start a new cycle of bacterial colony growth. A cell-density dependent signalling process, quorum sensing, can also be utilised by many bacteria to regulate biofilm density through gene expression in order to achieve an optimized physiological environment [141]. The density of the biofilm is adjusted through a mechanism controlled by factors that are important during biofilm formation, such as the synthesis of LPS [142] and the cell viability [143].

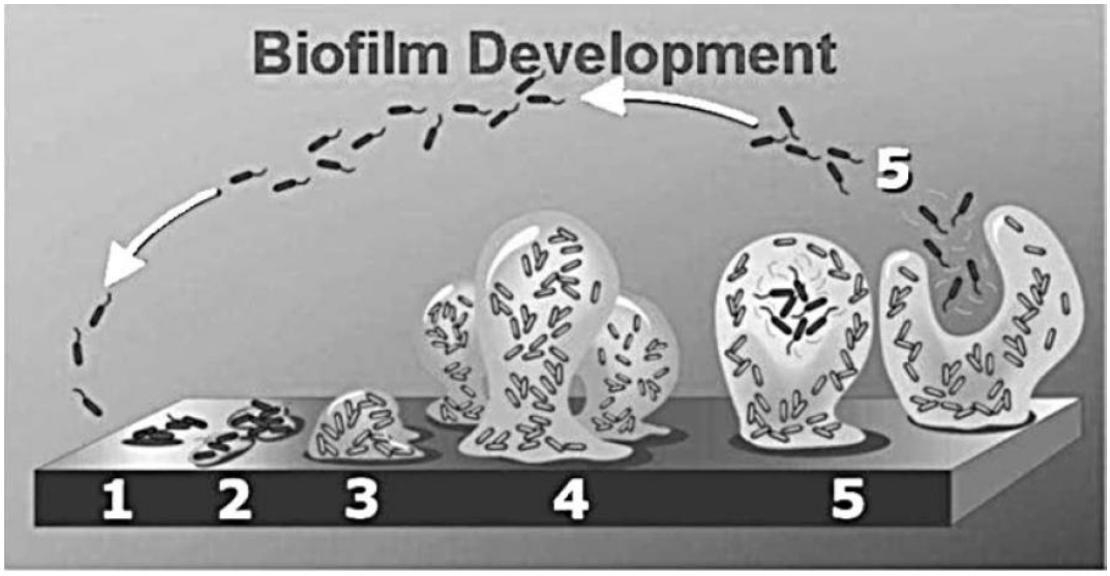

Figure 1. 12 Models of the development of a mature biofilm (adapted from [138])
1: Stage 1, initial bacterial attachment. 2: Stage 2, firmer attachment as a result of the production of extracellular polymer substances. 3: Stage 3, early biofilm development-bacterial colonial growth. 4: Stage 4, mature biofilm architecture, with mushroom-shape protrusions. 5: Stage 5, bacterial detachment.

The ability of bacteria to form biofilm, and the structures of the mature biofilms, vary from species to species, as certain bacterial structures can significantly facilitate biofilm growth. Cell appendages are crucial. They help to shape the structure of the mature biofilm. For instance, in a flow chamber with citrate minimal medium, *Pseudomonas aeruginosa* bacteria, with and without type IV pili, formed quite different biofilms: an irregular structure with protruding mushrooms for the non-motile ΔpilA and ΔpilAΔfliM mutants, whilst a flat biofilm was produced by the wild-type bacteria which was attributed to a twitching-motility powered by extension and retraction of type IV pili [124, 144]. The production of extracellular polymer matrix (EPM) also makes a difference. EPM is a slime-like bacterial secretion. It is highly hydrated and composed of polysaccharides, proteins and nucleic acids. EPM is often considered as the support for biofilm growth, to protect bacteria from the outer environment and help to define the biofilm structure [117, 138].

Biofilms are sensitive to the environment. Factors such as flow rate (flow shear), nutrient supply and temperature significantly alter the biofilm structure, thickness, density and morphology. For example, biofilms formed in nature always develop to patterns which mimic to the flow patterns in the environment [145]. The level of shear forces, the biofilm growth rate and the presence of protuberances can increase detachment, while substrate loading rate can accelerate the growth process [146]. The structure of the biofilm may be dependent on the carbon source used to support growth. For example, in the presence of citrate, benzoate or casamino acids, the mature *P. aeruginosa* biofilm appeared to be flat, but it was heterogeneous and with mushroom-shaped multicellular structures when glucose was used. The properties of the supporting substrate are also important. In general, biofilms develop more rapidly on rougher and more hydrophobic surfaces, but with exceptions [117]. Substrate roughness can affect the biofilm by influencing the convective mass transport of nutrients,

oxygen and water near the surface, providing shelter from shear forces and offering more anchoring sites for bacteria [147]. The biofilm thickness and surface morphology are thus a combined result of the conditions mentioned above.

1.5.5 Bacterial interaction with titanium

To understand bacterial adhesion and biofilm formation on titanium is of great significance, due to the extensive use of titanium in biomedical devices and the potential for implant failure after implantation caused by bacteria-induced infection. As a consequence, most of the research in this field is focused on the antibacterial properties of titanium through various surface modifications, either by altering the surface topography and roughness [148], or through certain chemical treatments such as ion implantation [149] and antibacterial coatings [150]. For example, a surface roughness above Ra=0.2 μm, considered as a threshold value, was reported to increase plaque accumulation on intraoral hard surfaces [133]. The surface topography also matters. Bacterial adherence (*Staphylococcus aureas*, *Staphylococcus epidermidis* and *Pseudomonas aeruginosa*) was reduced on electron beam evaporised nano-textured titanium surface [148], and both *Staphylococcus aureas* and *Pseudomonas aeruginosa* were found to attach better to nano-crystalline titanium due to the increase in surface roughness at the nano-scale [151]. Although bacteria preferentially colonise rougher surfaces, the effects of surface roughness and topography are not as prominent as that of chemical composition (antibacterial components) [152]. F^- and Ag^+ are well-accepted anti-bacterial components and their incorporation into titanium surfaces either by coating or ion implantation can significantly inhibit bacterial colonisation [152-154]. A more popular approach involves functionalised polymer coatings, such as silk [155], poly(methyl methacrylate) (PMMA) modified with carboxylate and sulphonate [156] and polysaccharides

conjugated with carboxymethyl chitosan [150], to inhibit bacterial adhesion as well as to enhance osteoblast cell adhesion.

However, despite the abundant usage of titanium as a biomaterial and the importance of the bacterial contribution to the final device failure, surprisingly little has been studied about the influence of the metallurgical features of titanium and its alloys on bacterial adhesion and proliferation. A thorough understanding of these aspects could be extremely helpful since most of these features are closely related to the manufacturing method. For example, refined grains, preferential grain orientations and twinning are common in cold- rolled material [157]. A nano-crystalline structure can be achieved through heavy plastic deformation such as equal channel angular pressing [158]. Direct laser deposition usually leads to the formation of long columnar grains [159].

1.6 Biomineralisation of HA via *Serratia*

The formation of biofilm has been intensely studied not only because of the numerous problems they caused due to their accumulation, but because of their ability to be 'tamed' for various commercial purposes. Biomineralisation is one amongst many potential applications. Biomineralisation is a process during which living organisms produce minerals. It is fairly common, such as in the formation of bone and urinary stones *in vivo* [160], heavy metal immobilisation [161, 162] and, of interest here, the formation of nano-phase calcium deficient HA by the bacterium *Serratia* sp. NCIMB 40259 [163, 164].

1.6.1 Mechanisms of biomineralisation

Proteins embedded in bacterial cell walls are intimately associated with metal ions. Mg^{2+} and Ca^{2+}, for example, exist naturally on the cell surface as structural components [120].

Moreover, the flexible polymer wall structure of the cells encourages the adsorption of various metals in certain salt forms. The accumulation of these minerals from the environment is called biomineralisation.

1.6.1.1 Biosorption

Biosorption encompasses the physical/chemical bindings of metal ions to the bacterial cell surface. It is driven by ion exchange, chelation, adsorption, diffusion, electrostatic and hydrophobic interactions, or by physical forces [118, 165]. Metal ions often diffuse through cell walls and concentrate in inter- or intra-fibrillar capillaries and spaces within the polysaccharide network. Ni^{2+} and Pb^{2+} were found to be taken up by *Phanerochaete chrysosporium* within 30 min, followed by a comparatively slow intracellular diffusion for around 3h to reach a final contact [166]. Bacterial structural components such as acetamido groups, polysaccharides, amino, amido, sulfhydryl and carboxyl groups are considered responsible in attracting and sequestering the metal ions [167]. The extracellular polymer matrix (EPM) is important as it is believed to be able to assist the biomineralisation process as a nucleus for crystal deposition.

The reactions during the process are complex and can be influenced by a number of factors. Pannanelli concluded that the adsorption of metals as Cu, Cd, and Fe by *Arthrobacter* sp. was mediated by ion exchange when the solution pH was lower than 5, otherwise probably through precipitation or co-precipitation on the cell wall surface [168]. The optimum pH range to remove Pd and Zn via *Streptoverticillium cinnanoneum* was different: 3.5-4.5 and 5.0-6.0, respectively [169]. The existence of competing ions was also found to be important [170].

1.6.1.2 Metal entrapment via bacteria catalysed oxidation

Bacteria can catalyse the oxidation of metals like Fe^{2+}, As^{3+} and Mn^{2+}. Numerous bacterial species are responsible for the oxidation of Fe^{2+} and As^{3+} in acid-sulfate-chloride geothermal springs [171]. They catalyse oxidation of Fe^{2+} to produce Fe^{3+} oxyhydroxide which precipitates internally or externally to the cell walls. Bacteria-bound proteins are of great importance during this process. *Escherichia coli* was reported to be able to oxidise vapor Hg to water soluble Hg^{2+}, which was attributed to a bacterial reaction catalysed by hydroperoxidases [172]. The protein Mms6 in *Magnetospirillum magneticum* AMB-1 showed iron binding activity, leading to the oxidation of ferrous hydroxide [173]. This protein was regarded as a template for nucleus formation and/or a growth regulator. As a result of the aggregation of the N-terminal region of protein Mms6, the negatively charged C-terminal region faced out and attracted cations such as Fe^{2+}/Fe^{3+}, providing a nucleation site for iron precipitation.

1.6.1.3 Sulphide precipitation

Sulphide-reducing bacteria can remove a wide range of metals, such as Fe, Zn, Cu, Pb, Ni and Cd from solution as highly insoluble sulphides [118]. Electron transfers are often involved in the process, with an organic substance as electron donor and the sulphur compound as electron acceptor. For example, with the cooperation of SO_4^{2-}, bacteria can consume lactate, possibly through an organic carbon-consuming reaction, to produce acetate, CO_2 and H_2S (Equation 1. 12). Metal ions (Fe^{2+}/Zn^{2+}) react further with the aqueous H_2S and precipitate as insoluble salts (FeS/ZnS, Equation 1. 13) [174].

$$2CH_3CHOHCOO^- + SO_4^{2-} \rightarrow 2CH_3COO^- + 2HCO_3^- + H_2S$$

Equation 1. 12

$$Fe^{2+}, Zn^{2+} + H_2S(aq) \rightarrow FeS, ZnS + 2H^+$$

Equation 1. 13

Other mechanisms may also be involved, for example, microbial-catalysed metal reduction. *Desulfotomaculum auripigmentum* was able to reduce As^{5+} to As^{3+} [175]. The subsequent precipitation of As^{3+} and S^{2-} as As_2S_3 was as expected since the compound has lower energy and was thus more stable.

1.6.1.4 Phosphate precipitation

The precipitation of metal ions as phosphates is another important method to remove heavy elements from solutions. A *Citrobacter* sp. (now renamed as *Serratia*) accumulated uranyl ions (UO^{2+}) as $NH_4UO_2PO_4$ or $NaUO_2PO_4$ [176]. Lipopolysaccharide (LPS) from the outer cell membrane was proposed to be the initial nucleation site due to the existence of phosphate groups within the structure [177]. This nucleation process intercepts the metals and thus protects the enzymes responsible for the cleavage and release of HPO_4^{2-} from organic phosphate [177]. It is the continuous diffusion of metal ions inward and HPO_4^{2-} outward that further facilitates the precipitation reactions [177]. The phospholipid groups of the double-membrane and outer-membrane-bound phosphatase may also contribute to the metal deposition, as a second nucleation and consolidation route [177]. Metal phosphates synthesised in this manner are often restrained within a mesh of fibrils or vesicles, allowing further diffusion, both incoming and outgoing [177].

1.6.2 *Serratia* and biomineralisation of HA

A *Serratia* sp., formerly identified as *Citrobacter*, was reported to accumulate HA at the

expense of $CaCl_2$ and organic phosphate and was proposed as a possible method for purifying waste water [178]. *Serratia* is a rod-shaped, Gram-negative, non-pathogenic bacterium with basic bacterial structures such as a double-layered cell wall on which are cell appendages such as curli, fimbriae and the flagella. While curli and fimbriae immobilise the cell during the biofilm formation, the flagella enable bacterial mobility inside the solution. An acid-type phosphatase enzyme (PhoN) is produced inside the periplasm within the double-membrane cell wall and can be exported through the outer membrane. It is this enzyme which catalyses the formation of HA both inside and outside the cell wall. Figure 1. 13 is a schematic diagram illustrating a possible mechanism of HA formation, based on the work of Macaskie *et al*. [162, 163, 178]. LPS is the initial nucleation sites where Ca^{2+} is bonded to the PO_4^{3-} functional part. The phosphatase enzyme catalyses the cleavage of organic phosphate (β-glycerol phosphate) from the solution and releases HPO_4^{2-}, which reacts with the entrapped Ca^{2+} on LPS to form a HA nucleus. Crystals grow further by a continuous diffusion of Ca^{2+} inward and HPO_4^{2-} outward and the reaction between these ions. As mentioned in 1.6.1, the crystals are restrained within a meshwork of fibrils or vesicles and are thus nano-scale in dimension [177].

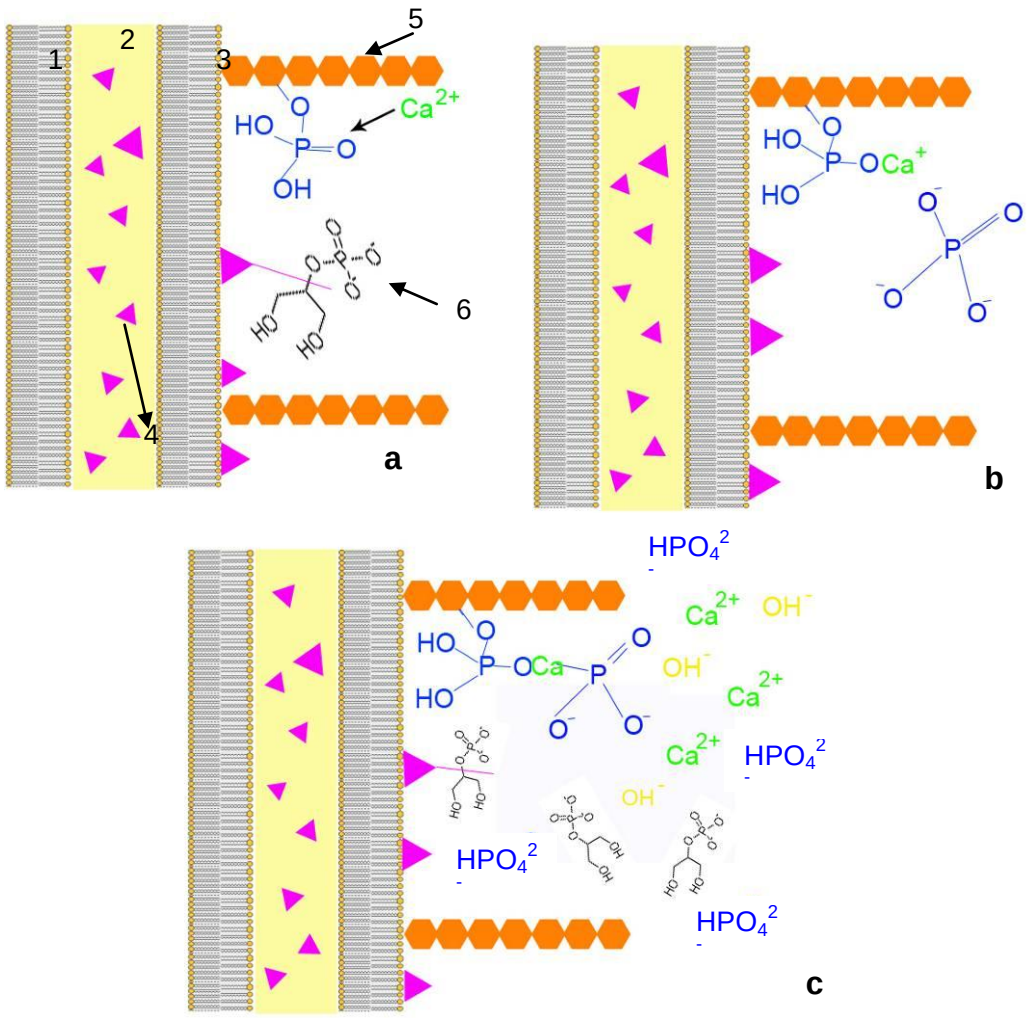

Figure 1. 13 Biomineralisation of HA by bacteria Serratia

1. Inner membrane; 2. Periplasm; 3. Outer membrane; 4. Acid phosphatase enzyme; 5. LPS; 6: β-GP.

a: Nucleation: initial interception of Ca^{2+} by the phosphate group within the LPS structure.

b: Reaction between the intercepted Ca^{2+} with HPO_4^{2-} which is cleaved and released by acid phosphatase enzyme, both inside the periplasm and on the outer membrane.

c: HA crystal growth: further precipitation of the incoming Ca^{2+} and the outgoing HPO_4^{2-}.

1.7 Aims and Objectives

The overall aim of this study is to evaluate the use of *Serratia* biomineralisation as a means of producing an HA coating on titanium substrates for biomedical and other applications. In the first part of this work, bacterial adhesion, proliferation and subsequent biofilm formation on various titanium substrates will be analysed in detail (Objectives 1, 2, 3, and 4). This research is of major clinical significance because of the importance of infection, and serves as a foundation for the subsequent study of mineralisation of HA on titanium via *Serratia.*

Orthopaedic implants are often coated with HA to facilitate cell attachment and to promote bone ingrowth. As a result, a faster and stronger bond can be achieved between the implant and the biological tissues. *Serratia* biomineralisation was developed as a coating method by previous researchers [163, 164, 178, 179]. In this study, its potential to apply HA coatings on titanium substrates and the properties of the biomineralised HA coating will be evaluated in detail (Objectives 5 and 6).

The objectives of the project are:

Bacterial interaction with titanium surfaces

1. **To establish a non-destructive method to study the relationship between bacterial distribution and metal alloy structure using electron microscopy.**

So far, only a few studies have been reported on the relationship between microbial distribution and metal surface alloy structure. However, the methods employed have various drawbacks. For example, some do not take into account the influence of surface roughness [180]; some do not directly examine the substrate but require further polishing and etching of the specimen to record the metal microstructure [181]; some can only offer general

information on the cell distribution on specimens but fail to provide information at the micro-scale level [182]. This work aims to establish a non-destructive method to examine the influence of titanium alloy microstructure on bacterial distribution directly, based on backscattered electron microscopy, electron backscattered diffraction and statistical image analysis.

2. **To analyse the influence of titanium microstructure and alloying composition on bacterial adhesion and proliferation.**

As potential bacterial adhesion and proliferation stimuli, the influence of the grain boundaries and grain orientation of pure titanium on representative Gram-positive and Gram-negative bacterial adhesion and proliferation will be investigated using the method established in Objective 1. The influence of the alloying elements in Ti 64 will also be studied in comparison with pure titanium, aluminium and vanadium.

3. **To examine the influence of titanium surface properties on *Serratia* biofilm formation.**

Mature biofilm development on different titanium surfaces has been rarely studied, however this is of great importance because of its role in clinical infection. In order to understand the influence of titanium surface properties on biofilm formation, *Serratia* biofilms will be grown on titanium substrates subjected to different surface treatments. The morphology of the biofilm and the amount of bacteria associated within the biofilm will be compared on differently treated surfaces, and the influence of titanium surface roughness, wettability and topography on biofilm formation will be investigated.

4. **To analyse *Serratia* biofilm formation on a porous titanium scaffold.**

Recent research concerning porous titanium for clinical applications has usually focused on mammalian cell adhesion and proliferation but knowledge of bacterial biofilm development on these scaffolds is still limited. This study will provide information on *Serratia* biofilm growth on a porous titanium wire mesh. Micro X-ray CT will be evaluated as a method to visualise bacterial distribution within the metal structure.

Serratia biomineralisation

The *Serratia* HA coatings will be studied on an Al_2O_3 grit-blasted pure titanium disc and on a porous titanium mesh.

5. **To coat titanium with HA via *Serratia* biomineralisation and to characterise the crystal coatings.**

The *Serratia* HA coated titanium system is composed of three components: the metal substrate, the *Serratia* biofilm and the HA crystals. Thus, in order to thoroughly characterise the coating properties, all these aspects will be considered. The relationship of the crystal coating structure to that of the biofilm and the substrate properties will be explored (extending Objective 3. On Al_2O_3 grit-blasted surfaces a combination of FIB/SEM/TEM cross section studies will be used to compare the crystals adjacent to the metal surface with those from the coating bulk. The crystal coatings will also be studied on titanium subjected to an alkali treatment (as used to promote HA formation from simulated body fluid) in comparison with untreated Ti and the influence of mineralisation solution ion concentration on the crystal composition and morphology will be examined.

6. To determine the influence of heat treatment on Serratia HA coated titanium

To avoid an inflammatory response after implantation, the *Serratia* HA coated titanium must

be heated to a sufficiently high temperature to destroy the biomass and all pyrogens. Sintering will not only affect the crystal coating, but also alter the structure of the titanium substrate. Therefore, the structure of the crystal coating, titanium substrate and the coating-substrate interface after sintering will be investigated both on titanium discs and on the porous mesh.

References

1. Peters F, Schwarz K, Epple M. The structure of bone studied with synchrotron X-ray diffraction, X-ray absorption spectroscopy and thermal analysis. Thermochimica Acta 2000;361(1-2):131-138.
2. Weiner S, Wagner HD. The material bone: structure-mechanical function relations. Annual Review of Materials Science 1998;28(1):271-298.
3. Simmer JP, Fincham AG. Molecular mechanisms of dental enamel formation. Critical Reviews in Oral Biology and Medicine 1995;6(2):84-108.
4. Rubin MA, Jasiuk I, Taylor J, Rubin J, Ganey T, Apkarian RP. TEM analysis of the nanostructure of normal and osteoporotic human trabecular bone. Bone 2003;33(3):270-282.
5. Hong S, Hong S, Kohn D. Nanostructural analysis of trabecular bone. Journal of Materials Science: Materials in Medicine 2009;20(7):1419-1426.
6. Brown WE, Eidelman N, Tomazic B. Octacalcium phosphate as a precursor in biomineral formation. Advances in Dental Research 1987;1(2):306-313.
7. Gajjeraman S, Schultz D, Cookson D, Qin C, Butler WT, Hao J, George A. Spatially and temporally controlled biomineralization is facilitated by interaction between self-assembled dentin matrix protein 1 and calcium phosphate nuclei in solution. Biochemistry 2005;44(49):16140-16148.
8. Romberg RW, Werness PG, Riggs BL, Mann KG. Inhibition of hydroxyapatite-crystal growth by bone-specific and other calcium-binding proteins. Biochemistry 1986;25(5):1176-1180.
9. Davis JR. Handbook of materials for medical devices. Materials Park, OH: ASM International 2003.
10. Legeros RZ. Calcium phosphate materials in restorative dentistry: a review. Advances in Dental Research 1988 August 1, 1988;2(1):164-180.
11. Vehof JWM, Spauwen PHM, Jansen JA. Bone formation in calcium-phosphate-coated titanium mesh. Biomaterials 2000;21(19):2003-2009.
12. Kay MI, Young RA, Posner AS. Crystal Structure of Hydroxyapatite. Nature 1964;204(4963):1050-1052.
13. Rao RR, Roopa HN, Kannan TS. Solid state synthesis and thermal stability of HAP and HAP – β-TCP composite ceramic powders. Journal of Materials Science: Materials in Medicine 1997;8(8):511-518.
14. Feng W, Mu-sen L, Yu-peng L, Yong-xin Q. A simple sol-gel technique for preparing hydroxyapatite nanopowders. Materials Letters 2005;59(8-9):916-919.
15. Layrolle P, Ito A, Tateishi T. Sol-gel synthesis of amorphous calcium phosphate and sintering into microporous hydroxyapatite bioceramics. Journal of the American Ceramic Society 1998;81(6):1421-1428.
16. Milev A, Kannangara GSK, Ben-Nissan B. Morphological stability of hydroxyapatite precursor. Materials Letters 2003;57(13-14):1960-1965.
17. Afshar A, Ghorbani M, Ehsani N, Saeri MR, Sorrell CC. Some important factors in the wet precipitation process of hydroxyapatite. Materials and Design 2003;24(3):197-202.
18. Cuneyt Tas A. Synthesis of biomimetic Ca-hydroxyapatite powders at 37^{o}C in synthetic body fluids. Biomaterials 2000;21(14):1429-1438.
19. Onuma K, Ito A. Cluster growth model for hydroxyapatite. Chemistry of Materials 1998;10(11):3346-3351.
20. Rodriuez-Clemente R, Lopez-Macipe A, Gomez-Morales J, Torrent-Burgues J, Castano VM. Hydroxyapatite precipitation: A case of nucleation-aggregation-agglomeration-growth mechanism. Journal of the European Ceramic Society 1998;18(9):1351-1356.
21. Navrotsky A. Energetic clues to pathways to biomineralization: Precursors, clusters, and nanoparticles. Proceedings of the National Academy of Sciences of the United States of America 2004 August 17, 2004;101(33):12096-12101.
22. Suvorova EI, Buffat PA. Electron diffraction and high resolution transmission electron microscopy in the characterization of calcium phosphate precipitation from aqueous solutions under biomineralization conditions.

European Cells and Materials 2001;1:27-42.
23. Bertazzo S, Zambuzzi WF, Campos DDP, Ogeda TL, Ferreira CV, Bertran CA. Hydroxyapatite surface solubility and effect on cell adhesion. Colloids and Surfaces B: Biointerfaces 2010;78(2):177-184.
24. Monchau F, Lefevre A, Descamps M, Belquin-myrdycz A, Laffargue P, Hildebrand HF. In vitro studies of human and rat osteoclast activity on hydroxyapatite, β-tricalcium phosphate, calcium carbonate. Biomolecular Engineering 2002;19(2-6):143-152.
25. Balazic M, Kopc J. Review: titanium and titanium alloy applications in medicine. International Journal of Nano and Biomaterials 2007;1(1):3-34.
26. Laquerriere P, Grandjean-Laquerriere A, Jallot E, Balossier G, Frayssinet P, Guenounou M. Importance of hydroxyapatite particles characteristics on cytokines production by human monocytes in vitro. Biomaterials 2003;24(16):2739-2747.
27. Laquerriere P, Grandjean-Laquerriere A, Addadi-Rebbah S, Jallot E, Laurent-Maquin D, Frayssinet P, Guenounou M. MMP-2, MMP-9 and their inhibitors TIMP-2 and TIMP-1 production by human monocytes in vitro in the presence of different forms of hydroxyapatite particles. Biomaterials 2004;25(13):2515-2524.
28. Ratner BD, Bryant SJ. Biomaterials: where we have been and where we are going. Annual Reviews of Biomedical Engineering 2004;6:41-75.
29. Helsen JA, Breme HJ. Metals as biomaterials. Chichester: John Wiley & Sons Ltd., 1998.
30. Wever DJ, Veldhuizen AG, Sanders MM, Schakenraad JM, van Horn JR. Cytotoxic, allergic and genotoxic activity of a nickel-titanium alloy. Biomaterials 1997;18(16):1115-1120.
31. Alberktsson T, Johansson C. Osteoinduction, osteoconduction and osseointegration. European Spine Journal 2001;10(2):96-101.
32. Eisenbarth E, Linez P, Biehl V, Velten D, Breme J, Hildebrand HF. Cell orientation and cytoskeleton organisation on ground titanium surfaces. Biomolecular Engineering 2002;19(2-6):233-237.
33. Yoshinari M, Oda Y, Inoue T, Shimono M. Dry-process surface modification for titanium dental implants. Metallurgical and Materials Transactions A 2002;33(3):511-519.
34. Kokubo T, Kim HM, Kawashita M, Nakamura T. REVIEW Bioactive metals: preparation and properties. Journal of Materials Science: Materials in Medicine 2004;15(2):99-107.
35. Ahmad M, Gawronski D, Blum J, Goldberg J, Gronowicz G. Differential response of human osteoblast-like cells to commercially pure (cp) titanium grades 1 and 4. Journal of Biomedical Materials Research 1999;46(1):121-131.
36. Eisenbarth E, Velten D, Muller M, Thull R, Breme J. Biocompatibility of beta-stabilizing elements of titanium alloys. Biomaterials 2004;25(26):5705-5713.
37. Ohgoe Y, Kobayashi S, Ozeki K, Aoki H, Nakamori H, Hirakuri KK, Miyashita O. Reduction effect of nickel ion release on a diamond-like carbon film coated onto an orthodontic archwire. Thin Solid Films 2006;497(1-2):218-222.
38. Browne M, Gregson PJ. Effect of mechanical surface pretreatment on metal ion release. Biomaterials 2000;21(4):385-392.
39. Sousa SR, Barbosa MA. Effect of hydroxyapatite thickness on metal ion release from Ti6Al4V substrates. Biomaterials 1996;17(4):397-404.
40. Bagno A, Di Bello C. Surface treatments and roughness properties of Ti-based biomaterials. Journal of Materials Science: Materials in Medicine 2004;15(9):935-949.
41. Wennerberg A, Hallgren C, Johansson C, Danelli S. A histomorphometric evaluation of screw-shaped implants each prepared with two surface roughnesses. Clinical Oral Implants Research 1998;9(1):11-19.
42. Rosa AL, Beloti MM. Effect of cpTi surface roughness on human bone marrow cell attachment, proliferation, and differentiation. Brazilian Dental Journal 2003;14:16-21.
43. Wennerberg A, Albrektsson T, Johansson C, Andersson B. Experimental study of turned and grit-blasted screw-shaped implants with special emphasis on effects of blasting material and surface topography. Biomaterials 1996;17(1):15-22.
44. Anselme K, Linez P, Bigerelle M, Le Maguer D, Le Maguer A, Hardouin P, Hildebrand HF, Iost A, Leroy JM. The relative influence of the topography and chemistry of TiAl6V4 surfaces on osteoblastic cell behaviour. Biomaterials 2000;21(15):1567-1577.
45. Klokkevold PR, Nishimura RD, Adachi M, Caputo A. Osseointegration enhanced by chemical etching of the titanium surface. A torque removal study in the rabbit. Clinical Oral Implants Research 1997;8(6):442-447.
46. Davies J. Understanding peri-implant endosseous healing. Journal of Dental Education 2003;67(8):932-949.
47. Masmoudi M, Capek D, Abdelhedi R, El Halouani F, Wery M. Application of surface response analysis to the optimisation of nitric passivation of CP titanium and Ti6Al4V. Surface and Coatings Technology 2006;200(24):6651-6658.

48. Wisbey A, Gregson PJ, Peter LM, Tuke M. Effect of surface treatment on the dissolution of titanium-based implant materials. Biomaterials 1991;12(5):470-473.
49. Zwilling V, Aucouturier M, Darque-Ceretti E. Anodic oxidation of titanium and TA6V alloy in chromic media. An electrochemical approach. Electrochimica Acta 1999;45(6):921-929.
50. Wever DJ, Veldhuizen AG, de Vries J, Busscher HJ, Uges DRA, van Horn JR. Electrochemical and surface characterization of a nickel-titanium alloy. Biomaterials 1998;19(7-9):761-769.
51. Kuromoto NK, Simao RA, Soares GA. Titanium oxide films produced on commercially pure titanium by anodic oxidation with different voltages. Materials Characterization 2007;58(2):114-121.
52. Michiardi A, Helary G, Nguyen PCT, Gamble LJ, Anagnostou F, Castner DG, Migonney V. Bioactive polymer grafting onto titanium alloy surfaces. Acta Biomaterialia 2009;6(2):667-675.
53. Hayakawa T, Yoshinari M, Nemoto K. Characterization and protein-adsorption behavior of deposited organic thin film onto titanium by plasma polymerization with hexamethyldisiloxane. Biomaterials 2004;25(1):119-127.
54. Harris LG, Tosatti S, Wieland M, Textor M, Richards RG. *Staphylococcus aureus* adhesion to titanium oxide surfaces coated with non-functionalized and peptide-functionalized poly(-lysine)-grafted-poly(ethylene glycol) copolymers. Biomaterials 2004;25(18):4135-4148.
55. Molitor P, Barron V, Young T. Surface treatment of titanium for adhesive bonding to polymer composites: a review. International Journal of Adhesion and Adhesives 2001;21(2):129-136.
56. Hench L. Ceramic implants for humans. Advanced Ceramic Materials 1986;1(4):310-324.
57. ElBatal HA, Azooz MA, Khalil EMA, Soltan Monem A, Hamdy YM. Characterization of some bioglass-ceramics. Materials Chemistry and Physics 2003;80(3):599-609.
58. Kitsugi T, Nakamura T, Oka M, Senaha Y, Goto T, Shibuya T. Bone-bonding behavior of plasma-sprayed coatings of BioglassR, AW–glass ceramic, and tricalcium phosphate on titanium alloy. Journal of Biomedical Materials Research 1996;30(2):261-269.
59. Balamurugan A, Balossier G, Kannan S, Michel J, Rebelo AHS, Ferreira JMF. Development and in vitro characterization of sol-gel derived CaO-P_2O_5-SiO_2-ZnO bioglass. Acta Biomaterialia 2007;3(2):255-262.
60. Floroian L, Savu B, Stanciu G, Popescu AC, Sima F, Mihailescu IN, Mustata R, Sima LE, Petrescu SM, Tanaskovic D, Janackovic D. Nanostructured bioglass thin films synthesized by pulsed laser deposition: CSLM, FTIR investigations and in vitro biotests. Applied Surface Science 2008;255(5, Part 2):3056-3062.
61. Lopez-Sastre A, Gonzalo-Orden JM, Altónaga JAR, Altónaga JR, Orden MA. Coating titanium implants with bioglass and with hydroxyapatite. International Orthopaedics 1998;22(6):380-383.
62. Krishna BV, Bose S, Bandyopadhyay A. Low stiffness porous Ti structures for load-bearing implants. Acta Biomaterialia 2007;3(6):997-1006.
63. Moroni A, Caja VL, Egger EL, Trinchese L, Chao EYS. Histomorphometry of hydroxyapatite coated and uncoated porous titanium bone implants. Biomaterials 1994;15(11):926-930.
64. Chen YJ, Feng B, Zhu YP, Weng J, Wang JX, Lu X. Fabrication of porous titanium implants with biomechanical compatibility. Materials Letters 2009;63(30):2659-2661.
65. Nicula R, Lüthen F, Stir M, Nebe B, Burkel E. Spark plasma sintering synthesis of porous nanocrystalline titanium alloys for biomedical applications. Biomolecular Engineering 2007;24(5):564-567.
66. Oh I-H, Nomura N, Masahashi N, Hanada S. Mechanical properties of porous titanium compacts prepared by powder sintering. Scripta Materialia 2003;49(12):1197-1202.
67. Xue W, Krishna BV, Bandyopadhyay A, Bose S. Processing and biocompatibility evaluation of laser processed porous titanium. Acta Biomaterialia 2007;3(6):1007-1018.
68. Kim CS, Hwang KE, Hwo SJ. Hard tissue conmpatibility of titanium phosphide layers obtained by diffusion in Ti-Ha interface. Annals of transplantation 2004;9(1):82-87.
69. Jones AC, Arns CH, Sheppard AP, Hutmacher DW, Milthorpe BK, Knackstedt MA. Assessment of bone ingrowth into porous biomaterials using MICRO-CT. Biomaterials 2007;28(15):2491-2504.
70. Kienapfel H, Sprey C, Wilke A, Griss P. Implant fixation by bone ingrowth. The Journal of Arthroplasty 1999;14(3):355-368.
71. Dean JC, Tisdel CL, Goldberg VM, Parr J, Davy D, Stevenson S. Effects of hydroxyapatite tricalcium phosphate coating and intracancellous placement on bone ingrowth in titanium fibermetal implants. The Journal of Arthroplasty 1995;10(6):830-838.
72. Nguyen HQ, Deporter DA, Pilliar RM, Valiquette N, Yakubovich R. The effect of sol-gel-formed calcium phosphate coatings on bone ingrowth and osteoconductivity of porous-surfaced Ti alloy implants. Biomaterials 2004;25(5):865-876.
73. Zhang Q, Leng Y, Xin R. A comparative study of electrochemical deposition and biomimetic deposition of calcium phosphate on porous titanium. Biomaterials 2005;26(16):2857-2865.
74. Zeng H, Chittur KK, Lacefield WR. Analysis of bovine serum albumin adsorption on calcium phosphate

and titanium surfaces. Biomaterials 1999;20(4):377-384.
75. Schwartz-Arad D, Mardinger O, Levin L. Marginal bone loss pattern around hydroxyapatite-coated versus commercially pure titanium implants after up to 12 years of follow-up. International Journal of Oral Maxillofac Implants 2005;20(2):238-244.
76. Wang H, Eliza N, Xiang Z, Hsu H, Spector M, Hobbs L. Early bone apposition *in vivo* on plasma-sprayed and electrochemically deposited hydroxyapatite coatings on titanium alloy. Biomaterials 2006;27(23):4192-4230.
77. Tsui YC, Doyle C, Clyne TW. Plasma sprayed hydroxyapatite coatings on titanium substrates Part 1: Mechanical properties and residual stress levels. Biomaterials 1998;19(22):2015-2029.
78. Inagaki M, Yokogawa Y, Kameyama T. Effects of plasma gas composition on bond strength of hydroxyapatite/ titanium composite coatings prepared by rf-plasma spraying. Journal of European Ceramic Society 2006;26(4-5):495-499.
79. Deram V, Minichiello C, Vannier RN, Le Maguer A, Pawlowski L, Murano D. Microstructural characterizations of plasma sprayed hydroxyapatite coatings. Surface and Coatings Technology 2003;166(2-3):153-159.
80. Yan L, Leng Y, Weng L-T. Characterization of chemical inhomogeneity in plasma-sprayed hydroxyapatite coatings. Biomaterials 2003;24(15):2585-2592.
81. Ji H, Marquis PM. Effect of heat treatment on the microstructure of plasma-sprayed hydroxyapatite coating. Biomaterials 1993;14(1):64-68.
82. Lu Y-P, Li M-S, Li S-T, Wang Z-G, Zhu R-F. Plasma-sprayed hydroxyapatite+titania composite bond coat for hydroxyapatite coating on titanium substrate. Biomaterials 2004;25(18):4393-4403.
83. Inagaki M, Yokogawa Y, Kameyama T. Bond strength improvement of hydroxyapatite/titanium composite coating by partial nitriding during RF-thermal plasma spraying. Surface and Coatings Technology 2003;173(1):1-8.
84. Zeng H, Lacefield WR. XPS, EDX and FTIR analysis of pulsed laser deposited calcium phosphate bioceramic coatings: the effects of various process parameters. Biomaterials 2000;21(1):23-30.
85. Tri LQ, Chua DHC. An investigation into the effects of high laser fluence on hydroxyapatite/calcium phosphate films deposited by pulsed laser deposition. Applied Surface Science 2009;256(1):76-80.
86. Dinda GP, Shin J, Mazumder J. Pulsed laser deposition of hydroxyapatite thin films on Ti-6Al-4V: Effect of heat treatment on structure and properties. Acta Biomaterialia 2009;5(5):1821-1830.
87. Bao Q, Chen C, Wang D, Ji Q, Lei T. Pulsed laser deposition and its current research status in preparing hydroxyapatite thin films. Applied Surface Science 2005;252(5):1538-1544.
88. Stoch A, Brozek A, Kmita G, Stoch J, Jastrzebski W, Rakowska A. Electrophoretic coating of hydroxyapatite on titanium implants. Journal of Molecular Structure 2001;596(1-3):191-200.
89. Yen S, Lin C. Catholic reactions of electrolytic hydroxyapatite coating on pure titanium. Materials Chemistry and Physics 2002;77:70-76.
90. Lin J-H, Chang C-H, Chen Y-S, Lin G-T. Formation of bone-like apatite on titanium filament by a simulated body fluid inducing process. Surface and Coatings Technology 2006;200(12-13):3665-3669.
91. Kokubo T. Apatite formation on surfaces of ceramics, metals and polymers in body environment. Acta Materialia 1998;46(7):2519-2527.
92. Takadama H, Kim H, Kokubo T, Nakamura T. TEM-EDX study of mechanism of bonelike apatite formation on bioactive titanium metal in simulated body fluid. Journal of Biomedical Materials Research Part B: Applied Biomaterials 2001;57(3):441-448.
93. Takadama H, Kim H-M, Kokubo T, Nakamura T. XPS study of the process of apatite formation on bioactive Ti-6Al-4V alloy in simulated body fluid. Science and Technology of Advanced Materials 2001;2(2):389-396.
94. Takadama H, Kim H-M, Kokubo T, Nakamura T. An X-ray photoelectron spectroscopy study of the process of apatite formation on bioactive titanium metal. Journal of Biomedical Materials Research 2001;55(2):185-193.
95. Muler FA, Muler L, Caillard D, Conforto E. Preferred growth orientation of biomimetic apatite crystals. Journal of Crystal Growth 2007;304(2):464-471.
96. Lu X, Leng Y. TEM study of calcium phosphate precipitation on bioactive titanium surfaces. Biomaterials 2004;25(10):1779-1786.
97. Feng QL, Wang H, Cui FZ, Kim TN. Controlled crystal growth of calcium phosphate on titanium surface by NaOH-treatment. Journal of Crystal Growth 1999;200(3-4):550-557.
98. Yas AC, Bhaduri SB. Rapid coating of Ti6Al4V at room temprature with a calcium phosphate solution similar to 10x simulated body fluid. Journal of Materials Research 2004;19(9):2732-2749.
99. Kim H-M, Takadama H, Kokubo T, Nishiguchi S, Nakamura T. Formation of a bioactive graded surface structure on Ti-15Mo-5Zr-3Al alloy by chemical treatment. Biomaterials 2000;21(4):353-358.

100. Ducheyne P, Radin S, King L. The effect of calcium phosphate ceramic composition and structure on *in vitro* behavior. I. Dissolution. Journal of Biomedical Materials Research 1993;27(1):25-34.
101. Kasten P, Luginbühl R, van Griensven M, Barkhausen T, Krettek C, Bohner M, Bosch U. Comparison of human bone marrow stromal cells seeded on calcium-deficient hydroxyapatite, beta-tricalcium phosphate and demineralized bone matrix. Biomaterials 2003;24(15):2593-2603.
102. Suzuki O, Kamakura S, Katagiri T, Nakamura M, Zhao B, Honda Y, Kamijo R. Bone formation enhanced by implanted octacalcium phosphate involving conversion into Ca-deficient hydroxyapatite. Biomaterials 2006;27(13):2671-2681.
103. Cai Y, Zhang S, Zeng X, Wang Y, Qian M, Weng W. Improvement of bioactivity with magnesium and fluorine ions incorporated hydroxyapatite coatings via sol-gel deposition on Ti6Al4V alloys. Thin Solid Films 2009;517(17):5347-5351.
104. Qi G, Zhang S, Khor KA, Lye SW, Zeng X, Weng W, Liu C, Venkatraman SS, Ma LL. Osteoblastic cell response on magnesium-incorporated apatite coatings. Applied Surface Science 2008;255(2):304-307.
105. Bhadang KA, Holding CA, Thissen H, McLean KM, Forsythe JS, Haynes DR. Biological responses of human osteoblasts and osteoclasts to flame-sprayed coatings of hydroxyapatite and fluorapatite blends. Acta Biomaterialia 2010;6(4):1575-1583.
106. Jantov S, Theiszov M, Letasiov S, Birosov L, Palou TM. In vitro effects of fluor-hydroxyapatite, fluorapatite and hydroxyapatite on colony formation, DNA damage and mutagenicity. Mutation Research/Genetic Toxicology and Environmental Mutagenesis 2008;652(2):139-144.
107. Khang D, Kim SY, Liu-Snyder P, Palmore GTR, Durbin SM, Webster TJ. Enhanced fibronectin adsorption on carbon nanotube/poly(carbonate) urethane: Independent role of surface nano-roughness and associated surface energy. Biomaterials 2007;28(32):4756-4768.
108. Deligianni DD, Katsala ND, Koutsoukos PG, Missirlis YF. Effect of surface roughness of hydroxyapatite on human bone marrow cell adhesion, proliferation, differentiation and detachment strength. Biomaterials 2001;22(1):87-96.
109. Dalby MJ, Giannaras D, Riehle MO, Gadegaard N, Affrossman S, Curtis ASG. Rapid fibroblast adhesion to 27 nm high polymer demixed nano-topography. Biomaterials 2004;25(1):77-83.
110. Roohani-Esfahani S-I, Nouri-Khorasani S, Lu Z, Appleyard R, Zreiqat H. The influence hydroxyapatite nanoparticle shape and size on the properties of biphasic calcium phosphate scaffolds coated with hydroxyapatite-PCL composites. Biomaterials 2010;31(21):5498-5509.
111. Chou Y-F, Huang W, Dunn JCY, Miller TA, Wu BM. The effect of biomimetic apatite structure on osteoblast viability, proliferation, and gene expression. Biomaterials 2005;26(3):285-295.
112. Blind O, Klein LH, Dailey B, Jordan L. Characterization of hydroxyapatite films obtained by pulsed-laser deposition on Ti and Ti-6Al-4V substrates. Dental Materials 2005;21(11):1017-1024.
113. Nagano M, Nakamura T, Kokubo T, Tanahashi M, Ogawa M. Differences of bone bonding ability and degradation behaviour *in vivo* between amorphous calcium phosphate and highly crystalline hydroxyapatite coating. Biomaterials 1996;17(18):1771-1777.
114. Ong JL, Hoppe CA, Cardenas HL, Cavin R, Carnes DL, Sogal A, Raikar GN. Osteoblast precursor cell activity on HA surfaces of different treatments. Journal of Biomedical Materials Research 1998;39(2):176-183.
115. Ball MD, Downes S, Scotchford CA, Antonov EN, Bagratashvili VN, Popov VK, Lo WJ, Grant DM, Howdle SM. Osteoblast growth on titanium foils coated with hydroxyapatite by pulsed laser ablation. Biomaterials 2001;22(4):337-347.
116. Costerton JW, Stewart PS, Greenberg EP. Bacterial biofilms: a common cause of persistent infections. Science 1999;284(5418):1318-1322.
117. Donlan RM. Biofilm formation: a clinically relevant microbiological process. Clinical Infectious Diseases 2001;33(8):1387-1392.
118. van Hullebusch E, Zandvoort M, Lens P. Metal immobilisation by biofilms: Mechanisms and analytical tools. Reviews in Environmental Science and Biotechnology 2003;2(1):9-33.
119. Cabeen MT, Jacobs-Wagner C. Bacterial cell shape. Nature Reviews Microbiology 2005;3(8):601-610.
120. Savage DC, Fletcher M. Bacterial adhesion. New York: Plenum Press, 1985.
121. Pallen MJ, Matzke NJ. From the origin of species to the origin of bacterial flagella. Nature Reviews Microbiology 2006;4(10):784-790.
122. Fronzes R, Remaut H, Waksman G. Architectures and biogenesis of non-flagellar protein appendages in Gram-negative bacteria. The Embo Journal 2008;27(17):2271-2280.
123. Yuehuei HA, Richard JF. Concise review of mechanisms of bacterial adhesion to biomaterial surfaces. Journal of Biomedical Materials Research 1998;43(3):338-348.
124. Klausen M, Heydorn A, Ragas P, Lambertsen L, Tolker-Nielsen T. Biofilm formation by *Pseudomonas aeruginosa* wild type, flagella and type IV pili mutants. Molecular Microbiology 2003;48(6):1511-1524.

125. Mabboux F, Ponsonnet L, Morrier J-J, Jaffrezic N, Barsotti O. Surface free energy and bacterial retention to saliva-coated dental implant materials -- an *in vitro* study. Colloids and Surfaces B: Biointerfaces 2004;39(4):199-205.
126. Boulange-Petermann L, Baroux B, Bellon-Fontaine M-N. The influence of metallic surface wettability on bacterial adhesion. Journal of Adhesion Science and Technology 1993;7(3):221-230.
127. Vanhaecke E, Remon J, Moores M, Raes F, Rudder D, Peteghem A. Kinetics of *Pseudomonas aeruginosa* adhesion to 304 and 316-L stainless steel: role of cell surface hydrophobicity. Applied and Environmental Microbiology 1990;56(3):788-795.
128. Li B, Logan BE. Bacterial adhesion to glass and metal-oxide surfaces. Colloids and Surfaces B: Biointerfaces 2004;36(2):81-90.
129. Donlan RM. Biofilms: microbial life on surfaces. Emerging Infectious Diseases 2002;8(9):881-891.
130. Poortinga AT, Bos R, Busscher HJ. Measurement of charge transfer during bacterial adhesion to an indium tin oxide surface in a parallel plate flow chamber. Journal of Microbiological Methods 1999;38(3):183-189.
131. Poortinga AT, Bos R, Busscher HJ. Charge transfer during Staphylococcal adhesion to TiNOX® coatings with different specific resistivity. Biophysical Chemistry 2001;91(3):273-279.
132. Li JX, Wang J, Shen LR, Xu ZJ, Li P, Wan GJ, Huang N. The influence of polyethylene terephthalate surfaces modified by silver ion implantation on bacterial adhesion behavior. Surface and Coatings Technology 2007;201(19-20):8155-8159.
133. Bollenl CML, Lambrechts P, Quirynen M. Comparison of surface roughness of oral hard materials to the threshold surface roughness for bacterial plaque retention: A review of the literature. Dental Materials 1997;13(4):258-269.
134. Emerson RJ, Bergstrom TS, Liu Y, Soto ER, Brown CA, McGimpsey WG, Camesano TA. Microscale correlation between surface chemistry, texture, and the adhesive strength of *Stephylococcus epidermidis*. Langmuir 2006;22(26):11311-11321.
135. Scheuerman TR, Camper AK, Hamilton MA. Effects of substratum topography on bacterial adhesion. Journal of Colloid and Interface Science 1998;208(1):23-33.
136. Lauga E, DiLuzio WR, Whitesides GM, Stone HA. Swimming in circles: motion of bacteria near solid boundaries. Biophysical Journal 2006;90(2):400-412.
137. Reisner A, Haagensen JAJ, Schembri MA, Zechner EL, Molin S. Development and maturation of *Escherichia coli* K-12 biofilms. Molecular Microbiology 2003;48(4):933-946.
138. Stoodley P, Sauer K, Davies DG, Costerton JW. Biofilms as complex differentiated communities. Annual Review of Microbiology 2002;56(1):187-209.
139. Picioreanu C, Loosdrecht MCMv, Heijnen JJ. Discrete-differential modelling of biofilm structure. Water Science and Technology 1999;39(7):115-122.
140. Katsikogianni M, Missirlis YF. Concise review of mechanisms of bacterial adhesion to biomaterials and of techniques used in estimating bacterial-material interactions. European Cells and Materials 2004;8:37-57.
141. Kozlova EV, Popov VL, Sha J, Foltz SM, Erova TE, Agar SL, Horneman AJ, Chopra AK. Mutation in the S-ribosylhomocysteinase (luxS) gene involved in quorum sensing affects biofilm formation and virulence in a clinical isolate of Aeromonas hydrophila. Microbial Pathogenesis 2009;45(5-6):343-354.
142. De Araujo C, Balestrino D, Roth L, Charbonnel N, Forestier C. Quorum sensing affects biofilm formation through lipopolysaccharide synthesis in *Klebsiella pneumoniae*. Research in Microbiology 2010;161(7):595-603.
143. Zhang K, Ou M, Wang W, Ling J. Effects of quorum sensing on cell viability in *Streptococcus* mutans biofilm formation. Biochemical and Biophysical Research Communications 2009;379(4):933-938.
144. Klausen M, Aaes-Jogensen A, Molin S, Tolker-Nielsen T. Involvement of bacterial migration in the development of complex multicellular structures in *Pseudomonas aeruginosa* biofilms. Molecular Microbiology 2003;50(1):61-68.
145. Gjaltema A, Arts PAM, Loosdrecht CMv, Kuenen JG, Heijnen JJ. Heterogeneity of biofilm on rotating annular reactors: Occurance, structure and consuquences. Biotechnology and Bioengineering 1994;44(2):194-204.
146. Peyton BM. Effects of shear stress and substrate loading rate on *Pseudomonas aeruginosa* biofilm thickness and density. Water Research 1996;30(1):29-36.
147. Characklis WG. Fouling biofilm development: a process analysis. Biotechnology and Bioengineering 1981;23(9):1923-1960.
148. Puckett SD, Taylor E, Raimondo T, Webster TJ. The relationship between the nanostructure of titanium surfaces and bacterial attachment. Biomaterials 2010;31(4):706-713.
149. Yoshinari M, Oda Y, Kato T, Okuda K. Influence of surface modifications to titanium on antibacterial activity in vitro. Biomaterials 2001;22(14):2043-2048.
150. Hu X, Neoh K-G, Shi Z, Kang E-T, Poh C, Wang W. An in vitro assessment of titanium functionalized with

polysaccharides conjugated with vascular endothelial growth factor for enhanced osseointegration and inhibition of bacterial adhesion. Biomaterials 2010;31(34):8854-8863.
151. Truong VK, Lapovok R, Estrin YS, Rundell S, Wang JY, Fluke CJ, Crawford RJ, Ivanova EP. The influence of nano-scale surface roughness on bacterial adhesion to ultrafine-grained titanium. Biomaterials 2010;31(13):3674-3683.
152. Jeyachandran YL, Venkatachalam S, Karunagaran B, Narayandass SK, Mangalaraj D, Bao CY, Zhang CL. Bacterial adhesion studies on titanium, titanium nitride and modified hydroxyapatite thin films. Materials Science and Engineering: C 2007;27(1):35-41.
153. Chen Y, Zheng X, Xie Y, Ji H, Ding C. Antibacterial properties of vacuum plasma sprayed titanium coatings after chemical treatment. Surface and Coatings Technology 2009;204(5):685-690.
154. Mo A, Liao J, Xu W, Xian S, Li Y, Bai S. Preparation and antibacterial effect of silver-hydroxyapatite/titania nanocomposite thin film on titanium. Applied Surface Science 2008;255(2):435-438.
155. Zhang F, Zhang Z, Zhu X, Kang E-T, Neoh K-G. Silk-functionalized titanium surfaces for enhancing osteoblast functions and reducing bacterial adhesion. Biomaterials 2008;29(36):4751-4759.
156. Anagnostou F, Debet A, Pavon-Djavid G, Goudaby Z, Hélary G, Migonney V. Osteoblast functions on functionalized PMMA-based polymers exhibiting Staphylococcus aureus adhesion inhibition. Biomaterials 2006;27(21):3912-3919.
157. Chun YB, Yu SH, Semiatin SL, Hwang SK. Effect of deformation twinning on microstructure and texture evolution during cold rolling of CP-titanium. Materials Science and Engineering A 2005;398(1-2):209-219.
158. Stolyarov VV, Zhu YT, Alexandrov IV, Lowe TC, Valiev RZ. Grain refinement and properties of pure Ti processed by warm ECAP and cold rolling. Materials Science and Engineering A 2003;343(1-2):43-50.
159. Wu X, Mei J. Near net shape manufacturing of components using direct laser fabrication technology. Journal of Materials Processing Technology 2003;135(2-3):266-270.
160. Clapham L, McLean RJC, Nickel JC, Downey J. The influence of bacteria on struvite crystal habit and its importance in urinary stone formation. Journal of Crystal Growth 1990;104(2):475-484.
161. Beveridge TJ. Role of cellular design in bacterial metal accumulation and mineralization. Annual Review of Microbiology 1989;43:147-171.
162. Macaskie LE, Bonthrone KM, Yong P, Goddard DT. Enzymically mediated bioprecipitation of uranium by a *Citrobacter* sp.: a concerted role for exocellular lipopolysaccharide and associated phosphatase in biomineral formation. Microbiology 2000;146(8):1855-1867.
163. Macaskie LE, Yong P, Paterson-Beedle M, Thackray AC, Marquis PM, Sammons RL, Nott KP, Hall LD. A novel non line-of-sight method for coating hydroxyapatite onto the surfaces of support materials by biomineralization. Journal of Biotechnology 2005;118(2):187-200.
164. L.Sammons R, Thackray AC, Ledo HM, Marquis PM, Jones IP, Yong P, Macaskie LE. Characterisation and sintering of nanophase hydroxyapatite synthesised by a species of *Serratia*. Journal of Physics: Confrence Series 2007;93:1-7.
165. Barkay T, Schaefer J. Metal and radionuclide bioremediation: issues, considerations and potentials. Current Opinion in Microbiology 2001;4(3):318-323.
166. Cerbasi IH, Yetis U. Biosorption of Ni(ii) and Pb(ii) by *Phanerochaete chrysosporium* from a binary metal system-kinetics. Water S A 2007;27(1):15-20.
167. Volesky B, Holan ZR. Biosorption of heavy metals. Biotechnology Progress 1995;11(3):235-250.
168. Pagnanelli F, Petrangeli Papini M, Trifoni M, Veglio F. Biosorption of metal ions on *Arthrobacter* sp.: biomass characterization and biosorption modeling. Environmental Science and Technology 2000;34(13):2773-2778.
169. Puranik PR, Paknikar KM. Biosorption of lead and zinc from solutions using *Streptoverticillium cinnamoneum* waste biomass. Journal of Biotechnology 1997;55(2):113-124.
170. Tsezos M, Remoudaki E, Angelatou V. A study of the effects of competing ions on the biosorption of metals. International Biodeterioration and Biodegradation 1996;38(1):19-29.
171. Inskeep WP, Macur RE, Harrison G, Bostick BC, Fendorf S. Biomineralization of As(V)-hydrous ferric oxyhydroxide in microbial mats of an acid-sulfate-chloride geothermal spring, Yellowstone National Park. Geochimica et Cosmochimica Acta 2004;68(15):3141-3155.
172. Smith T, Pitts K, McGarvey JA, Summers AO. Bacterial oxidation of mercury metal vapor, Hg(0). Applied and Environmental Microbiology 1998;64(4):1328-1332.
173. Amemiya Y, Arakaki A, Staniland SS, Tanaka T, Matsunaga T. Controlled formation of magnetite crystal by partial oxidation of ferrous hydroxide in the presence of recombinant magnetotactic bacterial protein Mms6. Biomaterials 2007;28(35):5381-5389.
174. Williams KH, Ntarlagiannis D, Slater LD, Dohnalkova A, Hubbard SS, Banfield JF. Geophysical imaging

of stimulated microbial biomineralization. Environmental Science and Technology 2005;39(19):7592-7600.
175. Newman D, Beveridge T, Morel F. Precipitation of arsenic trisulfide by *Desulfotomaculum auripigmentum*. Appllied Environmental Microbiology 1997;63(5):2022-2028.
176. Macaskie LE, Empson RM, Cheetham AK, Grey CP, Skarnulis AJ. Uranium bioaccumulation by a *Citrobacter* sp. as a result of enzymically mediated growth of polycrystalline HUO_2PO_4. Science 1992;257(5071):782-784.
177. Macaskie LE, Bonthrone KM, Yong P, Goddard DT. Enzymically mediated bioprecipitation of uranium by a *Citrobacter* sp.: a concerted role for exocellular lipopolysaccharide and associated phosphatase in biomineral formation Microbiology 2000;146:1855-1867.
178. Yong P, Macaskie LE, Sammons RL, Marquis PM. Synthesis of nanophase hydroxyapatite by a *Serratia* sp. from waste-water containing inorganic phosphate. Biotechnology Letters 2004;26(22):1723-1730.
179. Thackray AC, Sammons RL, Macaskie LE, Yong P, Lugg H, Marquis PM. Bacterial biosynthesis of a calcium phosphate bone-substitute material. Journal of Materials Science: Materials in Medicine 2004;15(4):403-406.
180. Gabriel BL, Gold J, Gristina AG, Kasemo B, Lausmaa J, Harrer C, Myrvik QN. Site-specific adhesion of *Staphylococcus epidermidis* (RP12) in Ti-Al-V metal systems. Biomaterials 1994;15(8):628-634.
181. Geesey GG, Gillis RJ, Avci R, Daly D, Hamilton M, Shope P, Harkin G. The influence of surface features on bacterial colonization and subsequent substratum chemical changes of 316L stainless steel. Corrosion Science 1996;38(1):73-95.
182. Faghihi S, Azari F, Li H, Bateni MR, Szpunar JA, Vali H, Tabrizian M. The significance of crystallographic texture of titanium alloy substrates on pre-osteoblast responses. Biomaterials 2006;27(19):3532-3539.

Chapter 2 Experimental methods

2.1 Choice of bacteria, bacterial adhesion and proliferation

Bacterial interaction with implant surfaces such as titanium can be influenced by numerous factors, among which the substrate surface properties have a major effect [1, 2]. The effect of titanium alloy structure bacterial adhesion and proliferation is investigated in this section.

Two Gram-positive bacteria, *Staphylococcus epidermidis* 11047 (*S. epidermidis*) and *Streptococcus sanguinis* GW2 (*S. sanguinis*) and two Gram-negative ones, *Escherichia coli* 10418 (*E. coli*) and *Serratia* sp. NCIMB 40259 (*Serratia*) were allowed to adhere to, and to proliferate on the metal substrates. *S. epidermidis* colonise the skin and mucous membrane of human body and are a major cause of nosocomial infections [3]. It is one of the most commonly isolated aerobic microbe from medical implant-infections. *S. sanguinis* often present in anaerobic environment such as in the human oral cavity. Their colonisation plays a major role in the initial stages of formation of dental plaque [4]. *E.coli* was used as a typical example of a Gram-negative bacterium usually present within the gut. *Serratia* was a Gram-negative bacterium closely related to *E. coli*. Compared with *E. coli*, *Serratia* is non-pathogenic and is more usually an environmental microorganism and, as such, would be more expected to form biofilms since the latter is the preferred format in nature. *Serratia* was also selected as a foundation for subsequent work on biofilm formation and biomineralisation.

2.1.1 Substrate preparation

Commercially pure titanium (CP Ti, TIMET, UK) and Ti6Al4V (Ti 64, TIMET, UK) discs with a diameter of 10 mm were ground and polished using a series of waterproof silicon

carbide papers (Struers, UK), from #400 to #1200, followed by a 9 μm diamond suspension (Struers, UK) and activated colloidal silica solution (Struers, UK). Polished pure aluminium (Goodfellows, UK) and vanadium (provided by Dr. Mark Ward, School of Metallurgy and Materials, University of Birmingham) discs prepared by the same procedure were used as controls. The specimens were cleaned in acetone, ethanol and distilled water in sequence in an ultrasonic bath, for 10 min in each solution.

2.1.2 Bacterial adhesion

The bacteria were grown in tryptone soya broth (TSB) overnight and harvested by centrifugation at 3000 rpm at 4 °C for 10 min (SANYO HARRIER 18/80). The growth conditions for each type of bacterium are listed in Table 2. 1. The cells were washed in sterile phosphate buffered saline (PBS) twice and resuspended in PBS to an optical density at 600 nm wavelength (OD_{600}) of 0.05. The OD_{600} was read using a BOECO s-22 UV/Vis Spectrophotometre with distilled water as a reference. PBS was used as a non-nutrient suspension medium to prevent bacterial proliferation. The metal discs were suspended vertically in the bacterial suspension and incubated in the same conditions used for the culture preparation for four hours.

Table 2. 1 Bacteria growth conditions

Bacteria	***Temperature****	***Atmosphere***
Serratia	30°C	Air (GALLENKAMP Plus II Incubator)
E. coli	37°C	Air (GALLENKAMP Plus II Incubator)
S. epidermidis	37°C	Air (GALLENKAMP Plus II Incubator)
S. sanguinis	36°C	80% N_2, 10% CO_2 and 10% H_2 (mini MACS Anaerobic Workstation)

**Serratia* was grown at 30 °C since as an environmental bacterium, its optimum growth condition (temperature) is lower than that of a pathogen, such as *E. coli* which was incubated at 37^{o}C. The aerobic (*S. epidermidis*) and anaerobic (*S. sanguinis*) conditions reflect the normal growth format of these strains.

2.1.3 *Serratia* proliferation on titanium substrates

Carbon-limited minimal medium was prepared according to a previous study [5] by aseptically combining sterile ionic medium and lactose solution, as seen in Table 2. 2. *Serratia* was cultured in 100 ml carbon-limited minimal medium in a shaking incubator (150 rpm) at 30°C for 72 hours (GALLENKAMP Plus II Incubator) to grow a primary culture. 10 ml of this primary culture were combined with 100 ml minimal medium and cultured for a further 72 hours to grow a secondary culture. This procedure promoted the development of fimbriae which are required for biofilm formation by this bacterium [6]. The metal samples were then suspended vertically in 200 ml of the secondary culture diluted with minimal medium to an OD_{600} of approximately 0.05 and incubated at 30°C for 24 hours to allow bacterial proliferation.

Table 2. 2 The chemical composition of the carbon-limited minimal medium

Ionic medium, pH adjusted to 7.2~7.3 with HCl		
Tris buffer, $(HOCH_2)_3CNH_2$,	Sigma 7-9® USA	12 g/L
KCl	Sigma USA	0.62 g/L
$(NH_4)_2HPO_4$	Fisons UK	0.96 g/L
$MgSO_4 \cdot 7H_2O$	Aldrich UK	0.063 g/L
$FeSO_4 \cdot 7H_2O$	BDH UK	0.00032 g/L
Polypropylene glycol	Sigma UK	5 μL/L
Lactose medium		
Lactose	Oxoid UK	0.6 g/L

2.2 *Serratia* biofilm formation on titanium substrates

2.2.1 Substrate preparation

Pure titanium discs supplied by commercial companies (for another cell culture study) which had received six different surface treatments, as detailed in Table 2. 3, were used as substrates for comparison of biofilm formation. These titanium discs, together with porous pure titanium mesh referred to as 'titanium web' (Hi-Lex Corp. Ltd, Japan) were directly loaded into an air-lift fermenter described below. The titanium web was designed as a mammalian cell carrier, and has been shown to lead to rapid bone formation *in vivo* [7, 8].

Table 2. 3 Titanium substrates

Sample ID	***Surface treatments***
Ti1	50 μm Al_2O_3 grit blasted pure titanium (at 5.5 MPa for 60 s)
Ti2	Mirror polished pure titanium (prepared as described in 2.1.1)
Ti3	Grit blasted 'Deep Profile Surface' (DPS) Titanium discs FRIOS® 10-5016, DENTSPLY FRIADENT Mannheim, Germany
Ti4	Plasma sprayed Titanium discs (TPS) Fa. Oraltronics, Bremen, Germany
Ti5	Acid etched Titanium discs Fa. Oraltronics, Bremen, Germany
Ti6	Grit blasted and Plus surface titanium discs FRIANDENT FRIOS® 00-055290, DENTSPLY FRIADENT Mannheim, Germany

2.2.2 Biofilm formation: fermentation

Biofilm was grown *in vitro* in an air-lift fermenter. Secondary *Serratia* culture was prepared as previously described in § 2.1.3.

Acid phosphatase enzyme activity assay

The acid phosphatase enzyme specific activity (Sp. Act) of the bacteria cultures was measured, and only those with the value higher than 1000 were used. A high phosphatase enzyme activity is important for biofilm formation and biomineralisation [6].

Specific activity was determined by the analysis of the p-nitrophenol (pNP) released from p-nitrophenyl phosphate (p-NPP) catalysed by the bacteria-produced enzyme [9]. The released pNP showed a bright yellow colour whose absorbance was recorded to calculate Sp. Act.

For the phosphatase activity assay, 1 ml of the bacterial suspension was diluted with 1 ml 20 mM MOPS buffer (3-(N-morpholino)-propane-sulphonic acid, Sigma USA, adjusted to

pH=7.0) and 0.4 ml 32 mM p-NPP (Acros Organics USA) was added. 5 ml 0.2 M NaOH was added later to stop the reaction, with the time of the reaction recorded. The absorbance was then read at wavelength 410 nm using a spectrophotometer (Boeco, S-22). A reference was obtained by adding NaOH before p-NPP. The optical density of the original bacterial suspension was also measured at 600 nm (OD_{600}), with distilled water as reference.

Bacterial acid phosphatase enzyme specific activity (unit: nmol of pNP liberated per minute per mg bacterial protein) can be calculated by the equation below [9]:

$$\text{Sp.Act} = \frac{\partial \text{A} \times 10^9}{\varepsilon_{410}} \times \frac{7.4}{1000} \times \frac{1}{0.278 \times 1 \times \text{OD}_{600} \times \text{t}}$$

Here,

∂A	Absorbance at 410 nm due to the liberated pNP
7.4/1000	Dilution factor of the assay
ε_{410}	Molar extinction coefficient (M^{-1} cm^{-1}) of pNP at 410 nm under the conditions of the assay, obtained from the pNP standard curve which was prepared using the assay solution. (A value of 18472 was used for the conditions described.)
$0.278 \times 1 \times OD_{600}$	The 1 ml protein content at OD_{600}, which was 0.278 mg ml^{-1} at OD_{600} = 1.000 by the Lowry method.
t	Time of the assay in minutes.

Fermenter column assembly

Figure 2. 1 shows the air-lift fermenter assembly used in this work. Titanium substrates were loaded inside the fermenter body (300 ml capacity) and the assembled fermenter apparatus was autoclaved at 121 °C for 20 minutes (1 bar pressure) (Prestige Medical autoclave). 30 ml of the secondary culture was injected aseptically into the sterilised fermenter body through the 'culture inlet' in Figure 2. 1a and minimal medium was pumped in through 'medium inflow'

to fill up the fermenter. The whole assembly was stood in a water bath at 30 °C. After 24 hours, the medium inflow was turned to continuous mode at a controlled speed of 30 ml/h for another 6 days. The fermenter body was wrapped in an aluminium foil to avoid potential photocatalytic inactivation of the bacteria due to the interaction between light and the thin oxide film on the titanium discs (TiO_2) and the subsequent formation of highly oxidising hydroxyl radicals (·OH) which will attack the bacterial cell wall [10, 11].

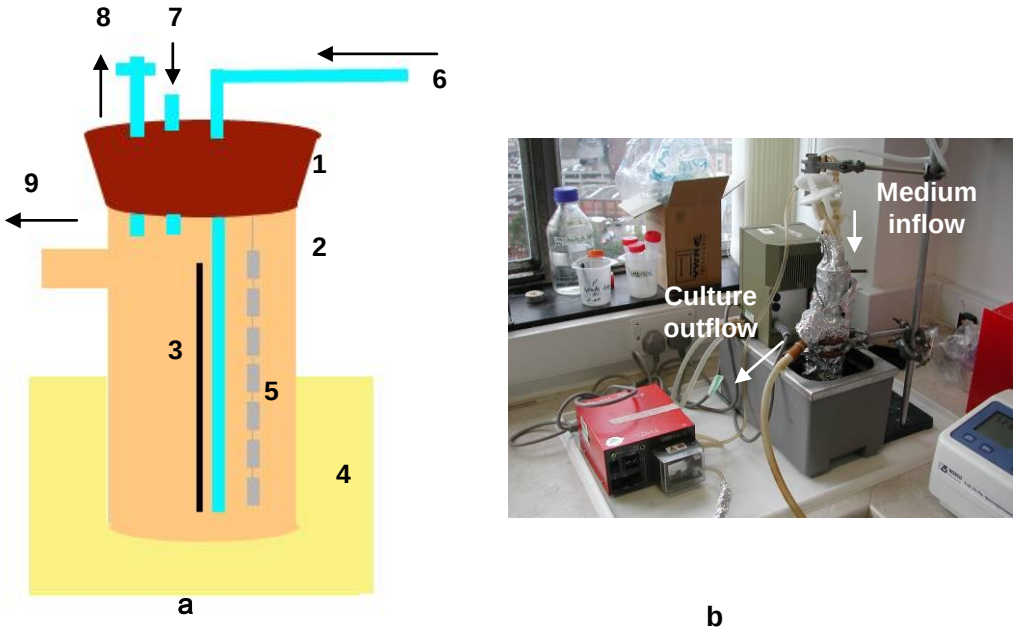

Figure 2. 1 The air-lift fermenter apparatus

a: A schematic diagram of the fermenter set.

1. Silicone fermenter stopper; 2. Fermenter body; 3. Glass central partition; 4. Water bath; 5. Metal samples; 6. Medium inflow; 7. Culture inlet; 8. Air outlet with air filter; 9. Culture outflow.

b: The assembled fermenter apparatus.

It was observed that if the samples were arranged in a string as illustrated in Figure 2. 1a, the thickness of the biofilm differed a lot, depending on the location of the sample within the fermenter body and whether there were other structures around to stimulate biofilm growth, such as porous substrates. The biofilm on specimens that were at the bottom of the fermenter (1 in Figure 2. 2a), the closest to the medium and air supply, or adjacent to any porous structure nearby (3 in Figure 2. 2a), usually tended to be thicker, whilst it was thinner on those that were near the liquid surface (4 in Figure 2. 2a), or were shielded by another structure (5 in Figure 2.2a). To minimise these artifacts, the specimens (for the biofilm formation on different titanium surfaces) were aligned in three horizontal rows on a wooden ladder positioned randomly and far enough apart to avoid ‘shielding’, as shown in Figure 2. 2b. The ladder was placed in the middle of the fermenter body.

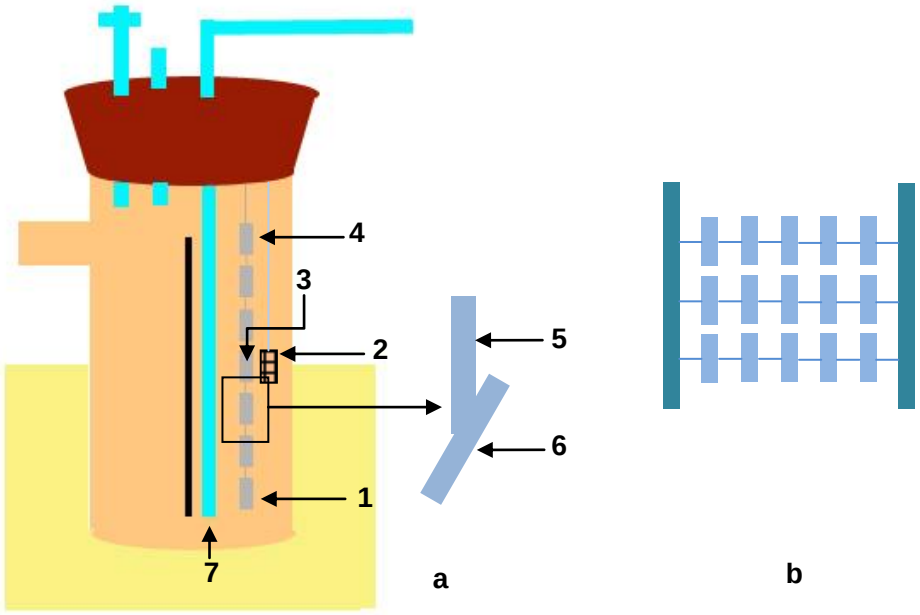

Figure 2. 2 Schematic drawing of sample locations in the fermenter

a: 1: A sample at the bottom of the fermenter body nearest to medium/air supply (7). 3: A sample with a porous structure (2) nearby. 4: A sample at the surface of the liquid (top of the fermenter) farthest from the medium/air supply. 5: A sample that is shielded by a certain structure (6) another sample, for example.

b: Specimens arranged on a wooden ladder.

2.3 Biomineralisation of HA on titanium substrates

2.3.1 Substrate and biofilm preparation

Pure titanium discs grit blasted with 50 μm Al_2O_3 (Ti1 in Table 2. 3) were used as substrates to support both biofilm and subsequent crystal coatings.

The Ti discs were treated with alkali and the influence of the alkali treatment on the bacterial biomineralisation was studied. The grit blasted discs were rinsed in 10 M NaOH (Sigma UK)

at 60 ºC for 24 hours. They were then heated to 600 ºC at 5 ºC/min in an air furnace (Elite Thermal Systems Limited) and held for 1 hour before being furnace cooled. The substrates were gently washed in distilled water before they were loaded into the fermenter for *Serratia* biofilm growth. The porous titanium webs (Hi-Lex. Ltd, Japan) were selected to test the ability of this method to apply a coating to a porous substrate.

Biofilm was pregrown on the titanium discs in the fermenter as described in § 2.2.2. To coat the Ti web, fresh minimal medium was pumped through for 4 days instead of 6 to obtain a thinner biofilm to avoid occluding the holes in the web.

2.3.2 Biomineralisation

Samples with the pregrown biofilms were arranged in a glass column (length: 250 mm; diameter: 25 mm) filled with mineralisation solution consisting of 50 mM AMPSO buffer ($C_7H_{16}NNaO_5S$, adjusted to pH=8.6, Sigma UK), 25 mM $CaCl_2$ (Sigma UK) and 50 mM β-glycerol phosphate (β-GP, $C_3H_9O_6P$, BDH UK), based on a previous study results which demonstrated that this mixture gave the highest crystal yield [9]. The apparatus, as shown in Figure 2. 3, was left still for 24 hours for nucleation before the medium flow was turned to 1.5 ml/h for another nine days. Alternatively, the inflow was controlled at 15 ml/h. One sample was taken out every day to examine the progress of the crystal formation during mineralisation. The crystal coated titanium samples were dried at 60 ºC for 24 hours.

Figure 2. 3 The bioreactor used for the biomineralisation.

a: A schematic diagram of the bioreactor. 1. Medium inflow; 2. Medium outflow.

b: The assembled bioreactor.

2.3.3 The influence of ion strength on crystal formation

Bacterial biomineralisation is sensitive to its environment such as ion concentration of the mineralisation solution, which was investigated in this section. It is very difficult to characterise systematically this influence directly on the crystal coatings obtained from § 2.3.2, due to reasons that was discussed in Chapter 8. Hence an artificial environment was created to mimic several possible conditions that may interfere with the biomineralisation, with either reduced calcium or phosphate (β-GP) source.

Bacterial suspensions were prepared according to Table 2. 4 with different ion concentrations. 20 ml of each solution was kept in a universal bottle and shaken at room temperature at a speed of 150 rpm for three days. The white precipitates in each suspension were harvested by centrifuging at 3000 rpm at 4 ºC for 10 min and dried at 60 ºC for 24 hours for further

analysis.

Table 2. 4 The ionic composition of calcium/phosphate deficient conditions

	AMPSO /mM (pH=8.6)	***$CaCl_2$ /mM***	***β-GP /mM***	***Serratia /OD_{600}***
Phosphate excess condition	50	2.5	50	0.5
Calcium excess condition	50	25	5	0.5

2.3.4 Heat treatment of coated titanium

Heat treatment of the nascent crystal coated titanium samples was carried out in an argon protected furnace (Pyro THERM FURNACES). As seen in Figure 2. 4, the temperature was ramped to 550 ºC at 5 ºC/min and held for 3 hours. This step was applied to burn off the biomass and any residual organic components [9]. The samples were then further sintered at 800 ºC for 5 hours (route 1) or 10 hours (route 2) before they were cooled down at 5 ºC/min. This was to sinter and consolidate the crystals.

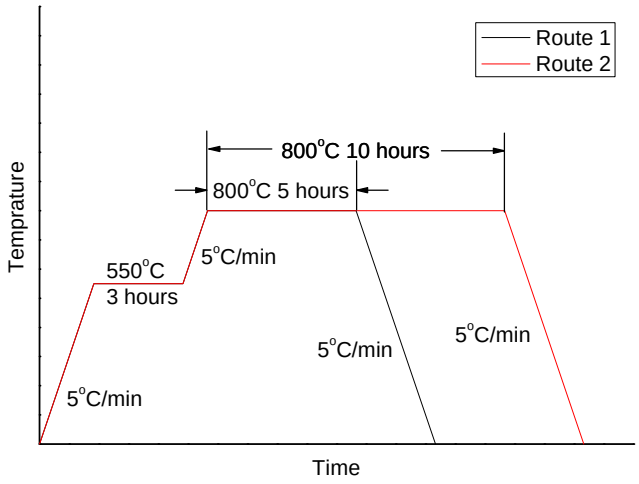

Figure 2. 4 Heat treatment routes

2.4 Characterisation

2.4.1 Substrate water contact angle measurement

Water contact angle measurements (WCA) on the metal substrates were carried out using a custom built contact angle goniometer. As shown in Figure 2. 5, distilled water was dropped gently to the test surface using a 25μL syringe, during which process the shape of the water drop was recorded continuously using a digital video camera. The (advancing) water contact angle was measured using Camtel FTA200 software automatically. Three measurements were taken from each sample at different locations and the average value was used.

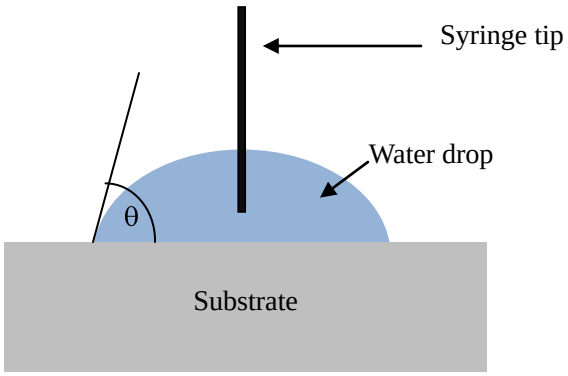

Figure 2. 5 Water contact angle (θ) measurement

2.4.2 Substrate surface roughness: Ra values

Substrate surface roughness in terms of Ra, the arithmetic average deviation of the surface valleys and peaks, was measured using a Talysurf 10 kit. Three measurements were taken from each specimen over a distance of 3 mm.

2.4.3 Quantitative analysis of the biofilm: protein assay

Due to the large number of bacteria within the biofilm, the direct counting method used in the bacterial adhesion and proliferation experiments was not appropriate, and a protein assay

based on a bicinchoninic acid (BCA) assay (Sigma UK) [12] was introduced, providing an indirect estimate of the amount of bacteria. It was carried out on three samples of each kind. The biofilm coated discs were placed in an ultrasonic bath in 0.1% Triton X-100 (Sigma UK) for 10 min to disperse the biofilm. (SEM examination of the samples following this procedure confirmed that although there were still a few attached bacteria on the sample surface, most of them had been removed.) 1 ml of this suspension was combined with 1 ml working reagent from the BCA assay kit, vortexed well until thoroughly mixed. It was then incubated at 37 ^{o}C for 2 hours and cooled to room temperature before the colour absorbance at 562 nm (wavelength) was recorded. The protein content in the specimen was calculated with reference to a standard curve, which was obtained by measuring the absorbance at 562 nm of standard samples prepared by combining the working reagent with a series of standard protein solutions.

2.4.4 XRD analysis

An X-ray diffractometer is commonly used to study crystalline and non-crystalline materials. A characteristic X-ray (Cu $K_{\alpha 1}$ radiation in this study) is directed at the specimen, either solid or powder, at a constant angular velocity through increasing values and is diffracted at certain angles which contains sample crystallographic information.

In this work, the biomineralised crystal structure was verified via a Philips X-pert diffractometer (SIEMENS D500) with Cu $K_{\alpha 1}$ radiation at 40 kV and 300 mA. Data were collected from 10^{o} to 60^{o}, with a scan speed of 2^{o}/min and scan step of 0.01^{o}.

2.4.5 Micro-CT

Micro X-ray computed tomography (Micro-CT) is a non-destructive technique which

provides high resolution images of the internal structure of samples. Micro-focal spot X-ray projections, acquired at hundreds of equally spaced angular positions around the object, are used to reconstruct a 3D database which represents the distribution map of the linear attenuation coefficients determined by the energy of the X-ray source and the atomic composition of the target material [13].

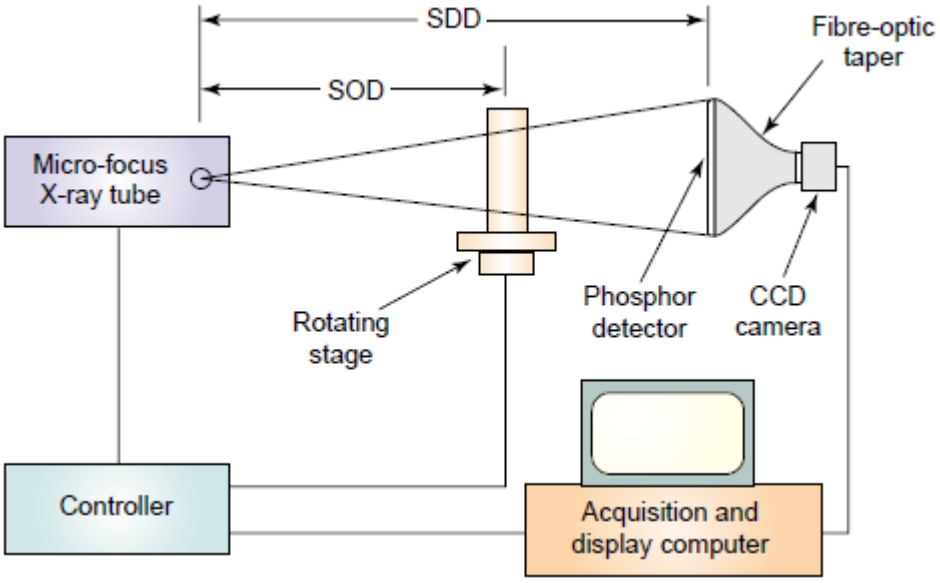

Figure 2. 6 Schematic drawing of micro X-Ray computed tomography (Micro-CT)(adapted from [13])

A Skyscan 1072 Micro X-Ray CT was used in this study to reconstruct the structure of the porous Ti web and to analyse the biofilm/crystal distribution within this scaffold. The equipment parameters are listed in Table 2. 5. The biological sample was fixed and dehydrated as described above before it was loaded into the equipment for the X-ray scan.

Table 2. 5 Micro-CT settings for the reconstruction of different specimens

Specimen	*Equipment parameter*
Ti web substrate	100 kV, 98 μA, filter (Al 0.5 mm)
Biofilm growth on Ti web	100 kV, 98 μA, filter (Al 0.5 mm)
Crystal coated Ti web	89 kV, 108 μA, filter (Al 0.5 mm)

2.4.6 Scanning Electron Microscopy

Electron microscopy is the major characterisation technique used in this work, including scanning electron microscopy (SEM), energy dispersive X-ray analysis (EDX), electron backscattered diffraction (EBSD) and transmission electron microscopy (TEM). SEM is mainly used to study bacterial distribution, the morphology of the *Serratia* biofilm and the biomineralised crystals. EDX is a powerful tool in chemical analysis. EBSD supplies information about substrate grain orientation. TEM will be introduced in § 2.4.7.

2.4.6.1 Instrument introduction

The scanning electron microscope is one of the most powerful tools in the exploration of the world in micro- or even nano-scale. It provides information of specimen surface features and topographies as with the naked eyes but at much higher magnifications. As shown in Figure 2. 7, the electron beam, usually at a voltage of 10-30 keV, is generated by an electron gun and focused by condenser lenses before it scans across the sample surface in a television raster yielding a large number of signals at or near the specimen surface, which are then amplified, processed and recorded by the imaging system.

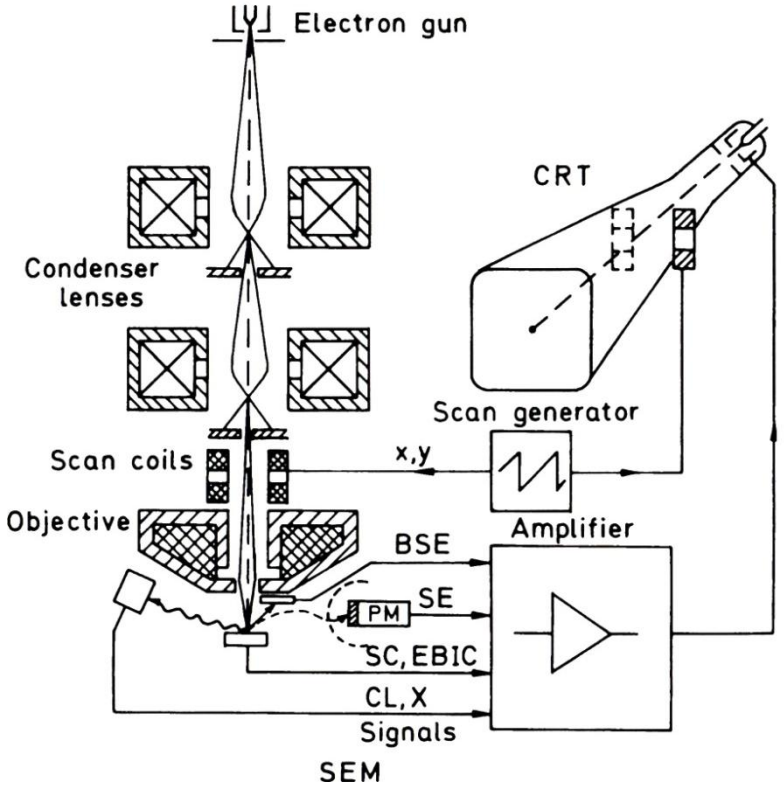

Figure 2. 7 A schematic diagram of a scanning electron microscope (adapted from [14])

Electron-material interaction

Electrons penetrating into a solid specimen undergo both elastic and inelastic scattering and produce various signals as shown in Figure 2. 8. Secondary electrons (SE), the dominating contribution to contrast, are inelastic excited electrons caused by the incident beam. They provide morphological information of the specimen. If the incident electrons go close enough to a specimen atom nucleus and rebound without energy loss, they are called backscattered electrons (BSE). The production of BSE is atomic number (Z)-related, thus offering information on substrate chemistry. Characteristic X-rays are another important signal generated during the electron-specimen interactions. When an electron from an inner atomic shell is dislodged by the incident beam, the atom will stabilise itself by allowing an outer

electron to fill the vacancy. The energy difference between the two states of the transitional electron will be emitted as characteristic X-rays, carrying information about the atom chemistry [14].

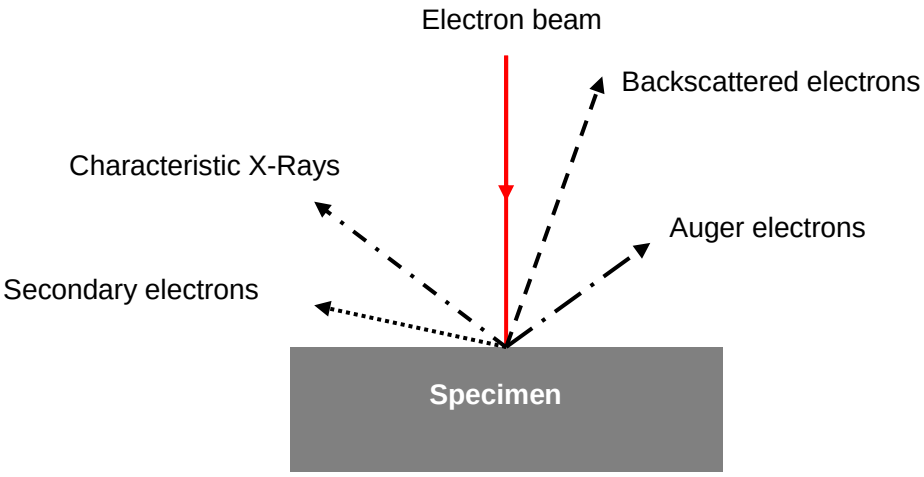

Figure 2. 8 Beam-specimen interactions

For a given bulk sample, there will be a finite depth beneath which no electrons have enough energy to escape the specimen surface - the so called interaction volume. The signals collected in an SEM are actually generated from this volume. Only those that are capable of escaping the specimen surface will be recorded, otherwise they are absorbed by the bulk material. Secondary electrons, for example, are usually from a surface layer of less than 2 nm, while backscattered electrons can escape from tens of hundreds of nanometres. The escape depth of X-rays is the greatest, from 1 to 5 μm, depending on the accelerating voltage and specimen density [14] [15].

Various detectors are employed to collect these signals, an SE detector for secondary electrons (specimen surface shape), a BSE detector for backscattered electrons (atomic number contrast) and EDX (energy dispersive X-ray analysis) and/or WDX (wavelength dispersive X-ray analysis) detectors for characteristic X-rays (chemical composition).

EBSD

The surface orientation of individual crystalline grains of the substrate can be obtained by the analysis of electron backscattered diffraction (EBSD) patterns, which contain crystallographic information. In a crystalline sample, the backscattered electrons, before exiting the sample, can be elastically scattered and strengthened at Bragg condition (Equation 2. 1), giving backscatter patterns equivalent to the Kikuchi lines observed in a TEM, which contains crystallographic information on the grain. The sample is usually tilted 70º toward the camera and these EBSD patterns are collected, recorded and analysed to give the orientation of the crystal surface at each location over which the beam scans, as seen in Figure 2. 10.

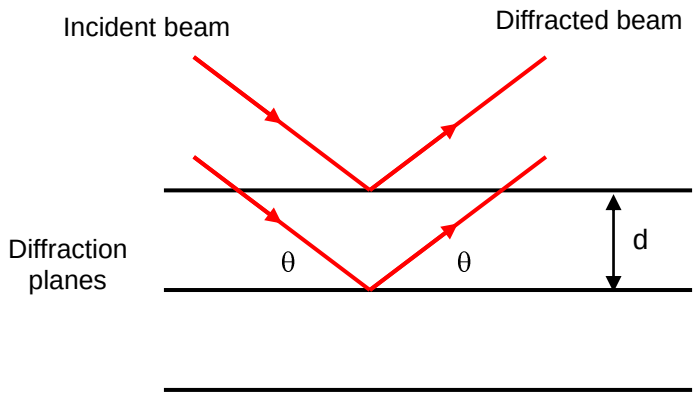

d: spacing of the crystal lattice planes responsible for a particular diffracted beam.

θ: the diffraction angle (Bragg angle).

Figure 2. 9 The incident electrons are diffracted by the crystal planes (Bragg condition)

$$\lambda = 2d_{hkl}\sin\theta$$

Equation 2. 1

λ=the wavelength of the incident beam , d_{hkl}=the spacing of the crystal planes, θ=Bragg angle

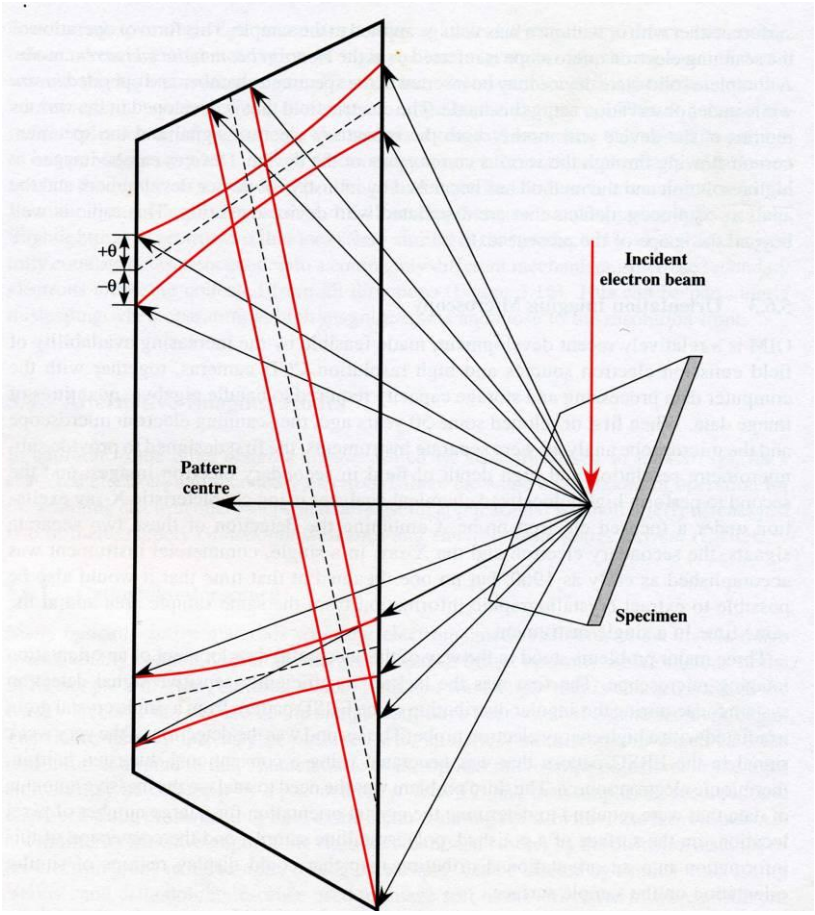

Figure 2. 10 Electron backscattered diffraction (adapted from [16])

2.4.6.2 Sample preparation and characterisation

The influence of grain boundary and grain orientation on bacterial adhesion and proliferation

To examine the bacterial distribution, the specimens were fixed in 2.5% EM grade glutaraldehyde buffer (25% E.M. Grade, Agar Scientific Ltd., UK) in 0.2 M sodium cacodylate (pH=7.3, Cacodylic Acid, Sigma, USA) for 10 min and dehydrated in an ethanol series from 20% to 100% for 10 min in each solution, using liquid CO_2 in a critical point drier (Polaron Critical Point Drier) as the final step.

Bacteria on each substrate were counted using secondary electron (SE) imaging (JEOL 7000,

Japan). For each bacterium tested, ten fields were chosen at random from each metal disc, with three discs of each material, and the number of cells in each field was counted. The relation of bacterial adhesion and proliferation to grain boundaries (GB) was determined by backscattered electron (BSE) imaging. Energy dispersive X-Ray (EDX, Oxford INCA) analysis was used to study the chemical composition of the substrates. Since the bacterial layer was rather thin, no coating was applied during the characterisation. However, a low accelerating voltage (10 kV) was essential to avoid charging.

The substratum grain orientation was studied by electron backscatter diffraction (EBSD, Oxford INCA). In spite of the thin layer of biofilm on the surface, the metal matrix was still sensitive enough to produce an adequate grain orientation map. However, unlike in the BSE images, the detector could not detect any signals from the bacteria. Thus the EBSD and BSE images of the same field were later analysed further using image processing software (Photoshop, Image J) to study the bacterial adhesion in relation to grain orientation. To achieve stronger signals, an accelerating voltage of 20 kV and large beam current were used when acquiring an EBSD map.

Serratia biofilm formation on titanium substrates

The topography of titanium substrates with different surface treatments was observed directly by an SEM (JEOL 7000, Japan) operated at 20 kV. To study the biofilm formation on titanium, specimens were fixed and dehydrated as described above and coated with gold to avoid charging (Emscope SC500). They were then examined by SEM.

Biomineralisation of HA on titanium substrate

The crystal coating, both prior to and after sintering, was examined directly by SEM (JEOL

7000, Japan) operated at either 10 kV (without any coating) or 20 kV (gold coated) (Figure 2. 11a). The coating was then scratched off to reveal the metal surface (Figure 2. 11b). This is to examine the effect of heat treatment on the titanium substrates. To study the cross section through the crystal coated titanium, the sample was mounted in Bakelite vertically, sectioned (Figure 2. 11c) and polished (Figure 2. 11d). The Ca/P ratio of the synthesised crystals was measured by EDX. However, due to the porosity of the coating, these results can only be considered as a rough measurement.

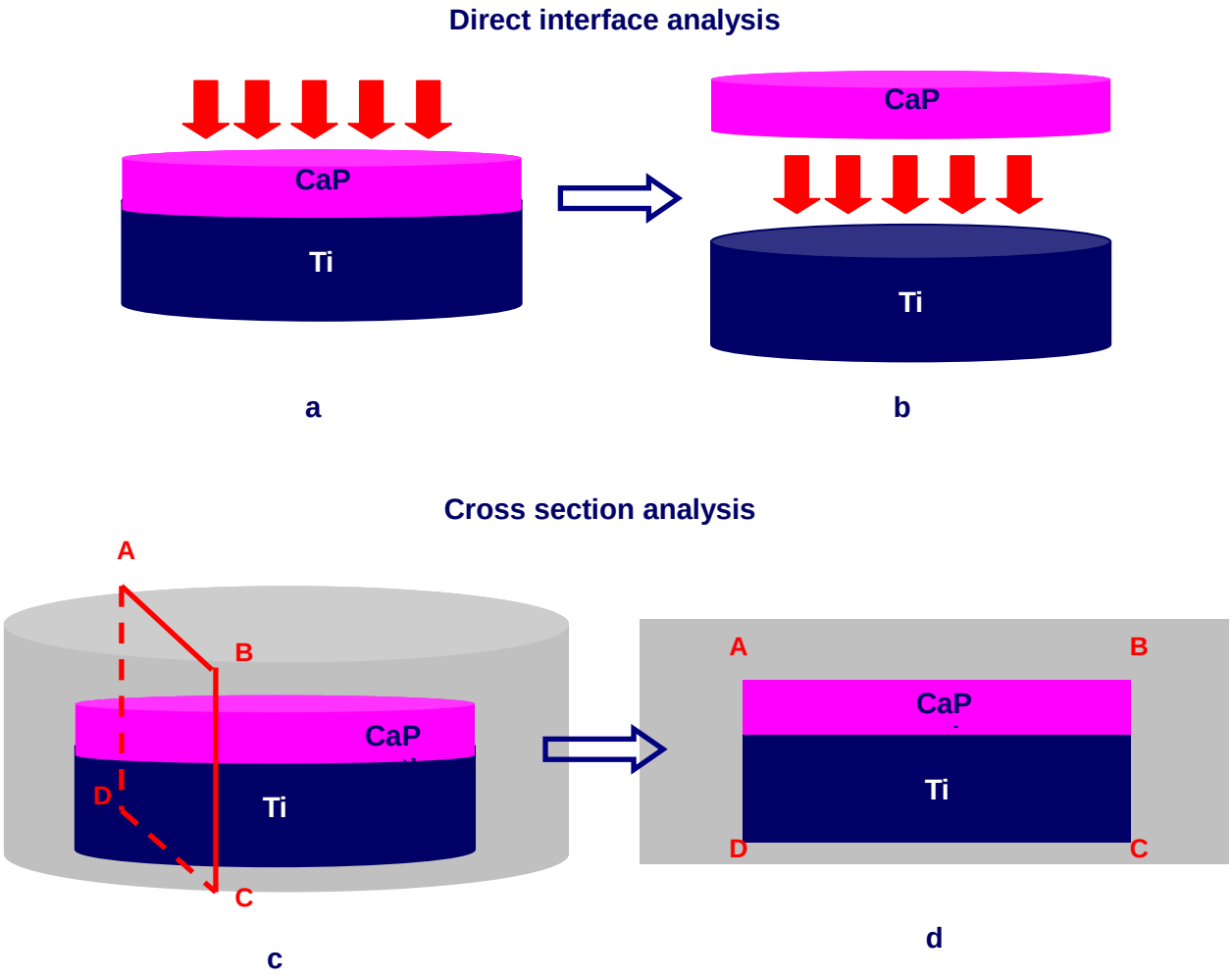

Figure 2. 11 Sample preparation for SEM analysis: calcium phosphate (CaP) coated Ti discs

a: A schematic drawing shows the CaP coated Ti discs. The coating was observed directly (red arrows) by an SEM. CaP represents both the nascent and the sintered crystal coating.

b: The crystal coating was scratched off to reveal the substrate surface directly (red arrows).

c: For a cross section analysis, the CaP coated Ti was mounted in bakelite (grey).

d: The mounted specimen was cut along the ABCD plane shown in (a) and polished to reveal the specimen cross section

2.4.7 Transmission Electron Microscopy

2.4.7.1 Instrument introduction

A transmission electron microscope (TEM), as shown in Figure 2. 13, is usually operated at higher voltage, typically 100~400 kV. Similar as in an SEM, the electron beam generated from the gun is focused by electromagnetic condenser lenses before it reaches the thin specimen [17]. Various signals are generated due to the electron-material interaction as shown inFigure 2. 12. However, unlike SEM where the electron beam is scattered at the sample surface, most of the signals in a TEM are generated at both sides of the sample, as illustrated in Figure 2. 10. It is mainly the transmitted electrons that are focused and enlarged on a fluorescent screen or recorded by the camera. Imaging using the transmitted primary beam is the bright field mode (BF), otherwise the dark field mode (DF) if it is excluded. Characteristic X-rays can also be detected for chemical analysis (EDX).

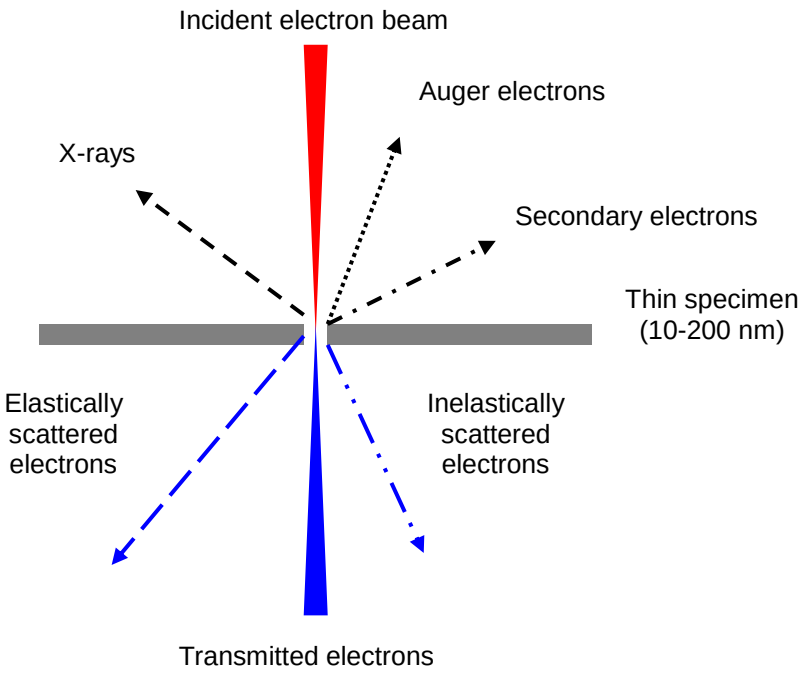

Figure 2. 12 Electron interactions with a thin TEM specimen

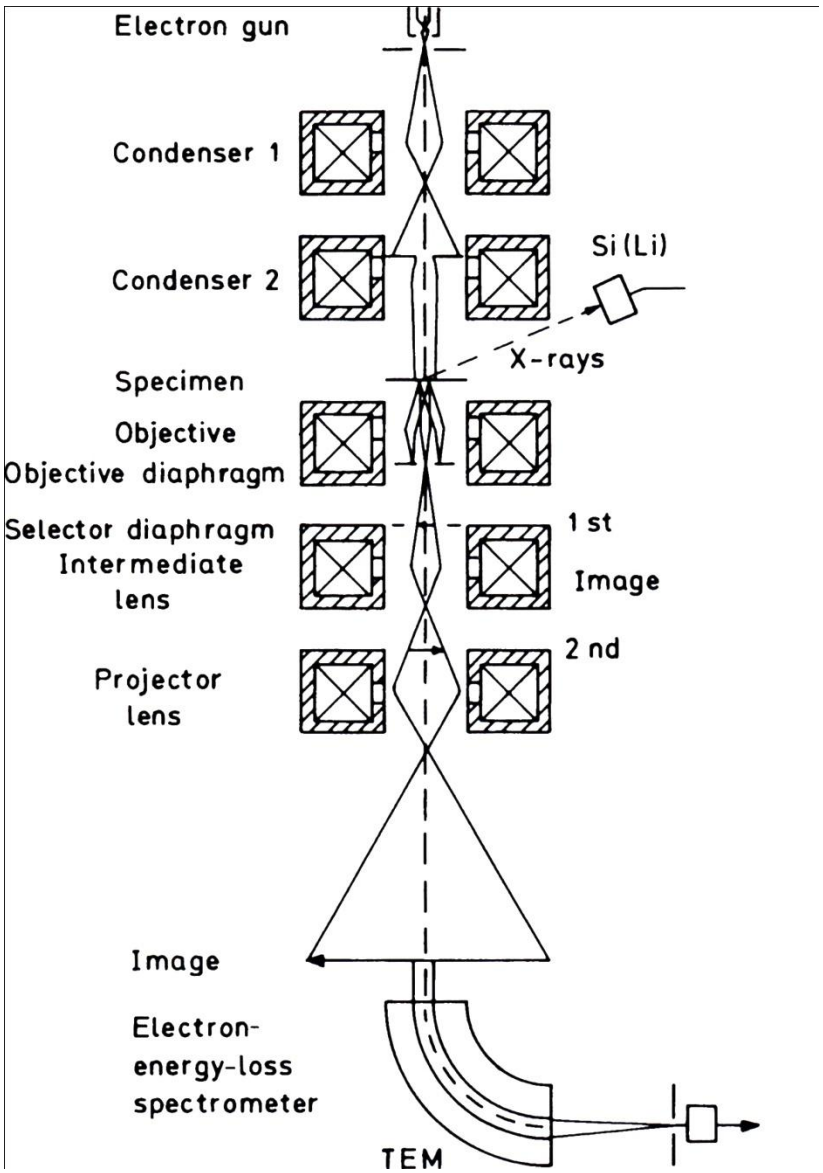

Figure 2. 13 A schematic drawing of a transmission electron microscope (adapted from [17])

The electron beam in a TEM can be focused and scanned across the specimen surface in a manner similar to that in an SEM, the so-called STEM mode. A number of detectors can be employed for STEM imaging: a bright field (BF) detector similar to that in TEM, an annular

dark field detector (DF) when the scattering angle is between 10 and 50 mrad and a high angle annular dark field detector (HAADF) when the electrons are scattered to even higher angles, >50 mrad, as shown in Figure 2. 14 [17]. The advantage of an HAADF STEM is that the contrast is mainly caused by inelastic scattering as almost none of the elastically scattered electrons can reach the detector [17]. Thus, its image is regarded as Z-contrast, closely related to the atomic number.

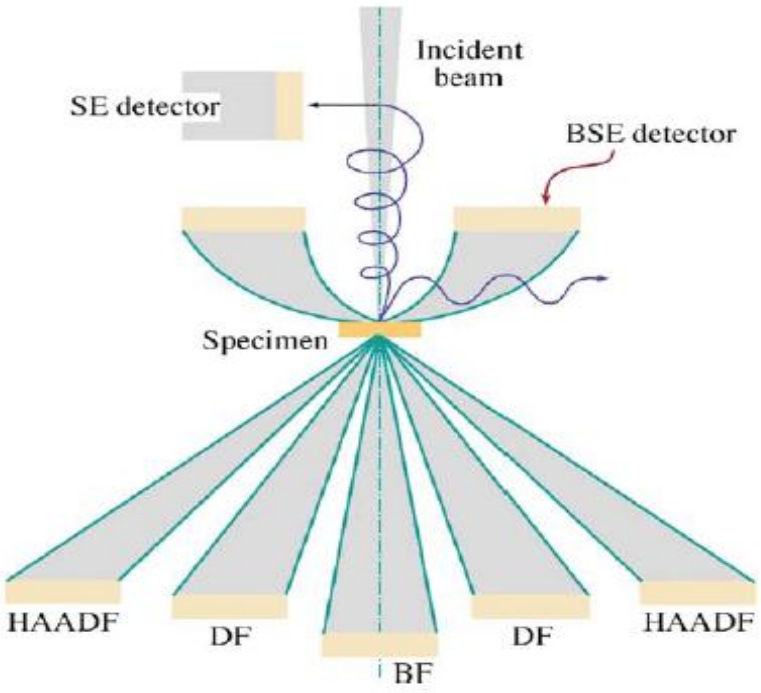

Figure 2. 14 Schematic drawing of STEM mode [17]

BF: bright field detector

DF: dark field detector

HAADF: high-angle annular dark field detector

With all the benefits of a TEM, there are inevitably certain drawbacks. Only a limited dimension can be studied: a standard TEM specimen is 3 mm in width, and electrons can only

penetrate locations that are less than 100 nm thick. Thus, in the pursuit of high resolution TEM analysis, a combination study with other techniques such as XRD and SEM is essential. Another shortcoming is the beam damage due to ionising radiation, which is particularly serious for polymers, certain minerals, ceramics and especially biological samples. However, this can be ameliorated via certain techniques such as cryo-microscopy (specimen cooling) and the use of low noise, charge-coupled devices (CCD) cameras.

2.4.7.2 Sample preparation and characterisation

The biomineralised crystals, both prior to and after sintering, were analysed further using TEM (JEOL 1200 TEM operated at 80 kV, JEOL 2100 TEM operated at 200 kV and FEI TECNAI F20 Field Emission TEM operated at 200 kV).

The crystals were scratched off the titanium disc and suspended in ethanol in an ultrasonic bath for 10 min. 3 μl of the suspension was dropped onto a carbon film supported by a copper grid and allowed to dry at room temperature. Alternatively, they were embedded in resin and sectioned to approximately 100 nm using a microtome (ULTRACUT, REICHERT-JUNG). Copper grids (Agar Scientific) were used as a support. A thin carbon coating was always applied to avoid charging, otherwise image drift was unavoidable. Coating/metal cross sections for TEM were produced using a focused ion beam scanning electron microscope (FIB/SEM, FEI QUANTA 3D FEG).

FIB/SEM is distinct as it involves a dual-beam system, an electron source combined with a high energy ion beam (FIB), as illustrated in Figure 2. 15. Focusing and scanning the ions across the specimen surface makes micro-machining possible as the matrix (specimen) atoms are knocked out of the surface. FIB was initially designed for the machining of electronic and optronic device components in the 1980s and was not widely used for scientific research until

recently [16]. It has been demonstrated to be powerful as a platform for micromachining, assisting microstructural analysis, serial sectioning, and producing TEM samples that are otherwise difficult to prepare, such as a cross-section or when a specific site of interest is concerned. However promising as it seems, there are several noticeable shortcomings of this technique. The size of the specimen, for instance, is quite limited. It can only produce TEM microscale samples. In addition there may be problems with curtaining (trenches due to beam channelling), sub-surface radiation damage and contamination due to re-deposition.

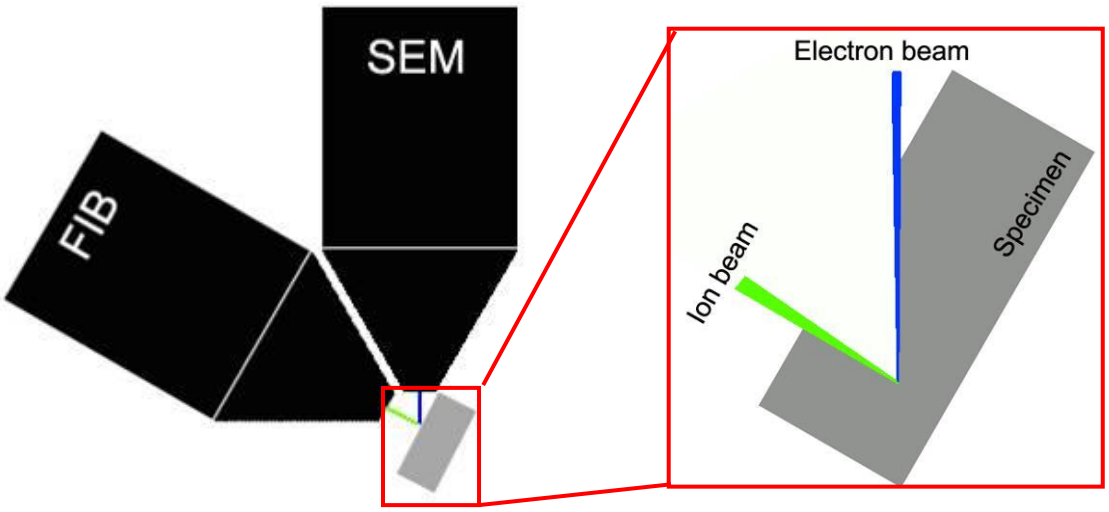

Figure 2. 15 Schematic drawing of the dual-beam FIB/SEM

FIB was used in this study to produce cross-sectional specimens for TEM analysis. Due to its inability to produce large samples, the surface layer of the coating was scratched off before the ion milling was carried out. The site of interest (16 μm× 4 μm) was coated with tungsten (W) as protection against ion milling. Two squares were milled symmetrically on both sides of the chosen region (Figure 2. 16a) and the W-coated 'partition' in between was thinned to around 1 μm before it was semi-detached from the matrix by an ion 'U-cut' (Figure 2. 16b). The thin slice was mounted on a W-needle (Figure 2. 16c), separated from the matrix (Figure

2. 16d) and mounted on a copper grid before it was finally thinned to around 100 nm and cleaned at low beam current. The sample (crystal coating) analysed in this study was not only porous but also beam sensitive. While the porosity, combined with the density difference between the coating and the substrate, can induce severe curtaining, the beam sensitivity may lead to amorphisation of the crystal coating. Different specimen thicknesses were tried, 90 nm and 150 nm, as will be discussed further in Chapter 6.

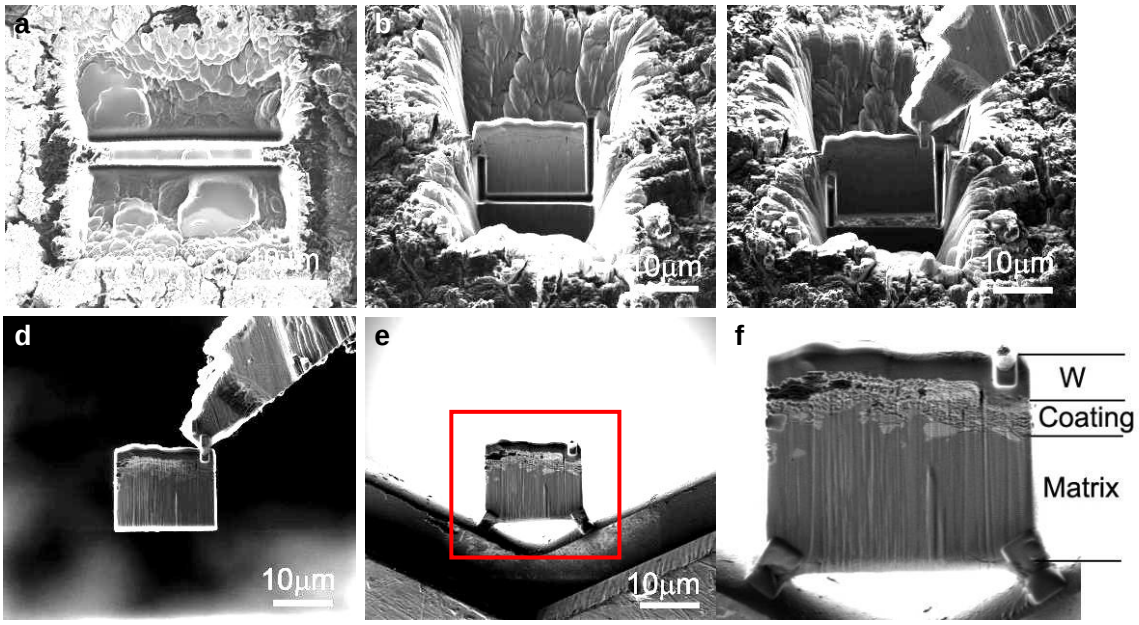

Figure 2. 16 TEM sample preparation by FIB/SEM

a: Ion milling. b: U-cut. c: Mounting on a W needle. d: Sample 'lift-out'. e: Mounting on a copper grid. f: The square site in (e) enlarged, showing the W protection layer, crystal coating and the matrix.

2.5 Data processing

The data achieved in this study for statistical analysis was processed as following:

Each measurement was repeated three times, the average of which will be used. The standard

deviation of the dataset was calculated using student t-test by Excel software and used as the error bars. Exceptions will be described later in the results.

References

1. An YH, Friedman RJ. Concise review of mechanisms of bacterial adhesion to biomaterial surfaces. Journal of Biomedical Materials Research 1998;43(3):338-348.
2. Katsikogianni M, Missirlis YF. Concise review of mechanisms of bacterial adhesion to biomaterials and of techniques used in estimating bacterial-material interactions. European Cells and Materials 2004;8:37-57.
3. Vuong C, Otto M. *Staphylococcus epidermidis* infections. Microbes and Infection 2002;4(4):481-489.
4. Black C, Allan I, Ford SK, Wilson M, McNab R. Biofilm-specific surface properties and protein expression in oral *Streptococcus sanguis*. Archives of Oral Biology 2004;49(4):295-304.
5. Yong P, Macaskie LE, Sammons RL, Marquis PM. Synthesis of nanophase hydroxyapatite by a *Serratia* sp. from waste-water containing inorganic phosphate. Biotechnology Letters 2004;26(22):1723-1730.
6. Allan VJM, Callow ME, Macaskie LE, Paterson-Beedle M. Effect of nutrient limitation on biofilm formation and phosphatase activity of a *Citrobacter* sp. Microbiology 2002;148(1):277-288.
7. Masago H, Shibuya Y, Munemoto S, Takeuchi J, Uneda M, Komori T, Kuboki Y. Alveolar ridge augmentation using various bone substitutes - a web form of titanium fibers promotes rapid bone development. Kobe Journal of Medical Science 2007;53(5):257-263.
8. Li D, Iku S, Nemoto K, Kokai Y, Odajima T, Toshimoto R, Kaku T, Katoh H, Shiota H, Seki Y, Ogura N, Abiko Y, Kuboki Y. Geometry of artificial ECM three-dimental structure of titanium-web (TW) promotes differentiation of human bone marrow mesenchymal cells into osteoblast. journal of Hard Tissue Biology 2005;14(2):333-334.
9. Thackray AC. Bacterial biosynthesis of a bone substitute material. PhD Thesis. University of Birmingham; 2005.
10. van Grieken R, Marugán J, Pablos C, Furones L, Lóez A. Comparison between the photocatalytic inactivation of Gram-positive E. faecalis and Gram-negative E. coli faecal contamination indicator microorganisms. Applied Catalysis B: Environmental 2010;100(1-2):212-220.
11. Shieh K-J, Li M, Lee Y-H, Sheu S-D, Liu Y-T, Wang Y-C. Antibacterial performance of photocatalyst thin film fabricated by defection effect in visible light. Nanomedicine: Nanotechnology, Biology and Medicine 2006;2(2):121-126.
12. Walker JM. The Bicinchoninic Acid (BCA) Assay for Protein Quantitation. Basic Protein and Peptide Protocols, 1994. p. 5-8.
13. Holdsworth DW, Thornton MM. Micro-CT in small animal and specimen imaging. Trends in Biotechnology 2002;20(8):S34-S39.
14. Egerton RF. Physical principles of electron microscopy: an introduction to TEM, SEM, and AEM. 3rd ed. New York: Springer, 2008.
15. Postek MT, Howard KS, Johnsom AH, McMichael KL. Scanning electron microscopy: a student's handbook: Ladd Research Industries, 1980.
16. Brandon D, Kaplan WD. Microstructural characterization of materials. 2nd edition ed. London: John Wiley & Sons Ltd. , 2008.
17. Williams DB, Carter CB. Transmission electron microscopy: a text book for materials science. New York: Springer.

Chapter 3 The influence of titanium alloy structure on bacterial adhesion and proliferation

3.0 Introduction

To understand the influence of titanium alloy structure on bacterial adhesion and proliferation is of great significance, because grain boundaries, grain orientation and phase structure are potential bacterial growth stimuli. Researchers have demonstrated that bacteria showed grain boundary- associated adhesion on stainless steels [1, 2]. However, comparatively little is known about titanium regarding to this aspect, although there were reports that *S. epidermidis* adhesion on Ti 64 was phase-sensitive [3], and both *Staphylococcus aureas* and *Pseudomonas aeruginosa* attached better to a nano-crystalline titanium surface [4]. The relationship between bacterial adhesion, proliferation and titanium alloy structure was investigated systematically in this chapter. This study is a pioneer research to statistically investigate the relation between bacterial distribution and substrate grain boundary and grain orientation. A novel approach and a non-destructive method were established for the above purpose.

3.1 Substrate microstructure and chemical composition

CP Ti used in this study is a single α phase (hcp) material, with a grain size of 20 to 70 μm, as shown in Figure 3. 1. Ti 64 is an α+β two-phase material, with a remnant bcc β phase (bright area in Figure 3. 1) embedded in an hcp α phase (dark area inFigure 3. 1). EDX analysis shows that the β phase of Ti 64 is rich in V, as seen in Table 3. 1.

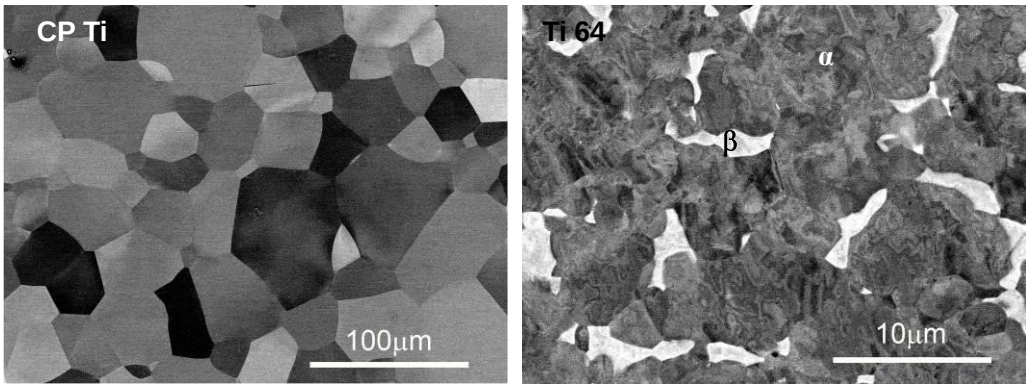

Figure 3. 1The microstructure of CP Ti and Ti 64 (BSE imaging)

Table 3. 1 EDX analysis of the chemical composition of CP Ti and Ti 64

Substrate		***Ti***	***Al***	***V***	***others***
CP Ti (at %)		99.81±0.15	------	------	0.20±0.16
Ti 64 (at %)	**α phase**	86.89±0.05	8.74±0.04	4.13±0.12	0.24±0.21
	β phase	81.05±0.14	4.71±0.09	14.15±0.43	0.09±0.06

3.2 Water contact angle measurements

The WCAs of all the four substrates were measured and are compared in Figure 3. 2. All four are hydrophilic, with WCA lower than 90°. CP Ti and Ti 64 show equivalent WCAs, as do Al and V; CP Ti and Ti 64 are slightly more hydrophilic than Al and V.

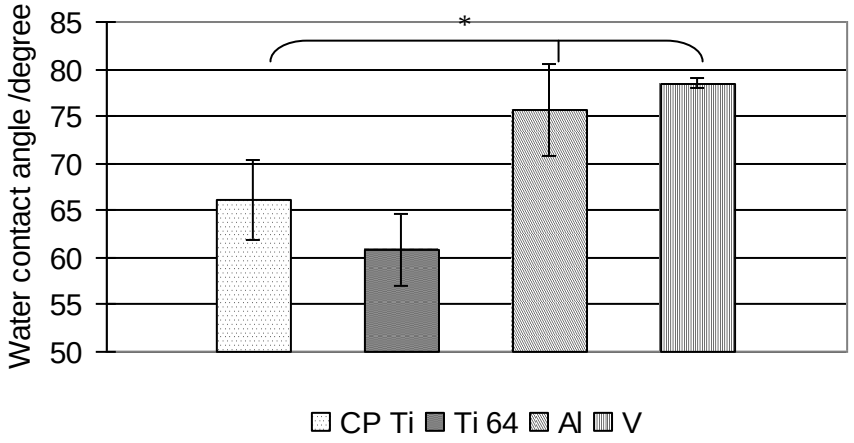

Figure 3. 2 Water contact angle measurements for CP Ti, Ti 64, Al and V (n=3)

*: $p<0.005$ (*p*: derived by student *t-test*)

3.3 Bacteria

Images of the bacteria used in this study are shown in Figure 3. 3. *S. epidermidis* (Figure 3. 3a) and *S. sanguinis* (Figure 3. 3b) are Gram-positive, spherical bacteria; *Serratia* (Figure 3. 3c) and *E. coli* (Figure 3. 3d) are Gram-negative, rod-shaped bacteria.

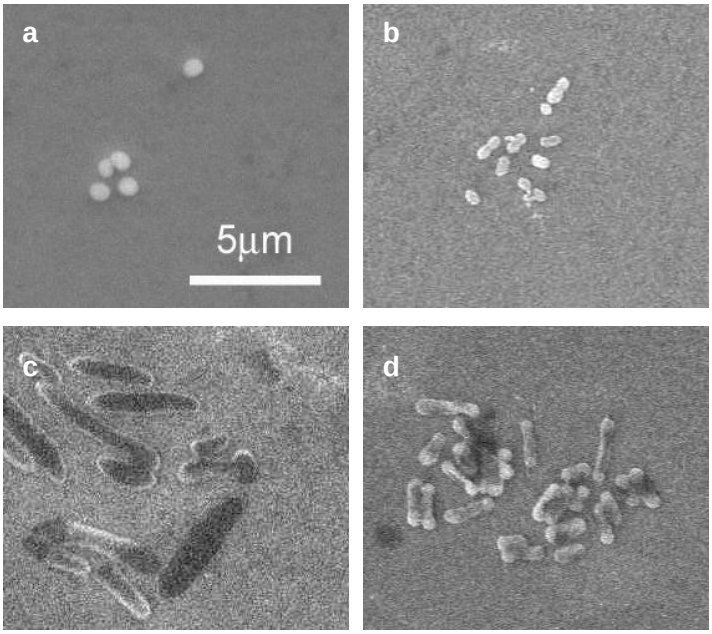

Figure 3. 3 The morphology of *S. epidermidis* on CP Ti (a), *S. sanguinis* on CP Ti (b), *Serratia* on CP Ti (c) and *E. coli* on Ti 64 (d)

(The scale bar in (a) applies to all images.)

3.4 The influence of titanium alloy structure on bacterial adhesion

In this section, the adhesion of *S. epidermidis*, *S. sanguinis*, *E. coli* and *Serratia* on CP Ti was investigated regarding to the GBs and grain orientations of the substrate. The distribution of *S. epidermidis* and *S. sanguinis* on Ti 64 was analysed to study the effect of substrate phase structure. The adhesions of the four bacteria were compared between CP Ti, Ti 64, Al and V, to study the influence of substrate chemical composition. The experiments in this section were repeated twice, with three samples of each material for each independent experiment.

3.4.1 The influence of substrate grain boundaries and grain orientation

Because of its compositional and structural simplicity, CP Ti was used to study the influence of grain boundaries and grain orientation on bacterial adhesion. The distribution of *S. epidermidis* on the substrate is displayed in Figure 3. 4a, with the grain boundaries and

bacteria highlighted in Figure 3. 4b. Clearly, the bacteria adhere randomly, showing no preference toward or away from any grain boundaries. The distribution of *S. sanguinis, E. coli* and *Serratia* with respect to GBs are displayed in Figure 3. 4c to Figure 3. 4h. All four bacteria attached randomly to titanium regardless of grain boundaries.

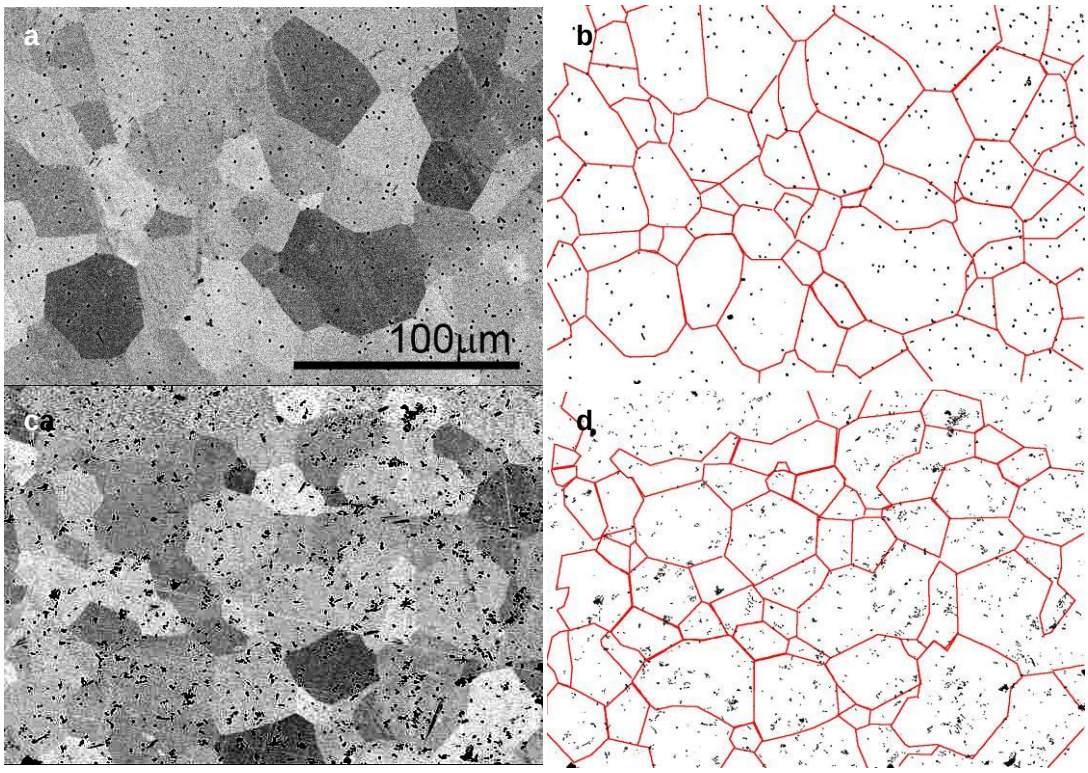

Figure 3. 4 The relation of bacterial adhesion to CP Ti grain boundaries.

a: The distribution of *S. epidermidis* on CP Ti (BSE imaging).

b: Processed image with only the bacteria and the GBs highlighted (image processed from (a) using Photoshop software).

c, d: The distribution of *S. sanguinis* distribution with respect to CP Ti grain boundaries.

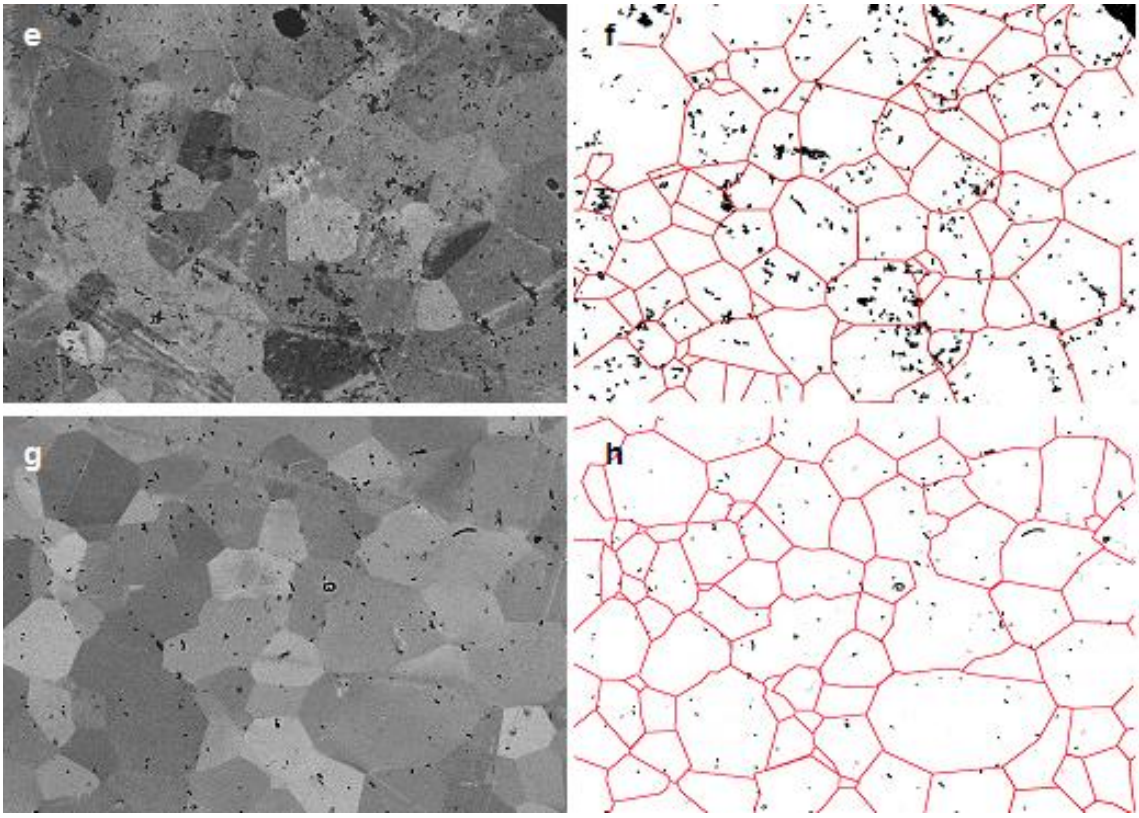

Figure 3. 4 The relation of bacterial adhesion to CP Ti grain boundaries - continued

e, f: The distribution of *E. coli* with respect to CP Ti grain boundaries.

g, h: The distribution of *Serratia* with respect to CP Ti grain boundaries.

(Images b-h are on the same scale as image (a).)

EBSD analysis was carried out on the same field of interest as in Figure 3. 4a to study the influence of substrate grain orientation. The grain texture was analysed with a misorientation tolerance of 15 degrees (Figure 3. 5b). (Grains with misorientation of below 15 degrees were considered as the same texture.) The percentage of bacteria within an area of specific orientation (B%) was divided by the area of that orientation (GO%). Figure 3. 5c indicates that *S. epidermidis* showed no preference for any particular grain orientation, as the B%/GO% value was always around 1. (Otherwise, it would be significantly different from 1 at certain grain orientations.) Similar results were acquired from the other three strains, with bacteria

randomly attached to the surface with no preference for any specific grain orientation, as seen in Figure 3. 6. The large error bars in both Figure 3. 5c and Figure 3. 6 are because of the low number of adherent cells.

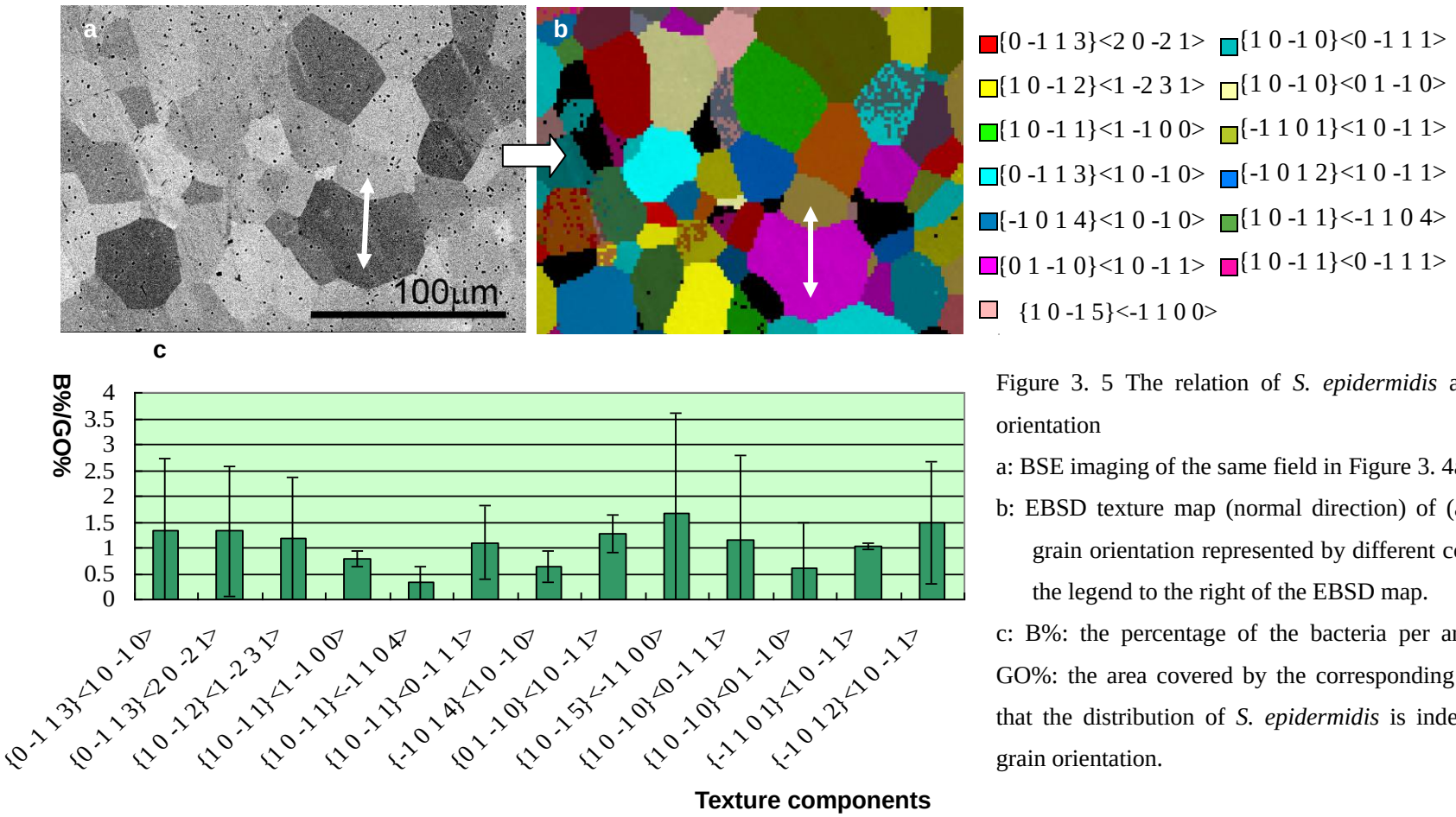

Figure 3. 5 The relation of *S. epidermidis* adhesion to CP Ti grain orientation

a: BSE imaging of the same field in Figure 3. 4a.

b: EBSD texture map (normal direction) of (a) showing the substrate grain orientation represented by different colours and interpreted by the legend to the right of the EBSD map.

c: B%: the percentage of the bacteria per area of the same texture; GO%: the area covered by the corresponding texture. It demonstrated that the distribution of *S. epidermidis* is independent on the titanium grain orientation.

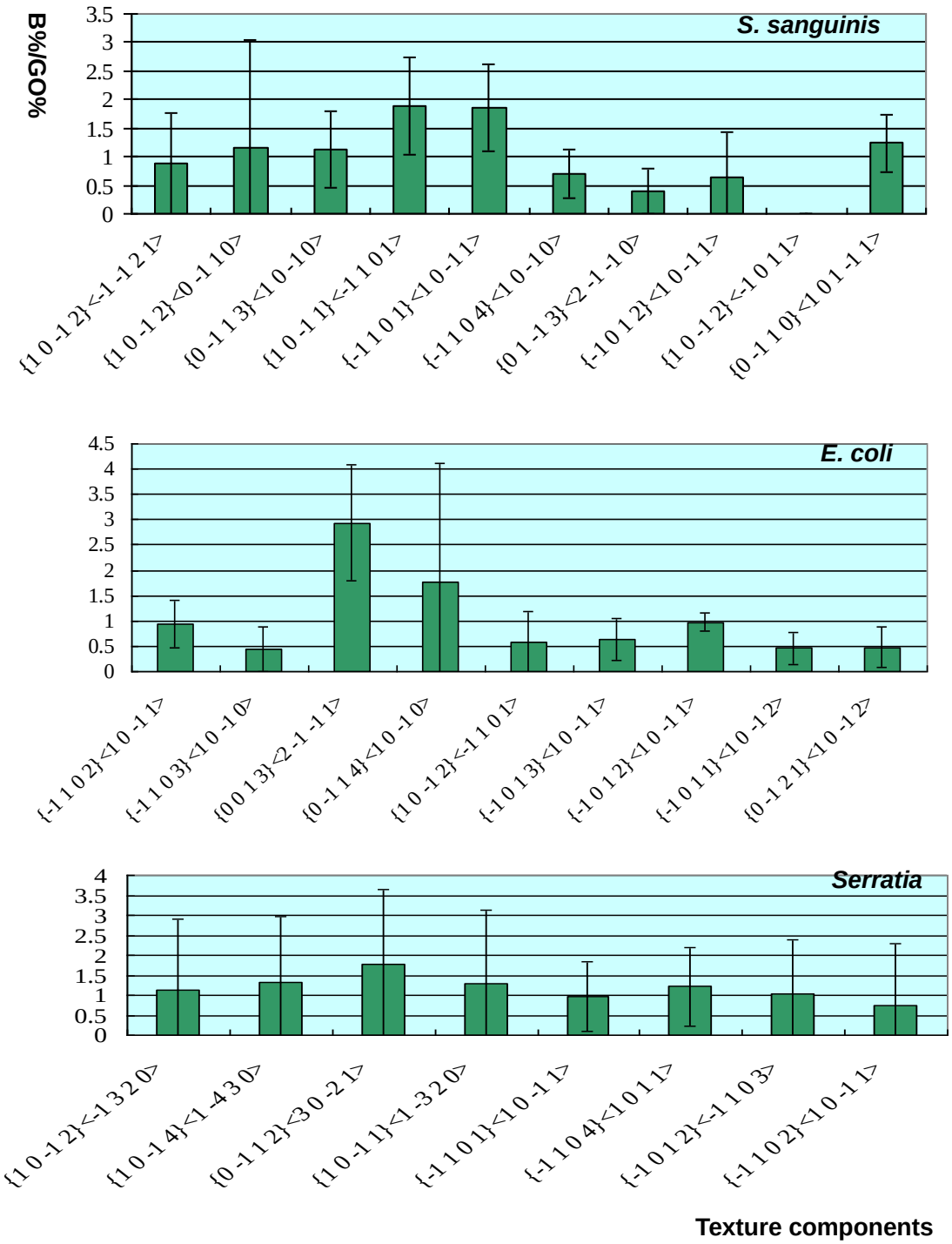

Figure 3. 6 The relation of *S. sanguinis*, *E. coli* and *Serratia* adhesion to CP Ti grain orientation

3.4.2 The influence of substrate chemical composition

Ti 64 is an important biomaterial with many orthopaedic applications. To study bacterial adherence to the alloy and to determine the individual effects of the Al and V components, the four bacterial strains were allowed to adhere to CP Ti, Ti 64, Al and V. The numbers of the cells of each strain on each material were counted and are compared in Figure 3. 7. These two Gram-negative bacteria showed similar patterns of response (Figure 3. 7a), as did the two Gram-positive strains (Figure 3. 7b). While most Gram-negative bacteria (*Serratia* and *E. coli*) were seen on Ti 64 and CP Ti, higher numbers of *S. epidermidis* and *S. sanguinis* were seen on V. All the four bacteria adhered equally well to CP Ti and Ti 64, and the lowest number of bacteria was observed on the Al surface in all four cases.

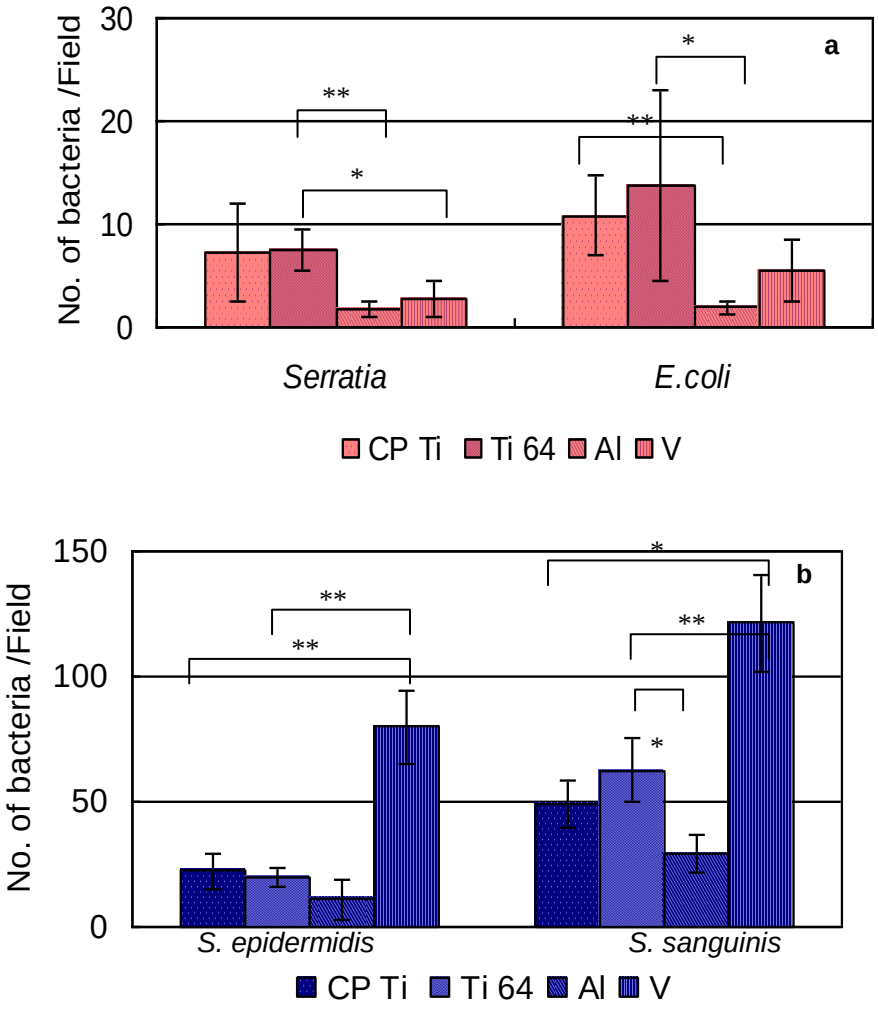

Figure 3. 7 Adhesion of *Serratia*, *E. coli*, *S. epidermidis* and *S. sanguinis* to CP Ti, Ti 64, Al and V

Independent experiments were repeated twice, with three sample of each material tested. *: $p<0.05$; **: $0.05<p<0.5$. P: derived from Student *t-test*.

3.4.3 The influence of Ti 64 phase structure

The relation of bacterial distribution to the phase structure of Ti 64 was studied using BSE imaging. Due to the small grain size of the substrate used (5~10 μm), which is similar in scale to the length of the *Serratia* and *E. coli* bacteria, only the distributions of *S. epidermidis* and *S.*

sanguinis were examined. The distribution of *S. epidermidis* and *S. sanguinis* was shown in Figure 3. 8. Both the bacteria adhered to Ti 64 randomly, independent of the phase structure.

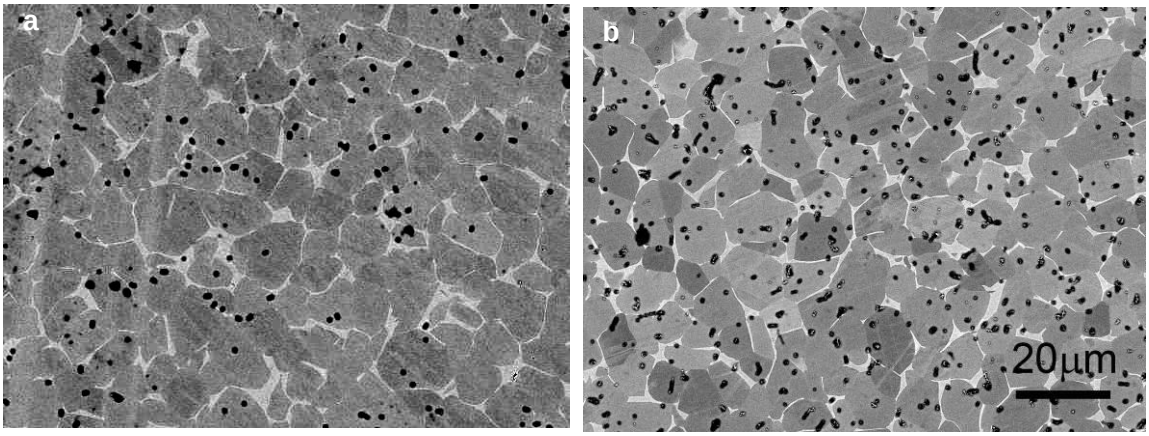

Figure 3. 8 The distribution of *S. epidermidis* (a) and *S. sanguinis* (b) on Ti 64

(BSE imaging, the scale bar is displayed in b)

3.5 The influence of titanium alloy structure on bacterial proliferation

In this section, *Serratia* proliferation on the four substrates was investigated in the same method as used in § 3.4. However, there is one aspect that needs to be clarified. To study the adhesion of *Serratia*, bacteria were cultured in TSB and resuspended in PBS, consistent with *S. epidermidis*, *S. sanguinis* and *E. coli*. To allow bacterial proliferation on metal substrates, nutrients must be supplied. Thus, PBS is not appropriate. However, TSB used to culture the bacteria is not suitable either, as it was observed that bacteria did not adhere well on metal surface in TSB. Thus, *Serratia* were cultured and resuspended in a carbon-limited minimal medium as described in § 2.1.3. The experiments in this section were repeated twice, with three samples of each material for each independent experiment.

3.5.1 The influence of grain boundaries and grain orientation

The *Serratia* distribution on CP Ti after 24 hours' proliferation is shown in Figure 3. 9. Although most of the cells appear to adhere randomly, there do appear to be colonies clinging to or growing along the GBs, as indicated by the arrows.

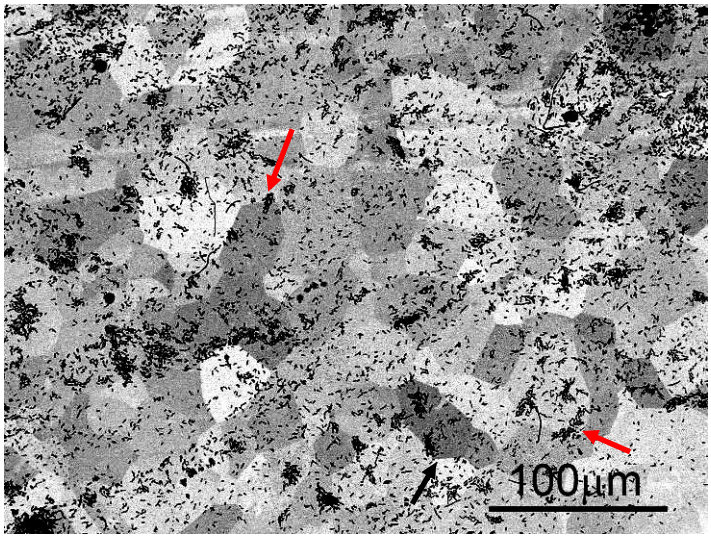

Figure 3. 9 *Serratia* proliferation on CP Ti (BSE imaging). The red arrows point to bacterial colonies at or adjacent to GBs.

This image was processed further using the software ImageJ to give a quatitative expression to the relation. Grains that touched the image frame were trimmed. GBs are highlighted in Figure 3. 10b, based on BSE imaging (Figure 3. 10) and the EBSD map (Figure 3. 11). Euclidean Distance Mapping (EDM) was carried out as shown in Figure 3. 10c. The distance of each pixel inside the grains from the nearest GB was recorded, as were the distance of the bacteria in Figure 3. 10a from the nearest GB (Figure 3. 10d). Histograms were then plotted of pixels and bacteria versus distance from GBs in Figure 3. 10e. It is apparent that they follow the same pattern, indicating that the bacteria do not adhere preferentially to GBs. Otherwise, the bacteria EDM histogram would be high at the initial part of the graph where the distance

away from the GBs is not too great (for example, the blue curve in Figure 3. 10e).

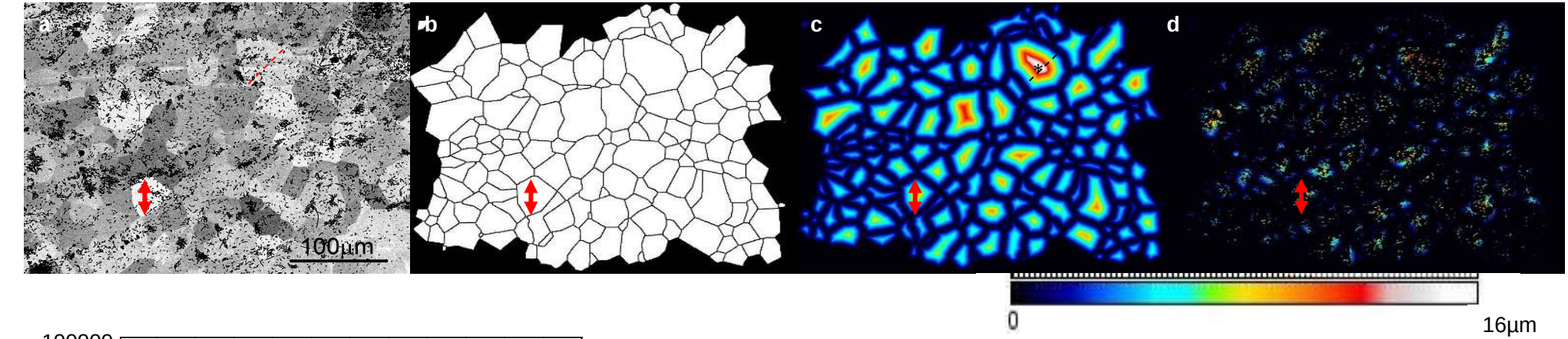

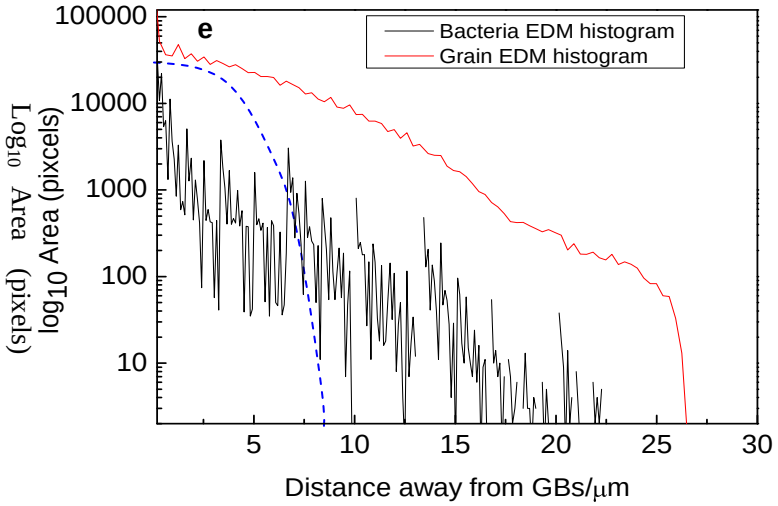

Figure 3. 10 The influence of GBs on *Serratia* proliferation:

a: BSE image in Figure 3. 9.
b: GBs in (a) were highlighted. (GBs that touch the image frame were trimmed.)
c: The points inside each grain were labelled with their distances away from the nearest GBs (Grain EDM). The distance was presented by the colour scale bar below (c) and (d). For example, the black lines will be GBs as their distance is 0 (excluding the image borders). The points marked by * in (c) is approximately 16 μm away from the GB, which makes the grain around 50 μm wide along the dotted line, with reference to the red dotted line in (a).
d: The bacteria in (a) were labelled with their distances away from the nearest GBs (Bacteria EDM).
e: Histogram of (b) and (c). The blue dotted line indicates the predicted bacteria EDM curve if bacterial adhesion was strongly GB-associated.
The double-headed arrows marked (the location of) the same grain in (a), (b) and (c).

The influence of grain orientation was analysed as described in § 3.3.1. Figure 3. 11shows a comparison of B%/GO% between all the different orientations, indicating that *Serratia* proliferate equally well regardless of the grain orientation.

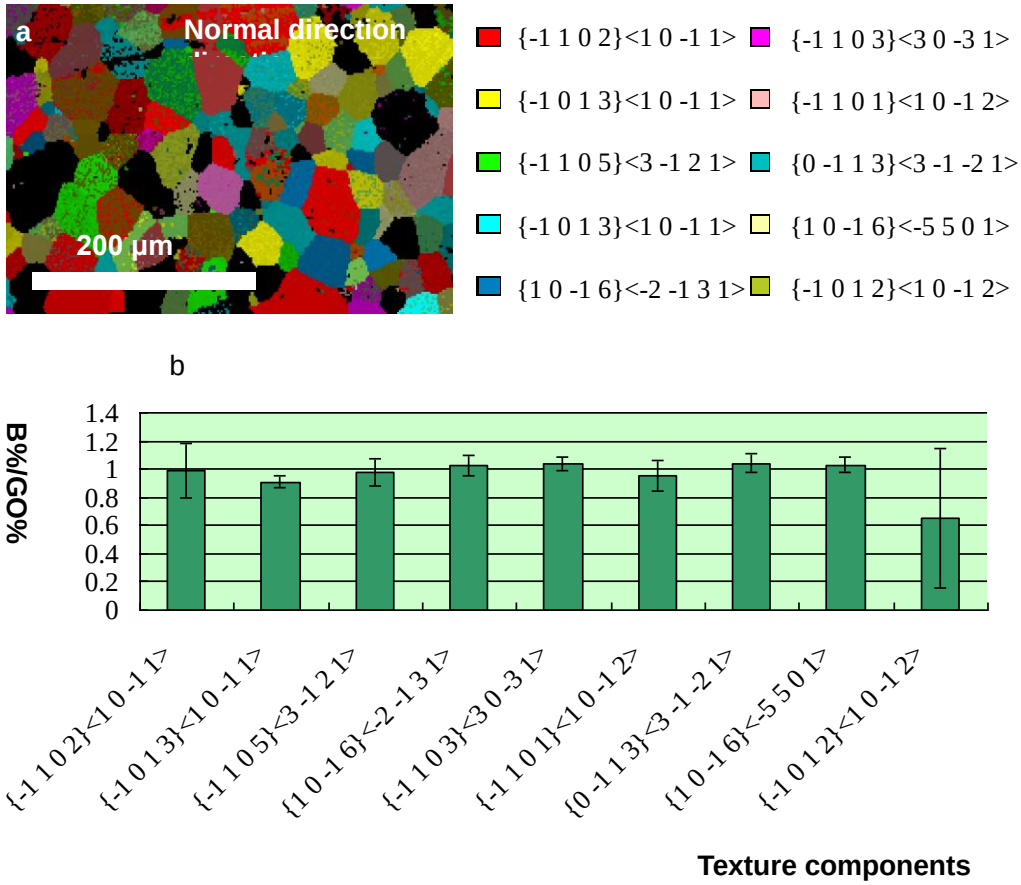

Figure 3. 11 The relation between *Serratia* proliferation and CP Ti grain orientation

a: EBSD map of the field of interest in Figure 3. 9 showing the substrate grain texture (with 15° spread).

b: B%: the percentage of the bacteria on the same grain orientation; GO%: area coverage contributed by the corresponding texture. The colour of each column represents the orientation component shown in (a).

3.5.2 The influence of substrate chemical composition

After 24 hours' proliferation, the difference between the amount of *Serratia* present on CP Ti and Ti 64 was still not significant, however larger than the adhesion. The fewest bacteria were found on Al. Compared with Al, there was a significant increase in the amount of bacteria on V after proliferation, as seen in Figure 3. 12.

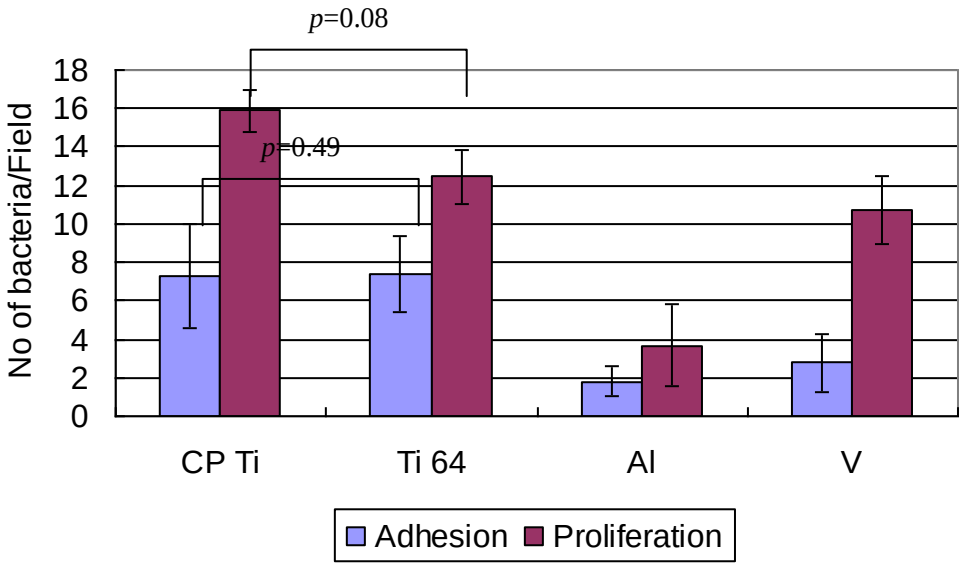

Figure 3. 12 Quantification of *Serratia* on CP Ti, Ti 64, Al and V: a comparison between adhesion and proliferation (*p*: obtained from Student *t-test*.)

3.6 Summary

Under the experimental conditions tested, grain boundaries and grain orientations were found to have no distinguishable effect on either bacterial adhesion or early proliferation.

When only adhesion was considered, similar attachment was observed on CP Ti and Ti 64, and the adhesion on Al was always low. The two *cocci* were found to adhere randomly to Ti 64, regardless of the chemical difference between the two phases of the substrate. The two

Gram-negative bacteria used in this study showed opposite adhesion pattern on titanium and vanadium when compared to the two Gram-positive bacteria. However, further analysis is required to verify this point.

After proliferation for 24 hours, *Serratia* were found to proliferate the worst on Al.

This chapter focused on bacterial adhesion and early proliferation. *Serratia* biofilm formation on titanium with different surface treatments is analysed in Chapter 4, and the results of both chapters are discussed in Chapter 5.

References

1. Sreekumari K, Nandakumar K, Kikuchi Y. Bacterial attachment to stainless steel welds: significance of substratum microstructure. Biofouling 2001;17(4):303-316.
2. Geesey GG, Gillis RJ, Avci R, Daly D, Hamilton M, Shope P, Harkin G. The influence of surface features on bacterial colonization and subsequent substratum chemical changes of 316L stainless steel. Corrosion Science 1996;38(1):73-95.
3. Gabriel BL, Gold J, Gristina AG, Kasemo B, Lausmaa J, Harrer C, Myrvik QN. Site-specific adhesion of *Staphylococcus epidermidis* (RP12) in Ti-Al-V metal systems. Biomaterials 1994;15(8):628-634.
4. Truong VK, Lapovok R, Estrin YS, Rundell S, Wang JY, Fluke CJ, Crawford RJ, Ivanova EP. The influence of nano-scale surface roughness on bacterial adhesion to ultrafine-grained titanium. Biomaterials 2010;31(13):3674-3683.

Chapter 4 *Serratia* biofilm formation on titanium substrates

Biofilms are the causes of many persistence infections [1]. Thus it is of clinical significance to understand the biofilm formation on titanium which is a common biomaterial. Moreover, a *Serratia* biofilm pregrown on titanium substrates can be used to produce HA coatings which are investigated in Chapter 6 and Chapter 7. The structure and morphology of this HA coating largely depends on the *Serratia* biofilm. Thus, this section also serves as a foundation for the subsequent biomineralisation. Due to limitation of sample appliance, the experiment in this section was carried out only once, with three sample analysed for each material.

4.1 *Serratia* biofilm formation on titanium with different surface treatments

In this section, the biofilms formed on titanium with six different surface treatments were examined and compared to investigate the effect of substrate surface properties on biofilm development.

4.1.1 Substrate characterisation

As described in Chapter 2, Ti1 (Al_2O_3 grit blasted Ti) and Ti2 (mirror-polished Ti) were prepared manually, while Ti3 (Deep profiled surface), Ti4 (plasma sprayed Ti), Ti5 (acid etched Ti) and Ti6 (grits blasted and acid etched Plus sample) were model surfaces of commercially available dental implants. Their topography, surface roughness and wettability were investigated and are compared.

4.1.1.1 Topography

The surface treatments significantly altered the surface morphology, as shown in Figure 4. 1. Figure 4. 1c & d show a mirror-like smooth surface after polishing. Figure 4. 1a, b, e & f

show a highly deformed surface with residual Al_2O_3 particles embedded in the substrate from the grit blasting. Unmelted titanium spheres with diameters of around 30-40 μm were visible on the plasma sprayed surface (Figure 4. 1g & h). Acid etching of a titanium surface produced surfaces features of elongated islands with micro-pores (Figure 4. 1i & j). The combination of grit blasting and acid etching led to a surface with dimples from 20 to 50 μm, and micro-pores on the dimple walls (Figure 4. 1k & l).

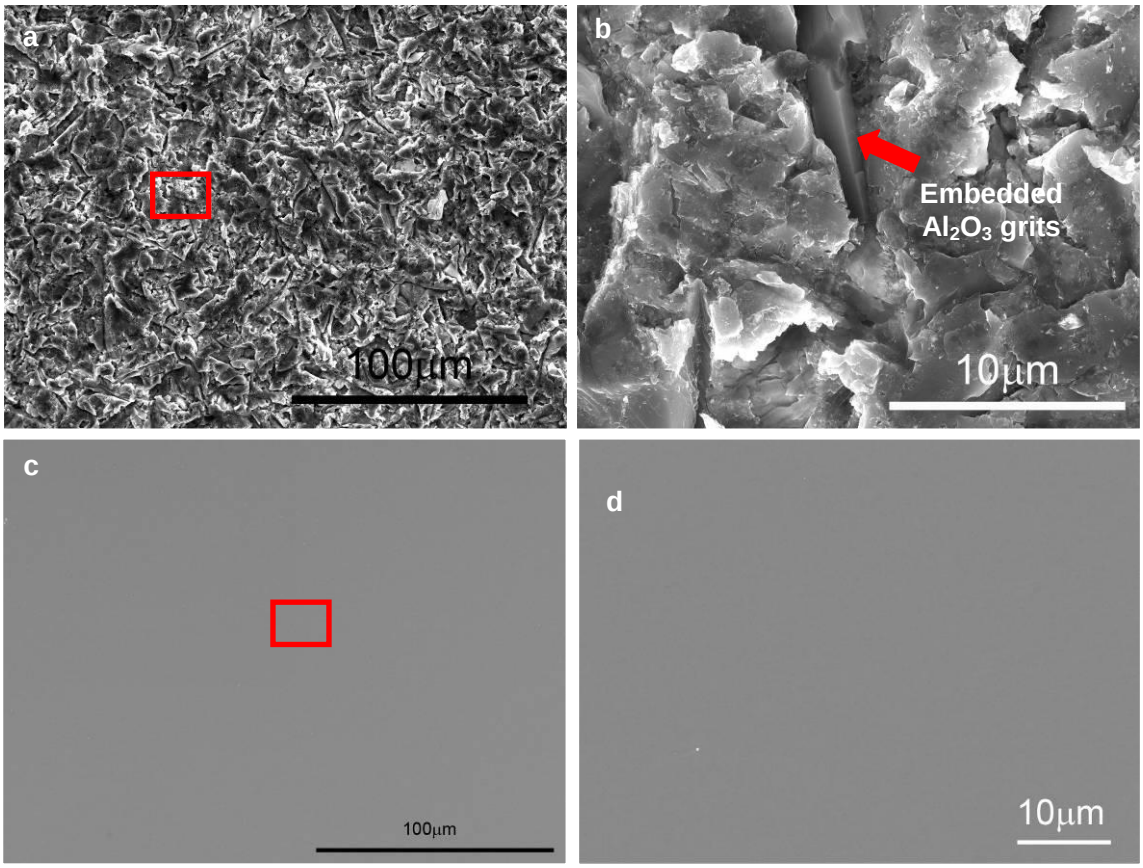

Figure 4. 1 The morphology of titanium substrates after different surface treatments (SE imaging)

a: 50 μm Al_2O_3 grit blasted pure titanium (Ti1).

b: The box in (a) at higher magnification.

c: Mirror-polished pure titanium (Ti2).

d: The squared site in (c) at higher magnification.

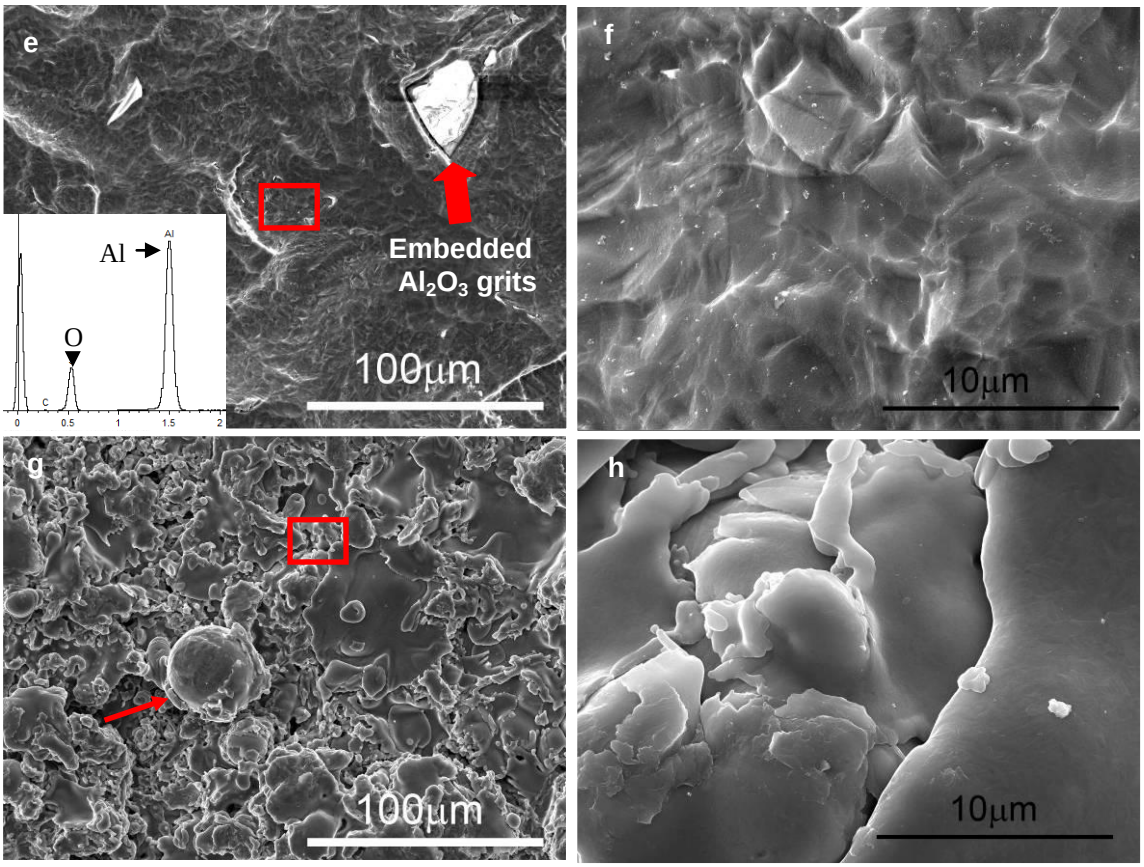

Figure 4.1 The morphology of titanium substrates after different surface treatments (SE imaging)

e: Deep Profile Surface, pure grit-blasted titanium (Ti3). The inset EDX spectrum shows that the embedded grit is Al_2O_3.

f: The squared site in (e) at higher magnification.

g: TPS plasma sprayed pure titanium (Ti4). The arrow points to a extruding titanium granule.

h: The squared site in (g) at higher magnification.

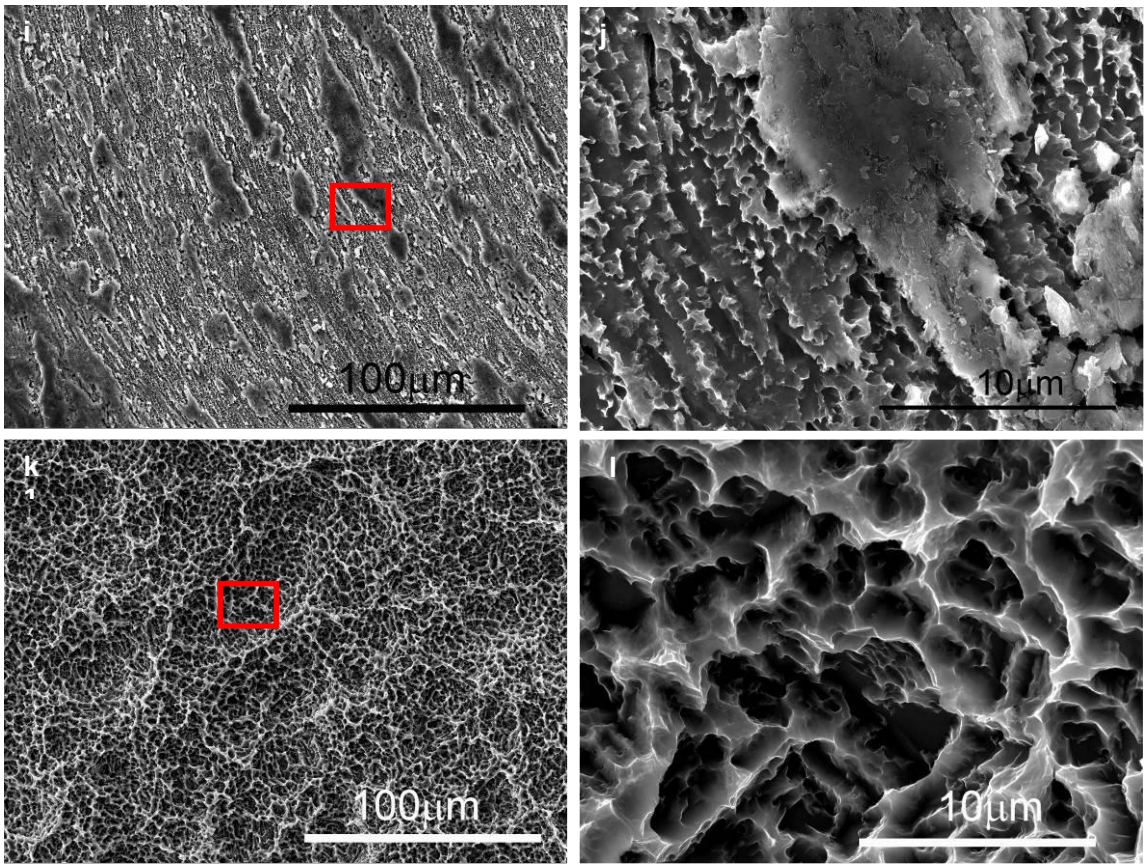

Figure 4. 1 The morphology of titanium substrates after different surface treatments

(continued)

i: Acid etched pure titanium (Ti5).

j: The squared site in (i) at higher magnification.

k: Grit-blasted and acid etched Plus titanium surface (Ti6).

l: The squared site in (k) at higher magnification.

4.1.1.2 Hydrophobicity

The substrate hydrophobicity is represented by water contact angle (WCA). The WCA of the substrates increased in sequence from Ti1 to Ti6, as listed in Table 4. 1 and compared in Figure 4. 2. Ti1 and Ti2 were hydrophilic (WCA<90^o), while Ti4 to Ti6 were hydrophobic (WCA>90^o), and Ti3 was in the transition between hydrophilic and hydrophobic (WCA≈90^o).

The estimated WCAs of Ti3 and Ti6 are comparable to previously reported results of 89.7° and 140.9°, respectively [2].

Table 4. 1 Substrate-water contact angle measurements

Substrate	***Ti1***	***Ti2***	***Ti3***	***Ti4***	***Ti5***	***Ti6***
WCA/°	26.44±2.41	66.20±4.26	85.65±5.07	107.39±0.66	122.95±6.03	151.53±0.66
Rupp *et al.* [2]	——	——	89.7	——	——	140.9

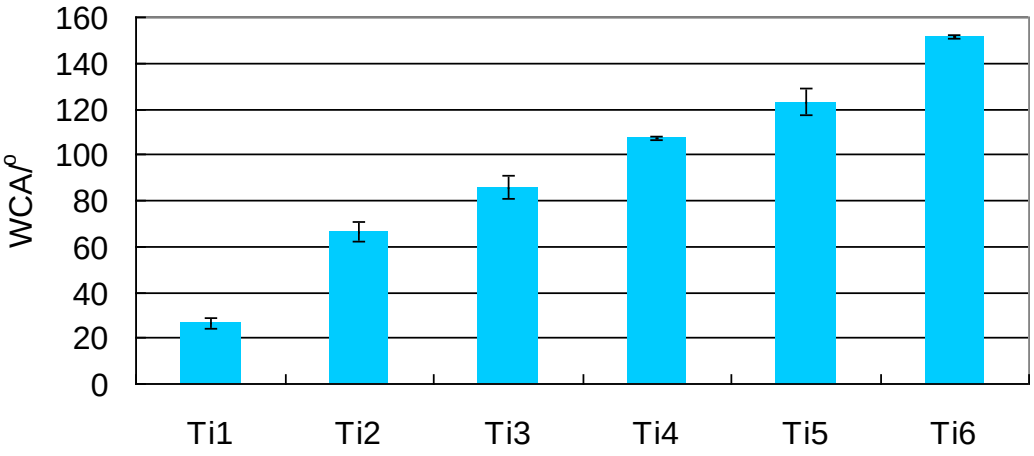

Figure 4. 2 Substrates water contact angle measurements (n=3)

4.1.1.3 Surface roughness

The surface roughness is measured as a Ra value, the arithmetic average deviation of the surface valleys and peaks. The results are shown in Figure 4. 3 and listed in Table 4. 2. The plasma sprayed surface Ti4 demonstrated the highest roughness, with an Ra value of 5.5 μm, followed by Ti6 (Ra=3.77±0.25 μm) and Ti3 (Ra=3.33±0.25 μm). The polished surface was the smoothest with a Ra value of 0.04±0.01 μm. The roughness measurements in this study

are compared with previous published results Table 4. 2.

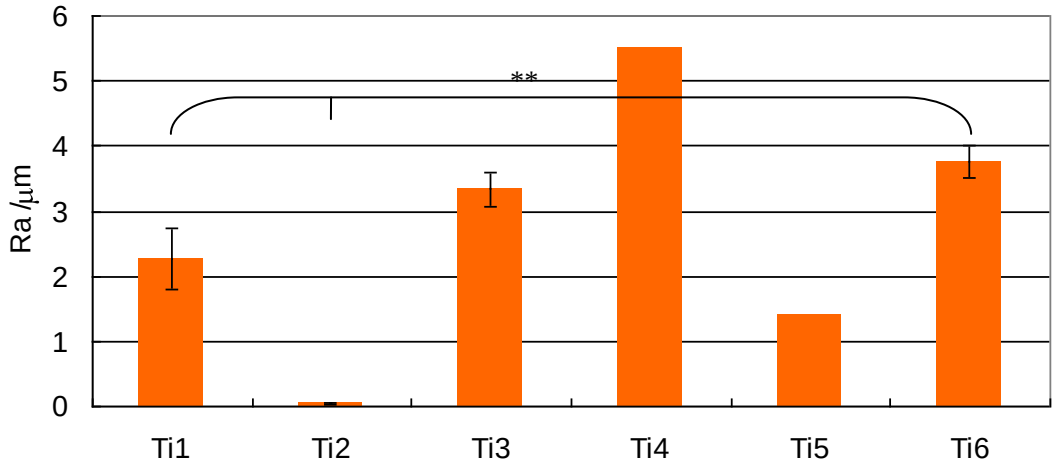

Figure 4. 3 Substrate surface roughness: Ra value for six different surfaces (n=3)

**: $p<0.005$ (p: derived by student *t-test*). Due to limitation of the sample appliance, Ra measurements on Ti4 and Ti5 were not repeated.

Table 4. 2 Substrate surface roughness: Ra values for six different surfaces

Substrate	***Ti1***	***Ti2***	***Ti3***	***Ti4***	***Ti5***	***Ti6***
Ra/μm	2.27±0.46	0.04±0.01	3.33±0.25	5.5	1.4	3.77±0.25
Sammons et al. [3]	——	——	2.41	3.5	0.86	2.75
Rupp et al. [2]	——	——	2.94	——	——	3.19

4.1.2 Biofilm characterisation

4.1.2.1 Bacterial protein assay

A protein assay was carried out to estimate bacterial accumulation on all the 6 substrates after

fermentation for 7 days as described in § 2.4.3. The results are summarised in Figure 4. 4 and listed in Table 4. 3. Judged by the protein present, the amount of bacteria on the substrates followed the sequence Ti2>Ti4>Ti1>Ti3>Ti5>Ti6. Significant differences are indicated on the figure.

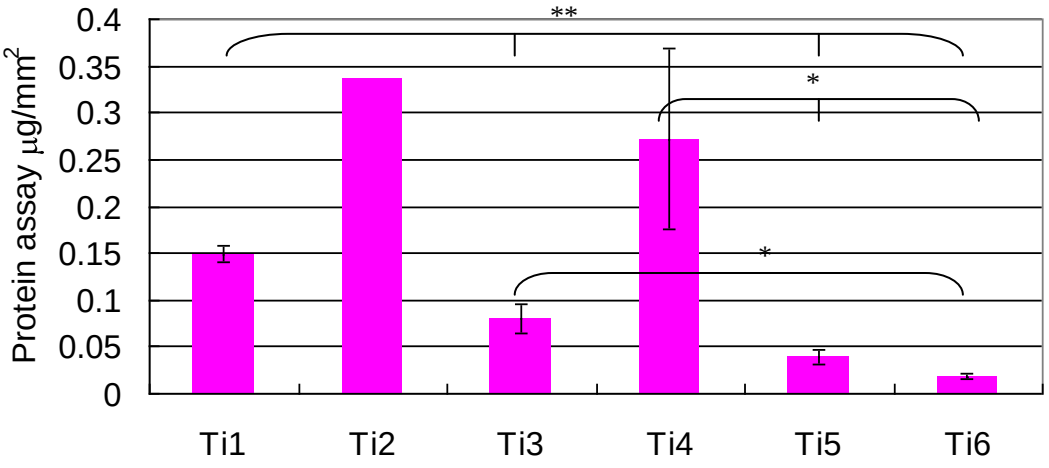

Figure 4. 4 Bacterial protein assay (n=3)

**: $p<0.005$; *: $0.005<p<0.05$ (P: derived from Student *t-test*). The measurement on Ti2 was not repeated due to sample limitation.

Table 4. 3 Bacterial protein assay

	Ti1	***Ti2***	***Ti3***	***Ti4***	***Ti5***	***Ti6***
Protein assay μg/mm^2	0.15±0.01	0.34	0.08±0.02	0.27±0.10	0.04±0.01	0.02±0.003

4.1.2.2 Biofilm morphology

The morphology of the 7-day old biofilm was studied by SEM. It was observed that the mature biofilm structures characterised by bacterial stacks only occurred on Ti1 and Ti2, as

seen in Figure 4. 5 and Figure 4. 6. On Ti1, the 50 μm Al_2O_3 grit blasted titanium, the bacterial clumps tended to grow perpendicularly to the substrate surface (Figure 4. 5b), and were composed of randomly intertwined cells (Figure 4. 5c). Due to the thickness of the biofilm, it was impossible to visualise the embedded Al_2O_3 particles underneath the bacterial layer using SEM. Thus, the effect of the Al_2O_3 particles on biofilm formation was not clear.

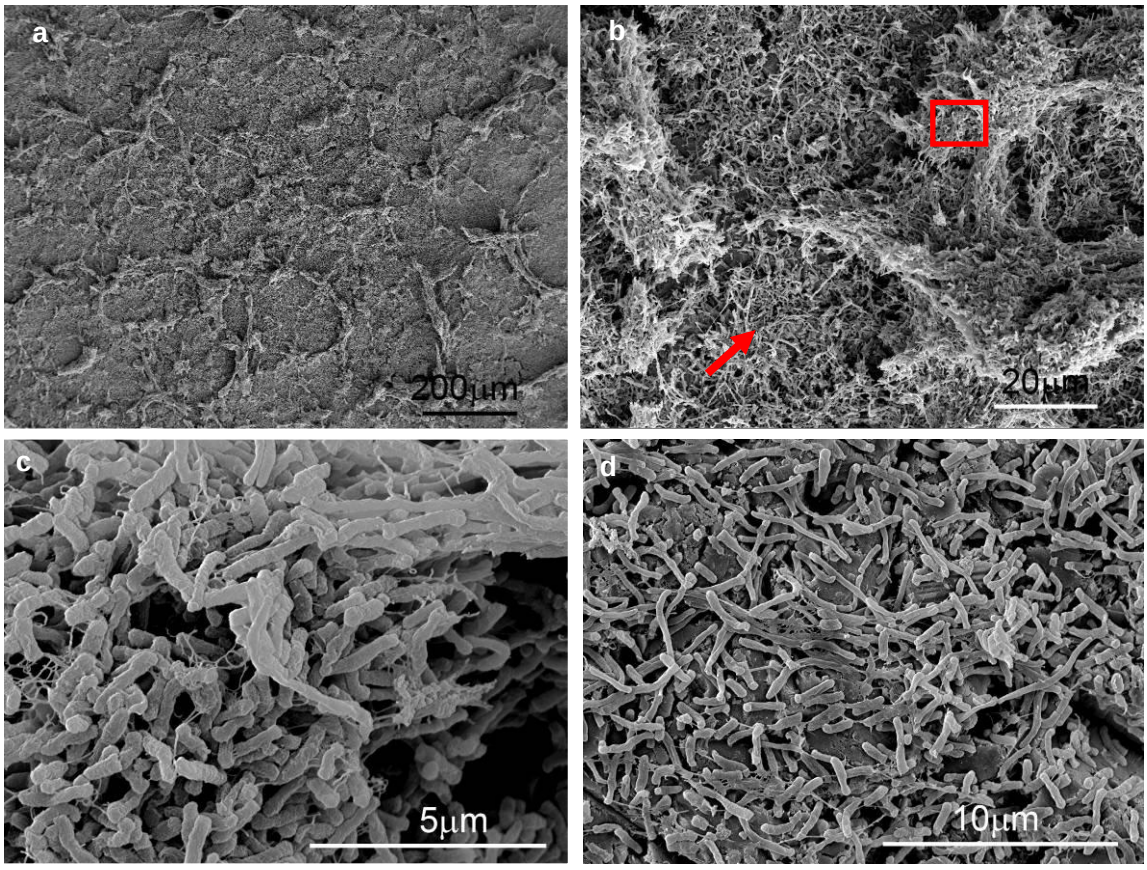

Figure 4. 5 The 7-day old biofilm on Ti1 (gold coated, SE imaging)

a: Low magnification image showing the overall morphology of the biofilm on Ti1 (Al_2O_3 grit-blasted Ti).

b: Higher magnification of the bacterial clumps.

c: Image of the bacterial clumps showing that they are composed of randomly intertwined bacteria (the box in (b)).

d: Bacterial matrix (the arrowed site in (b)).

On Ti2 - the mirror polished surface - the bacterial towers were comparatively flattened, and consisted of highly oriented bacteria, as seen in Figure 4. 6b. The cracks observed in the biofilm on both substrates are due to the drying procedure.

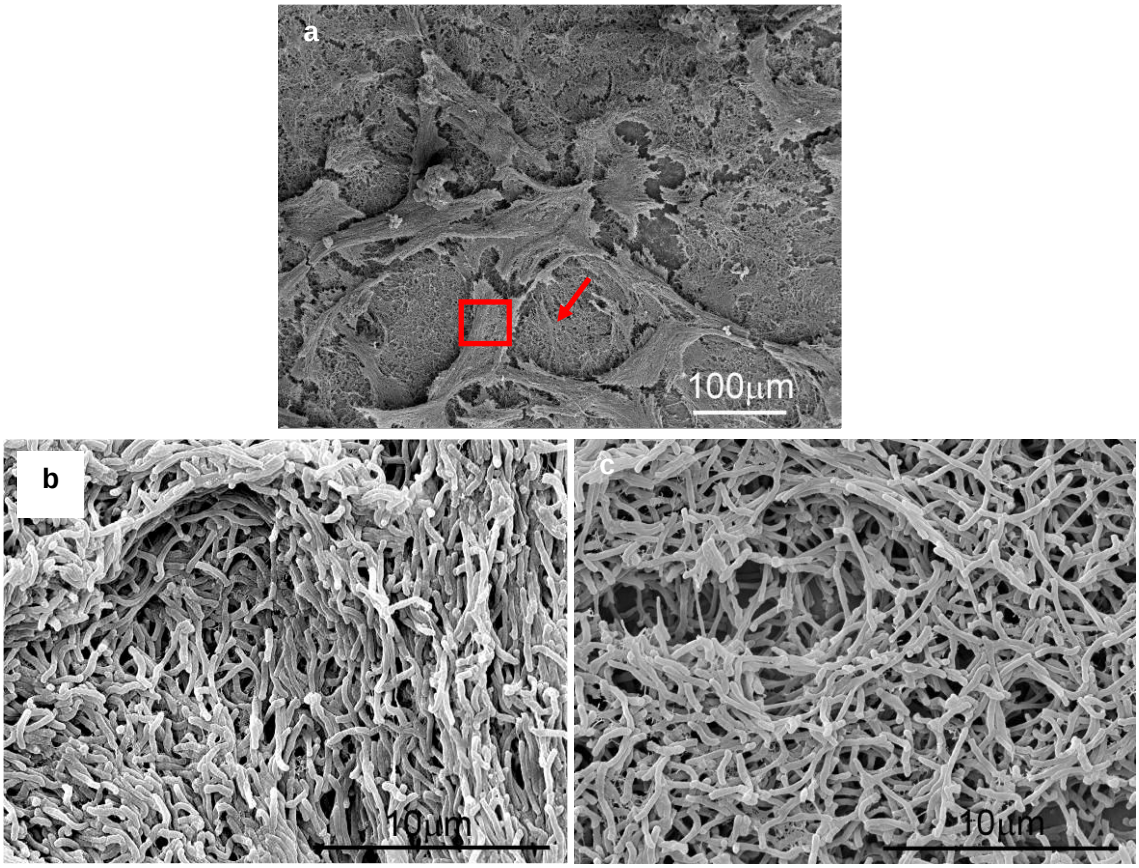

Figure 4. 6 The 7-day old biofilm on Ti2 (gold coated, SE imaging)

a: Low magnification image showing the overall morphology of the biofilm on Ti2: flattened bacterial colonies.

b: Higher magnification image of the box in (a) showing that the flattened colonies are composed of highly orientated bacteria.

c: Higher magnification image of the arrowed site in (a) showing the bacterial matrix.

A monolayer of bacteria formed on Ti3 (the Deep Profile surface) (Figure 4. 7a). The bacteria were randomly dispersed. The bacterial distribution was found to be similar on the titanium

substrate (Figure 4. 7b) and on the embedded alumina particles (Figure 4. 7c).

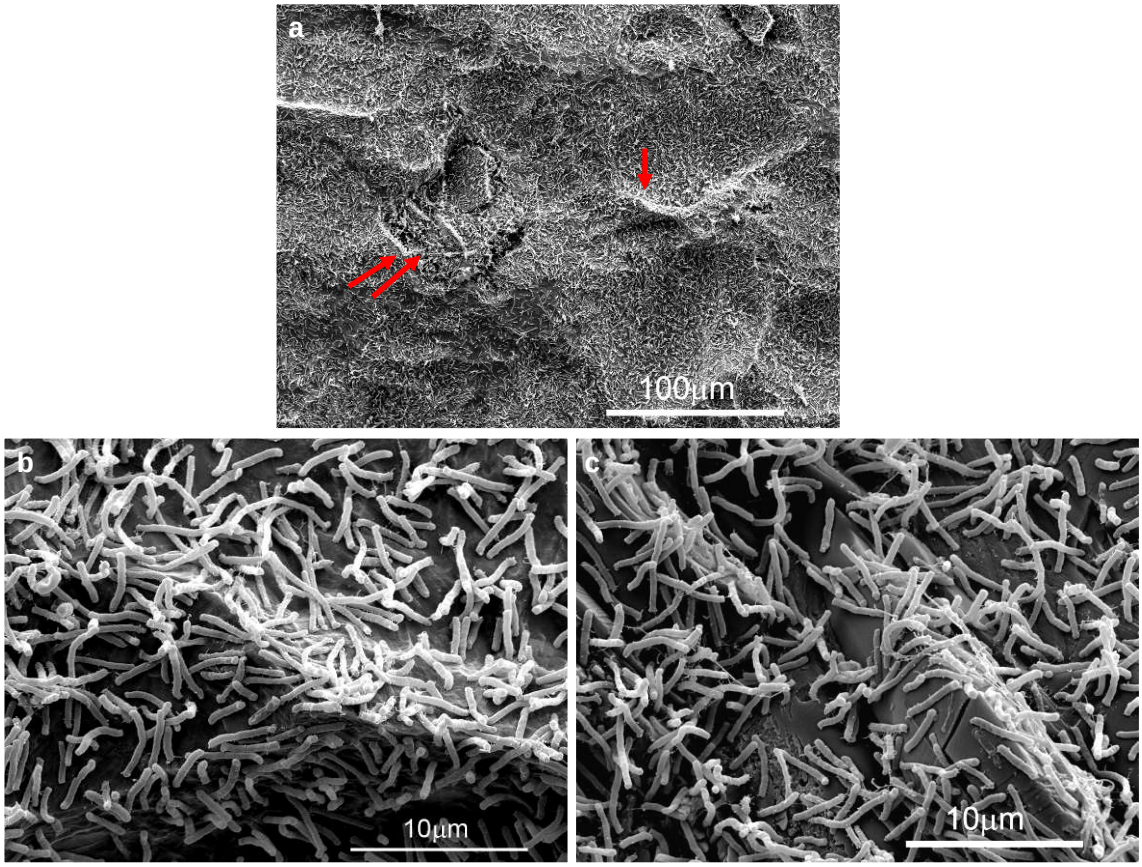

Figure 4. 7 The 7-day old biofilm on Ti3 (gold coated, SE imaging)

a: Low magnification image showing the overall morphology of the biofilm on Ti3.

b: Higher magnification image showing the biofilm on the rough titanium surface at the single-arrowed site in (a).

c: Higher magnification image showing the biofilm on embedded Al_2O_3 at the double-arrowed site in (a).

On Ti4, the plasma sprayed surface, bacterial bridges (the double-arrowed site in Figure 4. 8a) were observed composed of highly oriented bacteria (Figure 4. 8b) extended from the protruding titanium granules to the lower substrate. The bacterial matrix that covered evenly the entire surface was composed of randomly arranged cells (Figure 4. 8c).

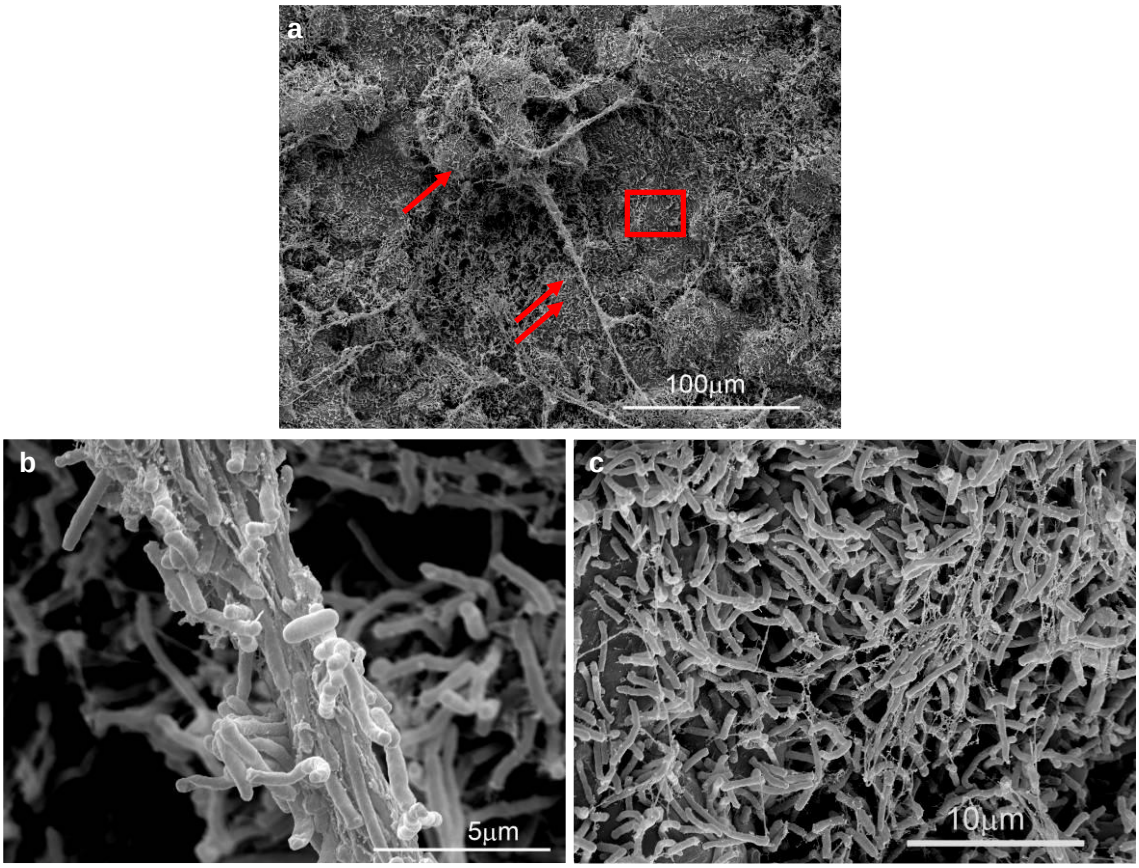

Figure 4. 8 The 7-day old biofilm on Ti4 (gold coated, SE imaging)

a: Low magnification image showing the overall morphology of the biofilm on Ti4. The single arrow indicates a titanium granule similar to the one in Figure 4. 1g.

b: Higher magnification image of the double-arrowed site in (a) showing a bacterial extension composed of highly oriented cells.

c: Higher magnification image of the box in (a) showing the bacterial matrix.

As on Ti3, the biofilm formed on Ti5 consisted only of a single bacterial layer that covered the whole substrate (Figure 4. 9a). At higher magnification, it was found that the bacteria tended to lie across the edge of the islands on the surface (arrows in Figure 4. 9b), but are randomly distributed at other sites.

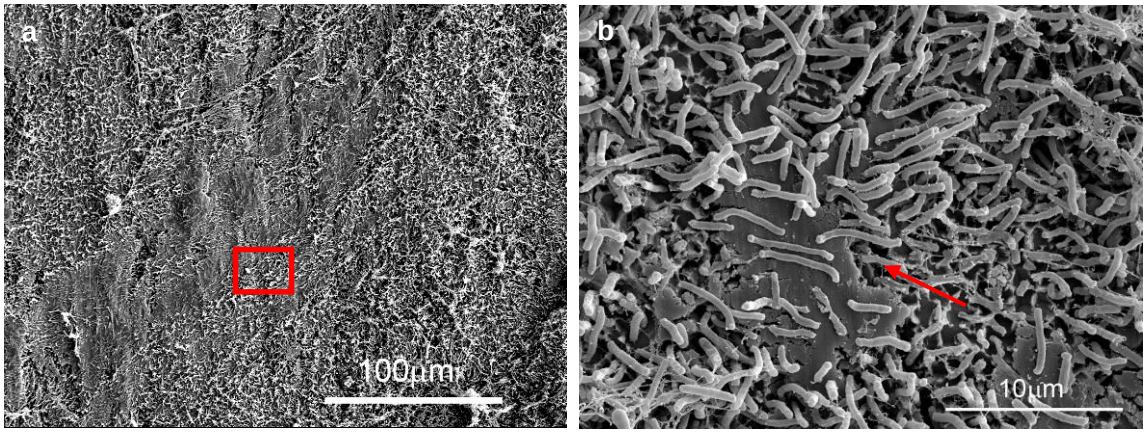

Figure 4. 9 The 7-day old biofilm on Ti5 (gold coated, SE imaging)

a: Higher magnification image showing the overall morphology of the biofilm on Ti5 (acid etched surface).

b: The biofilm in the box in (a) at a higher magnification. The arrow points to where bacteria lie across the edge of the islands on the surface.

The biofilm formed on Ti6, the blasted and etched Plus surface, had distinct features of bacterial 'platform' (~50 μm) supported by bacterial 'columns', as seen in Figure 4. 10a & b. In areas other than the plateau, the bacteria attached randomly to the pore walls of the substrate.

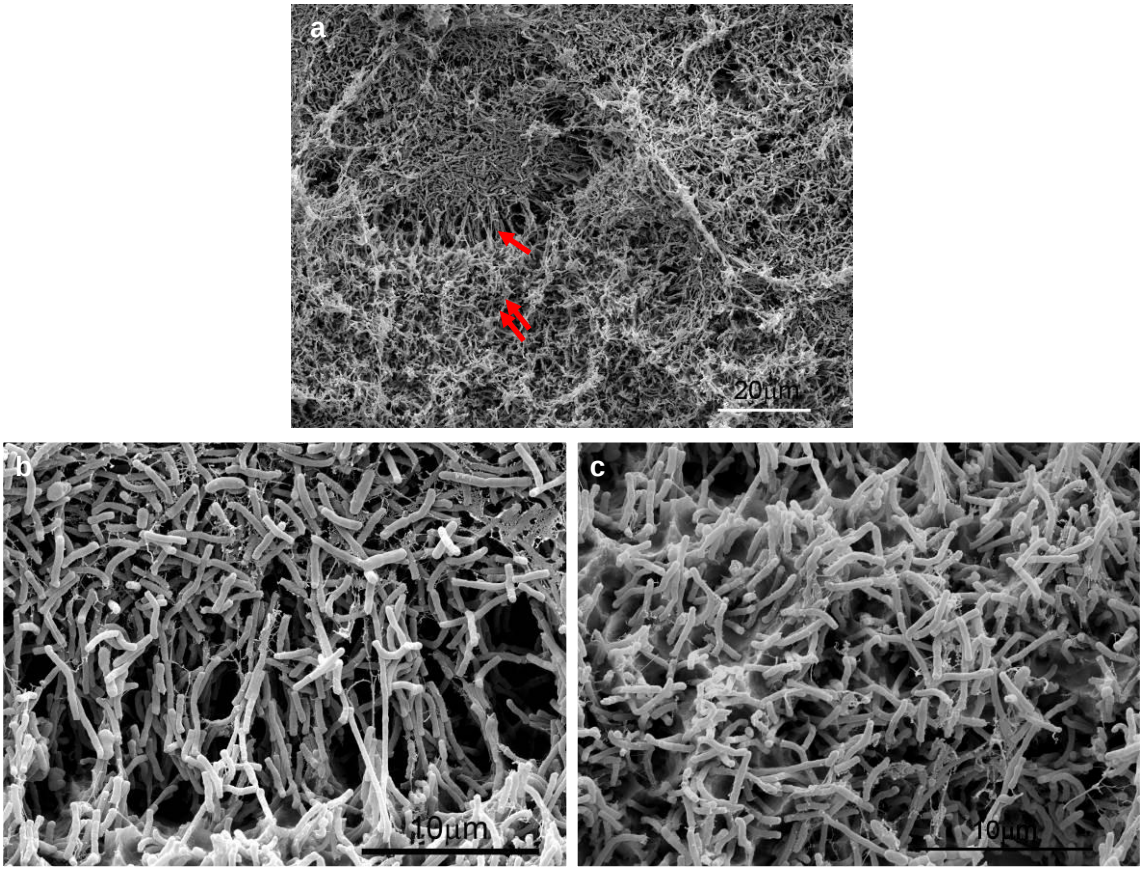

Figure 4. 10 The 7-day old biofilm on Ti6 (gold coated, SE imaging)

a: The overall morphology of the biofilm on Ti6.

b: The bacterial 'platform' supported by bacterial 'columns' (the single-arrowed site in a).

c: The bacterial matrix (the double-arrowed site in a).

By comparing Figures 4. 5 to 4. 10, it can be observed that the morphology of the 7-day-old biofilm is significantly different on different surfaces, suggesting a possible role of substrate topography in shaping biofilms.

4.2 *Serratia* biofilm formation on a porous titanium web

Porous structures are ideal scaffolds to support bacterial growth for potential applications such as bacterial fuels, biomineralisation, water purification and antibiotic production. In this study, the growth of *Serratia* biofilm on a porous titanium wire mesh, 'titanium web', was investigated in this section. This bacteria coated system will later go through a biomineralisation stage to produce HA on the titanium surface, as described later in Chapter 8.

4.2.1 Substrate characterisation

The porous scaffold is constructed from randomly knitted titanium fibres (Figure 4. 11a). These rectangular-cross-section fibres are approximately 50 μm wide. As seen in Figure 4. 11b & c, one side of the fibre is rougher than the others, with the topography displayed in Figure 4. 11d.

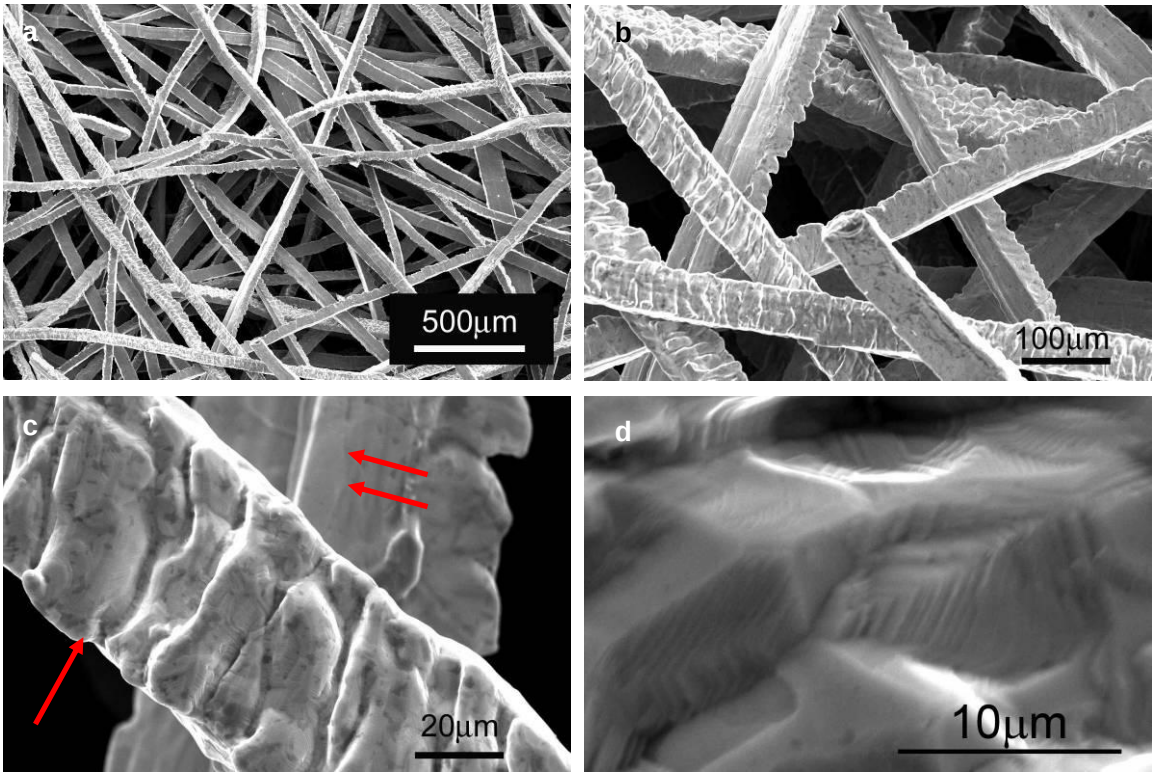

Figure 4. 11 Morphology of the titanium web by SEM

a: The web is composed of a network of Ti wires.

b: Each Ti wire is 50 μm across and has a rectangular cross-section.

c: The Ti wire is rougher on one side (the single-arrowed face) and smoother on the others (the double-arrowed side).

d: A Ti fibre at higher magnification, showing grain structure.

Micro X-ray CT was used to construct a 3D model of the porous structure, as illustrated in Figure 4. 12a and enlarged in Figure 4. 12b. Cross sections through the web are shown in Figure 4. 12c, d and e. It can be seen that most of the wires tend to incline towards the *xy* plane but are randomly orientated within this plane.

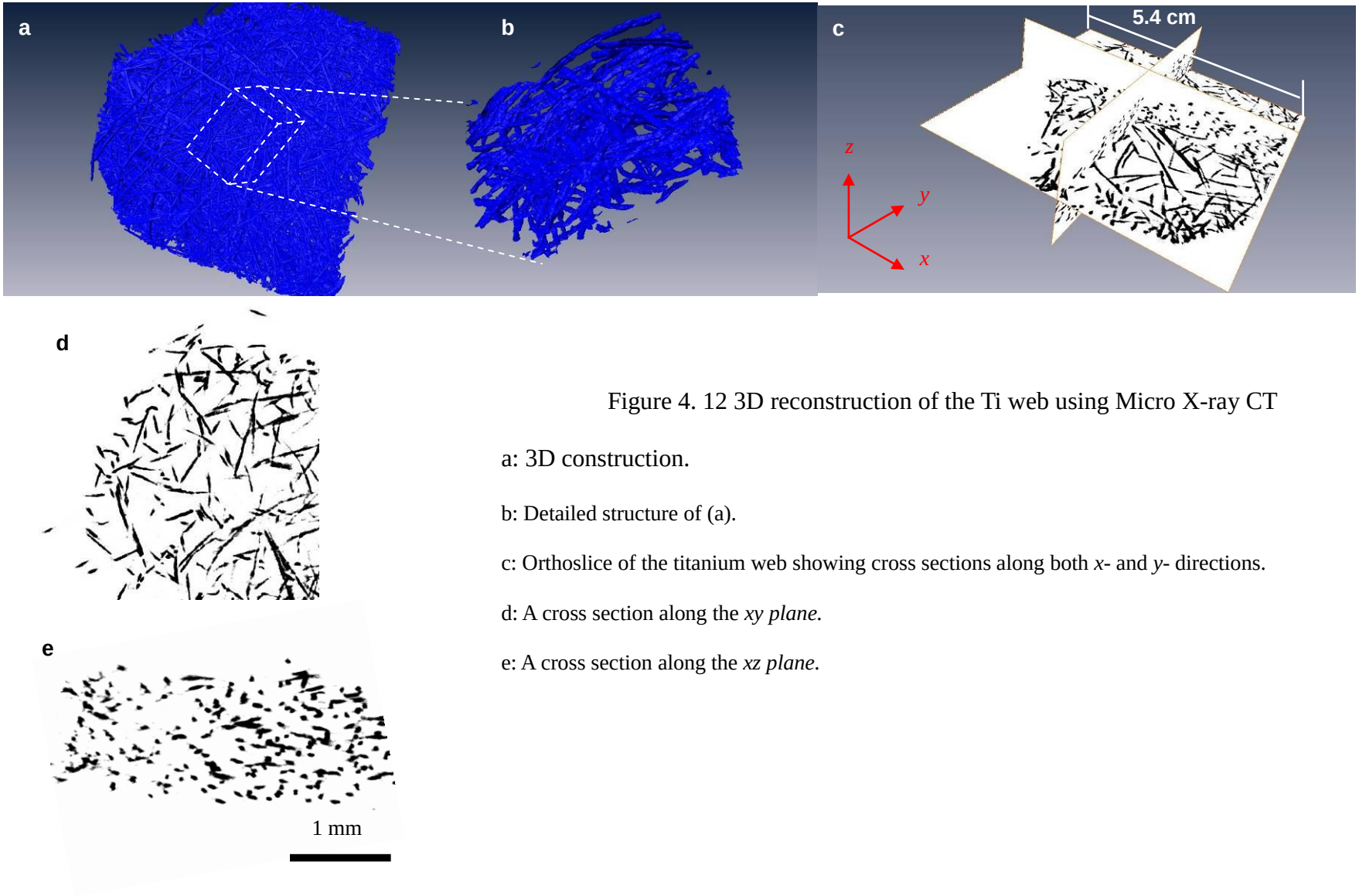

Figure 4. 12 3D reconstruction of the Ti web using Micro X-ray CT

a: 3D construction.

b: Detailed structure of (a).

c: Orthoslice of the titanium web showing cross sections along both *x*- and *y*- directions.

d: A cross section along the *xy plane.*

e: A cross section along the *xz plane.*

4.2.2 Biofilm characterisation

The biofilm formed on the porous Ti web is not homogeneous. Large bacterial clumps are found on some Ti fibres but not others (Figure 4. 13a & b). Nevertheless, every Ti wire is observed to be wrapped with *Serratia* cells, although the thickness of this bacterial layer differs markedly. On wires nearer to the surface of the structure, the biofilm is thicker and the bacteria are around 5 to 10 μm long (Figure 4. 13c & d). However, on the wire deep inside the structure, the film is usually thinner and the bacteria are much shorter, around 1 to 3 μm (Figure 4. 13e & f). In a summary, both the thickness of the biofilm and the length of the individual bacteria decrease as the distance away from the porous structure surface increases.

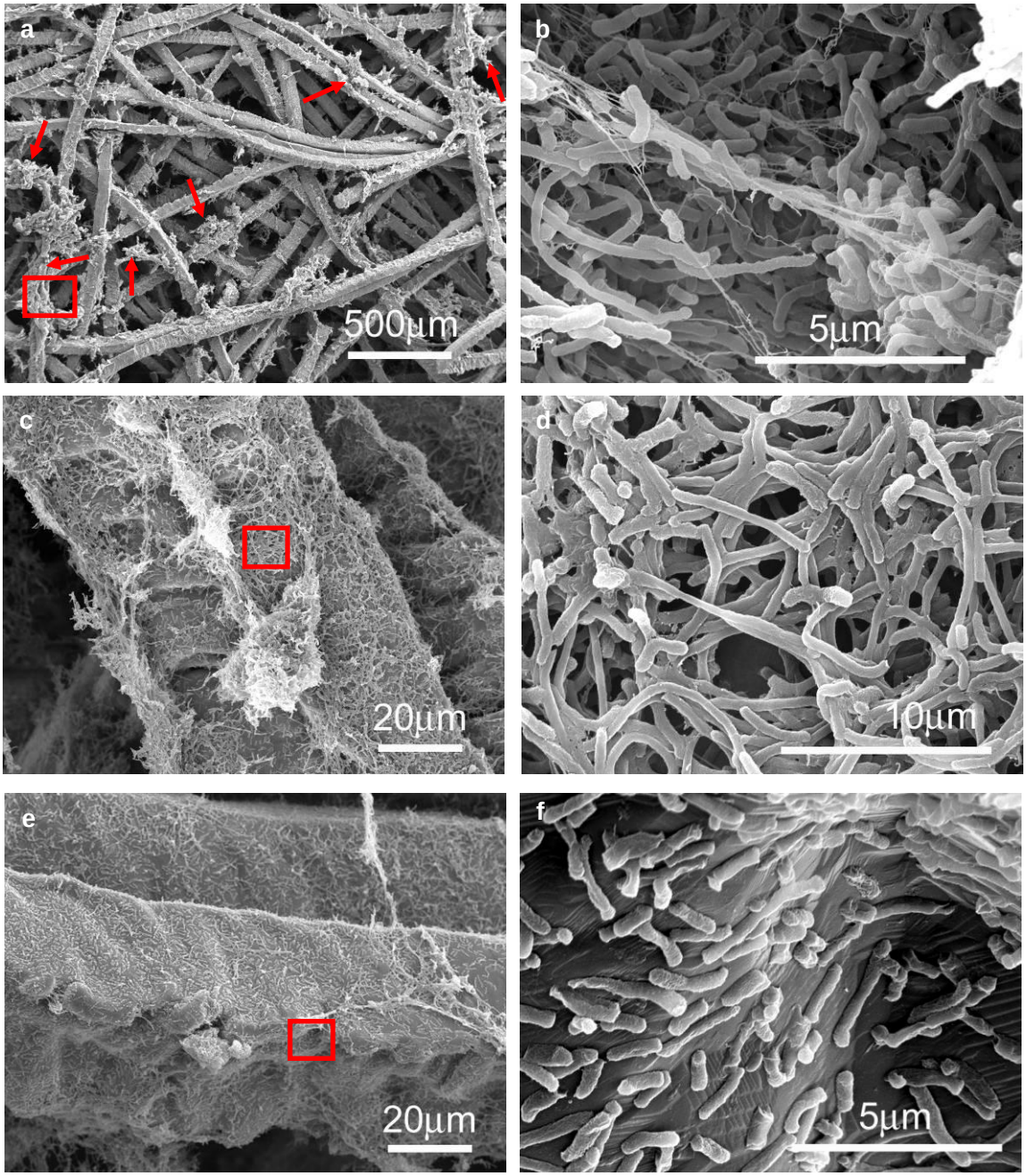

Figure 4. 13 5-day old *Serratia* biofilm on Ti web (gold coated, SE imaging)

a: The overall morphology (bacterial clumps on Ti surface, indicated by arrows).

b: A bacterial clump at higher magnification.

c: Thick biofilm on the outer Ti wire.

d: (c) at higher magnification.

e: Biofilm on an inner Ti wire: thin and barely covering the Ti fibre.

f: (e) at higher magnification: the bacteria are shorter when compared with those in (b) and (d).

The bacterial distribution within the porous system was studied further using Micro X-ray CT. However, due to the limited resolution of the method, only the large bacterial clumps could be imaged. Just as observed by SEM, the bacterial colonies disperse rather randomly within the system. As seen in Figure 4. 14, no obvious difference regarding the colony density was found between the periphery of the scaffold and the inner structure, which is very surprising since the periphery of the porous structure is expected to be the most favourable site for the formation of bacterial colonies as was indeed evident by the SEM observation. Micro X-ray CT, however, only gives a rather rough description of the bacteria distribution, as most of the features, including the biofilm surrounding each Ti wire, are 'invisible' to it.

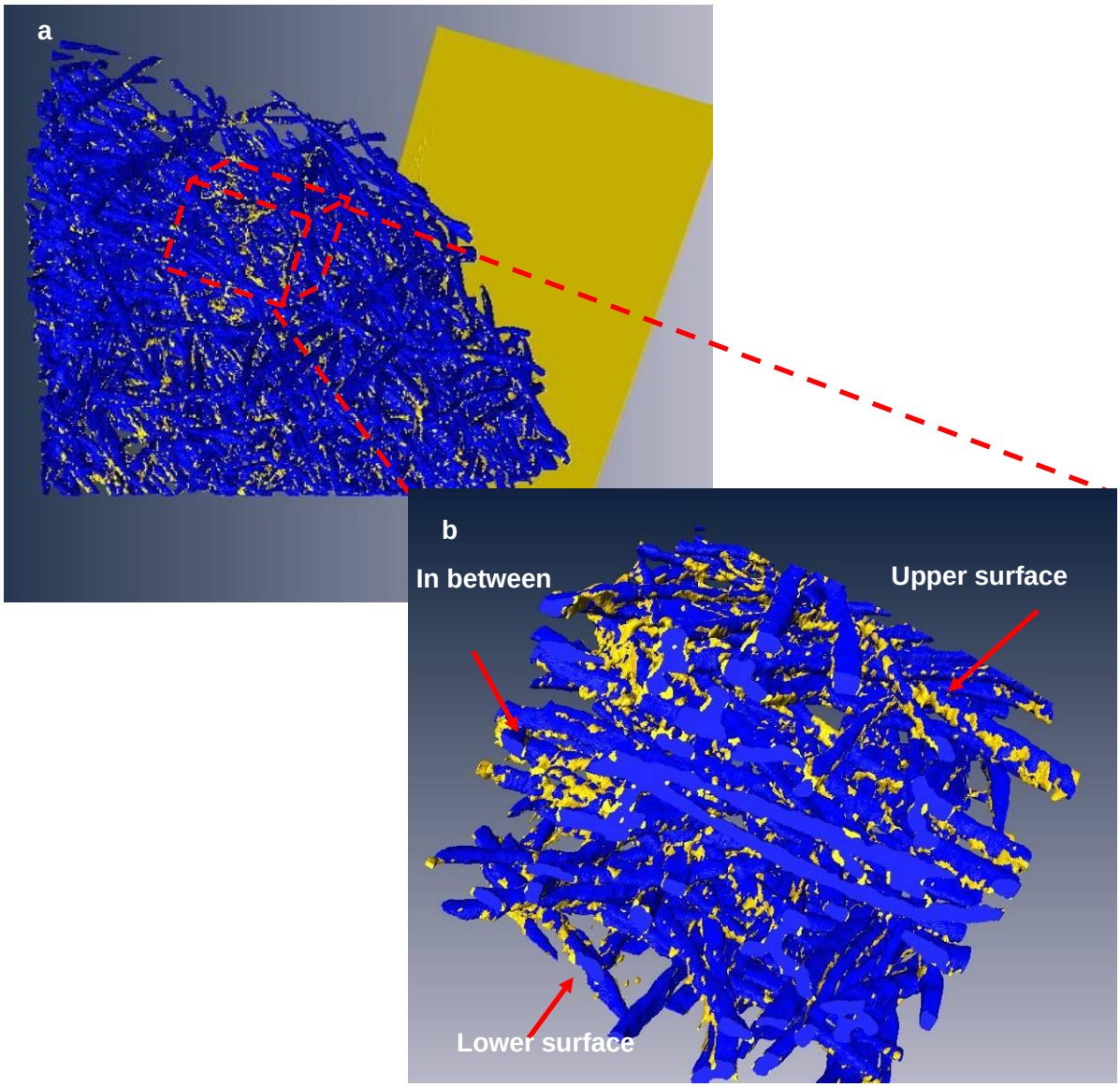

Figure 4. 14 3D reconstruction of 5-day old *Serratia* biofilm on porous Ti web by Micro X-Ray CT

a: The overall porous Ti web (blue) with *Serratia* colonies (yellow).

b: The cube in (a). Note that most of the titanium surface is apparently 'bacteria-less', apparently contradicting SEM observations.

4.3 Summary

Distinct differences in surface topography, wettability and roughness were observed on

titanium discs with different surface treatments. While the hydrophobicity followed the sequence Ti1<Ti2<Ti3<Ti4<Ti5<Ti6, the surface roughness, expressed in Ra value, was the highest on Ti4, followed by Ti6, Ti3, Ti1, Ti5 and Ti2.

The *Serratia* bacteria in the biofilm on each surface were quantified by a protein assay, which suggested that the most biofilm growth occurred on Ti2 and Ti4, followed by Ti1 > Ti3 > Ti5 > Ti6. Surface wettability may be a more important factor than roughness in influencing biofilm growth in this work, as the amount of bacteria on Ti1, Ti3, Ti5 and Ti6 decreased in the same order as the hydrophilicity of the four substrates.

The morphology of the biofilm differed on each type of substrate. Bacterial stacks were only observed on Ti1, Ti2 and Ti4, but not the others. Even on substrates with comparable amounts of bacteria according to the protein assay, as in the case of Ti2 and Ti4, or Ti5 and Ti6, the biofilm showed significant differences. These observations suggest that substrate surface topography contributes to biofilm architecture.

The porous titanium web was proved to be suitable as a support for biofilm development. Although in the SEM images bacteria appeared be longer at the periphery of the structure but shorter inside, a 3D reconstruction of the biofilm indicated that the distribution of large bacterial clumps was more or less similar regardless of their locations. However, the fixation and dehydration during sample preparation may introduce significant deformation of the biofilm. Moreover, the accuracy of micro CT is limited by its resolution. Therefore other techniques such as confocal microscopy will be used in the future work for a more accurate investigation.

References

1. Donlan RM. Biofilm formation: a clinically relevant microbiological process. Clinical Infectious Diseases 2001;33(8):1387-1392.
2. Rupp F, Scheideler L, Rehbein D, Axmann D, Geis-Gerstorfer J. Roughness induced dynamic changes of wettability of acid etched titanium implant modifications. Biomaterials 2004;25(7-8):1429-1438.
3. Sammons R, Lumbikanonda L, Gross M, Cantzler P. Comparison of osteoblast spreading on microstructured dental implant surfaces and cell behaviour in an explant model of osseointegration: a scanning electron microscopic study. Clinical Oral Implants Research 2005;16(6):657-666.

Chapter 5 Discussion-bacterial adhesion, proliferation and biofilm formation

This chapter is a general discussion of the results in Chapter 3 and Chapter 4: the influence of titanium alloy structure on bacterial adhesion and proliferation, and *Serratia* biofilm formation on titanium substrates.

5.1 The influence of titanium alloy structure on bacterial adhesion and proliferation

The results in Chapter 3 are discussed in this section. The importance of this work not only lies in the clinical fields, but also in its novel approach to study the relationship between microbial distribution and metal microstructure using a non-destructive method based on direct electron microscopy and image analysis.

5.1.1 The influence of CP Ti grain boundaries and grain orientations

GBs and grain orientations are metallurgical characteristics closely related to manufacturing methods. They are potential bacterial growth promoters/inhibitors due to the morphology and energy changes at GBs and between different grain orientations. If we had a better understanding of these potential influences, the adhesion and proliferation of bacteria on any metal surface could be manipulated by simply modifying the production methods to deplete or promote GBs and certain grain orientations.

The previous researchers to analyse the influence of metal microstructure on bacterial adhesion often used indirect methods, and sometimes did not consider the effect of surface roughness, as described in § 1.7. The surface used in this study was mirror-polished without etching, therefore the artefacts due to surface roughness avoided. The bacterial distribution and the metal microstructure are examined directly on the same surface using backscattered electron signals (BSE) and electron backscattered diffraction (EBSD) without any further

treatments such as polishing and etching. Thus, the statistical investigation is more reliable. Moreover, it is worth mentioning that some of the previous work failed to separate adhesion from proliferation. While adhesion is a physical chemical reaction between the bacteria and the surface, proliferation involves the growth and reproduction of the cells [1]. Walsh *et al.* (1993), for example, concluded that bacterial adhesion was random; it was not until the proliferation stage that the cells became sensitive to the substrate metallurgical features [2]. The introduction of PBS as the suspension medium in this study was essential to distinguish the adhesion stage, as no nutrients are available for bacterial growth. Moreover, unlike the stainless steels used in most of the previous studies, pure titanium obviously does not have any significant elemental segregation at the grain boundaries when compared with steels, hence, the only parameters, once it is properly polished and the influence of surface roughness is thus avoided, that may affect the bacterial behaviour are the energy and structure at the GBs and between different grain orientations.

The influence of grain boundaries

There have been reports of GB associated bacterial adhesion to stainless steels [3, 4], attributed to both the high surface energy and elemental accumulation at the GBs. Recently, bacterial adhesion was reported to be promoted on equal channel angular pressed titanium with a nano-crystalline structure (mirror polished), attributed to the increase of the surface roughness at the nano-scale due to its high concentration of GBs [5].

The random distribution of bacteria on CP Ti seen in this study, in both adhesion (*S. epidermidis*, *S. sanguinis*, *E. coli* and *Serratia*) and the early proliferation (*Serratia*) indicates that the GB itself is not enough either to promote bacterial adhesion, or to stimulate preferential colonisation. That is to say, the adhesion of *S. epidermidis*, *S. sanguinis*, *E. coli*

and *Serratia* and the early proliferation of *Serratia* are not sensitive to the energy or morphology change at titanium GBs. Unlike the nano-crystalline titanium surface where bacterial attachment was reported to be significantly increased [5], the titanium in this work is a commercially available cold-rolled substrate with grain size ranging from 10 to 100 μm. Thus, the GB density is much lower and the surface discontinuity due to the existence of GBs is not as frequent as on the nano-crystalline surface, but only occurs occasionally. It may be only when the GBs are so dense that they contribute to the surface roughness that the bacterial behaviour will be affected. The previously observed phenomenon of GB-associated bacterial accumulation on stainless steels may be entirely due to the elemental accumulation, rather than being a function of the chemical difference and energy change at the GBs as the authors concluded [3, 4].

The influence of grain orientation

This work is the first to investigate the influence of grain orientation on bacterial distribution. However, pre-osteoblast responses were demonstrated to be grain orientation-related [6]. The results in this work suggest that grain orientations may be irrelevant, as neither the Gram-positive nor the Gram-negative bacterial strains tested showed any preference toward any specific texture during either adhesion or early proliferation. The previous finding of grain orientation-related osteoblast cell attachment was obtained from experiments in which the authors compared the number of cells on two separate samples with different dominant orientations [6] rather than comparing cell behaviour in relation to each specific grain as in this work. They attributed the preferential attachment to the higher hydrophilicity of the $(10\bar{1}0)$ orientation dominant sample, but they failed to compare the cell behaviour on grains at a micro-scale. The random bacterial adhesion regardless of grain orientation in this work

suggests either that unlike osteoblast cells, bacteria are not sensitive to grain orientations, or even if they are, the slight difference at the micro-scale cannot trigger a grain orientation-specific bacterial adhesion.

As a conclusion, the observations in this work suggest that the surface energy/morphology change due to the microstructure of the substrate is not important, either in the adhesion or in the proliferation phase.

5.1.2 The influence of Ti 64 alloying components

A V-rich site-specific adhesion of *S. epidermidis* has been reported on Ti 64 [7]. However, the substrate used in that work was etched before being exposed to the cell culture, producing discontinuities on the surface [8]. Bacteria are sensitive to these features and tend to attach better on rougher surfaces. Therefore it is possible that their results were in fact caused by etching-induced roughness rather than by the surface chemistry difference. To avoid such confusion, in the present study the substrate was mirror-polished and backscattered electron imaging was used to reveal the distributions of *S. epidermidis* and *S. sanguinis* in relation to the substrate phase structure without the disturbance of roughness. As *Serratia* and *E. coli* bacteria have a similar size to the grains of Ti 64, their distribution to Ti 64 phase structure could not be analysed. Selective colonisation of the two Gram-positive bacteria was not observed. However the chemical composition does have an effect on bacterial behaviour, as could be indicated by the differential adhesion on separated CP Ti, Al and V shown in Figure 3. 7. The bias between the two phases in Ti 64 alloy – due to a higher content of V and lower content of Al in β phase - may not be high enough for bacteria to detect it at the attachment stage, since there was no noticeable distinction between the number of bacteria on CP Ti and Ti 64, nor was any phase-preferential attachment observed on Ti 64.

Interestingly, the two Gram-positive and the two Gram-negative bacteria showed different patterns when comparing their adhesion on CP Ti, Ti 64, Al and V which can be seen clearly in Figure 3. 7. The cell wall of a Gram-positive bacterium is constructed from peptidoglycan networks, but in a Gram-negative bacterium, it is always terminated by an extra outer membrane associated with lipopolysaccharide (LPS) [9]. This structural difference may contribute to the opposite adhesion behaviours observed in this study. However, further investigation including more bacterial strains is necessary for a thorough understanding of the phenomenon. In spite of the existence of Al and V, all the bacteria adhered equally well to CP Ti and Ti 64: this was true not only of the Gram-positive bacteria but also the Gram-negative ones which are far more sensitive to pure V, as indicated in Figure 3.7. This comparable adhesion between the two titanium systems is in good accordance with various previous reports [2, 7], and is attributed to the similar surface wettability of the two substrates in terms of water contact angles.

The chemical composition of the substrate is another important factor which may influence bacterial adhesion [1, 7, 10, 11]. Aluminium was found to inhibit bacterial adhesion and growth in this study. Illmer and Schinner (1997) reported that motility of *Pseudomonas* sp. (Gram-negative) and *Arthrobacter* sp. (Gram-positive) was distinctly decreased by Al^{3+} [12]. This may be caused by the bonding of Al^{3+} to ATP, which is responsible for energy transportation within cells. ATP exists as a complex with Mg^{2+}, but its ability to bond with Al^{3+} is 10^7 times higher than that with Mg^{2+} [13]. Hence, once Al enters the cell, the normal energy flow will be interrupted and the energy essential for bacterial movement and other activities will be inaccessible [13].

In spite of the protection of the oxide film in Ti 64, Al is theoretically able to escape from the

substrates into the solution as ions, and bacteria can contribute to the process. For example, microbial-induced corrosion is very common in concretes [14] and metals [15-17]. Bacterial metabolic products are implicated in this process. It has been reported that microbial secreted organic acids could result in the corrosion of aluminium and aluminium alloys [18, 19]. The oxide layer on Ti 64, in spite of the alloying elements of Al and V, is mainly composed of TiO_2 which is known to be stable and resistant to corrosion. It is possible that after a short exposure time of only four hours, it stays intact and the release of Al is negligible. Thus no difference is found when comparing the adhesion on Ti 64 with that on CP Ti. After proliferation for 24 hours, the difference between the number of *Serratia* on CP Ti and on Ti 64 was still not significant, suggestion that either that the oxide layer on Ti 64 is still intact, or the concentration of the escaped Al ions is not enough to affect bacteria behaviour. Further investigation will be necessary. The amount of bacteria on CP Ti and Ti 64 will be compared for a longer exposure time. More bacterial strains will also be involved.

5.2 *Serratia* biofilm formation on titanium substrates

The results in Chapter 4 are discussed in this section to investigate the biofilm development on solid titanium substrates and on a porous titanium mesh.

5.2.1 *Serratia* biofilm formation on titanium discs

Serratia biofilm formation was observed on six different titanium surfaces in order to understand the influence of substrate surface treatments on biofilm development. Previous studies usually focused on the early stages of biofilm development [20-25], and the morphology of the biofilm on titanium with different topographies is often overlooked. In this work, biofilm was allowed to grow for 7 days, and its formation was compared on titanium discs with different surface treatments, some of which were model dental implant surfaces.

Biofilm formation on any substrate involves 5 stages (§ 1.5.4): 1. initial bacterial attachment; 2. the production of extracellular polymer matrix (EPM) and thus firmer adhesion; 3. early biofilm development by bacterial colonial growth; 4. the formation of a mature biofilm architecture; 5. bacterial detachment. During this process, not only the initial bacterial attachment is important, but also the production of EPM, which is an important component of a biofilm as it provides a matrix which contributes to the biofilm structure [26]. With its help, firmer attachment can be achieved [27]. Substrate surface properties may affect the biofilm development by influencing the initial bacterial attachment and the spread of the EPM layers, and subsequent biofilm growth.

Due to the limitation of equipment, protein assay was used to evaluate the amount of bacteria in the biofilm. However, this method may not give an accurate result because there were still attached bacteria on the substrate after the specimen had been ultrasonicated in Triton X-100 solution. Judging by the SEM images, the number of bacteria on Ti1 (Figure 4. 5), Ti2 (Figure 4. 6) and Ti4 (Figure 4. 8) should be higher than that on Ti3 (Figure 4. 7), Ti5 (Figure 4. 9) and Ti6 (Figure 4. 10), due to the existence of large bacterial clumps on the former group. This is consistent with the protein assay (Figure 4. 4). In the SEM images, there appeared to be more bacteria on Ti6 (Figure 4. 10) than on Ti3 (Figure 4. 7) and Ti5 (Figure 4. 9), whereas the protein assay (Figure 4. 4) showed the opposite. It is possible that due to the micro-roughness on Ti6 (Figure 4. 1k & i), the biofilm was not removed as effectively as on the comparatively smoother Ti3 (Figure 4. 1e & f), and thus showed lower protein content during bacterial protein assay. The adhering strength of the attached biofilm will thus worth further analysis. However, SEM observation has its drawbacks as well, since only limited sites of interest can be observed. Thus, more accurate techniques will be used in the future work. If the protein assay results are reliable, the following discussions can be made.

5.2.1.1 The influence of substrate surface wettability

A weak positive effect of the substrate hydrophobicity on biofilm growth was observed, consistent with previous findings [28, 29]. The protein assay suggested that there were more bacteria on the hydrophilic Ti1, Ti2 (WCA<90º) and Ti3 (WCA~90º) than on the hydrophobic Ti5 and Ti6 (WCA>90º) (Figure 4. 2 and Figure 4. 4), with the biofilm on Ti4 appearing to be an exception: it is hydrophobic but a significant layer of biofilm has formed on its surface. EPM is highly hydrated, with 98% water and the rest polysaccharides, proteins and nucleic acids [26]. Undoubtedly, it binds much more easily to hydrophilic surfaces and is less capable of spreading on hydrophobic ones. Thus, it is possible that the spread of the bacteria/EPM matrix is easier and faster on hydrophilic substrates (Ti1, Ti2 and Ti 3) than on hydrophobic Ti5 and Ti6, which means they reach Stage 3 earlier, bacterial colonial growth, where most of the proliferation or adhesion happens within the bacterial colony but away from the substrate. After that, only bacteria-bacteria interactions are involved. Thus, the amount of bacteria on Ti1, Ti2 and Ti3 exceeds that on Ti5 and Ti6, possibly due to their abilities to allow EPM to spread over the surface in spite of their low Ra values.

5.2.1.2 The influence of substrate surface roughness

Surface roughness is generally considered as an important factor in bacterial adhesion and thus may be equally significant in biofilm growth. It is closely related to peri-implantitis, which is a chronic bacterial infection with the loss of supporting bone in the tissues surrounding the implant [30]. It is known that rougher surfaces promote initial bacterial attachment [10, 31] and are found to have a profound effect on plaque biofilm formation [23]. During a long-term follow-up study to compare the failure patterns of the Interpore IMZ implants and the Strauman ITI implants, Esposito *et al.* (1997) found that the rougher IMZ

implants showed a higher prevalence of late failures due to peri-implantitis [32]. In this study, however, surface roughness did not appear to have a major influence on biofilm formation. The number of bacteria on each surface (according to the protein assay, Figure 4. 4) seemed to be independent of the substrate roughness as indicated by Ra value (Figure 4. 3). The highest number of bacteria appeared on Ti2, the mirror polished titanium with the lowest Ra value of 0.04±0.01 μm. Ti6 is rougher than all the substrates except Ti4, yet appeared to have the fewest bacteria.

The better bacterial adhesion on rough surfaces is usually explained by more available bonding sites, as well as a sheltering effect. On a flat surface, the bacteria are bonded to the surface through reactions between proteins and the surface, as illustrated in Figure 5. 1a. On a rough substrate, this bonding can be strengthened further by more available bonding sites as well as by a potential physical anchorage of cell appendages such as fimbriae in the case of *Serratia* onto the protrusions on the surface (Figure 5. 1b). This may lead to a faster and more secure adhesion and contribute to a better bacterial adhesion to rough substrates. The sheltering effect can protect the attached bacteria against shear forces from medium flow, as seen in Figure 5. 2.

.

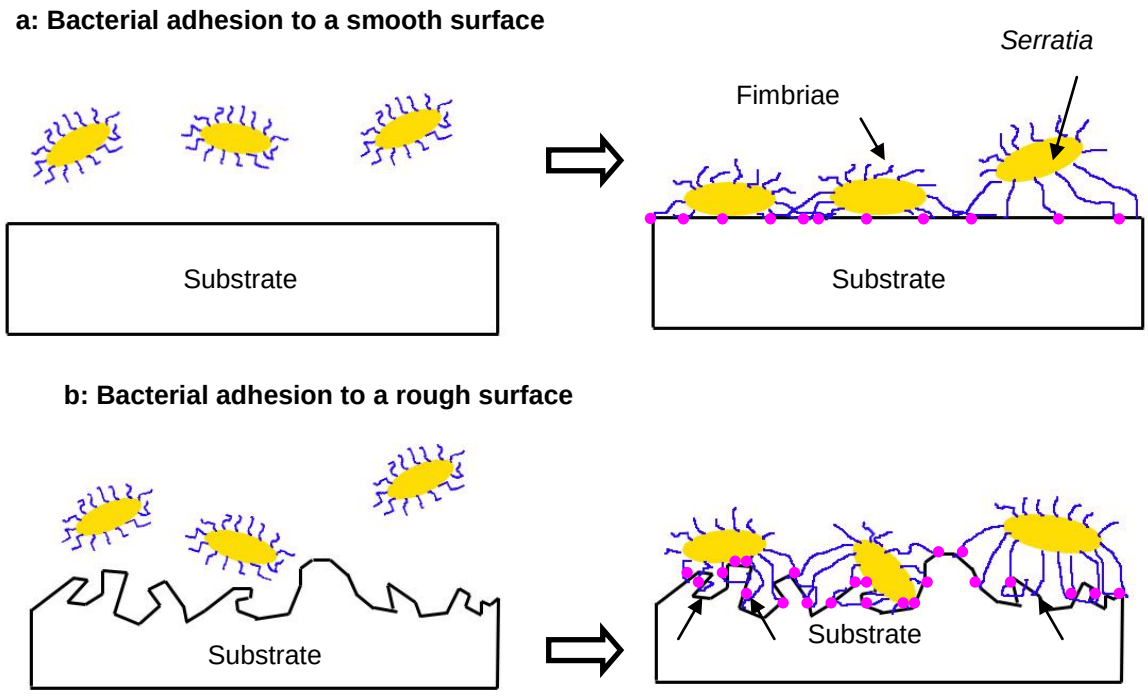

Figure 5. 1 Bacterial adhesion to a smooth/rough surface

a: Bacterial adhesion to a smooth surface where fimbriae have nothing to hang onto. The magenta spots at the interface suggest the possible bonding sites.

b: Bacterial adhesion to a rough surface where fimbriae are anchored by the surface extrusions. The magenta spots at the interface suggest possible bonding sites and arrows point to where the fimbriae are physically anchored by the surface protrusions.

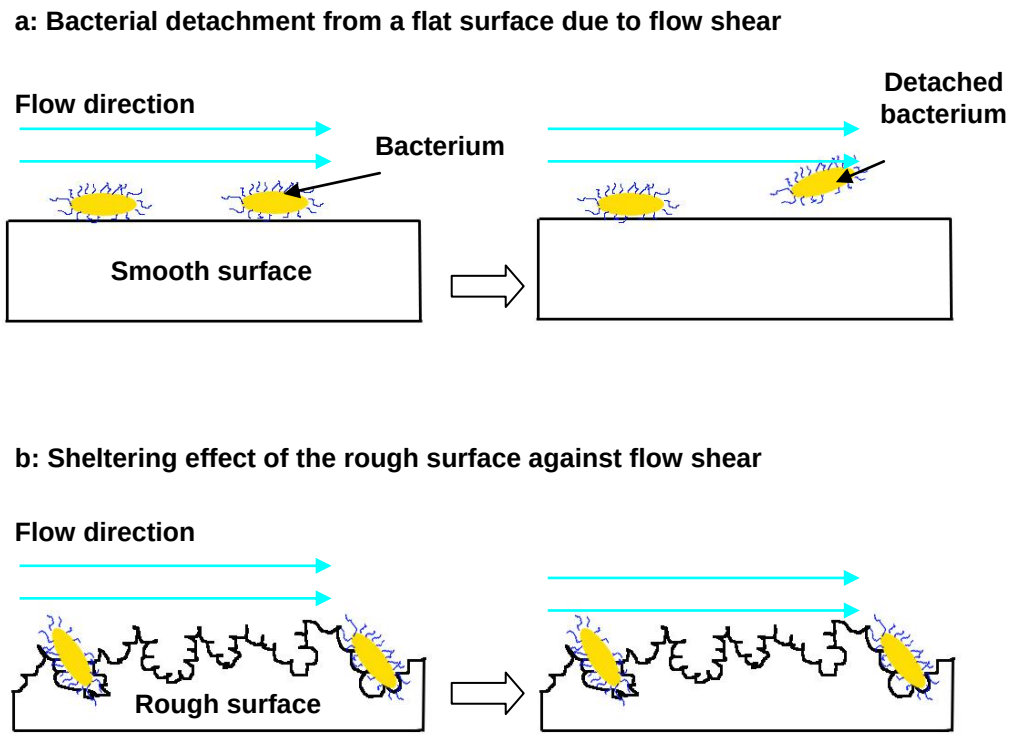

Figure 5. 2 A diagram showing the sheltering effect of a rough substrate to protect bacteria against flow shear

a: Bacterial attachment to a smooth surface: bacterial detachment due to flow shear

b: Bacterial attachment to a rough surface: the rough surface protects bacteria against the flow shear

It is possible that bacteria are more sensitive to surface roughness in the early biofilm development when they still have direct contact with the substrate surface (Figure 5. 3a). As soon as the colonies spread to cover the entire surface, or rather, the EPM forms a matrix to mask the substrate, the surface roughness will be obscured by these organic structures. In consequence, it is this organic matrix rather than the titanium surface that acts as the direct reaction layer with the newly attaching planktonic bacteria adding to the biofilm structure (Figure 5. 3b). Hence, after this complete coverage of the substrate, the substrate can only

influence the bacteria indirectly via the morphology of the already formed matrix (Figure 5. 3c), if the effect of substrate chemical composition is not taken into consideration.

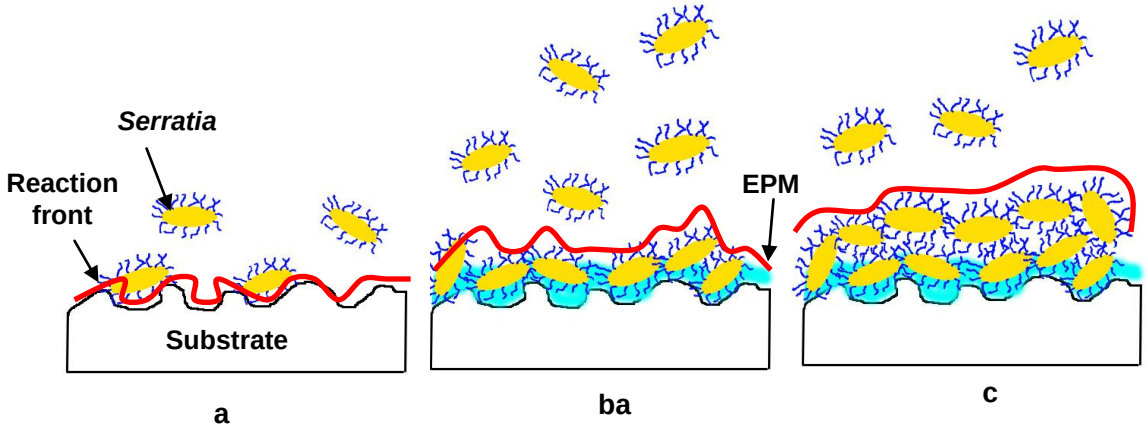

Figure 5. 3 Schematic drawing of the change of reaction front during biofilm formation

a: The initial bacteria adhesion, when the reaction front is at the bacteria-metal interface (the red line).

b: The complete coverage of the substrate by bacteria and EPM (the light blue part), when the reaction front changes to the bacteria/EPM matrix-newly attended bacteria interface. The topography of the substrate is thus obscured.

c: Further colonial growth through bacterial proliferation or addition of newly attached bacteria.

It is possible that for Ti1, Ti2, Ti3, Ti5 and Ti6, with Ra values much lower than that of Ti4 (Figure4. 3), the topographies of the EPM matrix are more or less the same after complete covering of the metal surface. However, the substrate topography of Ti4 may not be entirely masked even after complete coverage by the EPM matrix, due to the outstanding Ti granules which are approximately 40 μm in diameter (Figure 4. 1g). These granules are possibly features favouring biofilm development due to the sheltering effect, as bacterial colonies are

frequently found to extend from these granules to the underlying surface (Figure 4. 8). Thus, although it is hydrophobic, the amount of bacteria on it is the second highest of the six, comparable to Ti2.

5.2.1.3 The influence of substrate surface chemistry

The addition of planktonic bacteria is not the only route to biofilm growth. The proliferation of the adherent cells also contributes to this process. Here, the substrate surface chemistry will be very important as it may promote or inhibit the bacterial growth and thus the development of a biofilm is either enhanced or inhibited. A surprisingly high number of bacteria appear on the mirror polished Ti2 surface regardless of its smoothness. The reason that it outperforms even Ti1 and Ti3, which are both hydrophilic and much rougher, is possibly the Al released from the embedded Al_2O_3 particles in the last two. Al may be a potential bacterial growth inhibitor, as demonstrated in § 5.1.2. Although its influence on biofilm growth is yet unknown, Prado da Silva *et al.* (2003) reported that it took a longer time for human osteoblast-like cells to proliferate and reach confluence on an alumina grit blasted titanium surface regardless of its high surface roughness [33].The cell number on Ti1 is higher than that on Ti3, which could be a joint effect of both hydrophobicity and Al ion release, which is faster on Ti3 due to its higher surface area. The Al ion release from alumina grit blasted Ti 64 was found to be seven times higher than for the polished surfaces, which is attributed to the embedded particles and the greater surface area available for metal ion release [34]. However, it was also observed that bacteria attached equally well on the embedded Al_2O_3 and the titanium substrates on Ti3 (Figure 4. 7c). Therefore a more systematic study will be necessary to further investigate the role of Al, for example, to compare the biofilm development on Al_2O_3 grit blasted surfaces with that on surfaces with similar roughness but without Al.

5.2.1.4 The influence of substrate surface topography

Biofilm morphology was observed after fixation and dehydration of the specimen which may cause artefacts such as shrinkage and deformation of the biofilm during the process [35]. Nevertheless, they were found to differ considerably from substrate to substrate. Typical mature biofilm structures like 'stacks' were only observed on Ti1 (Figure 4. 5) and Ti2 (Figure 4. 6). However, these colonies are not the same: the colonies on Ti2 are flattened and composed of highly oriented bacteria, but on Ti1 they are much more outstanding and the bacteria are more randomly arranged.

Bacterial 'bridges' were seen on Ti4 to extend from the protruding granules to the substrate (Figure 4. 8). They are composed of highly oriented bacterial bundles, as may be seen in Figure 4. 8a & b. This 'hanging bridge-formation' is commonly observed in this work but never been reported elsewhere. It is of great interest, as it demonstrates the ability of *Serratia* to link together far separated features - from titanium granules to the substrate in this case (40 µm) and to cross between different titanium wires more than 100 µm apart (§ 4.2.2).

To date, the morphology of biofilm on titanium with different surface treatments has been rarely studied. Thus, it is still not clear what the exact role the substrate topography is on biofilm structure. In this study, it was observed that biofilms with comparable numbers of bacteria, for example, on Ti2 and Ti4, Ti5 and Ti6, showed entirely different morphologies (Figures 4. 6, 4. 8, 4. 9 and 4. 10). This study is the first to offer evidence that the substrate micro-topography may help to shape biofilm. Further studies with more complex biofilms are necessary.

The apparently low number of bacteria on Ti6 after a period of 7 days in the fermenter is of great interest. It is generally believed that the adhesion of either bacteria or cells is initiated by

protein absorption onto the substrate. Substrates with higher wettability are thus considered to be more suitable supports for cell growth [36]. It has been demonstrated that the Dentsply Friadent Plus surface (Ti6 in this work) changed from extremely hydrophobic to hydrophilic after a second contact with water during a dynamic water contact angle measurement, which was attributed to the presence of overhangs and hierarchical levels of micro-porosity and air-entrapment [37]. Similar phenomena were also observed during the WCA measurement in this work (data not shown). Sammons *et al.* (2005) found that osteoblast cells spread more rapidly on the Plus surface (Ti6 in this study) when compared to a plasma sprayed surface (Ti4), a grit blasted surface (Ti3) and an acid etched surface (Ti5) [36]. However, unlike mammalian cells, a inferior biofilm growth was observed on the Plus surface in this work. If the protein assay is reliable, these observations suggest that this kind of surface feature may promote mammalian cell adhesion whist inhibit biofilm formation, which can be clinically advantageous and merits further investigation. Similar observations have been reported by Puckett *et al.* (2008 & 2010) who observed that an electron beam evaporated titanium with a nano-rough surface favoured osteoblast inhabitation [38] but inhibited the adhesion of both *Staphylococcus* and *Pseudomonas* strains [39]. However not all nano-scale features have similar effects, as titanium with nano-tubular and nano-textured features can promote osteoblast adhesion as well as bacterial attachment [39].

5.2.2 *Serratia* biofilm formation on porous titanium web

To study the bacterial distribution within a 3D porous matrix is important, not only in terms of bacterial-induced infections, but also for applications such as bacterial biomineralisation and microbial fuel cells [40] and waste water treatment [41-43] where porous scaffolds are used as carriers for biofilm development.

After 5 days, bacteria were found to grow throughout the entire structure of the titanium web (in a continuous culture with fresh media flowing through). Although most of the colonies are found coating the titanium fibres, as seen in Figure 4. 12a, they are also able to form 'bridges' between different wires (Figure 4. 12e). Given the probable shrinkage of the biofilm during fixation and dehydration, it is very likely that even those colonies clinging to the titanium fibres, when still hydrated, actually are extended within the structure to form secondary structural scaffolds, rather than depending on any single titanium wires, as observed in the dehydrated condition (see Figure 5. 4). These bridges are very important as they will act as secondary pathways for HA formation independent of the titanium wires inside the structure, as will be returned to in Chapter 8. In summary, the results in this part of the work confirm the possibility of using porous titanium webs as a bacterial growth scaffold.

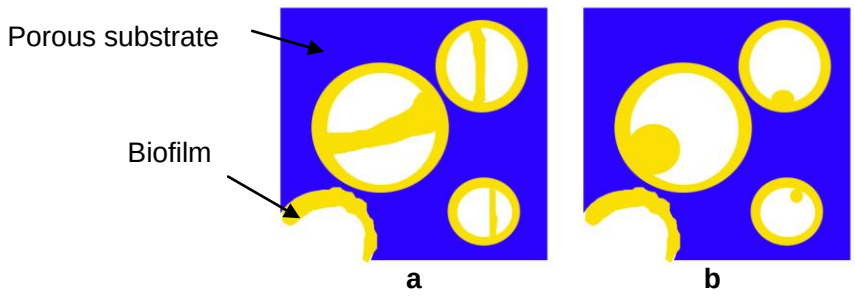

Figure 5. 4 Bacterial colony shrinkage due to fixation and dehydration

a: Hydrated condition: bacterial colonies form bridges across the pores.

b: Dehydrated condition: bacterial colonies shrink and cling on to the substrate.

The biofilm formation on a porous substrate is illustrated in Figure 5. 5. When a porous scaffold is exposed to a bacterial culture, at the beginning the entire structure has equal access to both bacteria and nutrient/air supply (Figure 5. 5b). At this stage, the chance of bacterial

adhesion and proliferation is more or less the same throughout the structure, regardless of location. However, further growth can significantly reduce the pore size of the scaffold and thus the permeability of the medium is restrained [44]. As a result, the bacterial growth at the periphery of the structure, where the medium is fresh and the air access good, may be much faster than that deep inside. Thus, the biofilm formation is started by bacterial colonisation at these preferred locations (Figure 5. 5c). Further colonial growth narrows the pores of the structure and in turn restricts the 'pathways' for the transportation of oxygen and nutrients, resulting in a medium/oxygen - deficient zone inside (Figure 5. 5d), which makes the biofilm growth in this zone even more difficult due to a lack of nutrients. In fact, biofilm growth on any porous substrate is nutrient supply-controlled. For example, bacterial proliferation throughout any 3D structure can be difficult in a soaking method if the solution is kept still [46]. Bacterial growth is likely to be limited to just a few layers in depth, otherwise as it is inhibited by the impeded access to nutrients from the external medium [45, 46]. In this study, although it is not clear whether bacteria preferentially colonise at the periphery of the porous matrix (due to the deformation of the biofilm during fixation and dehydration), bacteria are observed to be shorter and the biofilm thinner inside the porous scaffold (Figure 4. 13), suggesting that even in continuous culture with fresh medium flowing through, the situation as illustrated in Figure 5. 5 may still occur.

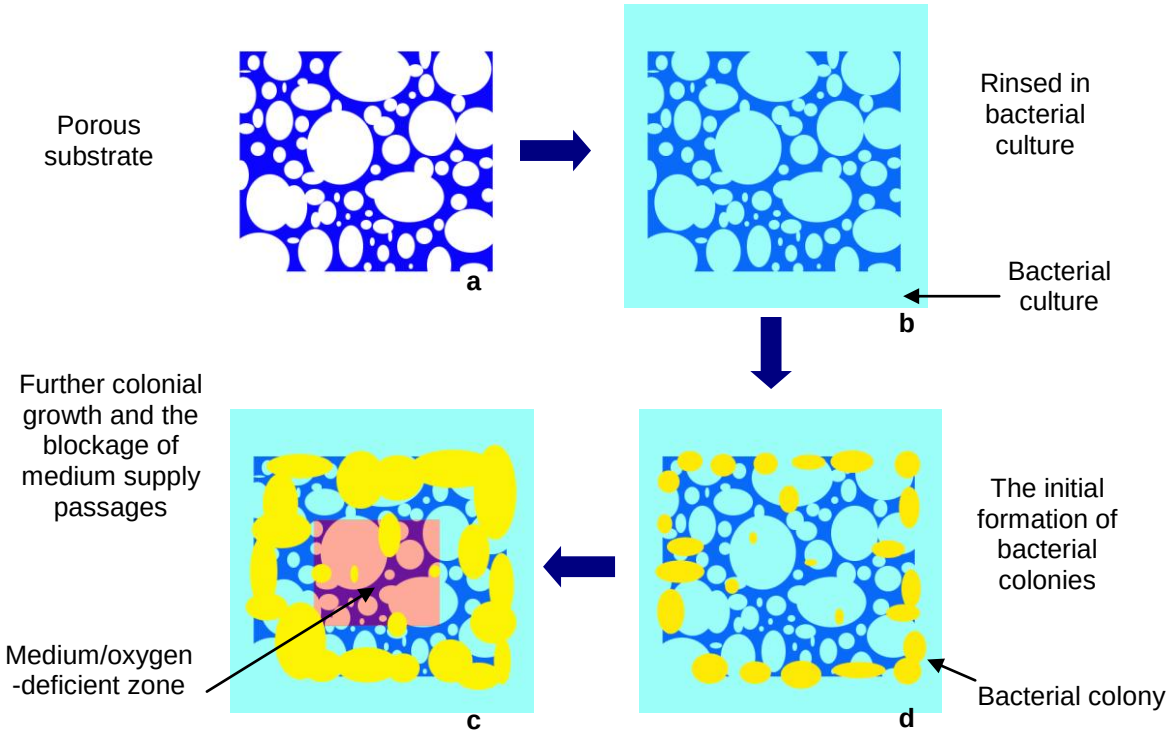

Figure 5. 5 Biofilm formation on a porous scaffold

a: A porous scaffold.

b: The scaffold is exposed to a bacterial culture.

c: Bacterial preferential colonisation at the periphery of the substrate.

d: Further growth of bacterial colonies and the blockage of medium supply passages, resulting in a medium/oxygen-deficient zone in the middle where biofilm growth is largely restrained.

Common techniques to analyse the structure of a biofilm usually include confocal microscopy [47, 48], scanning electron microscopy and florescence microscopy [45, 46]. The observation of bacteria in this work was by SEM, which, although it cannot distinguish the cell activity, has the advantages of permitting more precise observation of the bacterial geometries, locations, and their relations to the substrate. In this work, as judged by SEM, the biofilm is thicker and the bacterial cells are longer at the periphery of the Ti web, but thinner and shorter inside. The bacterial distribution was characterised further using Micro X-Ray CT. However,

due to the resolution limitation, only large clumps (>~50 μm) can be observed. The small colonies and the biofilm wrapping each titanium wire are undetectable. Thus, in terms of resolution, Micro X-Ray CT was not adequate to analyse bacterial distribution in this porous substrate. Nevertheless, it did confirm that bacterial colonies were present throughout the structure, which was surprising as they were hypothesised (from SEM) to concentrate at the periphery, presumably in areas where oxygen and nutrients were not limited.

References

1. Yuehuei HA, Richard JF. Concise review of mechanisms of bacterial adhesion to biomaterial surfaces. Journal of Biomedical Materials Research 1998;43(3):338-348.
2. Walsh D, Pope D, Danford M, Huff T. The effect of microstructure on microbiologically influence corrosion. Journal of the Minerals, Metals and Materials 1993;45(9):22-30.
3. Sreekumari K, Nandakumar K, Kikuchi Y. Bacterial attachment to stainless steel welds: significance of substratum microstructure. Biofouling 2001;17(4):303-316.
4. Sreekumari K, Takao K, Ujiro T, Kikuchi Y. High nitrogen stainless steel as a preferred substratum for bacteria and other microfouling organisms ISIJ International 2004;44(5):858-864.
5. Truong VK, Lapovok R, Estrin YS, Rundell S, Wang JY, Fluke CJ, Crawford RJ, Ivanova EP. The influence of nano-scale surface roughness on bacterial adhesion to ultrafine-grained titanium. Biomaterials 2009;31(13):3674-3683.
6. Faghihi S, Azari F, Li H, Bateni MR, Szpunar JA, Vali H, Tabrizian M. The significance of crystallographic texture of titanium alloy substrates on pre-osteoblast responses. Biomaterials 2006;27(19):3532-3539.
7. Gabriel BL, Gold J, Gristina AG, Kasemo B, Lausmaa J, Harrer C, Myrvik QN. Site-specific adhesion of *Staphylococcus epidermidis* (RP12) in Ti-Al-V metal systems. Biomaterials 1994;15(8):628-634.
8. Savage DC, Fletcher M. Bacterial adhesion. New York: Plenum Press, 1985.
9. Costerton JW, Ingram JM, Cheng KJ. Structure and function of the cell envelope of gram-negative bacteria. Microbiology and Molecular Biology Reviews 1974;38(1):87-110.
10. Katsikogianni M, Missirlis YF. Concise review of mechanisms of bacterial adhesion to biomaterials and of techniques used in estimating bacterial-material interactions. European Cells and Materials 2004;8:37-57.
11. Sarr MI, Moreno DA, Ranninger C, King E, Ruiz J. Influence of gas nitriding of Ti6Al4V alloy at high temperature on the adhesion of *Staphylococcus aureus*. Surface and Coatings Technology 2006;201(6):2807-2812.
12. Illmer P, Schinner F. Influence of aluminum on motility and swarming of *Pseudomonas* sp. and *Arthrobacter* sp. FEMS Microbiology Letters 1997;155(1):121-124.
13. Corain B, Nicolini M, Zatta P. Aspects of the bioinorganic chemistry of aluminium(III) relevant to the metal toxicity. Coordination Chemistry Reviews 1992;112:33-45.
14. Diercks M, Sand W, Bock E. Microbial corrosion of concrete. Cellular and Molecular Life Sciences 1991;47(6):514-516.
15. Otero E, Bastidas JM, Lopez V. Analysis of a premature failure of welded AISI 316L stainless steel pipes originated by Microbial induced corrosion. Materials and Corrosion 1997;48(7):447-454.
16. Bremer PJ, Geesey GG. Laboratory-based model of microbiologically induced corrosion of copper. Applied Environmental Microbiology 1991 July 1, 1991;57(7):1956-1962.
17. Geesey GG, Gillis RJ, Avci R, Daly D, Hamilton M, Shope P, Harkin G. The influence of surface features on bacterial colonization and subsequent substratum chemical changes of 316L stainless steel. Corrosion Science 1996;38(1):73-95.
18. Videla HA, Characklis WG. Biofouling and microbially influenced corrosion. International Biodeterioration & Biodegradation 1992;29(3-4):195-212.
19. Beech IB, Sunner J. Biocorrosion: towards understanding interactions between biofilms and metals. Current

Opinion in Biotechnology 2004;15(3):181-186.
20. Tsang C, Ng H, McMillan A. Antifungal susceptibility of *Candida albicans* biofilms on titanium discs with different surface roughness. Clinical Oral Investigations 2007;11(4):361-368.
21. Chin MYH, Sandham A, de Vries J, van der Mei HC, Busscher HJ. Biofilm formation on surface characterized micro-implants for skeletal anchorage in orthodontics. Biomaterials 2007;28(11):2032-2040.
22. Schwarz F, Sculean A, Wieland M, Horn N, Nuesry E, Bube C, Becker J. Effects of hydrophilicity and microtopography of titanium implant surfaces on initial supragingival plaque biofilm formation. A pilot study. Oral and Maxillofacial Surgery 2007;11(6):333-338.
23. Teughels W, Assche NV, Sliepen I, Quirynen M. Effect of material characteristics and/or surface topography on biofilm development. Clinical Oral Implants Research 2006;17(S2):68-81.
24. Carlen A, Nikdel K, Wennerberg A, Holmberg K, Olsson J. Surface characteristics and in vitro biofilm formation on glass ionomer and composite resin. Biomaterials 2001;22(5):481-487.
25. Morgan TD, Wilson M. The effects of surface roughness and type of denture acrylic on biofilm formation by *Streptococcus oralis* in a constant depth film fermentor. Journal of Applied Microbiology 2001;91(1):47-53.
26. Donlan RM. Biofilm formation: a clinically relevant microbiological process. Clinical Infectious Diseases 2001;33(8):1387-1392.
27. Stoodley P, Sauer K, Davies DG, Costerton JW. Biofilms as complex differentiated communities. Annual Review of Microbiology 2002;56(1):187-209.
28. Quirynen M, Marechal M, Busscher HJ, Weerkamp AH, Arends J, Darius PL, van Steenberghe D. The influence of surface free-energy on planimetric plaque growth in man. Journal of Dental Research 1989 May 1, 1989;68(5):796-799.
29. Everaert E, Mahieu H, Chung R, Verkerke G, van der Mei H, Busscher H. A new method for *in vivo* evaluation of biofilms on surface-modified silicone rubber voice prostheses. European Archives of Oto-Rhino-Laryngology 1997;254(6):261-263.
30. Klinge B, Hultin M, Berglundh T. Peri-implantitis. Dental Clinics of North America 2005;49(3):661-676.
31. Bollenl CML, Lambrechts P, Quirynen M. Comparison of surface roughness of oral hard materials to the threshold surface roughness for bacterial plaque retention: A review of the literature. Dental Materials 1997;13(4):258-269.
32. Esposito M, Hirsch JM, Lekholm U, Thomsen P. Failure patterns of four osseointegrated oral implant systems. Journal of Materials Science: Materials in Medicine 1997;8(12):843-847.
33. Prado da Silva MH, Soares GDA, Elias CN, Best SM, Gibson IR, DiSilvio L, Dalby MJ. In vitro cellular response to titanium electrochemically coated with hydroxyapatite compared to titanium with three different levels of surface roughness. Journal of Materials Science: Materials in Medicine 2003;14(6):511-519.
34. Browne M, Gregson PJ. Effect of mechanical surface pretreatment on metal ion release. Biomaterials 2000;21(4):385-392.
35. Chang HT, Rittmann BE. Biofilm loss during sample preparation for scanning electron microscopy. Water Research 1986;20(11):1451-1456.
36. Sammons R, Lumbikanonda L, Gross M, Cantzler P. Comparison of osteoblast spreading on microstructured dental implant surfaces and cell behaviour in an explant model of osseointegration: a scanning electron microscopic study. Clinical Oral Implants Research 2005;16(6):657-666.
37. Rupp F, Scheideler L, Rehbein D, Axmann D, Geis-Gerstorfer J. Roughness induced dynamic changes of wettability of acid etched titanium implant modifications. Biomaterials 2004;25(7-8):1429-1438.
38. Puckett S, Pareta R, Webster TJ. Nanorough micro patterned titanium for directing osteoblast morphology and adhesion. International Journal of Nanomedicine 2008;3(2):229-241.
39. Puckett SD, Taylor E, Raimondo T, Webster TJ. The relationship between the nanostructure of titanium surfaces and bacterial attachment. Biomaterials 2010;31(4):706-713.
40. Rabaey K, Verstraete W. Microbial fuel cells: novel biotechnology for energy generation. Trends in Biotechnology 2005;23(6):291-298.
41. Yong P, Macaskie LE, Sammons RL, Marquis PM. Synthesis of nanophase hydroxyapatite by a *Serratia* sp. from waste-water containing inorganic phosphate. Biotechnology Letters 2004;26(22):1723-1730.
42. Macaskie LE, Bonthrone KM, Yong P, Goddard DT. Enzymically mediated bioprecipitation of uranium by a *Citrobacter* sp.: a concerted role for exocellular lipopolysaccharide and associated phosphatase in biomineral formation. Microbiology 2000;146(8):1855-1867.
43. Paterson-Beedle M, Macaskie LE, Lee CH, Hriljac JA, Jee KY, Kim WH. Utilisation of a hydrogen uranyl phosphate-based ion exchanger supported on a biofilm for the removal of cobalt, strontium and caesium from aqueous solutions. Hydrometallurgy 2006;83(1-4):141-145.
44. Shafahi M, Vafai K. Biofilm affected characteristics of porous structures. International Journal of Heat and Mass Transfer 2009;52(3-4):574-581.

45. Gutierrez MC, Carcia-Carvajal ZY, Hortiguela MJ, Yuste L, Rojo F, Ferrer ML, Monte Fd. Biocompatible MWCNT scaffolds for immobilization and proliferation of *E. coli*. Journal of Materials Chemistry 2007;7(29):2992-2995.
46. Akay G, Erhan E, Keskinler B. Bioprocess intensification in flow-through monolithic microbioreactors with immobilized bacteria. Biotechnology and Bioengineering 2005;90(2):180-190.
47. Dongari-Bagtzoglou A, Kashleva H, Dwivedi P, Diaz P, Vasilakos J. Characterization of mucosal *Candida albicans* biofilms. PLoS One 2009;4(11):7967-7976.
48. Bol M, Mohle RB, Haesner M, Neu TR, Horn H, Krull R. 3D finite element model of biofilm detachment using real biofilm structures from CLSM data. Biotechnology and Bioengineering 2009;103(1):177-186.

Chapter 6 Biomineralisation of HA on titanium discs

Serratia biomineralisation of hydroxyapatite was utilised by Thackray *et al*. (2005) as a potential process to fabricate bone graft substitute material [1], and the products were characterised by Sammons *et al*. in 2007 to be HA [2]. In this study, this method was explored further for its potential to produce HA coated titanium substrates for medical applications. Independent biomineralisation was repeated 5 times, with 10 samples loaded in the bioreactor in each experiment. The samples were taken from the bioreactor randomly for examination. The representative data were shown in this Chapter.

6.1 Al_2O_3 grit blasted pure titanium as substrate

Al_2O_3 grit blasted pure titanium discs were used as substrates to support HA coatings for the following reasons. First of all, Al_2O_3 grit blasting is a well developed technique for roughening surfaces which is widely used on clinical devices such as titanium dental implants and hip replacements, to increase the surface area and improve bone interlocking. Secondly, according to the previous study described in Chapter 4, the biofilm structure on this kind of specimen consists of a thin bacterial layer (one cell thick) superimposed on which were bacterial stacks of several layers of bacteria, producing a porous structure. This kind of architecture is of great interest because if it could be maintained following mineralisation and subsequent sintering it would provide a porous coating and thus a high surface area for cell and bone attachment to an implant. During the following biomineralisation stage, the *Serratia* biofilm acts as the template for the crystal coating. In other words, the shape of the crystal coating may follow that of the biofilm and determines the final morphology.

As illustrated in Chapter 4, Al_2O_3 grit blasting results in a roughened surface with alumina particles embedded in the surface, as shown in Figure 6. 1a & b. Although an undesirable

consequence of grit-blasting, such embedded particles are commonly seen on implant surfaces. A cross section study provides further confirmation (Figure 6. 1c). It was also found that the substrate microstructure was modified. Three different regions were observed: a heavily deformed surface layer consisting of nano-crystalline grains (less than 1 μm thick, 3 in Figure 6. 1e), lying underneath which was a second layer around 5 μm thick deformed mainly by twinning (4 in Figure 6. 1e) beneath which was the non-deformed substrate (2 in Figure 6. 1d).

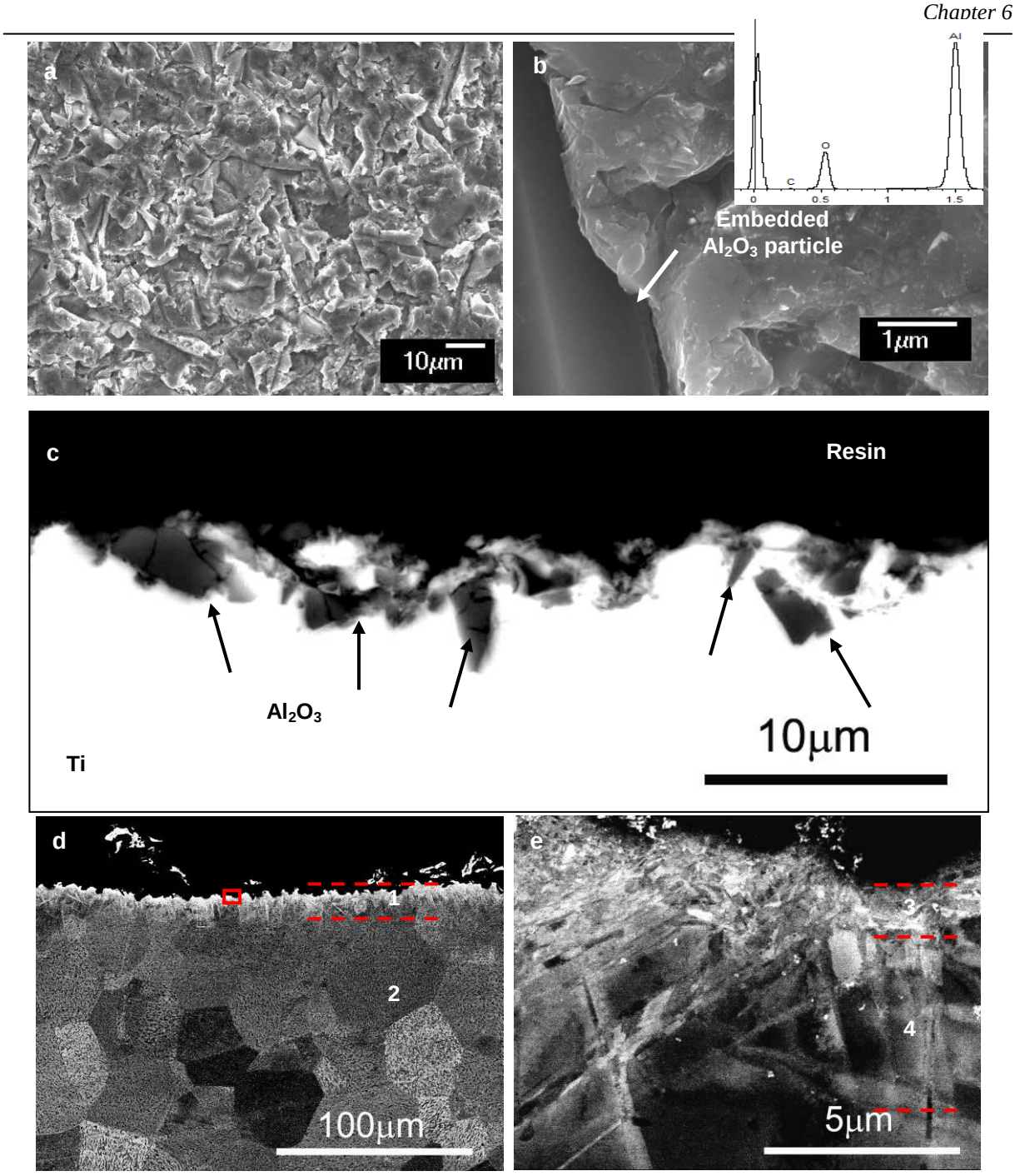

Figure 6. 1 The influence of Al_2O_3 grit blasting on the morphology and microstructure of a titanium substrate

a: A roughened surface (SE imaging).

b: (a) at higher magnification showing the embedded Al_2O_3 particle (SE imaging).The inset EDX spectrum confirmed the particles are alumina.

c: BSE imaging of the cross section showing the embedded Al_2O_3 particles (arrows).

d: Substrate microstructure change due to grit blasting (BSE imaging). Note the severely deformed layer on the sample surface. 1: deformed layer; 2: unaffected titanium substrate.

e: Microstructure of the deformed layer at higher magnification (the square site in (d), BSE imaging), composed of a nano-crystalline surface (3) and a twinned zone (4).

The Ti discs then were incubated in the fermenter where *Serratia* biofilm formed on the surface (see § 2.2.2), and subsequently biomineralisation for 10 days where a thick crystal coating was produced to cover the entire sample (see § 2.3.2). The crystal-coated Ti discs were dried at 60 ^{o}C for 24 hours before they were characterised by XRD, SEM and TEM.

6.2 XRD analysis of the crystal coating

XRD analysis was carried out on the coating crystals. The XRD pattern of the biomineralised crystals (nascent crystals) is compared with that of a commercial available CAPTAL HA in Figure 6. 2. Peaks matching (0002), $(21\bar{3}1)$, $(21\bar{3}3)$ and (0004) of HA can be found in the pattern of the nascent crystals, and the overall distribution of this pattern is similar to that of CAPTAL HA, suggesting that the crystals may be a precursor form of HA. The broad peaks of the nascent crystals suggest nano-scale crystals.

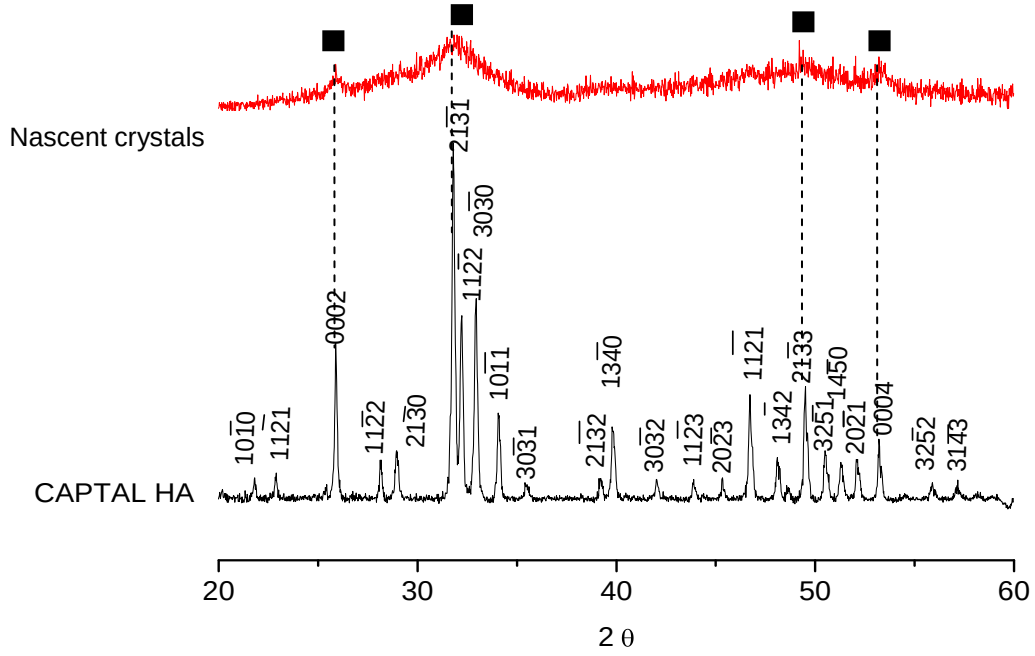

Figure 6. 2 XRD pattern of the crystals in comparison with that of CAPTAL HA

▌ marks where the peak matches HA standard (PDF reference code: 00-024-0033).

6.3 An SEM analysis of the coating

6.3.1 Coating morphology

The biomineralised coating was porous, consisting of large crystal lumps superimposed on a comparatively even crystal matrix, as can be seen in Figure 6. 3a. The plan views show that both the clumps (Figure 6. 3b) and the matrix (Figure 6. 3c) consist of crystal spheres which are usually several micrometres in size. Cracks are found throughout the coating, as seen in Figure 6. 3c. The coating can be easily scratched or squashed.

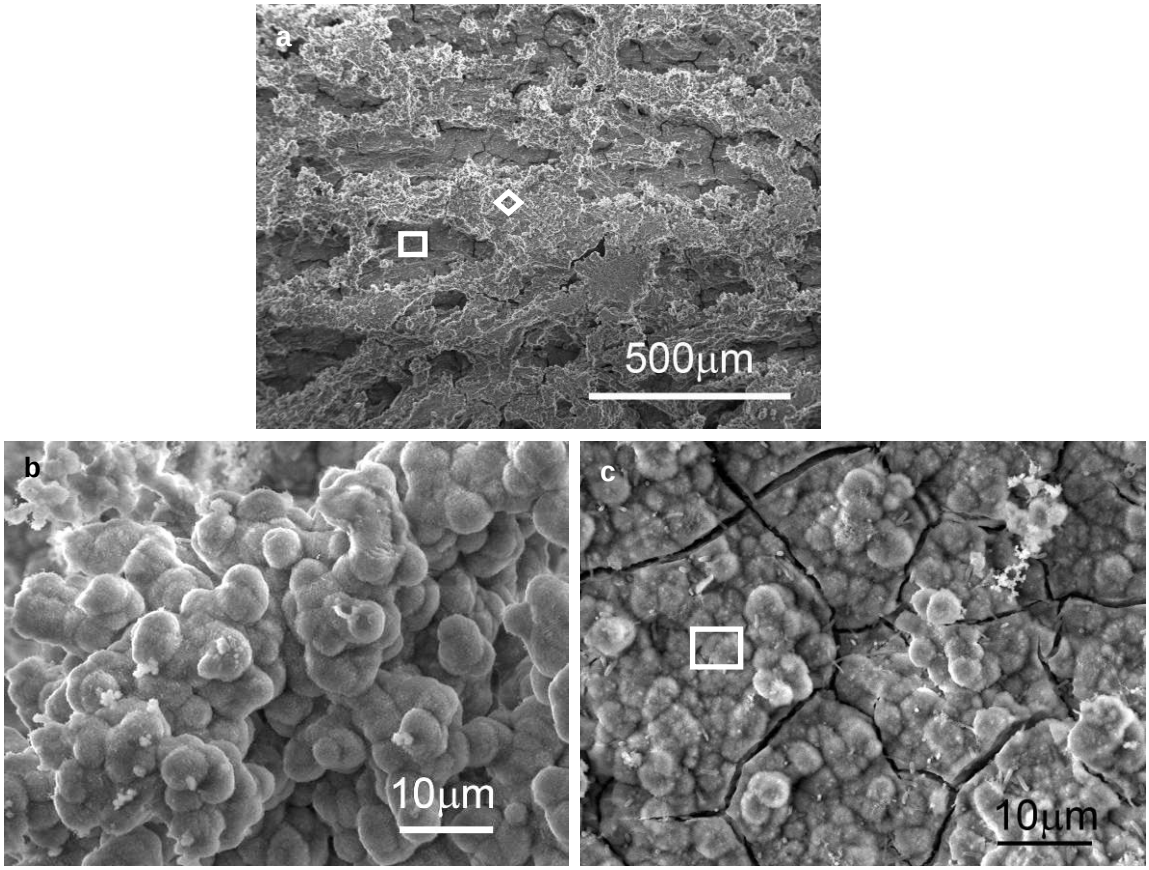

Figure 6. 3 The structure of the crystal coating formed on titanium (SE imaging)

a: Plan view: crystal clumps (diamond) and crystal matrix (square) structure.

b: The morphology of the crystal clumps, ◊ site in (a).

c: The morphology of the crystal matrix, □ site in (a).

Figure 6. 4a is a cross section through the crystal coated titanium (see Figure 2. 9d), demonstrating the porous coating observed in Figure 6. 3a. While the crystal matrix is flat and thin and around 10 μm deep, the clumps can be as thick as 100 μm. The coating is porous within both the clumps and the matrix, as confirmed in Figure 6. 4b. No significant difference can be observed between crystals adjacent to the titanium substrate (single arrowed site) and those on the coating surface (double-arrowed site) (Figure 6. 4b). A detailed analysis of the cross section shows that the coating consists of small (0.5 to 1 μm) spheres (black arrows in

Figure 6. 4c), occasionally covered by shells (red arrows in Figure 6. 4c & Figure 6. 4d). The clusters are generally smaller than those observed in the plan view, indicating that those observed in Figure 6. 3 are possibly the crystal shells.

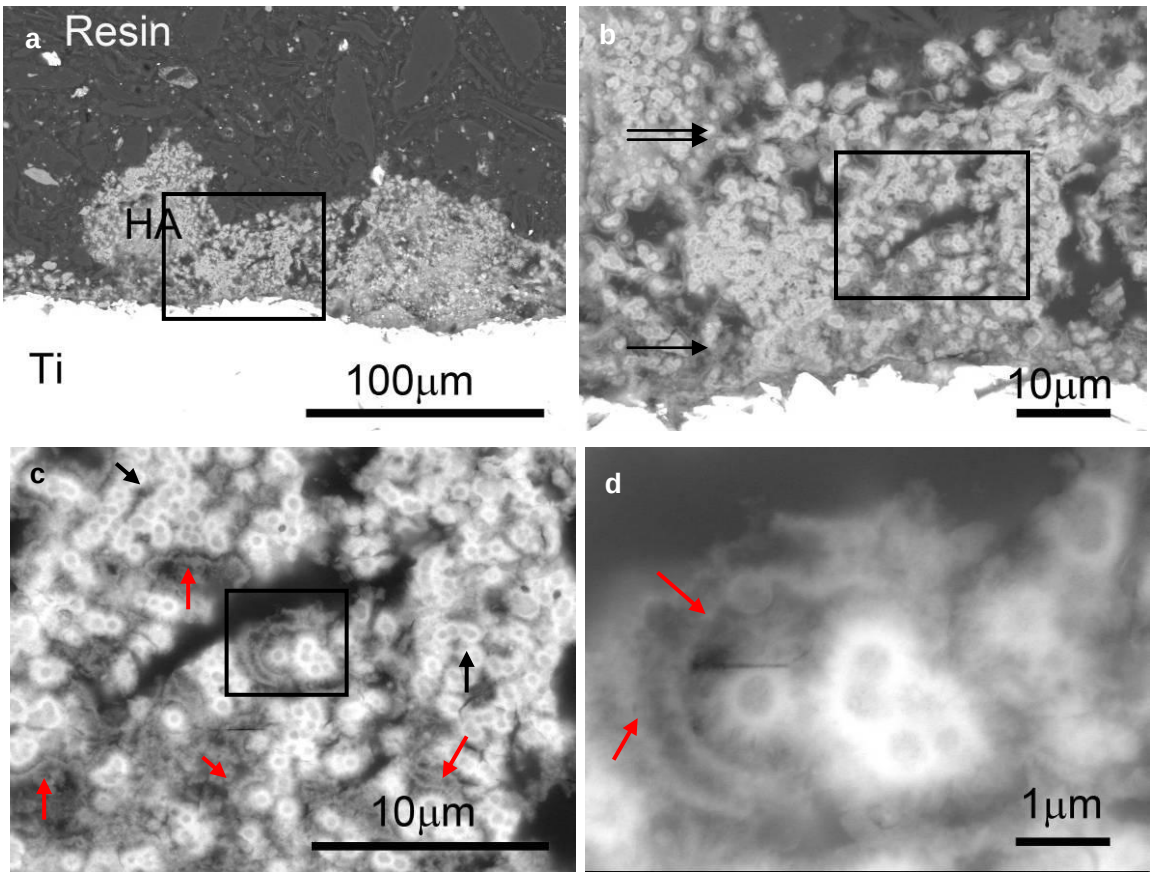

Figure 6. 4 The structure of the crystal coating formed on titanium (BSE imaging)

a: Cross section through the crystal coated titanium.

b: Crystals near the titanium substrate (single arrowed site) and 30 μm away from titanium (double-arrowed site) are similar. This image is the rectangular in (a) at higher magnification.

c: The squared site in (b) at higher magnification, showing crystal clusters (the brightest area, indicated by the black arrows) and crystal shells surrounding the crystal clusters (red-arrowed sites).

d: The squared site in (c) at higher magnification. The arrows point to the crystal shells covering the crystal clusters.

6.3.2 Crystal morphology

At higher magnification, the ‘micro-spheres’ shown in Figure 6. 3b&c are observed to consist of nano-scale crystals. Three different morphologies can be found via SEM: spheres with a fluffy appearance (Figure 6. 5a), spheres consisting of nano-scale curved plates (around 200 nm wide, Figure 6. 5b & c) and spheres composed of crystal plates (around 1 μm wide, Figure 6. 5d). The curved plate-like structure is dominant, and the plates if any are found buried deep inside the coating. However, the resolution of SEM is insufficient to explore the crystal morphology any further. For example, it is not possible to give a detailed description of the crystals in Figure 6. 5a, which are very likely to have the same morphology as those in Figure 6. 5b, but much smaller and thus not distinguishable by SEM.

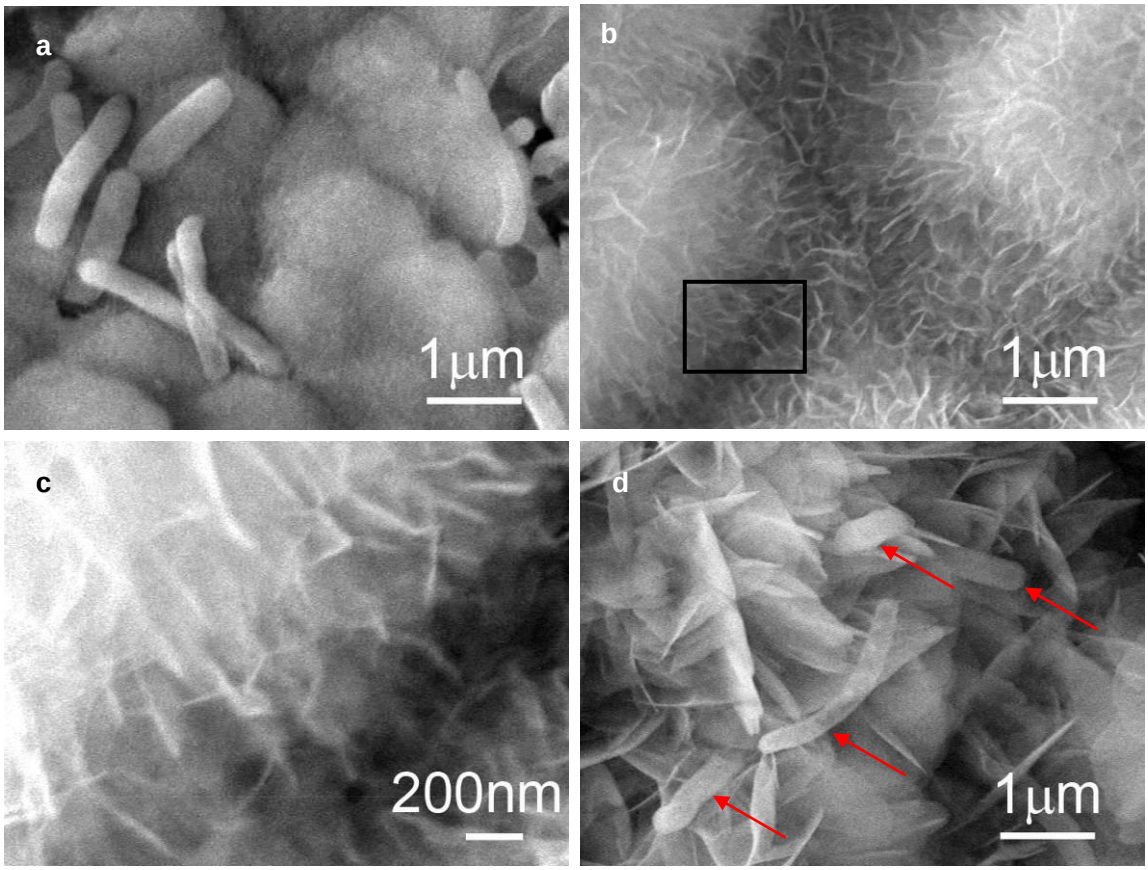

Figure 6. 5 The morphology of the crystal coating* (SE imaging)

a: Spheres with a fluffy appearance. The rods in the image are *Serratia* bacteria.

b: Curved plate-like crystals.

c: The crystals in (b) at higher magnification (the squared site in (b)).

d: Plate-shaped crystals (the rods indicated by the arrows are *Serratia* cells).

* Biomineralisation was repeated independently for 5 times, with 10 samples in each experiment. A set of representative data from one sample chosen randomly from all the specimens was presented in Figure 6.5

6.4 A TEM analysis of the coating crystals

The crystals were characterised further by TEM. However, they are extremely beam sensitive. At 200 kV, the morphology changes almost immediately. In less than 10 s, the borders of the

plate-shaped crystals merge and form structures shown in Figure 6. 6b, which makes the observation of the crystals difficult.

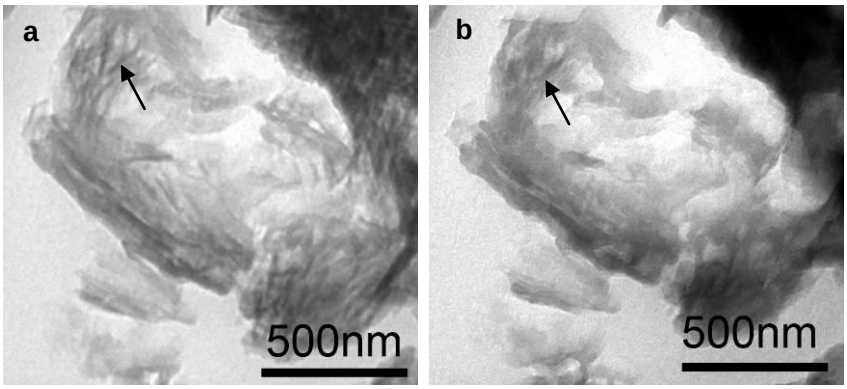

Figure 6. 6 Crystal morphology changes under TEM after 10 s' observation

(b) is the same site as (a) after 10 s at 200 kV accelerating voltage. The arrow in (a) points to the border of a crystal plates which is no longer visible in (b).

Nevertheless, both the curved plates (Figure 6. 7a) and the flatter plates (Figure 6. 7b), corresponding to the features displayed in Figure 6. 5, can be found by TEM. While the curved plates are around 100 to 200 nm across, the flat plates are much larger, from several hundreds of nm to around 1 to 2 μm wide. A cross section through the crystals is shown in Figure 6. 7c. They are all fairly thin, usually around 5 nm.

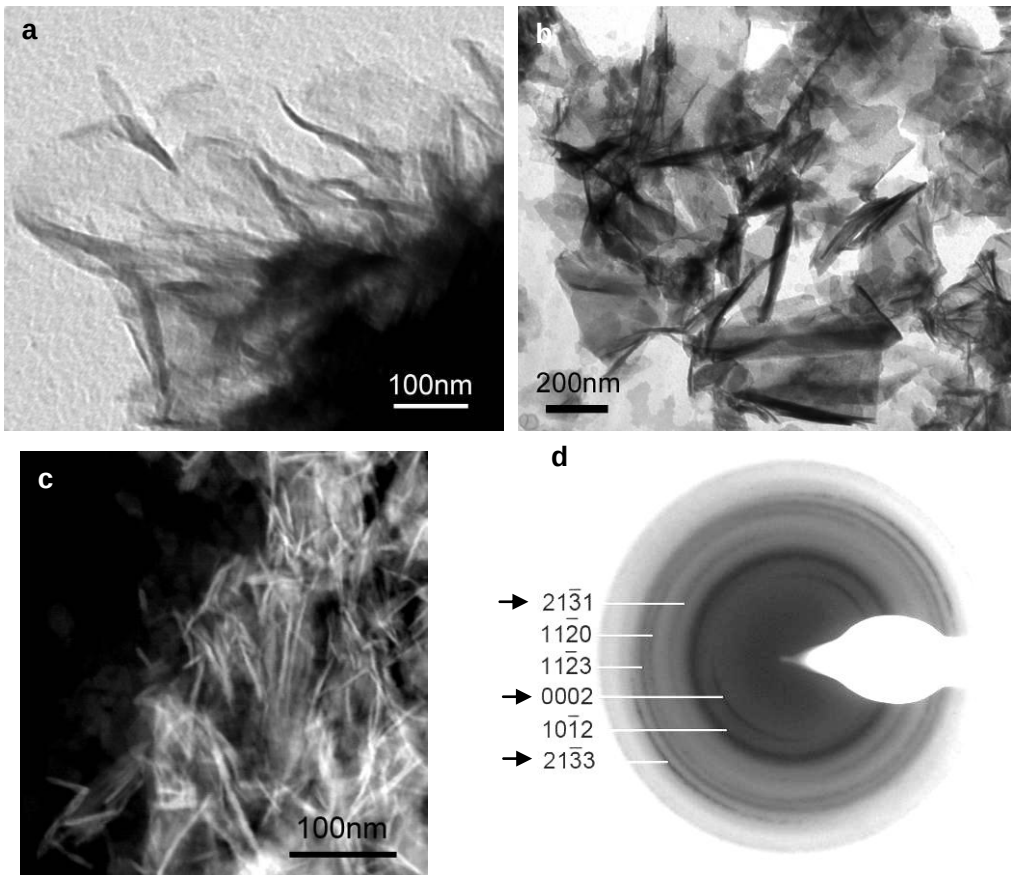

Figure 6. 7 The morphology of the crystals in the TEM

a: The curved plate-like crystals at higher magnification (bright field imaging, 80kV);

b: The plate-shaped crystals (bright field imaging, 80kV);

c: Cross section through the crystal (HAADF, 200 kV);

d: Selected area diffraction (SAD) pattern of (c) (200 kV). The arrows point to partial rings, indicating preferential crystal orientation.

The polycrystalline diffraction pattern displayed in Figure 6. 7d corresponds well with HA. The arced rings of (0002), $(21\bar{3}1)$ and $(21\bar{3}3)$ indicated by the arrows in Figure 6. 7d suggest a preferential crystal orientation. Diffraction patterns obtained from single crystals are displayed and indexed in Figure 6. 8, confirming further that the crystals are indeed HA.

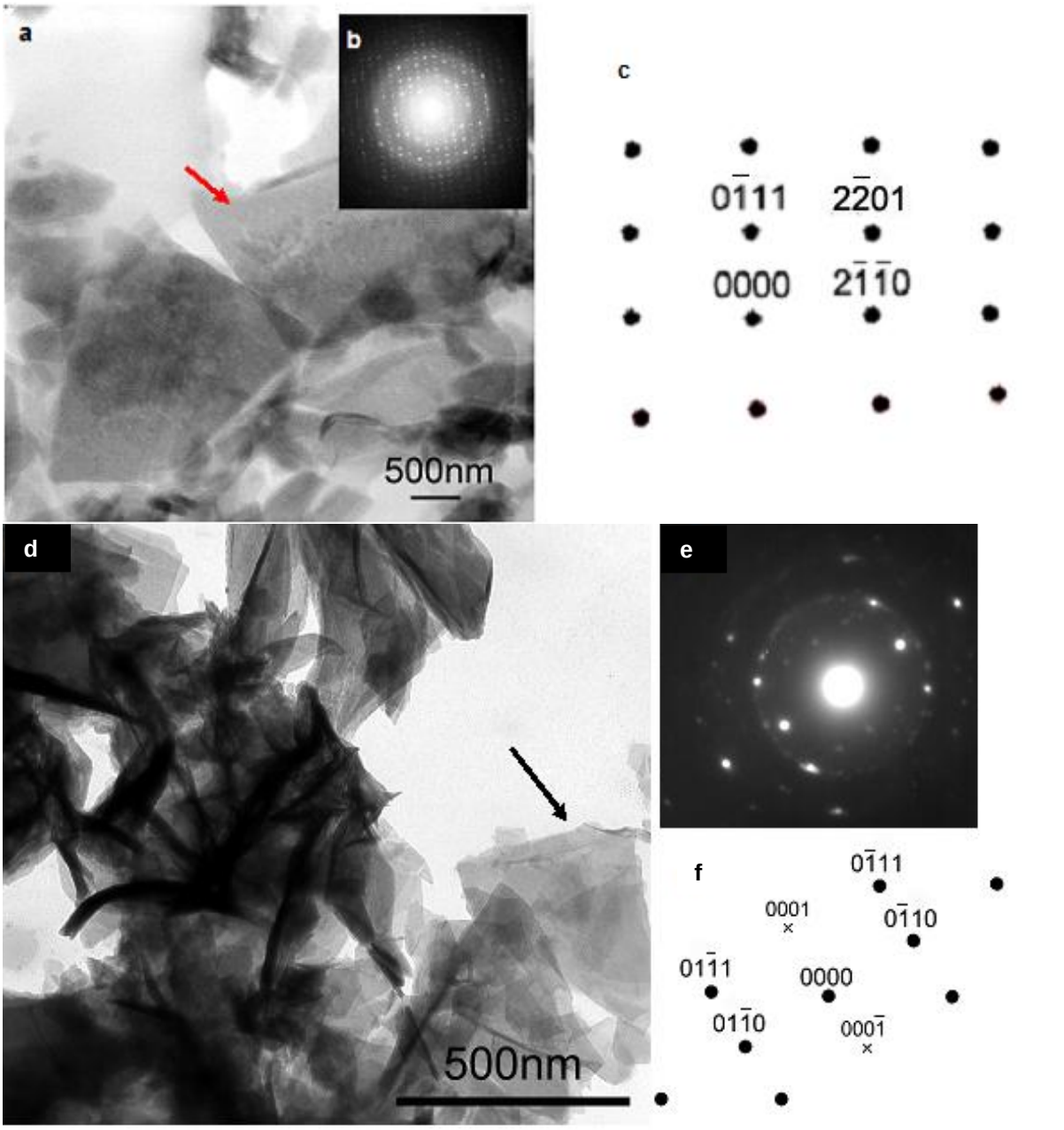

Figure 6. 8 SAD patterns of the crystals and their indexing

(b) is a SAD pattern obtained from the arrowed crystal in (a). It is indexed in (c): zone axis = $[0\bar{1}12]$.

(e) is the SAD pattern obtained from the arrowed crystal in (d). It is indexed in (f): zone axis =$[2\bar{1}\bar{1}0]$.

TEM/EDX analysis shows a Ca/P ratio of 1.27 ± 0.11, lower than that of stoichiometric HA, which is 1.67. Trace amounts of Na and Cl were also observed. A typical EDX spectrum is shown in Figure 6. 9.

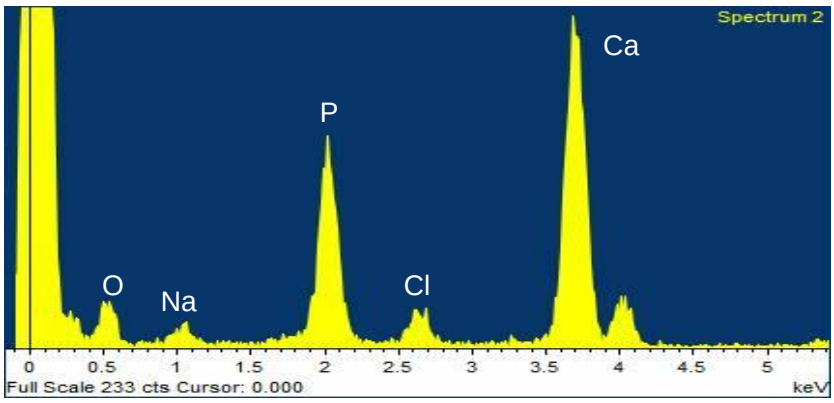

Figure 6. 9 A typical TEM/EDX spectrum from the nascent crystals

6.5 Crystal-substrate interface structure

To analyse the coating-substrate interface is crucial. Not only that it will help to understand how the coating is bonded to titanium, but other information may be obtained, such as whether the metal substrate interferes with bacterial mineralisation. This interface study was carried out using a FIB to create a trench in the surface in order to observe the cross-section. The method was described in § 2.4.7.2. The specimen was coated with tungsten (W, 1 in Figure 6. 10a) as a protection layer before ion milling. As seen in Figure 6. 10, the interface region consists of *Serratia* (arrows in Figure 6. 10b), the bacteria-synthesised HA (2 in Figure 6. 10a), embedded Al_2O_3 (3 in Figure 6. 10a) and Ti substrate (4 in Figure 6. 10a). The severely deformed titanium is composed of nano-grains and titanium twins (Figure 6. 10a & c).

Electron charging at the interface area made observations at higher magnification difficult, as

neither the crystal layer nor the embedded Al_2O_3 particles are conductive. As a result, the interface between 2 and 3, indicated by the red line in Figure 6. 10, was not clear. Although bacteria-shaped structures can be seen easily in Figure 6. 10a, either because of charging, or due to the re-deposition during ion milling, the fine features of the coating crystals (Figure 6. 5 and Figure 6. 7) are not observed.

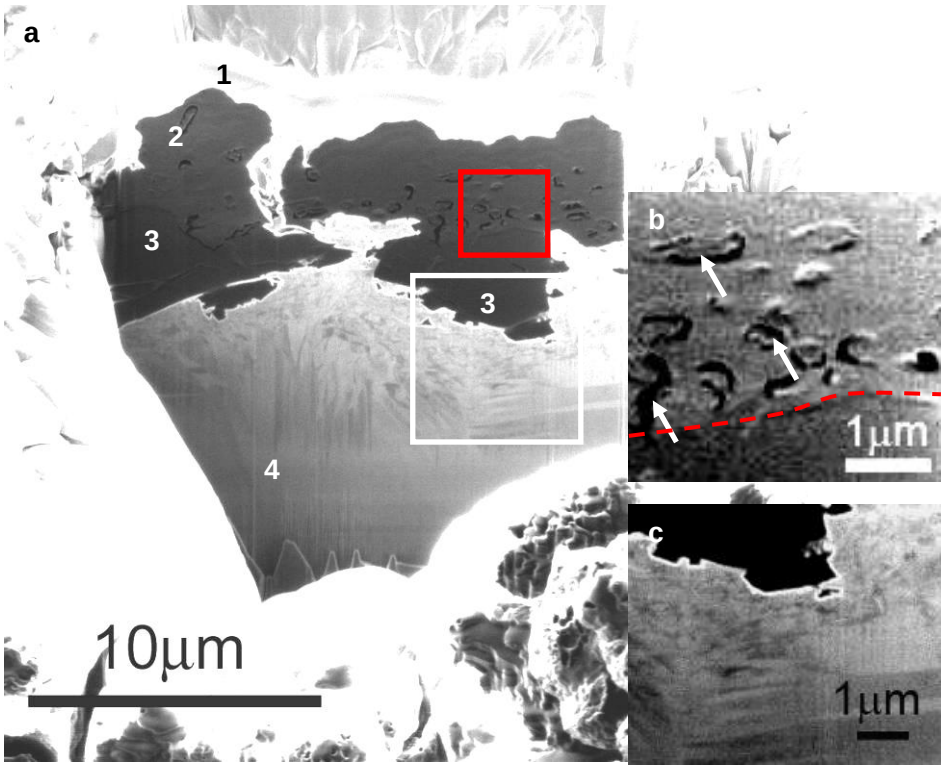

Figure 6. 10 The coating-substrate interface (SE imaging)

a: The coating-substrate interface. (1. W coating. 2. Biomineralised HA coating. 3. Embedded Al_2O_3 during the grit blasting. 4. Ti substrate.)

b: Enlarged red-squared site in (a) showing *Serratia* (indicated by the arrows). The interface between the crystal coating and Al_2O_3 follows the red line.

c: Enlarged white-squared site in (a) showing the heavily deformed titanium surface due to Al_2O_3 grit blasting.

A TEM specimen around 90 nm thick was prepared by FIB, as shown in Figure 6. 11a. The hole indicated by the arrow is a naturally existing crack in the coating, and others were caused by ion milling in FIB/SEM. The crack goes through the entire coating and does not terminate until it reaches the substrate surface. However, it can be seen that at sites other than at the crack, an intimate contact is achieved at the interface (Figure 6. 11c).

Bacteria-shaped features are observed by TEM, always in company with holes, as seen in Figure 6. 11b (arrows). However, it is not clear whether these holes suggest a 'crystal-exclusive' zone around the bacteria, because they are likely to be artefacts during drying, ion milling and characterising using TEM. During drying, the coating lost most of its water, including that from within the bacteria. Thus, in spite of the solid crystal support, bacteria will shrink to a certain extent, leaving holes inside the coating. The author also observed during the EM analysis that the organic matters such as bacteria, if not coated which is the case in Figure. 6. 11, would easily shrink and deform during the characterisation. The introduction of cryo technique will be needed in further investigation.

Although weak, a polycrystalline diffraction ring pattern can be obtained from the coating crystals (Figure 6. 11d). However, unlike in Figure 6. 5 and Figure 6. 7, the morphology of the crystals here resembled bubble-like features changing constantly when observed at 200 kV. It is known that ion milling can introduce beam damage to the specimen, resulting in an amorphous surface even when preparing metal samples. The crystal coating in this study is beam sensitive. Thus, during the ion milling and thinning, the fine crystal structure was destroyed entirely, resulting in the bubble-like features (2 in Figure 6. 11c) which are destroyed even further by the high energy electron beam in the TEM. Preparing the sample in a cryo-FIB may solve the problem, or simply using a thicker sample (§ 6.7.3).

TEM analysis confirms further that grit blasting changes radically not only the morphology but the microstructure of the titanium substrate at the surface (Figure 6. 11b), compared to its original structure as shown in Chapter 3, Figure 3. 1. The superficial 1~3 μm is a layer of super-fine crystals, around 100 nm in size, with a twinning zone several micrometres thick underneath. SAD patterns obtained from the titanium substrate and the embedded alumina are displayed in Figure 6. 12 and Figure 6. 13, respectively.

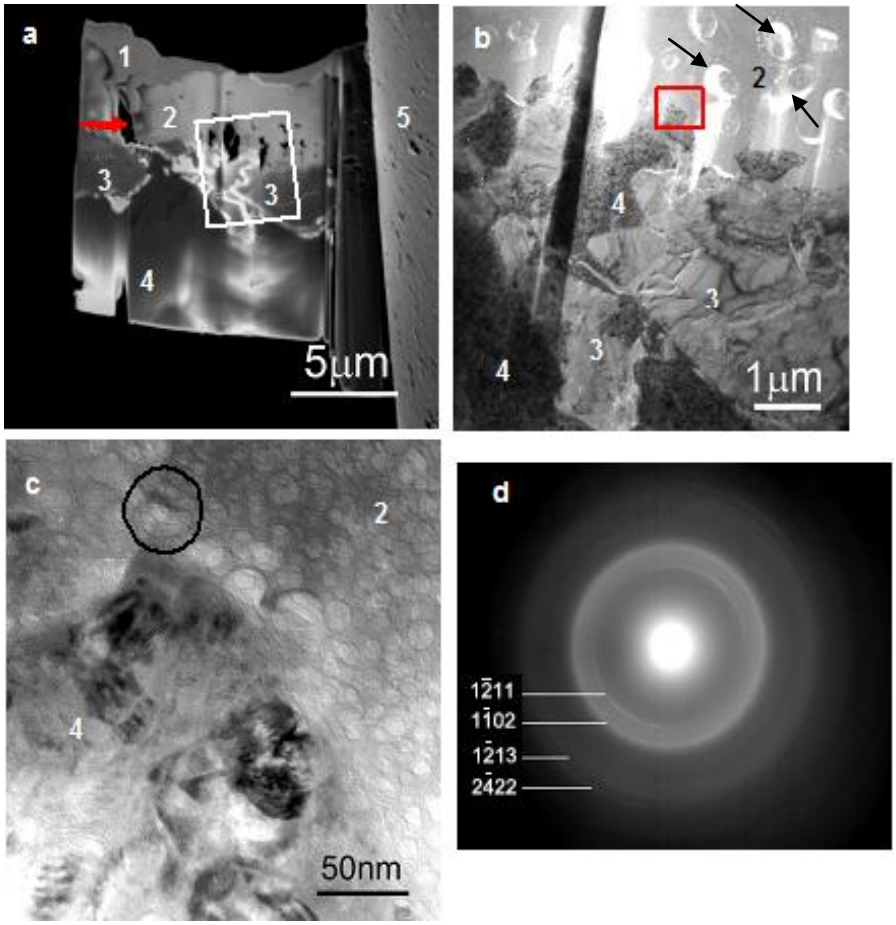

Figure 6. 11 A FIB/TEM study of the coating-substrate interface
a: A TEM sample prepared by FIB (SE imaging). 1. Tungsten coating. 2. Biomineralised HA coating. 3. Al_2O_3 embedded during the grit blasting. 4. Ti substrate. 5. Copper grid. Sample thickness: ~100 nm. SAD patterns of the titanium substrate (4) are shown in Figure 6. 12.
b: TEM BF imaging of the squared site in (a). SAD patterns of the alumina are shown in Figure 6. 13. The arrows points to
c: The squared site in (b) at higher magnification, showing HA-Ti interface (TEM BF imaging).
d: Poly-crystalline diffraction pattern of the coating crystals (SAD pattern of the circular area in (c)).

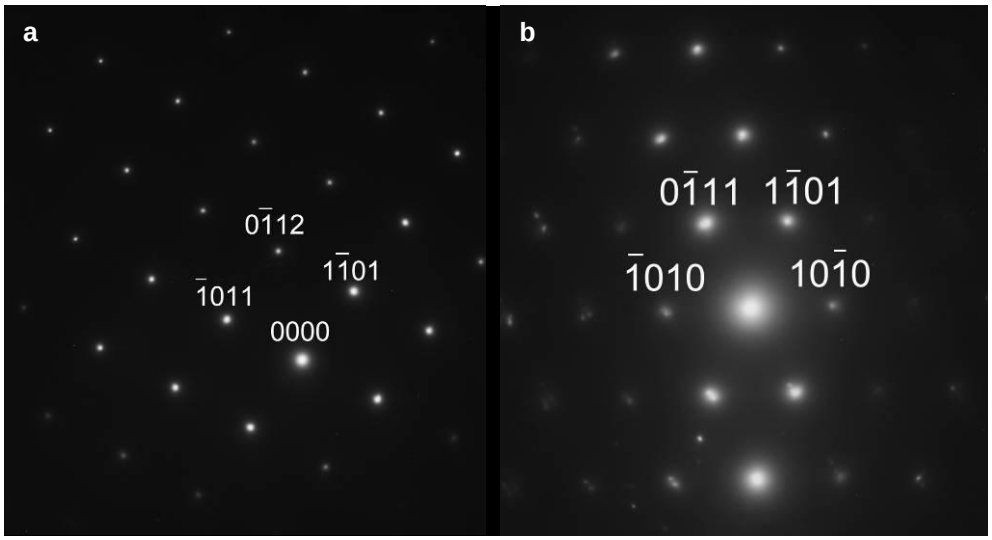

Figure 6. 12 SAD patterns of Ti

((a): zone axis = $[0\bar{1}11]$. (b): zone axis = $[1\bar{2}\bar{1}3]$)

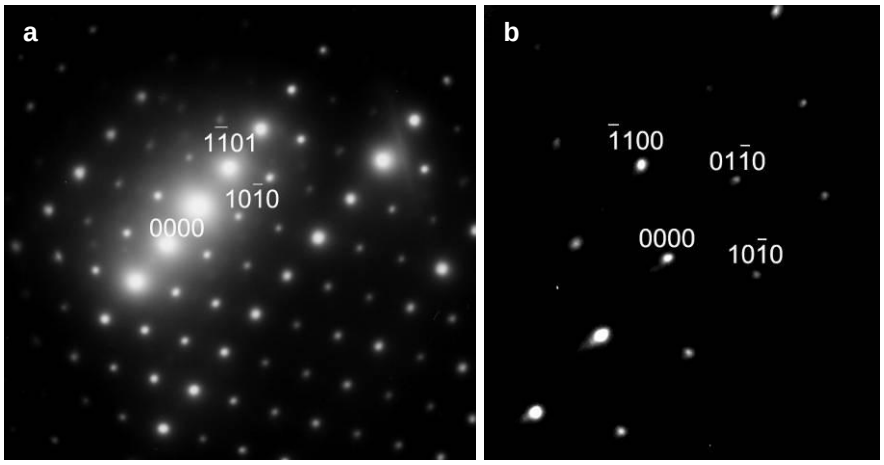

Figure 6. 13 SAD patterns of Al_2O_3

((a): zone axis = $[1\bar{2}\bar{1}3]$. (b): zone axis = [0001])

6.6 The influence of flow rate and challenge time

The influence of both medium flow rate and challenge time on the crustal formation was investigated by a simple SEM/EDX analysis of the Ca/P ratio of the crystals formed at two different flow speeds and different stages during the biomineralisation. It can be seen in Figure 6. 14 that the Ca/P ratio is not significantly affected by either the flow rate (1.5 ml/h and 15 ml/h or the challenge time (from day to day 9). However, these EDX data may not be accurate enough due to the reasons that will be discussed in Chpater 9. To examine the hydroxyapatite formed by planctonic *Serratia* cells in flasks at different time points by TEM/EDX may be a more propriated choice, which will be investigated in the future.

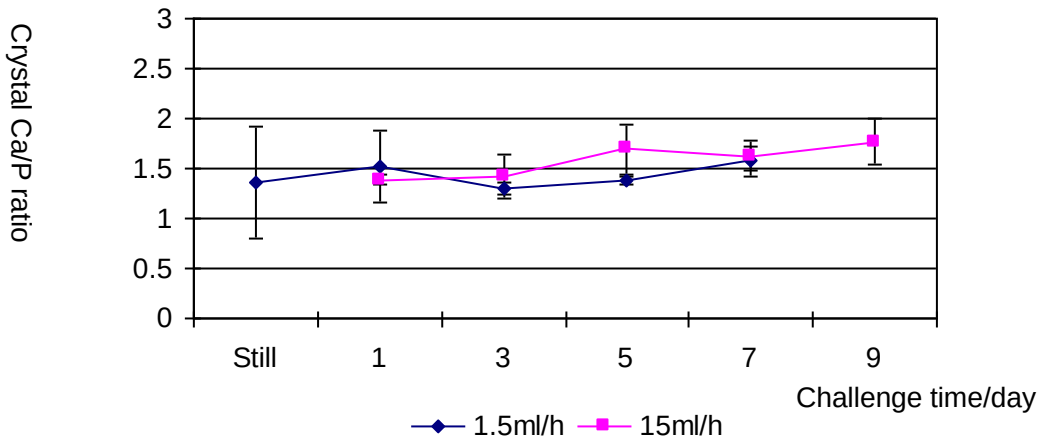

Figure 6. 14 The influence of medium flow rate and challenge time on the Ca/P ratio of the nascent crystals (obtained from SEM/EDX)

6.7 The influence of alkali treatment

HA has been shown to form spontaneously on alkali treated titanium in SBF as described in § 1.4.1.4 [3, 4]. This treatment was introduced in this study to improve the coating-substrate contact due to the potential ingrowth of HA into the alkali influenced layer. The influence of

this layer on *Serratia* HA formation and the crystal structure at the coating/substrate interface was investigated.

6.7.1 The influence of alkali treatment on the titanium substrate

Alkali treatment alters the substrate topography as well as the chemical composition. A nano-scale open cell structure is produced on the grit blasted titanium surface, as seen in Figure 6. 15. The cross section of this alkali influenced layer is displayed in Figure 6. 15c and enlarged in Figure 6. 15d. It is around 1 μm thick and covers both the Al_2O_3 particles and the titanium substrate (Figure 6. 15c). However, cracks can be observed, possibly artefacts produced during drying.

An SEM/EDX map showed that the layer was composed of Ti, Na and O (WDX map) (Figure 6. 16), consistent with previous reports that alkali treatment produces a thin film of sodium titanate on the titanium surfaces [4]. Although the specimen has been heat treated at 600 °C, the embedded Al_2O_3 particles appear to be stable, without significant diffusion into the substrate. It is also worth noting that Al had not diffused into the sodium titanate layer either (Figure 6. 16).

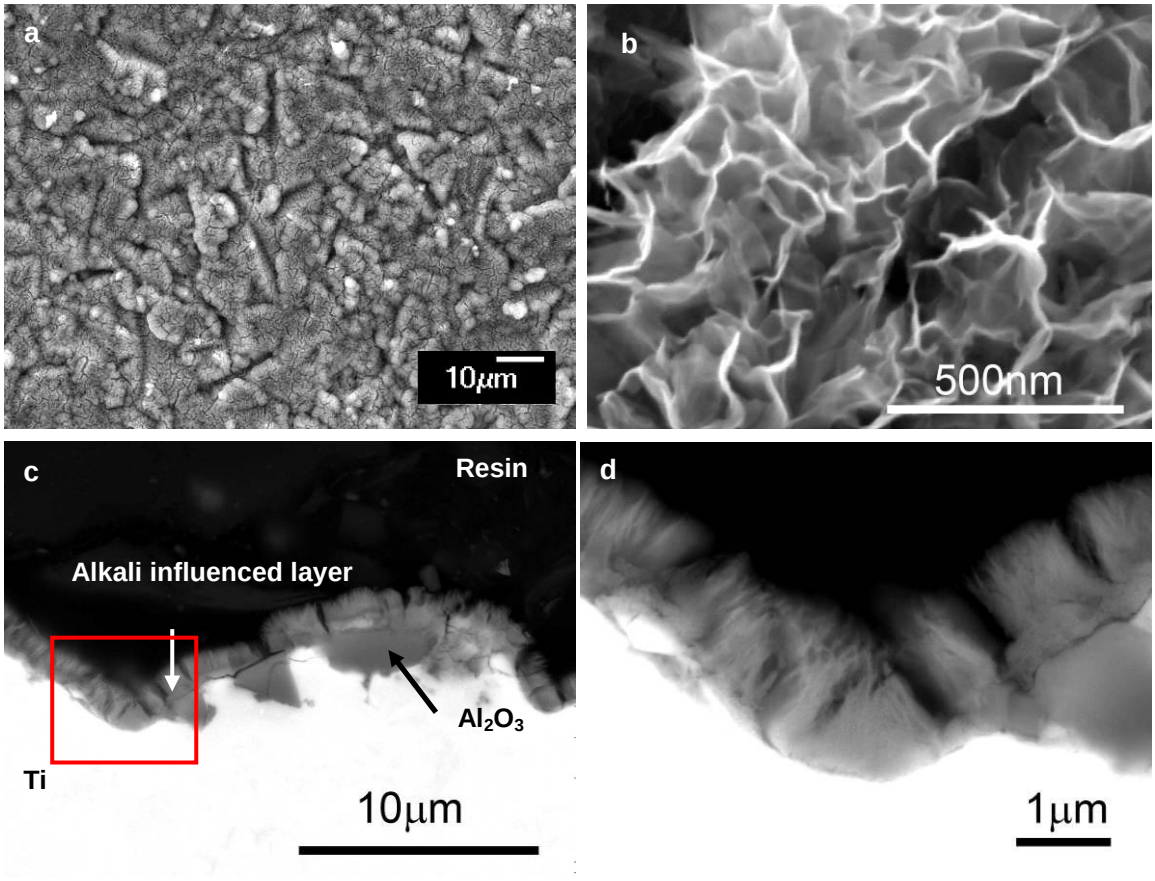

Figure 6. 15 The influence of alkali treatment on the grit-blasted titanium

a: The morphology of the grit blasted titanium treated with NaOH (SE imaging).

b: Higher magnification of (a) showing the morphology of the alkali-influenced layer (SE imaging).

c: Cross section through the alkali-influenced layer (BSE imaging).

d: The rectangular area in (c) at higher magnification, showing the cross section of the alkali-induced layer in detail.

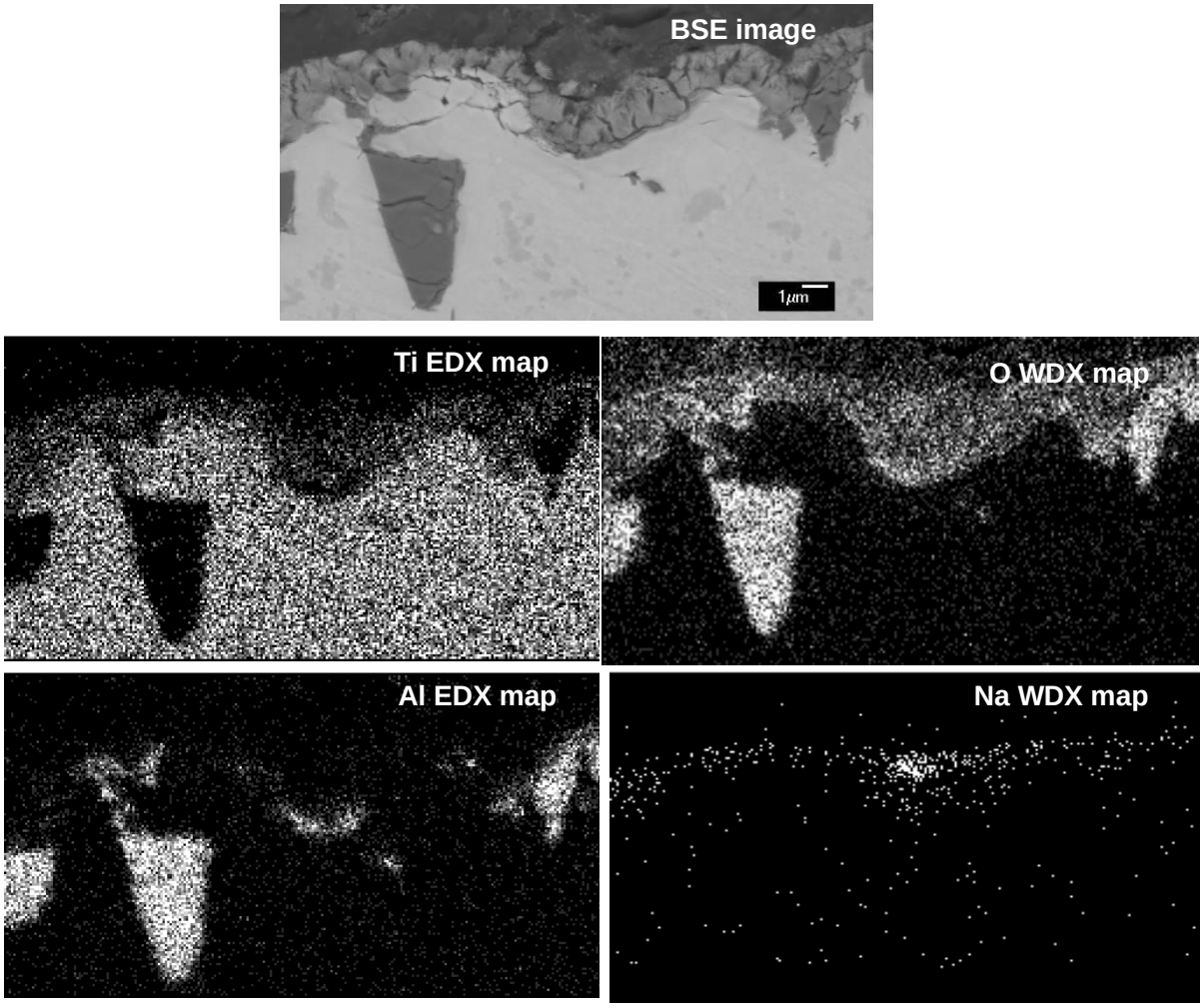

Figure 6. 16 SEM/EDX/WDX map of the alkali treated Al_2O_3 grit blasted titanium (cross section)

6.7.2 Nascent *Serratia* HA coating on alkali treated titanium

Neither the XRD profile (Figure 6. 17) nor the morphology of the crystals formed on titanium substrates with (Figure 6. 18) and without alkali treatment (Figure 6. 5) differed, indicating that the crystals formed on both substrates have the same composition.

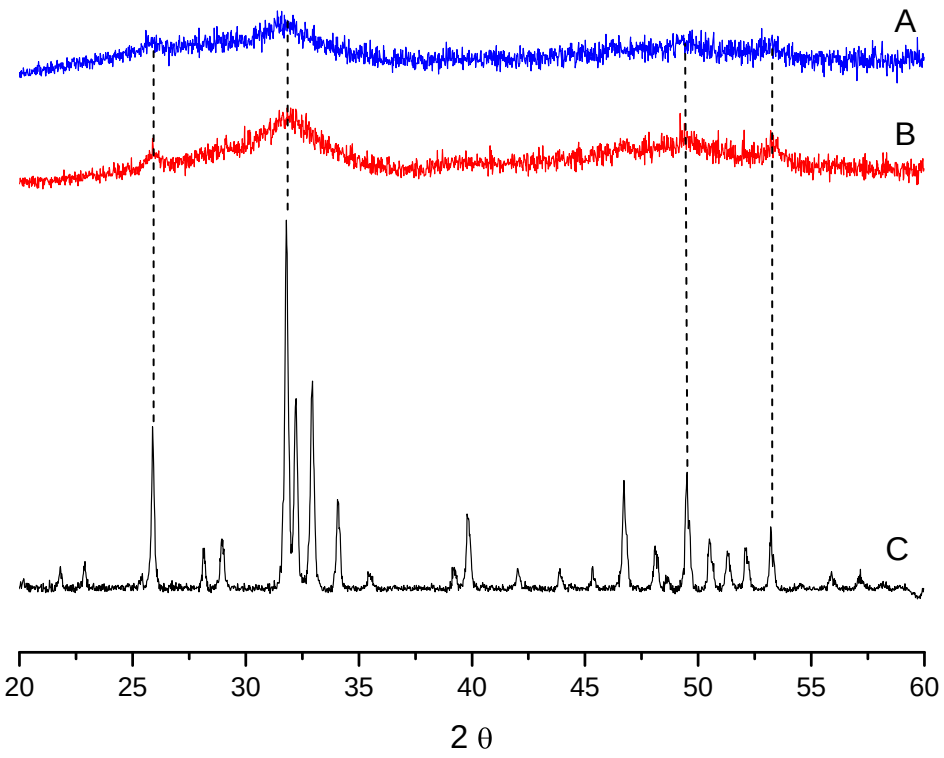

Figure 6. 17 XRD spectrum of the crystals formed on the alkali treated titanium in comparison with those formed on the untreated titanium and CAPTAL HA

A: The crystals formed on a grit blasted titanium substrate (with alkali treatment).

B: The crystals formed on a grit blasted titanium substrate (without alkali treatment).

C: CAPTAL HA.

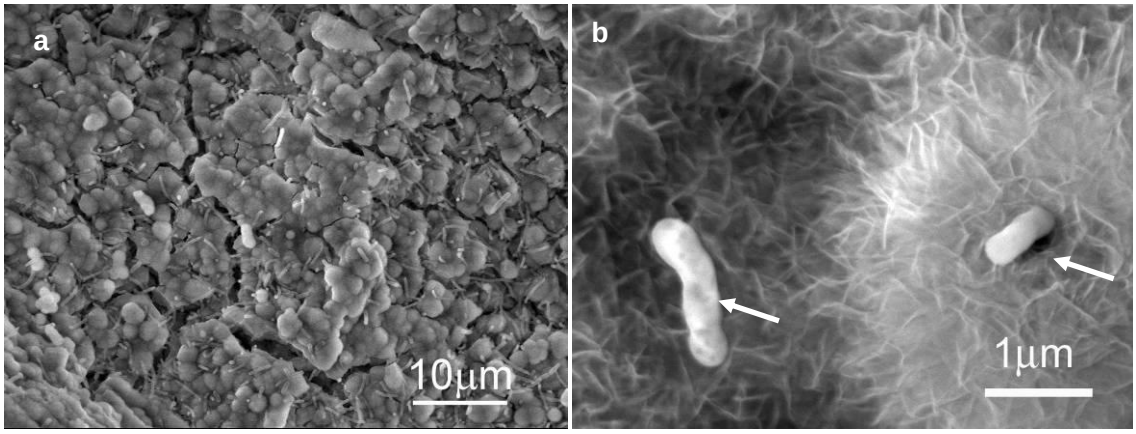

Figure 6. 18 Morphology of crystal coating on alkali treated titanium (SE imaging)

a: The coating consists of microspheres.

b: (a) at a higher magnification, showing the crystal morphology. Bacteria can be seen (arrows) occasionally.

6.7.3 Coating-substrate interface study

The coating-substrate interface was studied as described in § 6.5. As seen in Figure 6. 19, the alkali influenced layer is still quite obvious. The morphology of this layer is exactly as that prior to biomineralisation, indicating the stability of this layer even after sterilisation, fermentation and mineralisation. The coating on the surface is in good contact with the alkali treated layer. No spacing or cracks were observed at the interface.

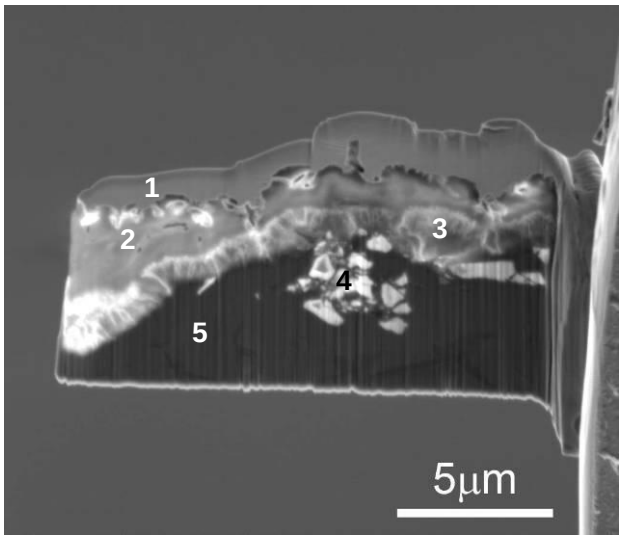

Figure 6. 19 Cross section through the coating-substrate interface produced by FIB/SEM

1. W coating. 2. Biomineralised HA coating. 3. The alkali treated layer. 4. Embedded Al_2O_3 particles. 5. Titanium substrate.

The interface structure was studied further by TEM. It was shown in § 6.5 that the beam damage in a commercial FIB is enough to destroy entirely the crystal structure of a specimen around 90 nm thick. On the other hand, the sample has to be thin enough, otherwise the electron beam will be blocked or absorbed. Thus, this specimen was thinned to approximately 150 nm in this section. To produce a TEM specimen using FIB/SEM is a difficult and time-consuming procedure. Thus, only one sample was observed, which was chosen randomly from the specimens.

As seen in Figure 6. 20, a STEM/EDX QuantMap shows the elemental distribution at the coating-substrate interface of the alkali treated specimen. The contrast in Figure 6. 20c represents the atomic % of each element. Ca and P exist mainly in the crystal coating, but they are also found within the sodium titanate layer (indicated by the double-headed arrow), although at lower concentration, which suggests the formation of HA. The red arrows point to where HA filled the gaps in sodium titanate, when the maps of Ca and P are compared with that of Ti. The embedded Al_2O_3 is stable, without any significant diffusion into the sodium titanate, as seen from the Al map in Figure 6. 20c.

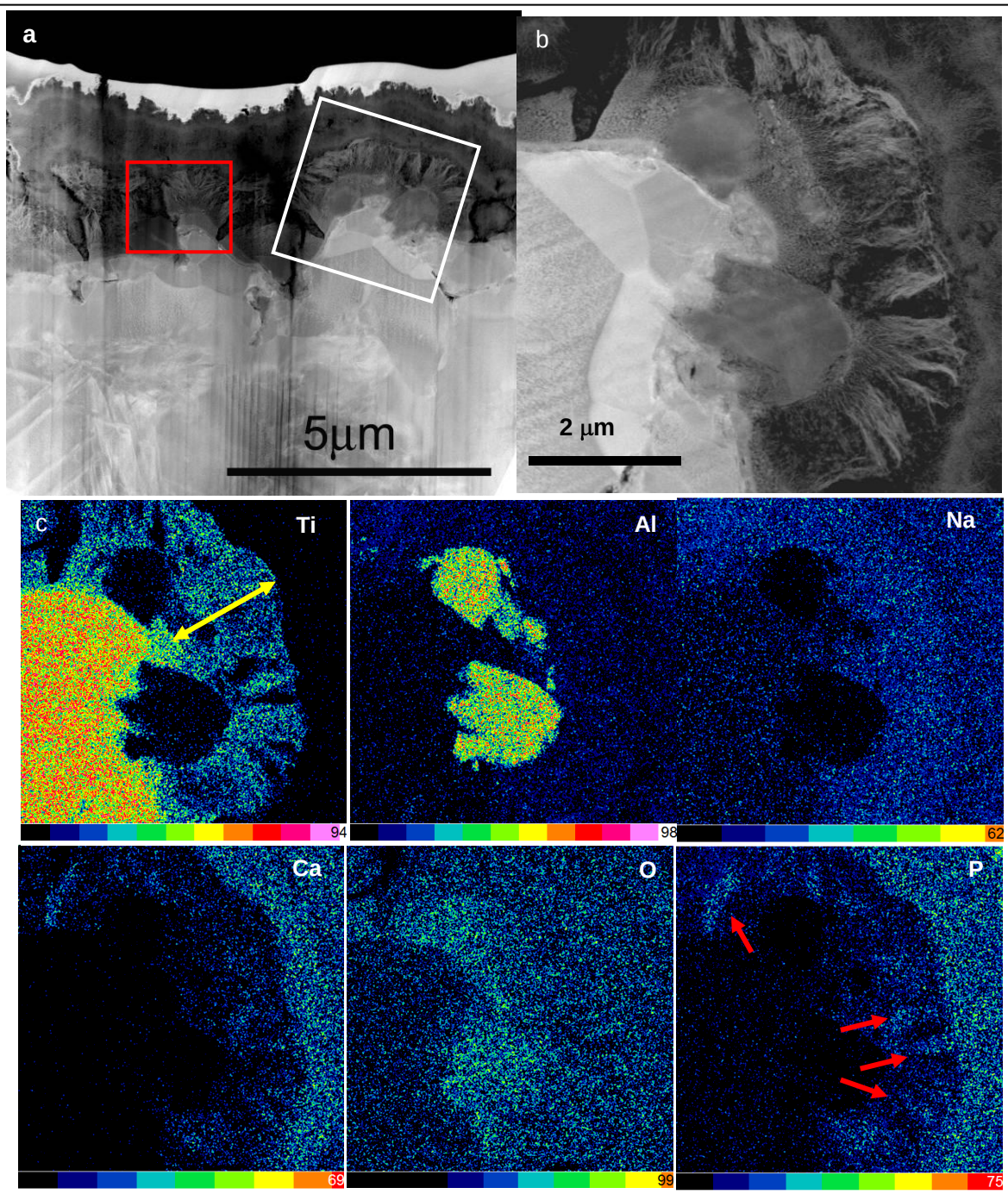

Figure 6. 20 TEM/EDX map of the interface structure

a: HAADF image of the interface (sample thickness: ~150 nm).The red box is enlarged in Figure 6. 22. The double-headed arrow in (c) indicates the sodium titanate layer.

b: The white box in (a) at higher magnification (HAADF image).

c: TEM/EDX QuantMap of (b). The yellow arrow indicates the sodium titanate layer. The red arrows point to where HA fills gaps inside this layer. The atomic % of each element is indicated by a different colour. The scale is displayed below each image.

As seen in Figure 6. 21, at this thickness, the crystal structure is preserved. However, the sample is too thick, because instead of a single layer of HA crystals, an overlap of several crystal layers was examined and it was difficult to focus at higher magnification. In addition, the beam damage when studied by a TEM at 200 kV is unavoidable and the crystal structure is changed gradually.

Nevertheless, both the HA and the sodium titanate appear to be highly textured. The sodium titanate layer is composed mainly of highly oriented 'leaves' perpendicular to the substrate, with the bottom adjacent to the substrate consisting of randomly arranged nano-crystals (Figure 6. 21b). The thickness of the sodium titanate film ranges from 500 nm to 1 μm, although this differed between on Ti and Al_2O_3, as compared further in Figure 6. 22. It is hard to tell where the exact interface between the HA and sodium titanate occurs other than by crystal size, as seen in Figure 6. 21c. The clearer interface in Figure 6. 21a compared with Figure 6. 21c is due to the difference in contrast. Just like the sodium titanate layer, HA changes from randomly arranged crystals to oriented ones, as seen in Figure 6. 21c, and appears much denser than the sodium titanate crystals. The specimen is so thick (to minimise beam damage during ion milling) that no acceptable diffraction patterns were obtained.

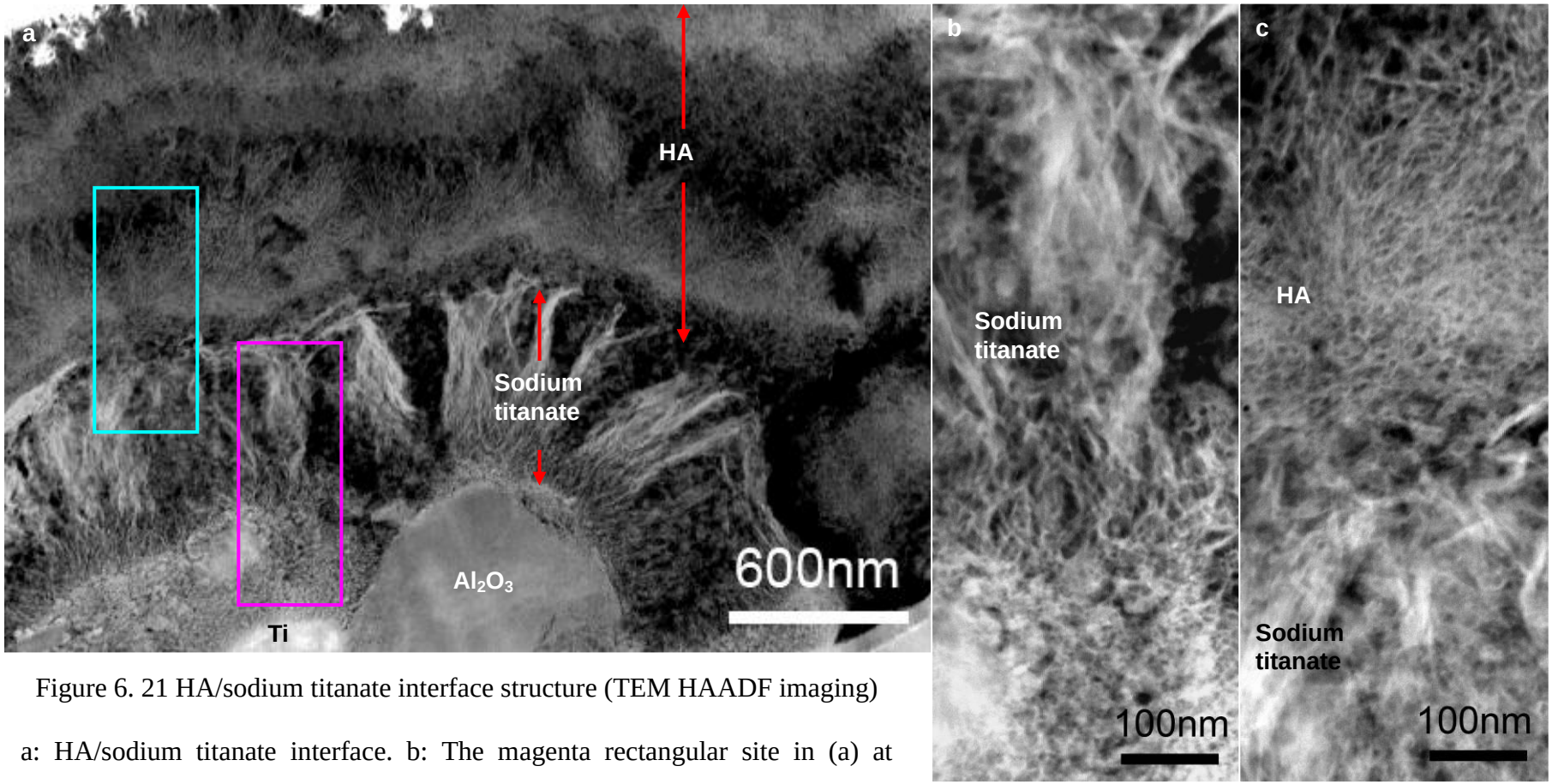

Figure 6. 21 HA/sodium titanate interface structure (TEM HAADF imaging)

a: HA/sodium titanate interface. b: The magenta rectangular site in (a) at higher magnification, showing the sodium titanate layer.

c: The cyan rectangular site in (a) at higher magnification, showing the HA/sodium titanate interface.

Further analysis confirmed the growth of HA into the sodium titanate layer, as the gaps in this layer are filled with HA, as indicated by both the EDX map in Figure 6. 20 and the crystal morphology difference in Figure 6. 22a (block arrows). The amorphous appearance is more likely to be an artefact caused by ion beam damage by FIB and TEM. It was also found that the sodium titanate formed on Al_2O_3 was slightly different from that on Ti. On the former, sodium titanate crystals quickly develop to large 'leaves' around 200 to 300 nm long (Layer 1 in Figure 6. 22b). On the latter, however, underneath a similar layer of textured 'leaves', an extra layer composed of fine randomly arranged crystals can be observed, usually 200 nm thick (Layer 2 in Figure 6. 22c). The boundary between Layer 1 and Layer 2 replicates that between Layer 2 and the titanium substrate.

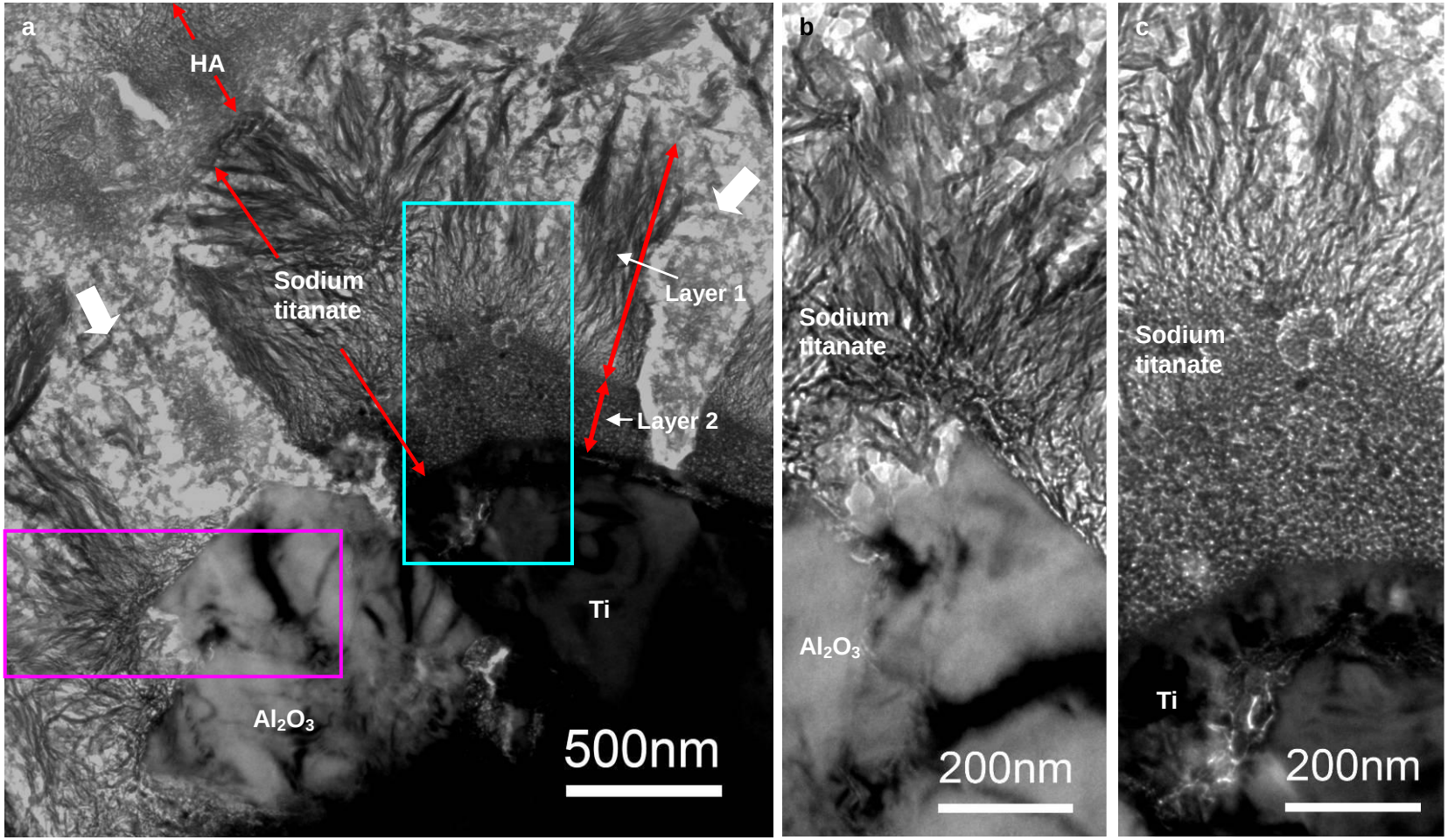

Figure 6. 22 TEM BF image of the interface structure-HA coated titanium treated with alkali

a: The red squared site in Figure 6. 20a at higher magnification. The block arrows suggest HA ingrowth into the gaps of sodium titanate.

b: The magenta rectangular site in (a) rotated by 90º - sodium titanate on Al_2O_3.

c: The cyan rectangular site in (a)-sodium titanate on Ti.

6.8 The influence of solution composition on crystal size

Although most of the crystals observed in this work were nano-scale (Figure 6. 5c and Figure 6. 7a), they were able to grow to around 1 μm wide (Figure 6. 5d and Figure 6. 8a). Many factors may contribute to this phenomenon, and the influence of the composition of the mineralisation solution was investigated in this section. The experiment was carried out once. The measurements of crystal size and Ca/P ratio were repeated three times.

Table 6. 1 Comparison of the solution composition and crystal formation in calcium and phosphate excess conditions and in the control solution

	AMPSO /mM (pH=8.6)	***$CaCl_2$ /mM***	***β-GP /mM***	***Serratia /OD_{600}***	***Crystal size***	***Ca/P ratio***
β-GP excess condition	50	2.5	50	0.5	30 to 50 nm wide	1.12 ± 0.06
Calcium excess condition	50	25	5	0.5	Above 100 nm wide	1.28 ± 0.07
Control	50	25	50	0.5	-------	1.26 ± 0.10

Fresh mineralisation solutions were prepared according to Table 6. 1. Compared with the normal mineralisation solution used above (§ 6.2 to § 6.7) which contained 25 mM $CaCl_2$ and 50 mM β-GP, the solutions used in this section was either phosphate (β-GP) excess or calcium excess. *Serratia* cells were suspended in these solutions shaken at 150 rpm at room temperature and mineralisation was allowed for three days. It was observed that HA crystals form normally in both phosphate and calcium excess conditions, although with different morphologies (Figure 6. 23) and Ca/P ratio (Table 6. 1). The crystals formed in the phosphate (β-GP) excess solution are nano-scale plates, as indicated by the arrow in Figure 6. 23b. They are usually around 30 to 55 nm across and 3 to 4.5 nm thick. The Ca/P ratio was measured to

be 1.12 ± 0.06. The HA crystals formed in the calcium excess solution have curved plate-like structures (the arrow in Figure 6. 23d). They are wider but thinner than those formed when calcium is scarce (the arrow in Figure 6. 23b). The Ca/P ratio of these crystals is measured to be 1.28 ± 0.07 –higher than that in the phosphate excess condition. The crystals formed in the control solution are displayed in Figure 6. 23e & f. The image quantity is too poor to measure the size of the crystals. However, the Ca/P ratio was measured to be 1.26 ± 0.10, higher than the β-GP excess crystals (1.12 ± 0.06), and comparable to the calcium excess crystals (1.28 ± 0.07).

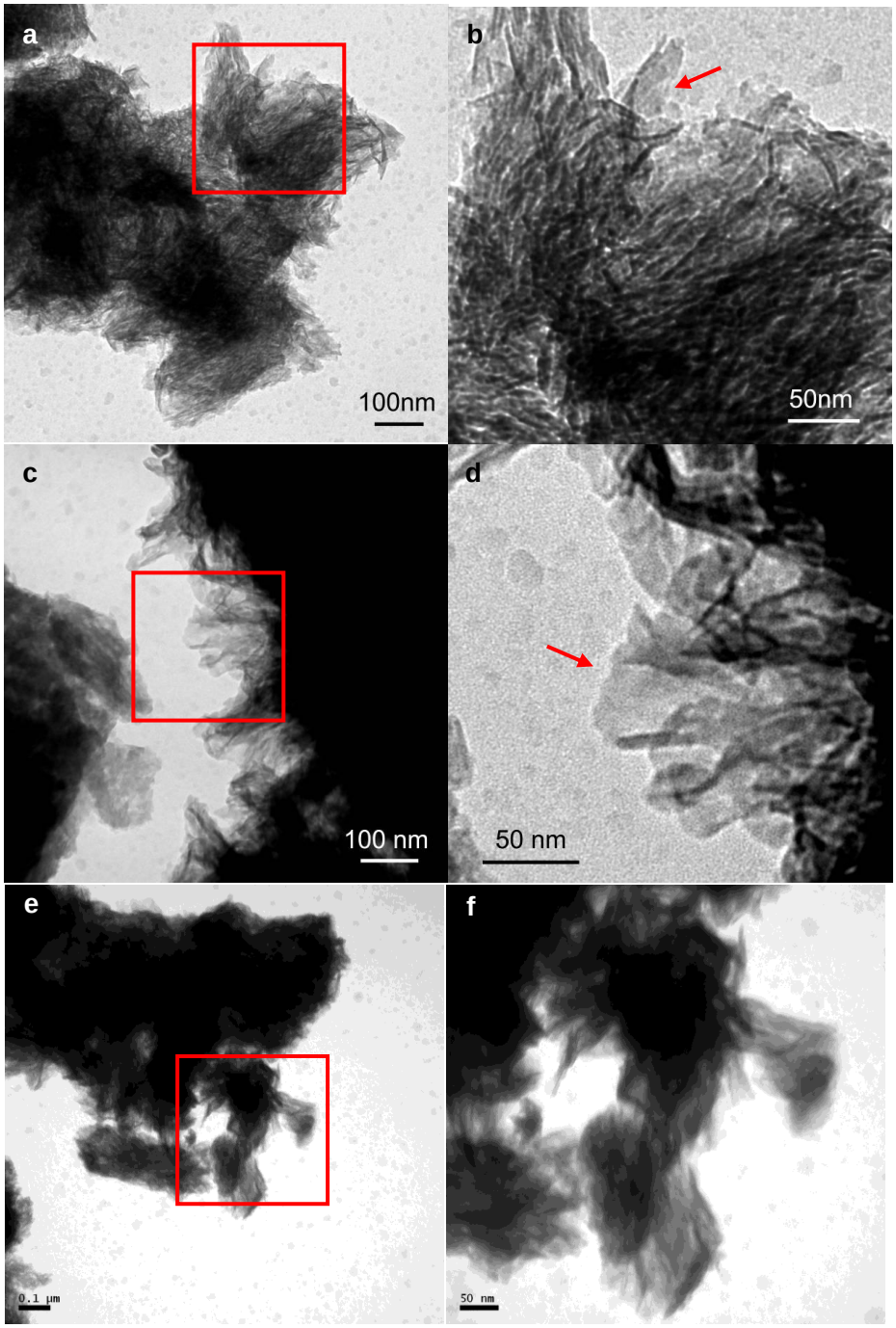

Figure 6. 23 The influence of ion strength on crystal formation (TEM BF imaging)

a: The crystals formed in phosphate excess condition (JEOL 2100, 200 kV).

b: The square in (a) at higher magnification (JEOL 2100, 200 kV).

c: The crystals formed in calcium excess condition (JEOL 2100, 200 kV).

d: The square in (c) at higher magnification (JEOL 2100, 200 kV).

e: The crystals formed in the control solution (JEOL 1200, 80 kV)..

f: The square in (e) at higher magnification (JEOL 1200, 80 kV).

The dependence of crystal size on solution ion strength is very interesting, but it may not be the only factor that can contribute to this phenomenon, which will be discussed further in Chapter 9. More systematic studies are required in the future for a thorough understanding of this aspect.

6.9 The role of *Serratia* in HA precipitation

The role of *Serratia* bacteria to liberate inorganic phosphate (HPO_4^{2-}) from its organic form (β-GP) is well established [5-7]. However, their role during HA precipitation is yet not clear: *Serratia* may either catalyse HA deposition, or not be involved in the precipitation. On the other hand, the biomineralisation solution used in this work (§ 6.2 to § 6.7 and in Chapter 8) was a phosphate-rich solution with a Ca/P ratio of 0.5, comparing to HA of 1.67 and the nascent crystal Ca/P ratio of 1.21 which was the mineralised products in this study. To understand the exact role of *Serratia* in HA precipitation and to offer evidence on the state of the redundant phosphate, such an experiment was designed:

Planktonic *Serratia* cells harvested from secondary culture (§ 2.2.2) were suspended in mineralisation solution (50 mM AMPSO, 25 mM $CaCl_2$ and 50 mM β-GP) with OD_{600} adjusted to 0.5. 20 ml of such solution was shaken for 24 hours at 150 rpm before it was centrifuged at 3000 rpm at 4 °C for 10 min. The white precipitate (HA) formed was removed by centrifuging and the remnant solution was filtered using a 0.2 μm filter to remove residual bacteria or crystals in the solution. This solution was autoclaved to demolish bacterial activity. (Sp. Act value of this autoclaved solution was measured to be 0.) 1 ml of 25 mM $CaCl_2$ was then added to this solution. With the addition of $CaCl_2$, precipitation formed immediately; the precipitates were harvested by centrifugation for SEM/TEM analysis. A control solution was prepared by adding 1 ml of 25 mM $CaCl_2$ to the same volume of mineralisation solution

(without previously added bacteria). No deposits were observed in the control solution.

In the autoclaved solution, with the addition of fresh $CaCl_2$, deposits formed immediately, whilst the control solution remained clean. The deposits consisted of nano-scale crystals as can be observed by both TEM (Figure 6. 24a & b) and SEM (Figure 6. 24c & d). They are around 50 nm wide and 100 to 200 nm long. The Ca/P ratio of these crystals is extremely low, 0.16 ±0.01 (TEM/EDX), and Na is incorporated into the structure, as shown in Figure 6. 25. The polycrystalline diffraction pattern indicates (0002) and $(10\bar{1}2)$ planes of HA (the inset diffraction ring pattern in Figure 6. 24a). These crystals are extremely beam sensitive, fusing immediately when observed by 100 keV electrons and forming morphologies shown in Figure 6. 24b. They were further characterised by JEOL 7000 SEM with an accelerating voltage of 20 kV, as shown in Figure 6. 24c (BF mode) and Figure 6. 24 (STEM mode). Each cluster appears to be composed of several crystals, but the magnification is too small for a precise morphological description of an individual crystal.

These results suggest that the once the inorganic phosphate is released by the bacteria, precipitation of the crystals, which are very likely to be HA, is not bacteria-associated. Hydrolysis of β-GP in the hot solution was precluded since no precipitates was observed in the control. However, this experiment was only carried out once. Further work will be necessary.

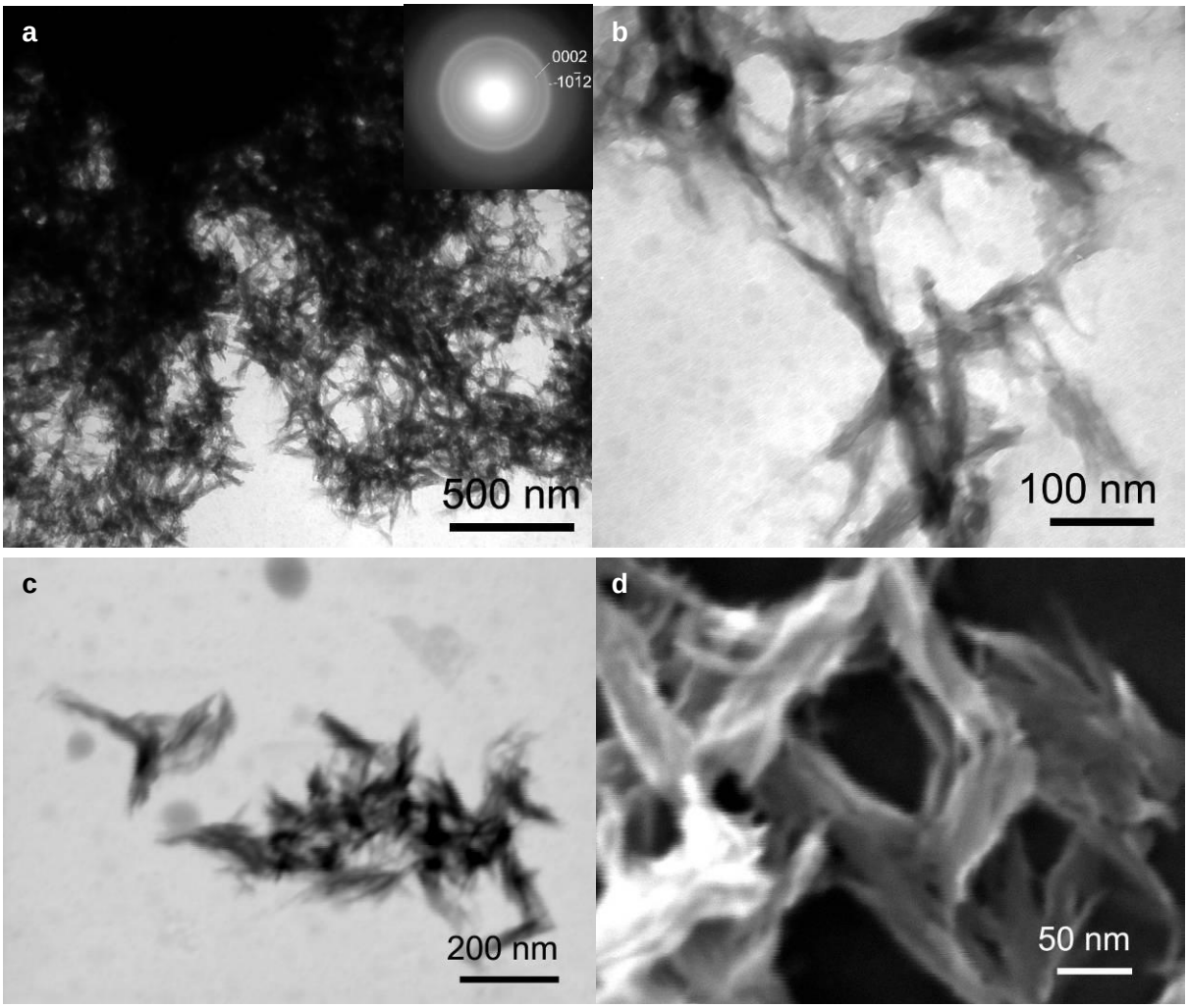

Figure 6. 24 Morphology of the precipitates formed in the filtered solution with the addition of fresh $CaCl_2$

a: TEM BF imaging. The inset picture is the SAD pattern. (TEM, 200 kV)

b: The morphology of the beam sensitive crystals at higher magnification (TEM BF imaging, 80 kV).

c: Crystal morphology (JEOL 7000 SEM, BF mode, 20 kV).

d: Crystal morphology (JEOL 7000 SEM, STEM mode, 20 kV).

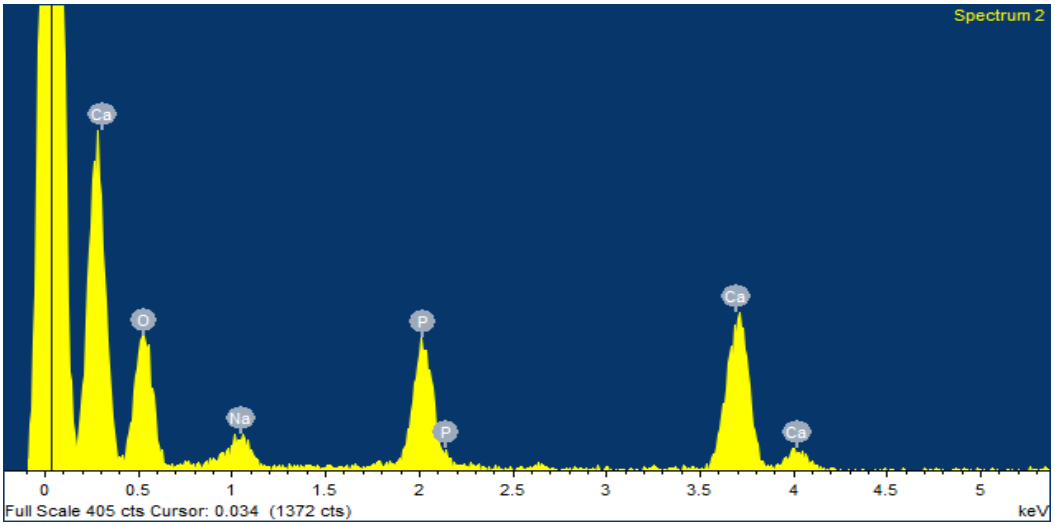

Figure 6. 25 A typical TEM/EDX spectrum of the precipitates in Figure 6. 24 (200 kV)

6.10 Summary

Grit blasting results in a roughened surface with embedded Al_2O_3 particles. The grit blasted surface is severely deformed and consists of a nano-crystalline layer underneath which is a layer deformed via twinning. An alkali treatment produces a surface sodium titanate layer around 1 μm thick, which consists of leaf-like plates standing vertically on the substrate.

Biomineralisation via *Serratia* successfully coats the titanium discs with crystals. Crystals are characterised to be calcium deficient HA containing Na and Cl. Although cracks can be found throughout the coating, an intact attachment of the deposited HA layer to the Ti substrate is achieved. Titanium and the embedded alumina do not affect the precipitation of HA. The alkali treatment does not have any noticeable influence on crystal formation. HA was observed to grow within sodium titanate.

The coating formed via this biomineralisation method is extremely porous, consisting of micro-scale crystal spheres which are in turn built up of nano-scale curved plate-like crystals. The crystal size of these plates is not constant, but tends to be larger at the bottom of the

coating or inside the porous titanium structure and smaller on the surface.

Both the crystal size and the Ca/P ratio of the nascent HA appear to be related to the ion concentration of the mineralisation solution, forming smaller but thicker curved plates (also possibly plates) with lower Ca/P ratio when Ca^{2+} is scarce (2.5 mM) but larger and thinner curved plates with higher Ca/P ratio when phosphate is rare (5 mM).

Although bacteria *Serratia* are closely involved in the liberation of β-GP to provide inorganic HPO_4^{2-} which is used in the precipitation of HA, the latter reaction may be independent of bacteria.

References

1. Thackray AC. Bacterial biosynthesis of a bone substitute material. PhD Thesis. University of Birmingham; 2005.
2. Sammons R, Thackray AC, Ledo HM, Marquis PM, Jones IP, Yong P, Macaskie LE. Characterisation and sintering of nanophase hydroxyapatite synthesised by a species of *Serratia*. Journal of Physics: Conference Series 2007;93:1-7.
3. Kokubo T. Apatite formation on surfaces of ceramics, metals and polymers in body environment. Acta Materialia 1998;46(7):2519-2527.
4. Takadama H, Kim H, Kokubo T, Nakamura T. TEM-EDX study of mechanism of bonelike apatite formation on bioactive titanium metal in simulated body fluid. Journal of Biomedical Materials Research Part B: Applied Biomaterials 2001;57(3):441-448.
5. Jeong BC, Kim HW, Macaskie LE. Phosphotransferase activity of acid phosphatases of a *Citrobacter* sp. FEMS Microbiology Letters 1997;147(1):103-108.
6. Macaskie LE, Bonthrone KM, Yong P, Goddard DT. Enzymically mediated bioprecipitation of uranium by a *Citrobacter* sp.: a concerted role for exocellular lipopolysaccharide and associated phosphatase in biomineral formation Microbiology 2000;146:1855-1867.
7. Macaskie LE, Yong P, Paterson-Beedle M, Thackray AC, Marquis PM, Sammons RL, Nott KP, Hall LD. A novel non line-of-sight method for coating hydroxyapatite onto the surfaces of support materials by biomineralization. Journal of Biotechnology 2005;118(2):187-200.

Chapter 7 Heat treatment of the HA coated titanium discs

With the aim to destroy the biomass and to sinter the crystals, heat treatment was applied to the *Serratia* HA coated titanium discs. Its effect on the coating, substrate and the coating/substrate interface was investigated in this chapter. The specimens were heated at 550 ºC for 3 hours to destroy all the organic components [1] and at 800 ºC to sinter the crystal coating. For heat treatment route 1, the specimens were held at 800 ºC for 5 hours and 10 hours for heat treatment route 2.

7.1 The influence of heat treatment on the HA coating

7.1.1 XRD analysis

XRD analysis shows that after heat treatment at 550 °C for 3 hours and 800 °C for 5 hours, HA changes to sodium calcium phosphate ($Ca_{10}Na(PO_4)_7$) (PDF reference code: 00-045-0339). According to the lattice parameter, its crystallographic structure is very similar to that of β-TCP ($Ca_3(PO_4)_2$, PDF reference code: 00-009-0169), as compared with β-TCP and HA ($Ca_{10}(PO_4)_6(OH)_2$, PDF reference code: 00-024-0033) in Table 7. 1.

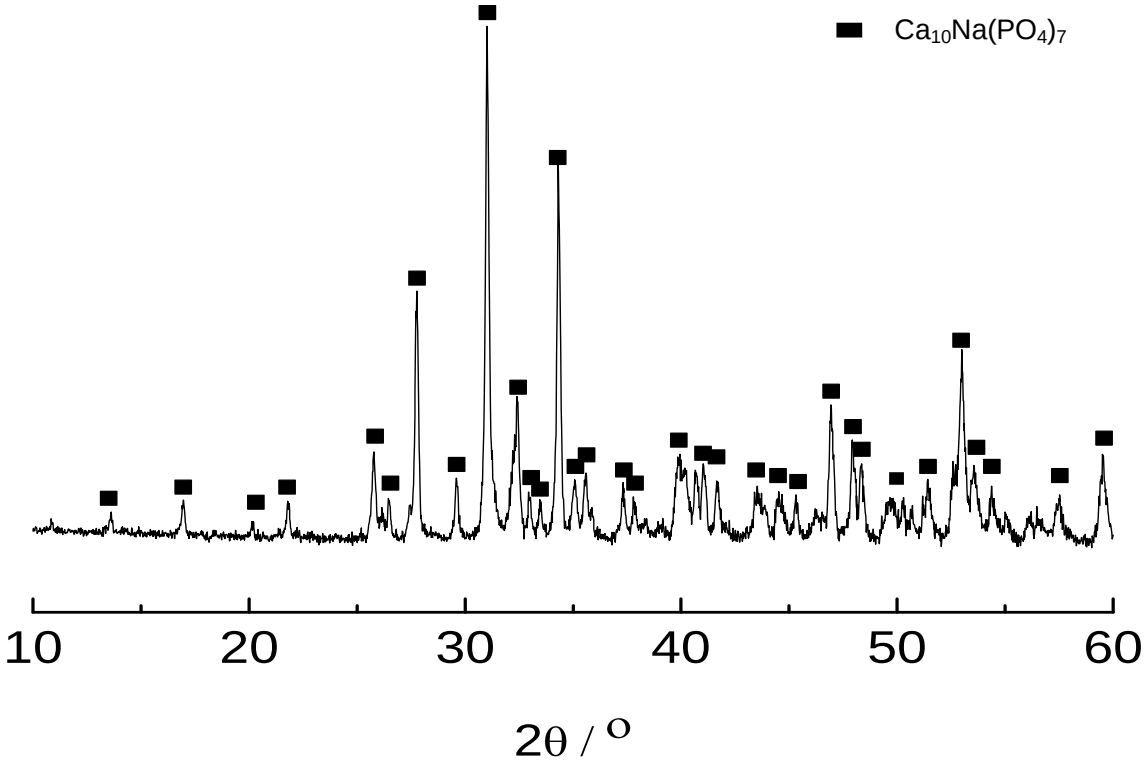

Figure 7. 1 XRD pattern of the heat treated crystals

Table 7. 1 Crystallographic parameters of the heat treated and sintered crystals

Compound	***Space group***	***Lattice parameter*** $(\overset{o}{A})$					
		a	**b**	**c**	**α**	**β**	**γ**
$Ca_{10}Na(PO_4)_7$	R3c	10.4402	10.4402	37.3034	90	90	120
β-TCP	R3c	10.4290	10.4290	37.38	90	90	120
Stoichiometric HA	P63/m	9.4320	9.4320	6.8810	90	90	120

7.1.2 The influence of heat treatment on the coating structure

The coating structure remains intact after the heat treatment (Figure 7. 2a). The crystal clusters are preserved (Figure 7. 2a & e). As in the un-sintered specimens, the coating is still composed of micro-spheres varying in sizes (Figure 7. 2b, d & f), covered by crystal shells (Figure 7. 2d & f). Holes (indicated by the arrows in Figure 7. 2b and Figure 7. 2f) and bacteria-shaped crystals

(Figure 7. 2c) can be found within the coating. After sintering, no apparent difference could be observed between crystal adjacent to titanium (Figure 7. 2g) and those in the bulk (Figure 7. 2f), although the crystal shells found in Figure 7. 2f could be rarely seen in Figure 7. 2g.

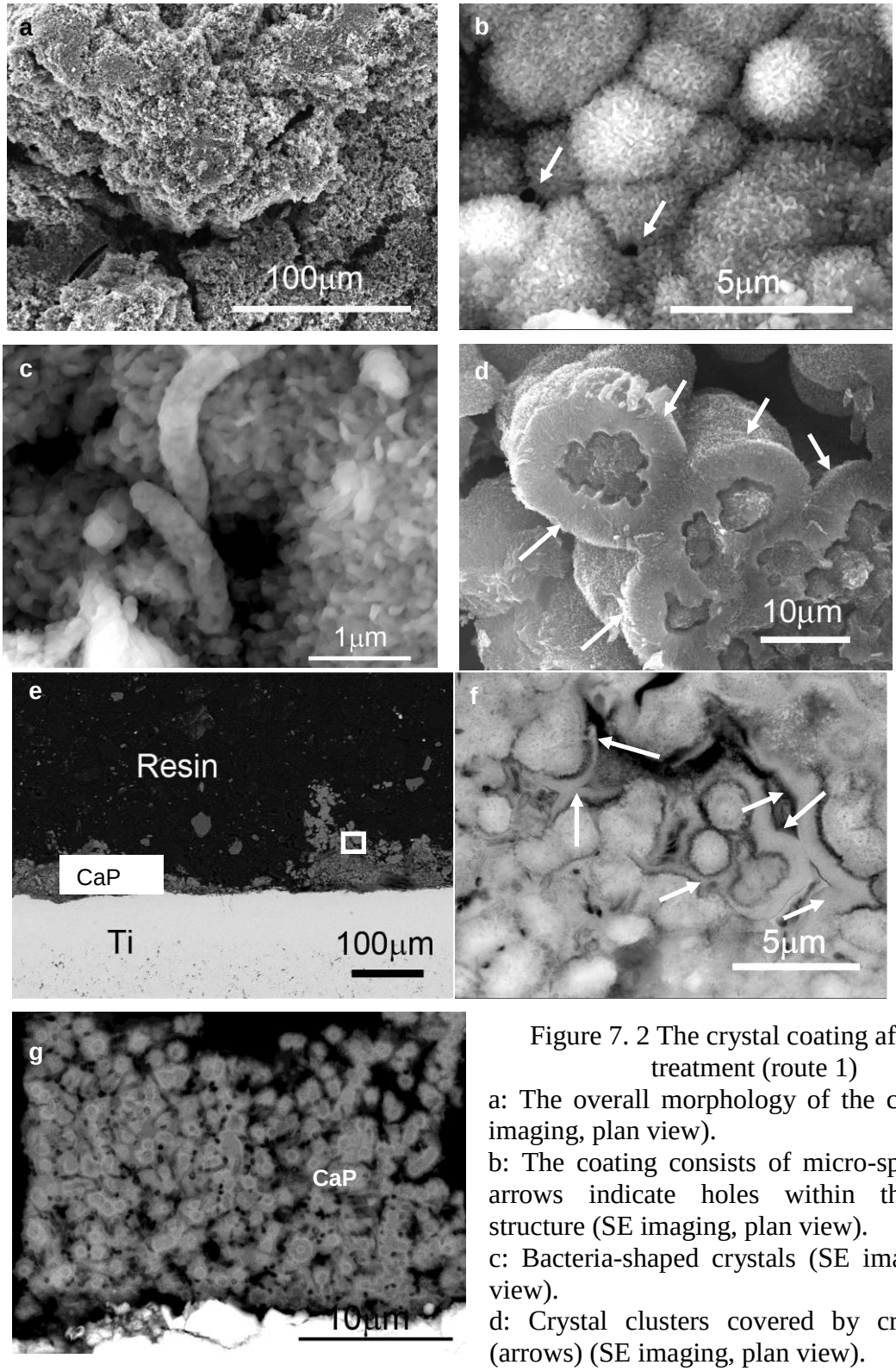

Figure 7. 2 The crystal coating after heat treatment (route 1)

a: The overall morphology of the coating (SE imaging, plan view).

b: The coating consists of micro-spheres. The arrows indicate holes within the coating structure (SE imaging, plan view).

c: Bacteria-shaped crystals (SE imaging, plan view).

d: Crystal clusters covered by crystal shell (arrows) (SE imaging, plan view).

e: The crystal clusters are preserved after the heat treatment (BSE imaging, cross section).

f: The squared site in (e) at higher magnification: crystal spheres covered by crystal shells (arrows) (BSE imaging, cross section).

g: The sintered crystal coating adjacent to titanium surface.

7.1.3 The influence of heat treatment on the coating crystals

Two morphologies are found within the sintered crystals: nano-particles and crystal plates, as illustrated in Figure 7. 3. While the nano-particles are dominant (Figure 7. 3a), crystal plates are quite rare (Figure 7. 3b). These are if present usually found underneath the surface crystals. The crystal size of both the nano-particles and the plates varies considerably, from several tens of nanometres to approximately 1 μm. Increasing the holding time at 800 ºC from 5 hours to 10 hours did not noticeably increase the crystal size, as compared in Figure 7. 3, possibly due to the wide distribution of crystal size before the heat treatment.

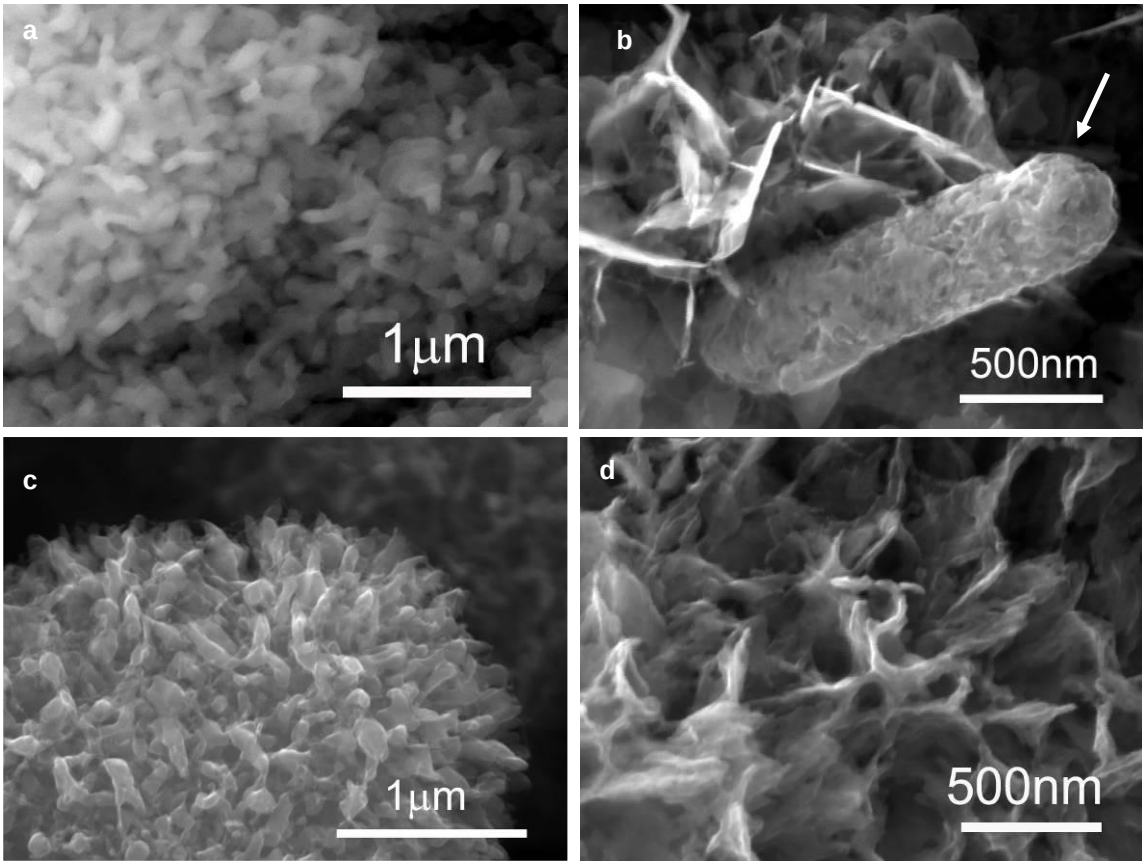

Figure 7. 3 The morphology of the sintered crystals (SE imaging)

a: Nano-particle structure (route 1).

b: Plate- and calcium phosphate-fossilised bacteria (arrow) (route 1).

c: Nano-particle structure (route 2).

d: Curly plate-shaped crystal (route 2).

The sintered crystals were further characterised by TEM. Compared with the nascent crystals, they are more stable when examined by high energy electron beam (200 keV). They are irregular in shape and from approximately several tens of nanometres to around 200 nm in size, as shown in Figure 7. 4. TEM/EDX analysis suggests a Ca/P ratio of 1.16 ± 0.05. The foreign elements such as Na and Cl that were detected in the nascent crystals were preserved after the heat treatment (Figure 7. 5). The Cu shown in the spectrum is from the copper grids

to support the TEM specimen. SAD patterns of the single crystals are consistent with $Ca_{10}Na(PO_4)_7$, as shown by the inset patterns in Figure 7. 4.

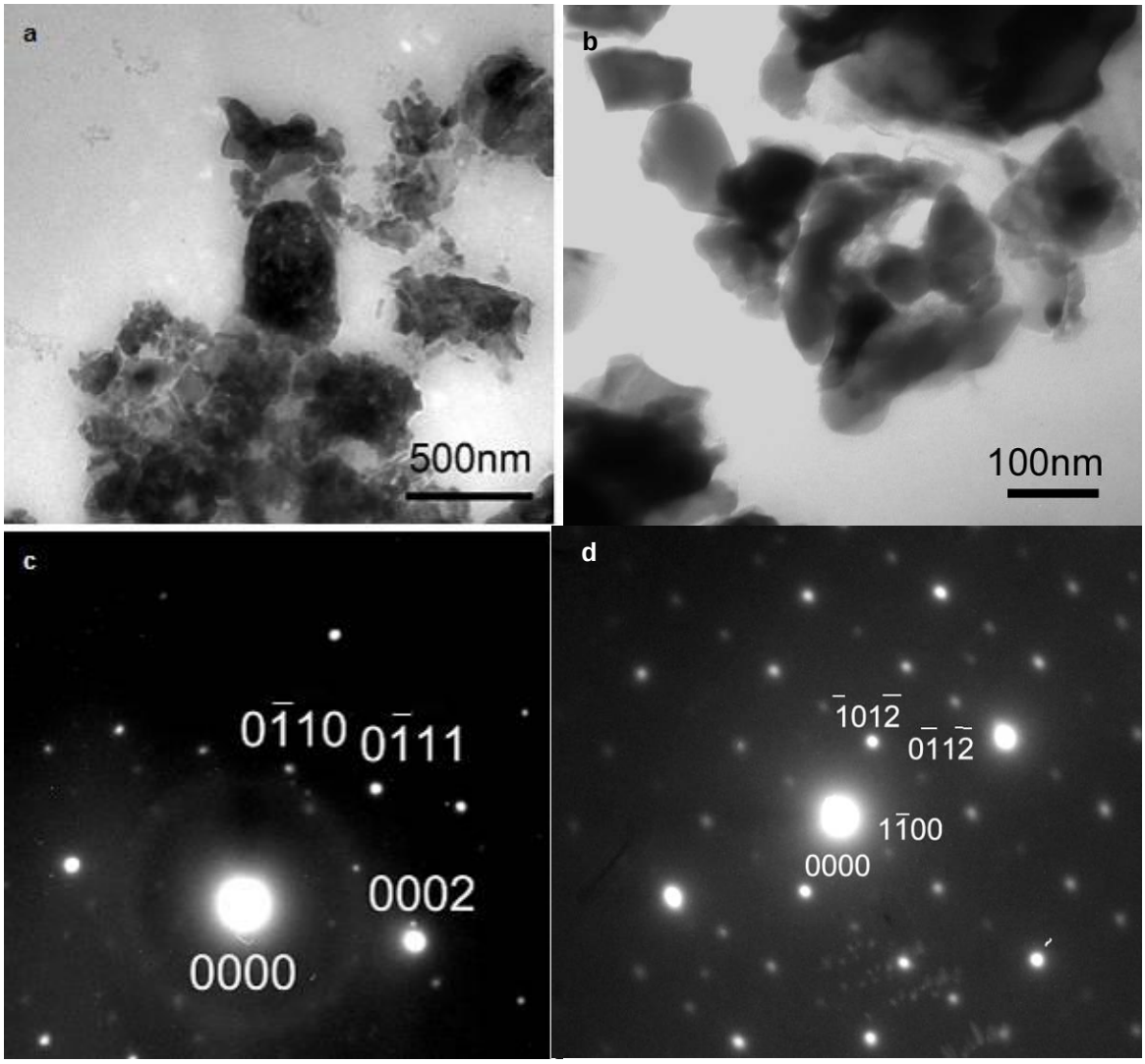

Figure 7. 4 TEM analysis of the sintered crystals (route 1)

a: The morphology of the heat treated crystals (TEM BF imaging, 200 kV).

b: Irregularly-shaped nano-scale crystals at higher magnification (TEM BF imaging, 200 kV) and SAD patterns: (c) & (d). (c): zone axis = $[2\bar{1}\bar{1}0]$; (d): zone axis = $[\bar{2}4\bar{2}3]$

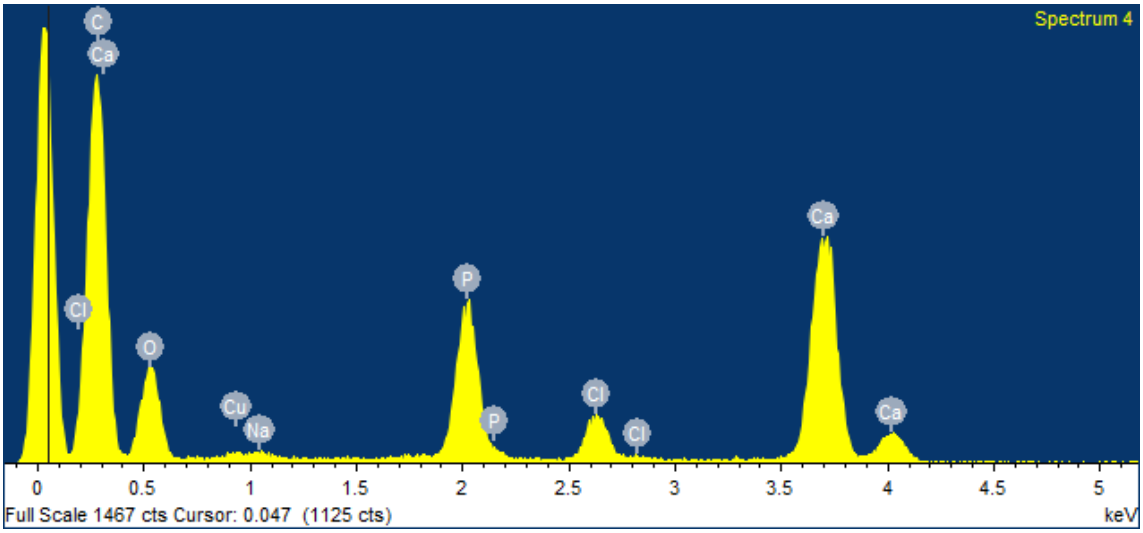

Figure 7. 5 A TEM/EDX spectrum of the heat treated crystals (route 1)

7.2 The influence of heat treatment on coating-Ti interface structure

It is important to study the interface structure of the heat treated specimens because of the potential existence of a complicated transition zone caused by elemental diffusion during heating. Both the substrate and the coating in this region may be affected, showing different features when compared with the bulk structure.

7.2.1 The interface between the sintered coating and the grit blasted titanium substrate

The crystal coating was gently scratched off to reveal the surface of the metal substrate. It is rather rough (Figure 7. 6a), consisting of superfine grains (Figure 7. 6b) with morphologies noticeably different from that of the sintered crystals (Figure 7. 3 and the area within the dotted curve in Figure 7. 6). Compared to the original grit-blasted specimen (Figure 6.1c), the cross section of the sintered sample is very different: the surface layer is porous with holes ranging from a few hundreds of nanometres to around 2 μm, suggesting the existence of a transition layer.

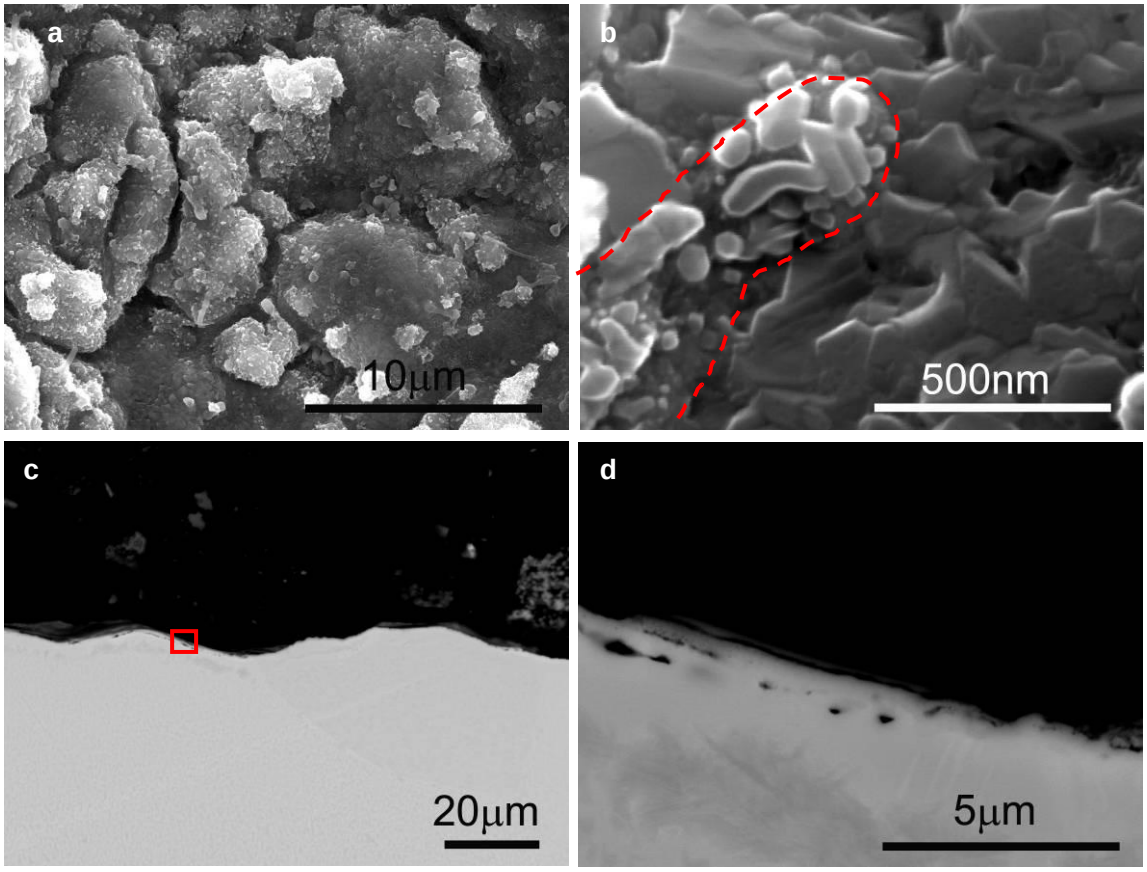

Figure 7. 6 The interface morphology between the sintered coating and the grit blasted titanium substrate (route 1)

a: The overall morphology of the interface (SE imaging, plan view).

b: The interface of the metal substrate consists of nano-scale crystals (SE imaging, plan view). The area circled by the dotted curve is sintered calcium phosphate.

c: BSE imaging of the cross section.

d: The interface has a porous structure (the box in (c), BSE imaging).

The transition layer is confirmed by SEM/EDX elemental maps to be mainly P-rich titanium of around 2 to 3 μm thick, as shown in Figure 7. 7. Note the P-deficient layer (Layer 2) displayed in the P distribution map, suggesting that the P in the P-rich Ti (Layer 3) may mainly diffuse from this P-deficient zone.

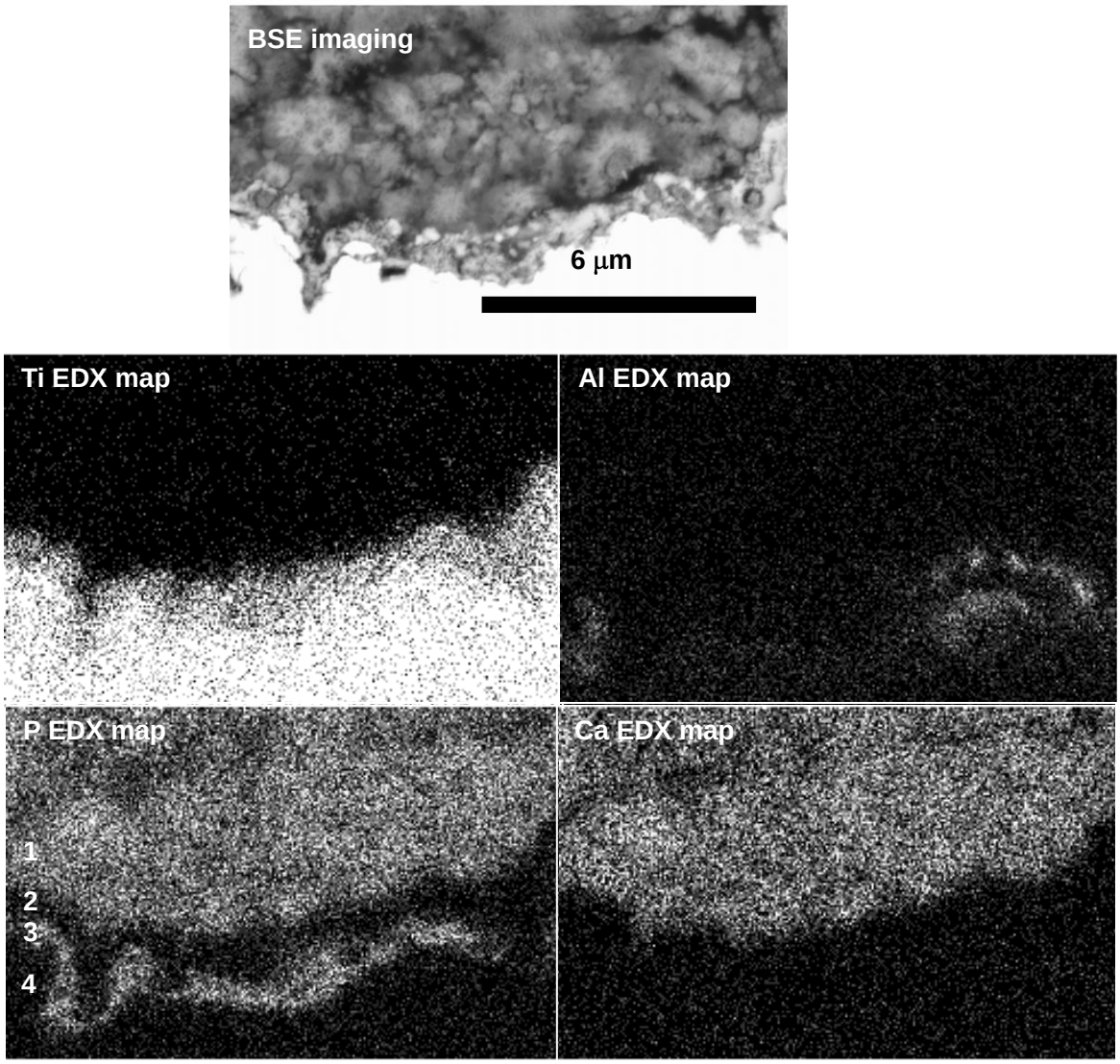

Figure 7. 7 Cross section SEM/EDX elemental maps of the sintered specimen

Layer 1: The sintered calcium phosphate coating. Layer 2: The P-deficient calcium phosphate coating. Layer 3: the P-rich Ti layer. Layer 4: the Ti substrate.

The coating-substrate interface was studied further by TEM. The specimen was prepared by FIB/SEM. Although the crystal structure was preserved after ion thinning, 'curtaining' was severe, producing stripes across the entire specimen as shown in Figure 7. 8a. This might be caused by the high porosity of the coating after sintering. After milling, due to the density difference, when the coating was almost 'transparent' to the electrons, the titanium substrate

was still thick. Nevertheless, it can be observed in Figure 7. 8a & b that the transition layer at the interface is around 1 to 2 μm thick indicated by the double-headed arrow, judging by the morphology changes, and is mainly composed of small particles around 50 nm across (Figure 7. 8c).

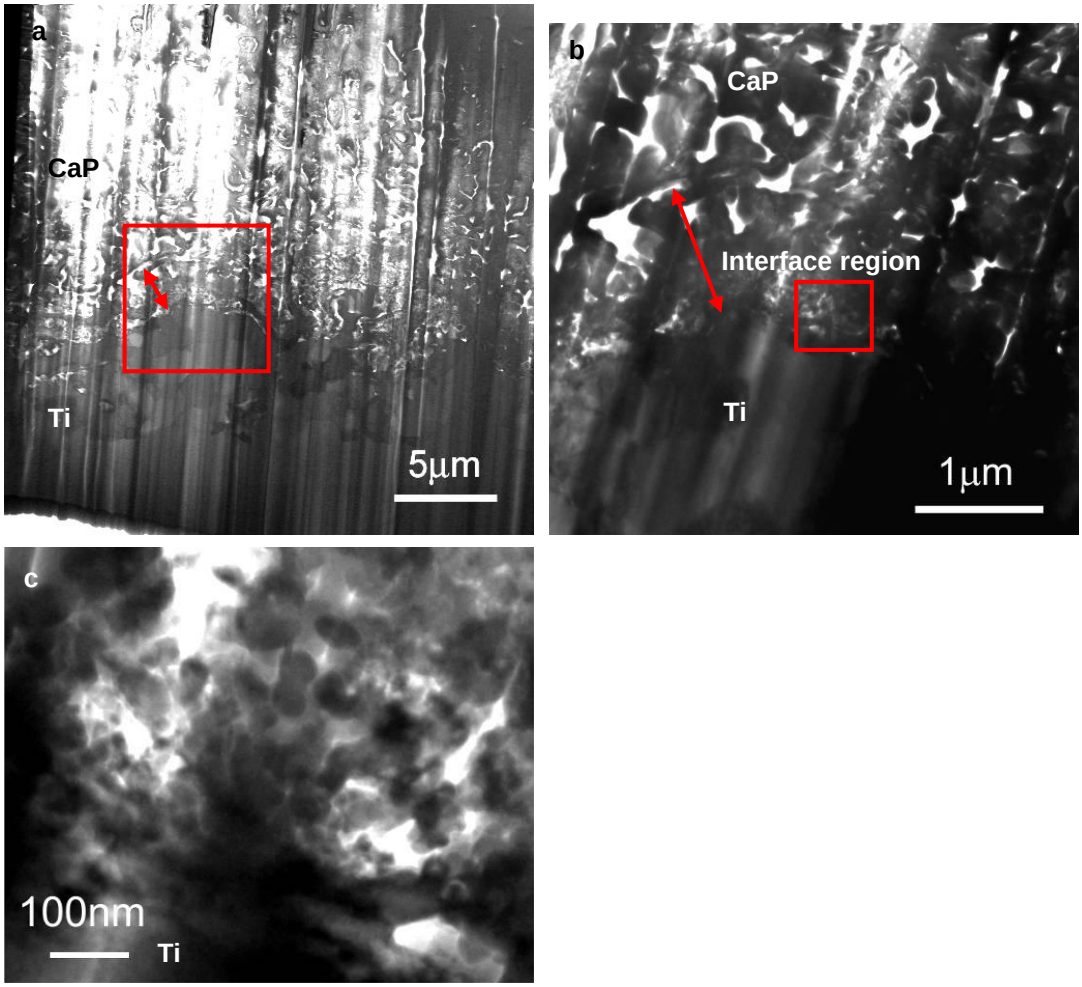

Figure 7. 8 Coating-substrate interface structure (heat treatment: route 1. TEM BF imaging)

a: Curtaining effect due to ion beam milling during sample preparation. The double headed arrow shows the boundaries of the transition layer.

b: The box in (a) showing the transition from the coating to the substrate, with the double headed arrow indicating the interface zone.

c: The interface structure is composed of nano-scale crystals (the box in (b)).

STEM/EDX analysis (Figure 7. 9) showed severe contamination over the entire specimen, especially by Ti, which is detected in areas which should be composed of calcium phosphate alone. This is possibly caused by redeposition during ion milling. The holes within the coating only make it even more difficult to produce a satisfying specimen because of a severe curtaining effect. Unlike the continuous P-rich layer observed using SEM shown in Figure 7. 7, this layer was shown to be discontinuous when studied at higher magnification by TEM, corresponding to the porous structure at the interface. The transition layer was found to be mainly composed of regions of Ti and P-rich Ti, as demonstrated in Figure 7. 9b. The EDX linescan suggests that P can diffuse beyond the Al-rich Ti, possibly through the gaps and cracks at the titanium surface produced during grit blasting. In summary, sintering resulted in an interface region consisting of nano-scale Ti, CaP, Al-rich Ti and P-rich Ti.

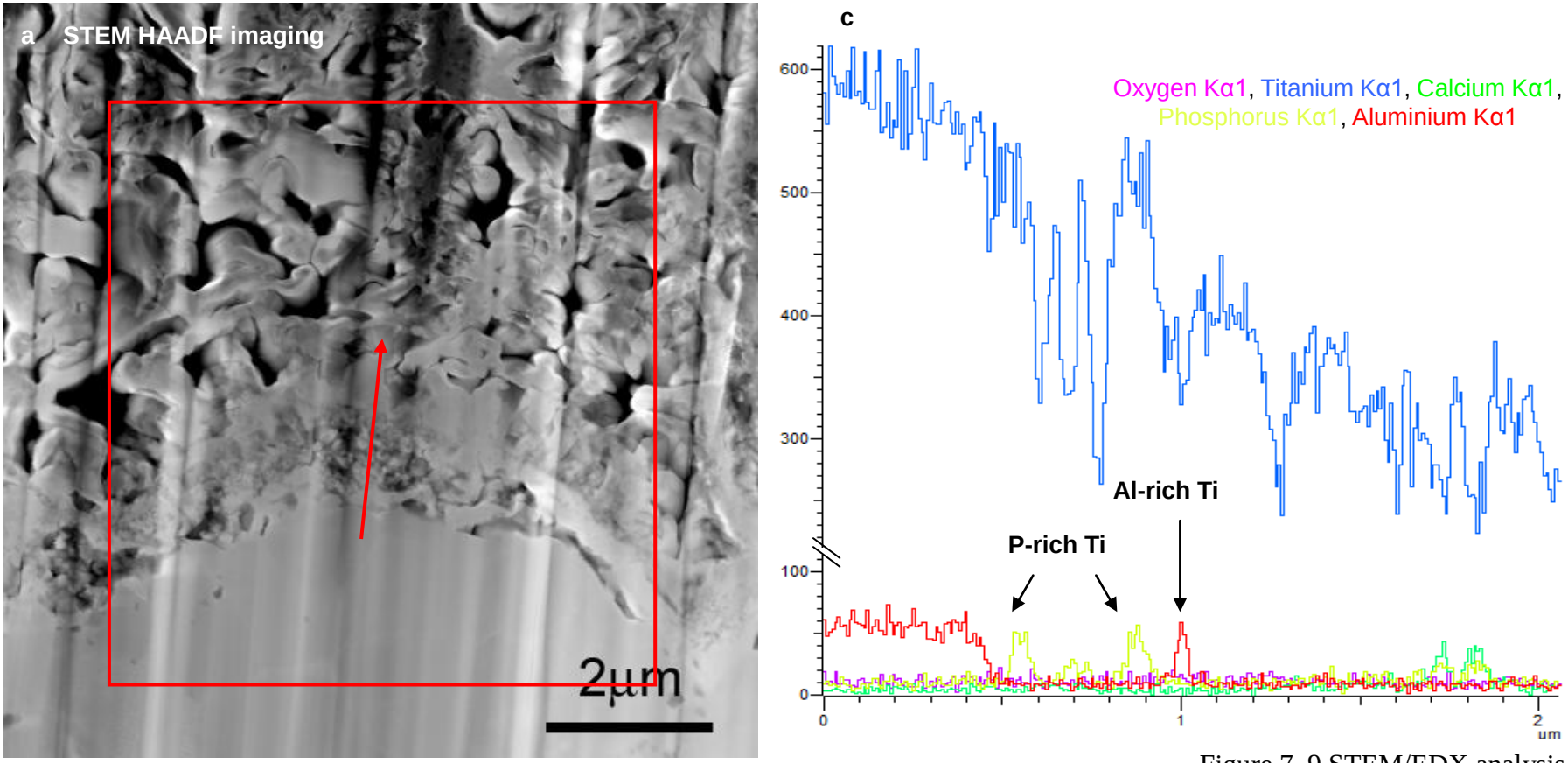

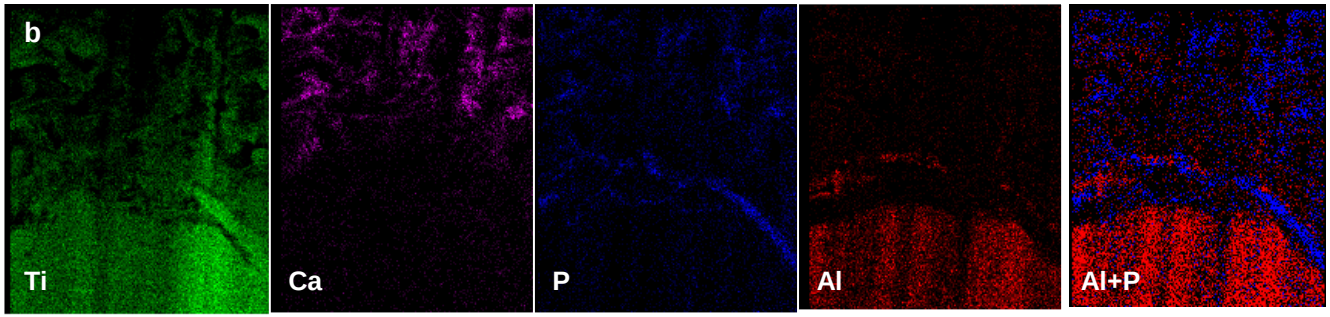

Figure 7. 9 STEM/EDX analysis of the interface after heat treatment (route 1)

(b) is the element maps in the box in (a).

(c) is a linescan along the red arrow in (a).

7.2.2 The interface between the sintered coating and the alkaline treated grit blasted titanium

In samples that were pre-treated with NaOH, after the heat treatment a similar transition layer is observed at the interface. It is also composed of nano-grains (Figure 7. 10b), but these are thicker (around 5 μm) and more porous (Figure 7. 10a, b & d) than those without the alkali treatment (Figure 7. 6). The pores increase in size as they get nearer to the solid substrate (Figure 7. 10d), forming gaps as long as 20 μm, as indicated by the arrows in Figure 7. 10c. Neither the sodium titanate layer nor the embedded Al_2O_3 particles are visible after the heat treatment.

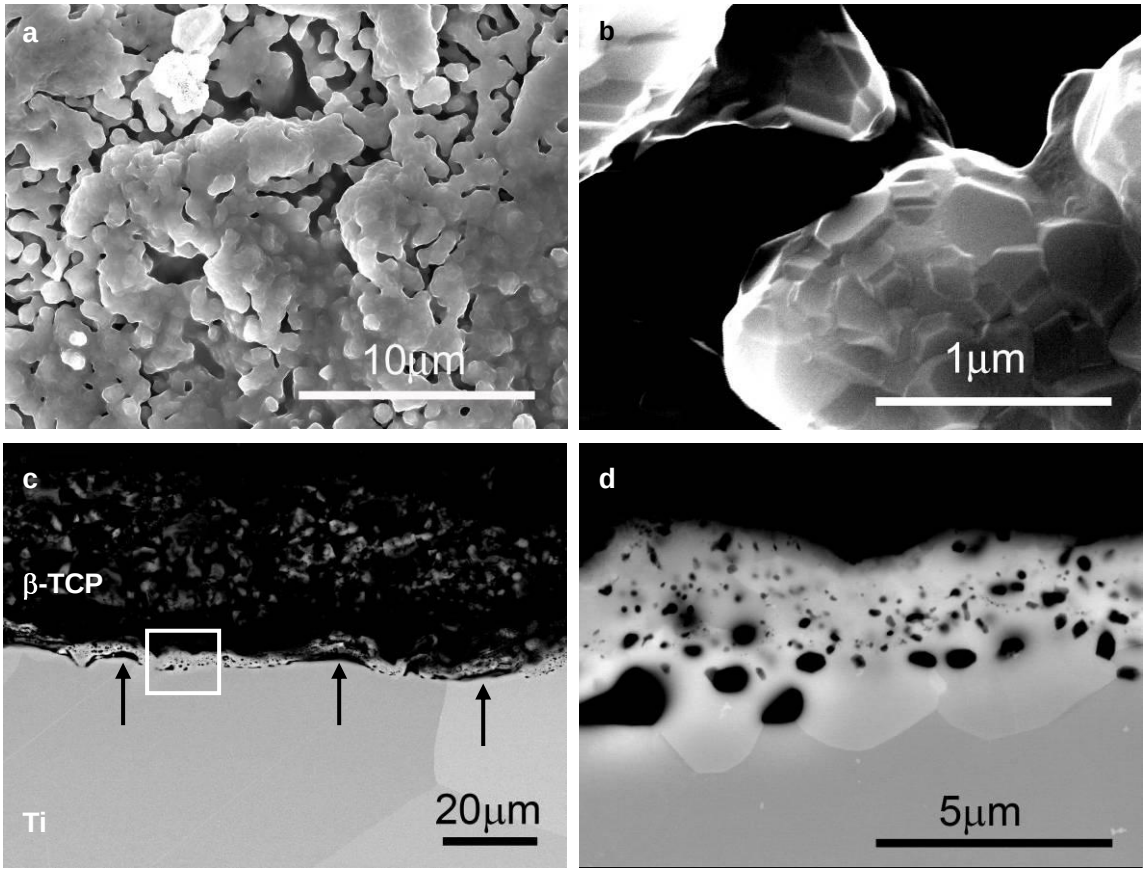

Figure 7. 10 The interface between the sintered coating and the alkaline treated grit blasted titanium (route 1)

a: The interface is porous (SE imaging, plan view).

b: The transition layer is composed of nano-grains (SE imaging, plan view)

c: BSE imaging of the cross section.

d: The porous interface at higher magnification (BSE imaging of the box in (c)).

Similar to Figure 7. 9, the interface here is also a complicated structure composed of Ti, Al-rich Ti and P-rich Ti (1, 2, 3 in Figure 7. 11, respectively). Note that P can diffuse beyond the Al-rich Ti layer, resulting in localised P-rich titanium, as indicated by the red arrows in Figure 7. 11.

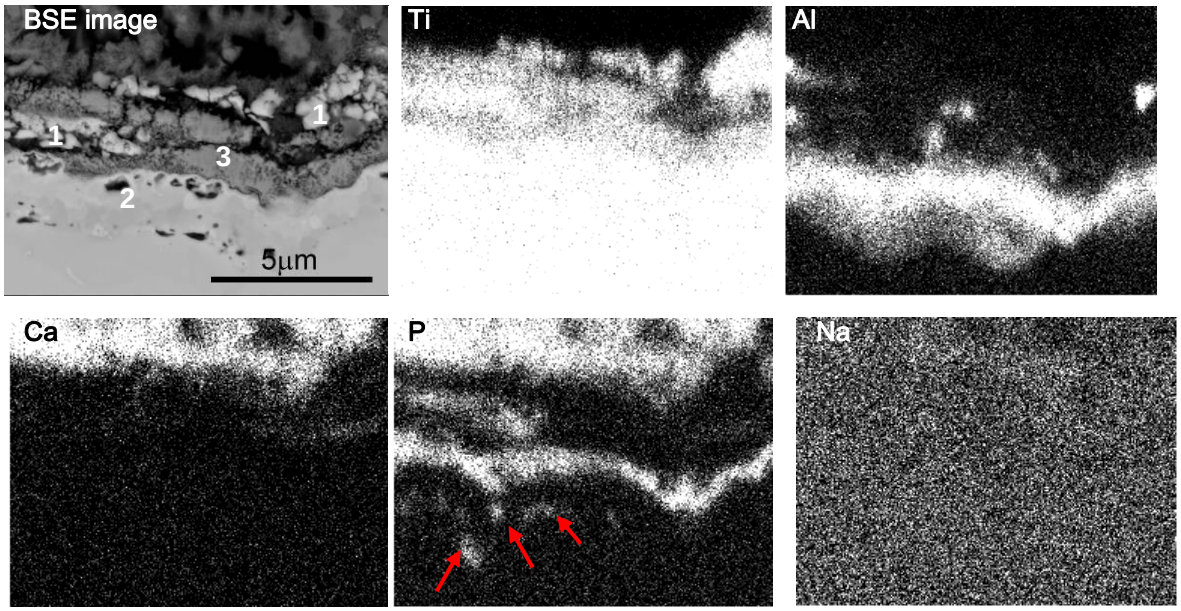

Figure 7. 11 Cross section SEM/EDX elemental maps of the sintered specimen (alkali-treated) (1: Ti. 2: Al-rich Ti. 3: P-rich Ti. The red arrows indicate the phosphorus rich region beneath the Al-rich Ti layer.)

7.3 The influence of heat treatment on the titanium substrate

Heat treatment leads to significant crystal growth in the substrate, as illustrated in Figure 7. 12: 20-70 μm in the un-treated specimen, 100-300 μm when the specimen is heated to 800 ºC and held for 5 hours (heat treatment route 1), and almost 500 μm if the time is increased to 10 hours (heat treatment route 2).

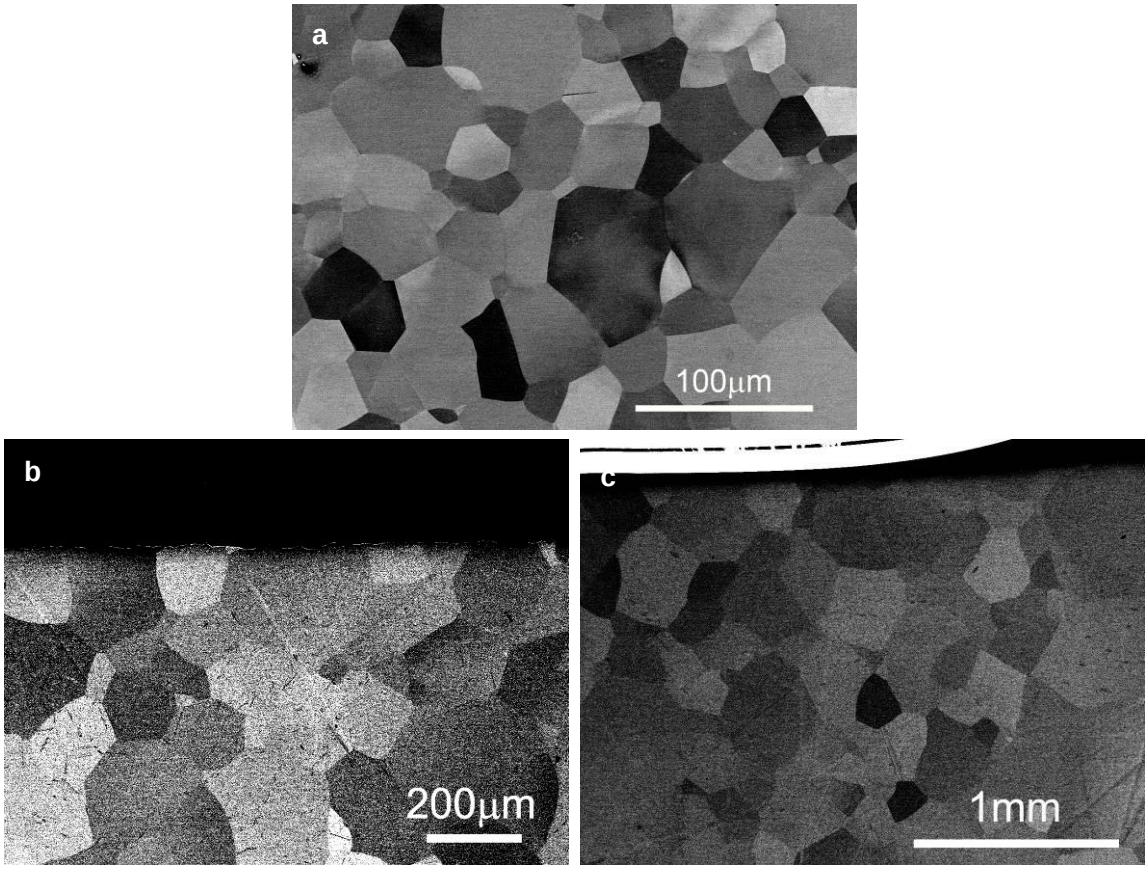

Figure 7. 12 The influence of heat treatment on substrate crystal size (BSE imaging)

a: The grain size of the un-treated titanium substrate.

b: The grain size of the titanium substrate after heat treatment route 1.

c: The grain size of the titanium substrate after heat treatment route 2.

(Note that (a), (b) and (c) are at different magnifications, ×500, ×100, ×43, respectively.)

7.4 Summary

After the heat treatment, HA decomposes to mainly $Ca_{10}Na(PO_4)_7$, a structure closely resembling β-tricalcium phosphate, as confirmed by both XRD and TEM. The crystal coating structure is not altered much, although most of the nano-plate-shaped crystals change to irregular nano-particles. No noticeable crystal size change can be observed when the heat treatment duration at 800 ºC was increased from 5 hours to 10 hours, although the crystal size

of the titanium substrate is significantly increased.

An interface composed of Ti, P-rich Ti and Al-rich Ti can be observed between the calcium phosphate coating and the titanium substrate and is attributed to diffusion of P and Al during heat treatment. Instead of being solid, this layer is porous, consisting of nano-scale crystals. This phenomenon is more profound if the substrate is pre-treated with alkali, yielding an interface that is both thicker and more porous.

Reference

1. Thackray AC. Bacterial biosynthesis of a bone substitute material. PhD Thesis. University of Birmingham; 2005.

Chapter 8 Biomineralisation of HA on titanium webs

8.1 Biomineralisation of a thick HA coating on the titanium web

Because of the motility of bacteria in an aqueous environment, biofilm can form on the walls inside a porous structure, such as observed in § 4.2. This phenomena inspired a non line-of-sight method to coat porous scaffolds with hydroxyapatite through *Serratia* biomineralisation [1]. This was used by Thackray *et al.* (2004) to coat a polyurethane foam in order to produce a porous calcium phosphate bone-substitute material [2]. On the other hand, porous titanium grafts and titanium with porous surfaces are increasingly popular as orthopedic and dental implants [3]. Compared with solid grafts, protein absorption, cell adhesion and bone ingrowth can be significantly promoted on a porous surface [4, 5]. So far, the most successful methods to apply HA coatings on porous titanium structures include the simulated body fluid (SBF) biomimetic method and electrochemical deposition [6]. In this section, the possibility to apply HA coatings on porous Ti using bacterial biomineralisation was tested. The experiments in this part were repeated twice, with three samples in each experiment.

8.1.1 Coating structure

In this section, *Serratia* biofilm was pregrown on the Ti web in an air-lift fermenter as described in § 2.2.2. After fermentation, the webs were transferred into a bioreactor and biomineralisation was allowed for 10 days in total, as described in § 2.3.2.

After mineralisation, the entire titanium web was covered by a porous coating, as seen in Figure 8. 1a. The coating consisted of microspheres (Figure 8. 1b). The surface crystals were scratched off to reveal the inner structure (Figure 8. 1c). This also consisted of crystal spheres

(Figure 8. 1d), but they were slightly larger (20-30 μm) than those outside (around 10 μm diameter).

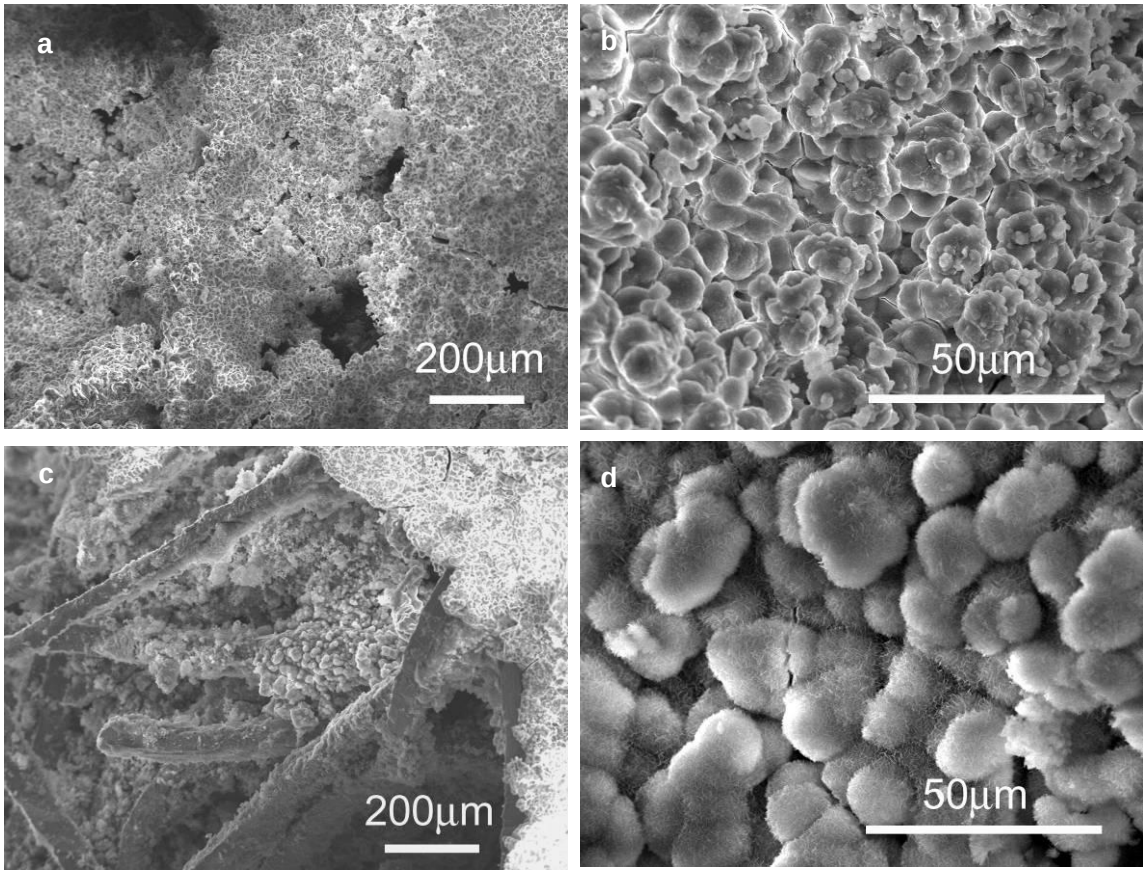

Figure 8. 1 Biomineralisation of thick HA on porous titanium webs (SE imaging)

a: The overall morphology of the HA coated Ti web.

b: The coating is composed of micro-spheres.

c: The morphology of the crystal coating inside the structure. (The matrix was pressed gently to get rid of the outer crystals.) The linear structures are the crystal coated Ti wires.

d: The crystals inside also form microspheres. Note that they are much larger than the ones on the surface of the webs (b).

Micro X-Ray CT was used to analyse the distribution of the crystals within the system and to reconstruct the coating. The entire metal system is very well coated, as shown in Figure 8. 2a.

The magenta part represents HA while the blue fibres are the titanium hidden inside. The coating is considerably porous, consisting of crystal clumps (Figure 8. 2c). HA has also formed within the structure and the crystals fill almost all the gaps within the porous matrix (Figure 8. 2b & d) so that the porosity of the system is significantly reduced, when comparing Figure 8. 2 with Figure 4. 12.

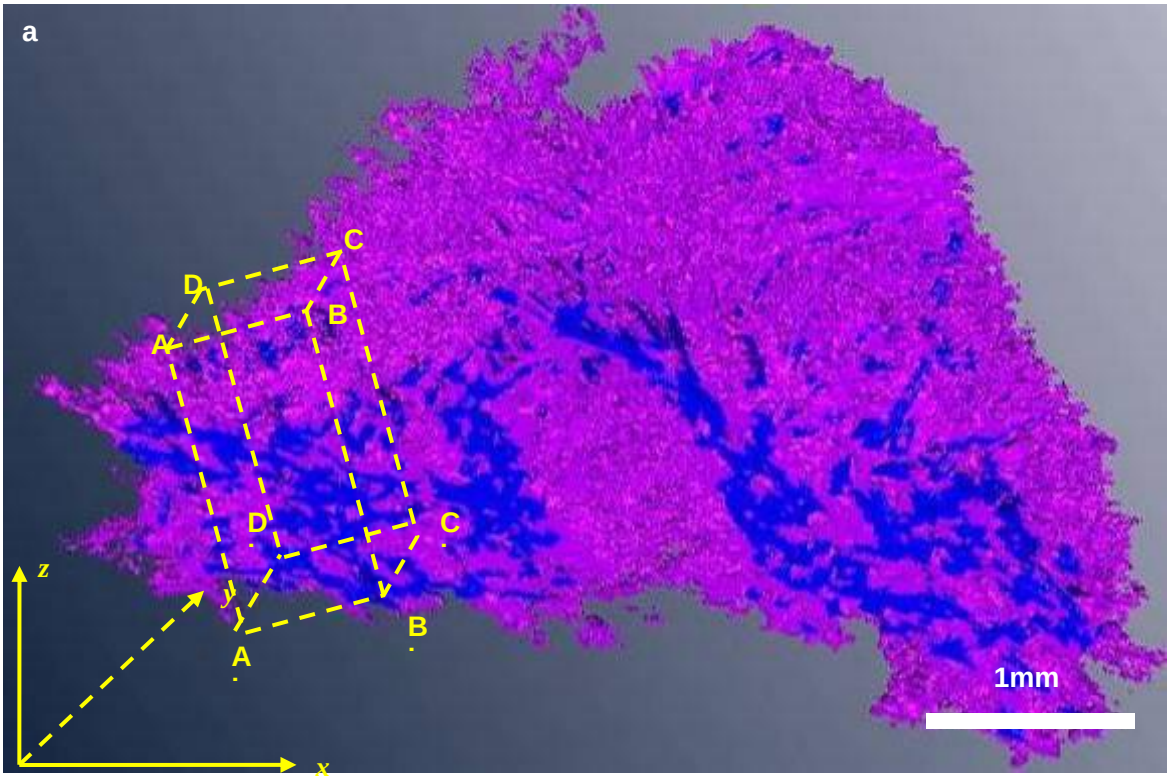

Figure 8. 2 3D reconstruction of the HA (magenta) coated porous titanium web (blue) using micro X-ray CT

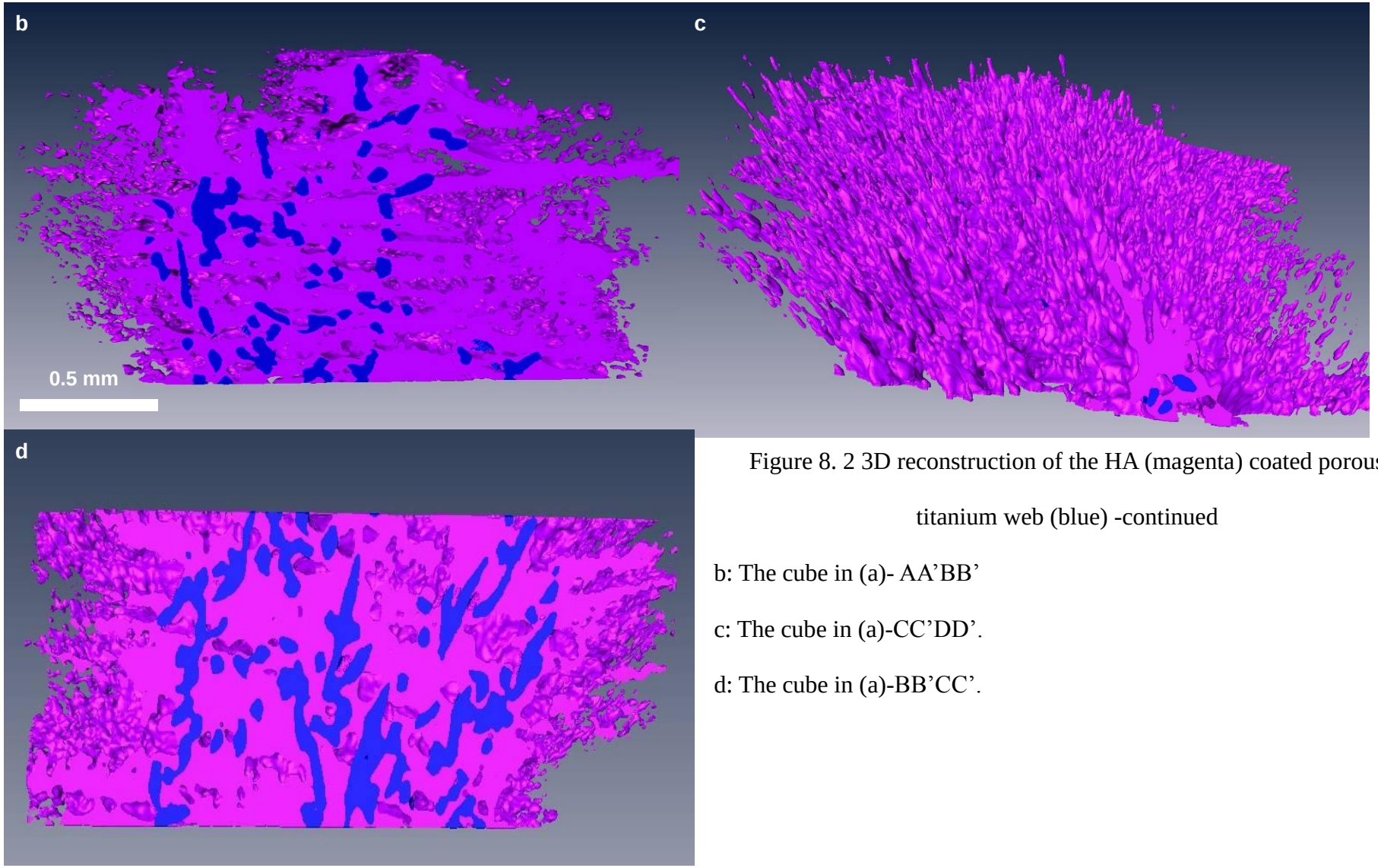

Figure 8. 2 3D reconstruction of the HA (magenta) coated porous titanium web (blue) -continued

b: The cube in (a)- AA'BB'

c: The cube in (a)-CC'DD'.

d: The cube in (a)-BB'CC'.

8.1.2 Crystal morphology

The crystal morphology found within the HA/Ti web system was similar to that on the HA coated Ti disc: HA with different crystal sizes. While the crystals formed on the very surface of the structure were extremely small (Figure 8. 3a & b), those underneath this layer were much larger and often in the shape of curved plates, as seen in Figure 8. 3c & d.

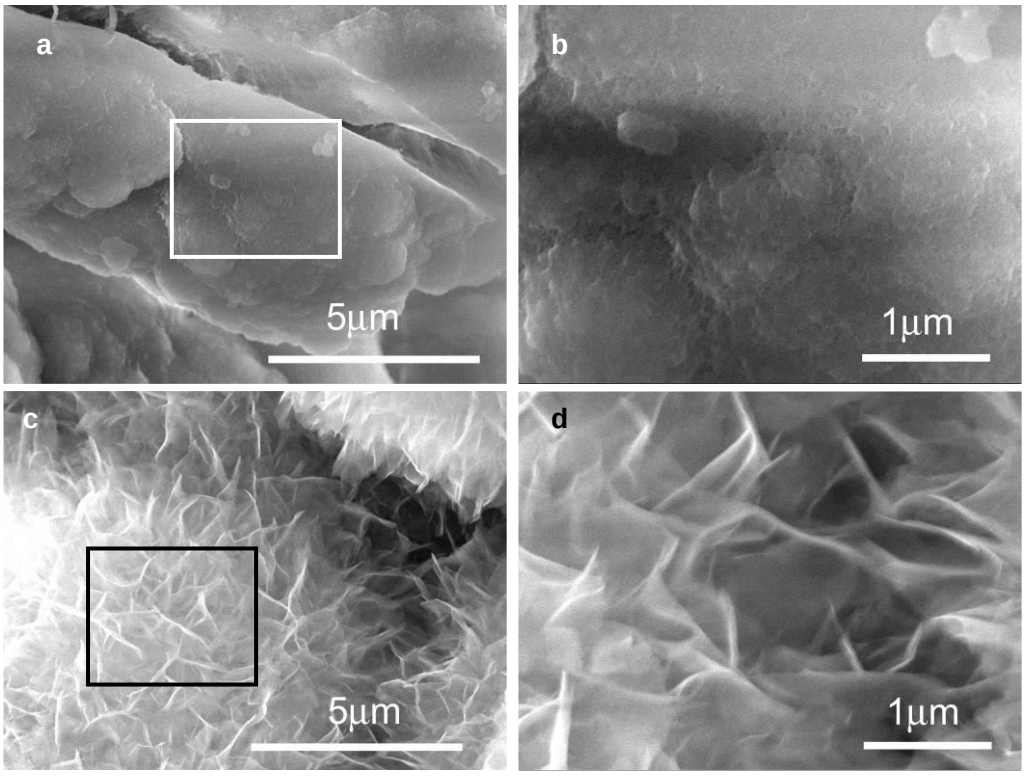

Figure 8. 3 Morphology of the HA crystals formed on a titanium web (SE imaging)

a: Extremely fine crystals, mainly found at the outside of the HA/Ti web system. .

b: The squared site in (a) at higher magnification.

c: Curved plate-like crystals, mainly found inside.

d: The squared site in (c) at higher magnification.

8.1.3 The sintered HA coating

The nascent HA coated Ti webs were sintered following heat treatment route 1 in § 2.3.4. The argon protected furnace was ramped to 550 ºC at 5 ºC/min and held for 3 hours before it was heated to 800 ºC and held for another 5 hours.

The morphology of the sintered Ti web is shown in Figure 8. 4. Although there was significant crystal loss when compared with the nascent structure before sintering (Figure 8. 1a), the remaining crystal coating was still thick enough to cover each Ti wire (Figure 8. 4a). The coating was porous, with cracks frequently observed, as shown in Figure 8. 4b.

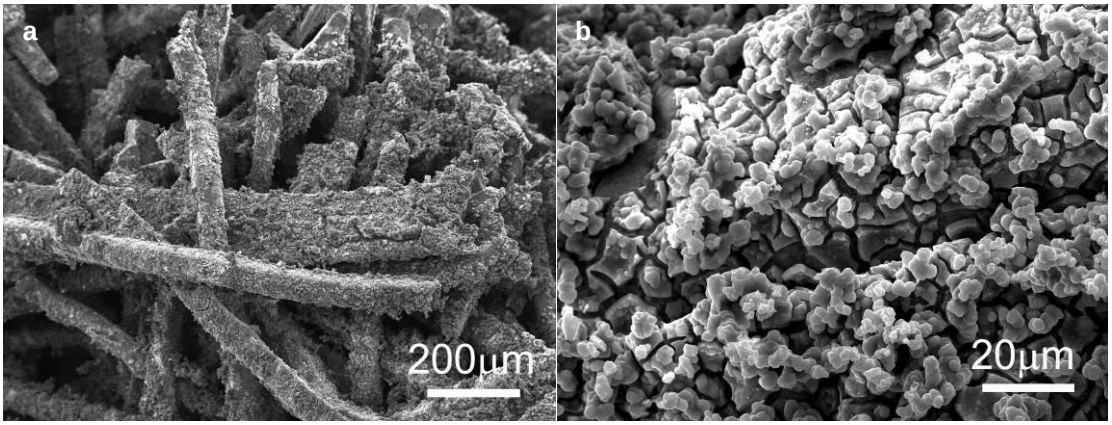

Figure 8. 4 The sintered thick HA coated Ti web

a: The overall morphology of the HA coated Ti web after sintering.

b: Cracks were observed throughout the remaining coating.

8.2 Biomineralisation of a thin HA coating on the titanium web

As shown in § 8.1, when the *Serratia* biofilm was prepared in the fermenter, a thick HA coating was achieved on the porous Ti web. For a thinner crystal coating, a thinner biofilm is necessary. Therefore, instead of incubating the Ti web in the air-lift fermenter, it was suspended in secondary *Serratia* culture diluted with minimal medium (20 ml bacterial

culture in 180 ml minimal medium) in a flask. The flask was incubated in a shaking incubator (150 rpm) at 30°C for 72 hours. The Ti web was then transferred into the bioreactor for biomineralisation as described in § 2.3.2. The experiment in this section was carried out only once, with two samples investigated.

8.2.1 Serratia biofilm

The biofilm formed on the Ti web in this manner is shown in Figure 8. 5. It was much thinner than that formed in the air-lift fermenter (Figure 4. 13), especially than the biofilm at the periphery of the Ti web (Figure 4. 13c & d). The individual *Serratia* cells were shorter as well when comparing Figure 8. 5b and Figure 4. 13f. Nevertheless, bacteria were still able to form bacterial bridges across different Ti fibers. This bridge was a loose connection of bacterial cells and residual polymer threads, as shown in Figure 8. 5c &d.

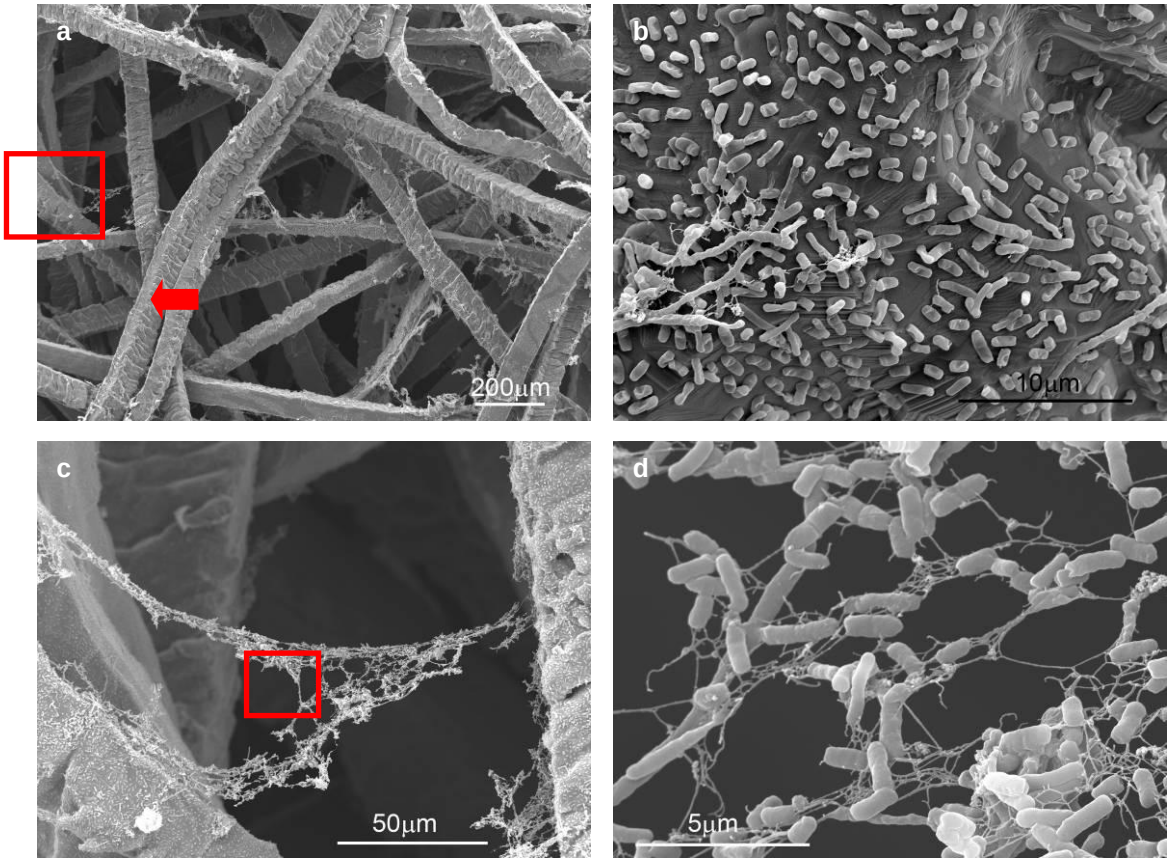

Figure 8. 5 3-day old *Serratia* biofilm formed on Ti web in a flask

a: The overall morphology. Biofilm is thinner than the 5-day old *Serratia* biofilm formed on Ti web in an air-lift fermenter (Figure 4. 13)

b: The arrowed site in (a) showing the formation of a mono-bacterial layer on the surface of the Ti fibre.

c: The rectangular in (a) at higher magnification showing the formation of a 'bacterial bridge' across two far separated Ti wires (approximately 100 μm).

d: The rectangle in (c) at higher magnification showing the bacterial bridge which is a network of *Serratia* cells extracellular polymer material.

8.2.2 The nascent HA coating

This thin layer of *Serratia* biofilm was adequate to produce a thinner HA coating, as shown in

Figure 8. 6. The individual Ti wires with HA coating were clearly seen without the crystal shell observed in Figure 8. 1a. However, the crystal coating was not even, with thickness ranging from 10 to 20 μm (Figure 8. 6b) to approximately 1 μm (Figure 8. 6c). Cracks were common features, as indicated by the arrows in Figure 8. 6b & c. The HA crystals were similar as those in Figure 8. 3c, mainly being curved plates (Figure 8. 6d).

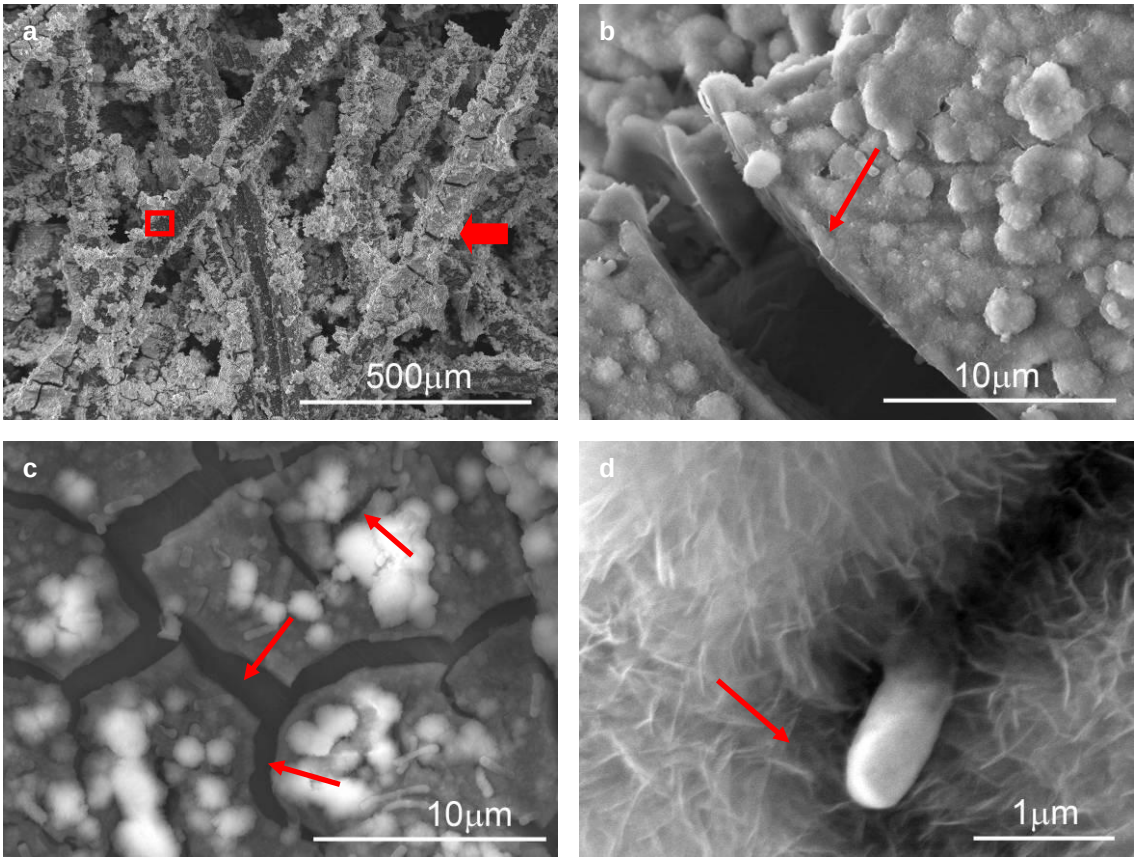

Figure 8. 6 Biomineralisation of thin HA coating on a porous titanium web with 3-day old *Serratia* biofilm pregrown in a flask

a: The overall morphology of the HA coated Ti web.

b: The arrowed site in (a) at high magnification showing a thicker coating of approximately 10 μm. The coating is composed of micro-spheres. The arrow points to a crack within the coating.

c: The rectangle in (a) at high magnification showing the morphology of a thinner coating.

d: The morphology of the curved plate-shaped HA crystals within the coating. The arrow points to a *Serratia* bacterium.

8.2.3 The sintered HA coating

This HA coated porous titanium web was sintered following heat treatment route 1 described

in § 2.3.4, and the morphology of the sintered web was displayed in Figure 8. 7. The coating was preserved well after the heat treatment. This was confirmed further by an EDX elemental map of the cross section of the specimen (Figure 8. 8), which demonstrated the existence of a thin calcium phosphate layer surrounding the titanium wires. Cracks were commonly observed. However, they may not form entirely during sintering, as they were also seen on the unsintered sample as shown in Figure 8. 6d.

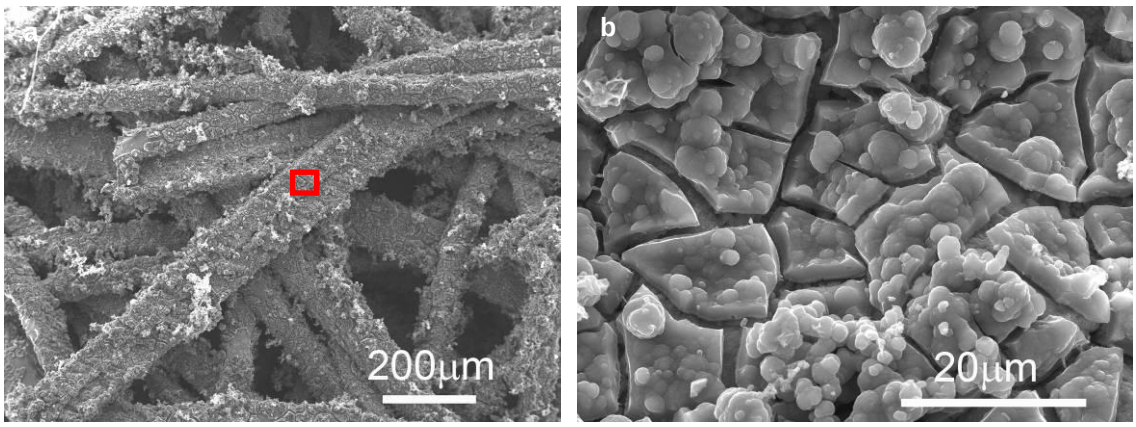

Figure 8. 7 The morphology of the thin HA coated Ti web after sintering

a: The overall morphology of the sintering Ti web.

b: The rectangular site in (a) at higher magnification showing that the coating was preserved after the heat treatment.

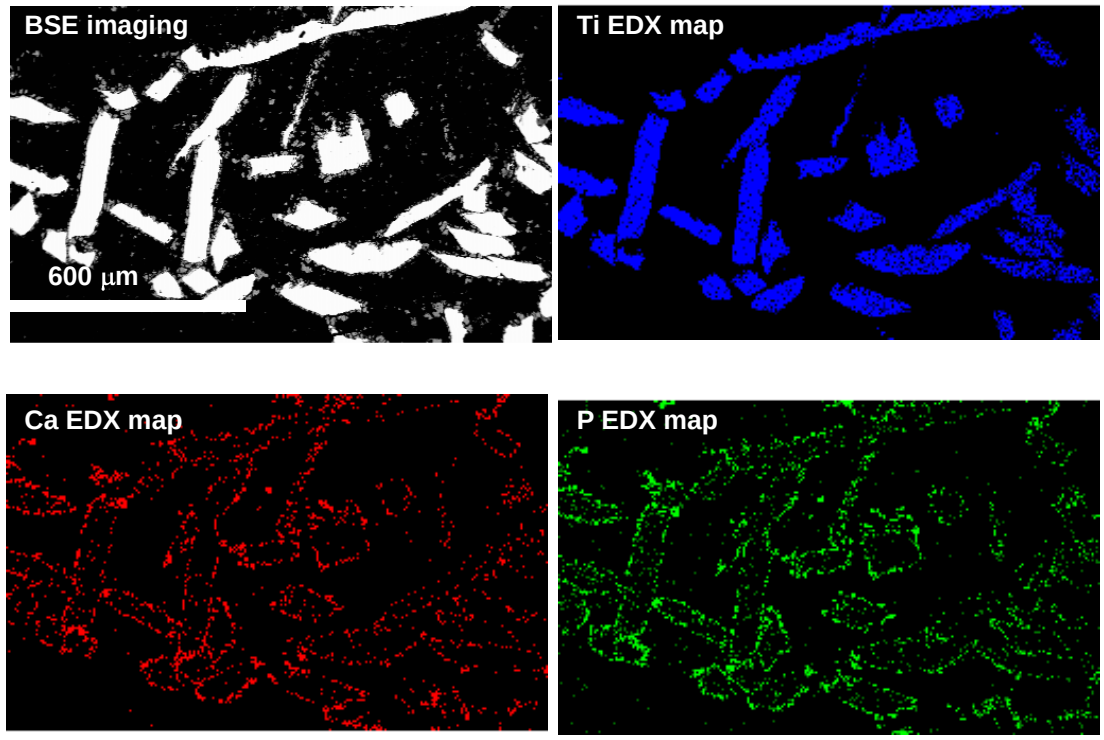

Figure 8. 8 SEM/EDX elemental map of the sintered HA coated Ti web: cross section

8.3 Summary

Biomineralisation via *Serratia* was successfully applied to form HA coatings with various thicknesses on a porous titanium web. The coating consisted of micro-scale spheres which were composed of nano-crystals.

When the biofilm was prepared in an fermenter following the method described in previous studies [1], a thick HA coating was achieved. Using Micro X-ray CT, it was observed that due to this thick layer of crystal, the porosity of the structure was significantly decreased. The coating was thicker at the periphery of the supporting structure, forming a crystal shell covering the entire scaffold. This crystal shell was destroyed when it was sintered at 800 ^{o}C for 5 hours. However, a thinner crystal coating was preserved around the Ti wires. This remaining crystal coating was not smooth, but were rather course and with the existence of

cracks.

The 3-day old *Serratia* biofilm on the Ti web prepared in a flask was much thinner than that formed in the fermenter (5-day old). Only a monolayer of bacteria was observed on the Ti surface. Bacterial bridges were also present, which were a loose network of bacterial cells and residual polymer threads.

The crystal coating formed on the Ti web with a 3-day old biofilm pregrown in a flask was much thinner than that with a 5-day old biofilm prepared in the fermenter. The coating was not even, with a thickness ranging from 1μm to approximately 20 μm. This coating was preserved well after sintering, although cracks were quite common.

References

1. Macaskie LE, Yong P, Paterson-Beedle M, Thackray AC, Marquis PM, Sammons RL, Nott KP, Hall LD. A novel non line-of-sight method for coating hydroxyapatite onto the surfaces of support materials by biomineralization. Journal of Biotechnology 2005;118(2):187-200.
2. Thackray A, Sammons R, Macaskie L, Yong P, Lugg H, Marquis P. Bacterial biosynthesis of a calcium phosphate bone-substitute material. Journal of Materials Science: Materials in Medicine 2004;15(4):403-406.
3. Geetha M, Singh AK, Asokamani R, Gogia AK. Ti based biomaterials, the ultimate choice for orthopaedic implants - A review. Progress in Materials Science 2009;54(3):397-425.
4. Jansson E, Tengvall P. Adsorption of albumin and IgG to porous and smooth titanium. Colloids and Surfaces B: Biointerfaces 2004;35(1):45-51.
5. Li JP, Habibovic P, van den Doel M, Wilson CE, de Wijn JR, van Blitterswijk CA, de Groot K. Bone ingrowth in porous titanium implants produced by 3D fiber deposition. Biomaterials 2007;28(18):2810-2820.
6. Zhang Q, Leng Y, Xin R. A comparative study of electrochemical deposition and biomimetic deposition of calcium phosphate on porous titanium. Biomaterials 2005;26(16):2857-2865.

Chapter 9 Discussion - biomineralisation on titanium

Bacterial biomineralisation has been widely investigated for applications such as waste recycling [1], energy fuels [2] and various powder productions [3]. In this study, its ability as a coating method studied is described systematically in Chapter 6 to Chapter 8 and the results are discussed in this chapter.

9.1 Biosynthesis of crystalline HA

The biomineralisation of HA via *Serratia* bacteria is a process that still merits extensive investigation. Some of the aspects are discussed in this section. The properties of the biosynthesised HA are discussed, with respects to their morphology, chemical composition and crystal structure. Potential factors such as solution ion concentration that could influence the crystal development during biomineralisation was also investigated. The role of *Serratia* cells in HA precipitation was discussed, and three possible nucleation sites were offered.

9.1.1 The nascent crystals prior to sintering

Chemical composition

Combining the results of XRD and TEM, it can be concluded that the crystals formed by *Serratia* bacteria on titanium are indeed HA, consistent with previous studies [4-7]. They are, however, imperfect, being calcium deficient and usually contain Na^+ and Cl^-, which are picked up from the mineralisation solution: Na^+ from the AMPSO buffer (sodium salt) or β-GP (sodium salt) and Cl^- from $CaCl_2$. This demonstrates the ability of this method to incorporate certain elements within the crystal structure. Parallel studies by other researchers have demonstrated the ability to replace Ca^{2+} with Mg^{2+} or Sr^{2+} to form substituted HA or a

combination of the three (Sammons *et al.*, unpublished data). The formation of Mg/Sr substituted apatite could be advantageous as Mg can promote bone formation [8] and Sr is used in the treatment of osteoporosis and enhancement of bone remineralisation [9].

If the bacterial HA is considered as a potential bone graft substitute material, the fact that it is calcium deficient could be advantageous. Calcium deficient HA was observed to attract more osteoclasts than stoichiometric HA and histological analysis showed that larger osteoblast surface and higher bone volume formed on the calcium-deficient HA surface after implantation [10]. The Ca/P ratio of the nascent crystals is lower than suggested by Ledo *et al.* in 2008 [5], who measured a Ca/P ratio of 1.62 ± 0.04 by TEM (after 14 days' mineralisation). In this study, this value was found to be 1.57 ± 0.14 by SEM/EDX, but only 1.27 ± 0.11 by TEM/EDX (after 9 days' mineralisation). As the measurement by SEM/EDX was carried out directly on the crystal coating that is rough and porous, the SEM/EDX measurements are less reliable. The difference between the Ca/P ratios of these two studies may be due to the different challenge time used, as the Ca/P ratio of the crystals slightly increased from day 1 to day 9 (Figure 6. 14), which suggests a gradual maturation of the HA during the mineralisation. This is not unusual since the Ca/P ratio of the deposited HA formed on alkali treated titanium increased from 1.40 (immersed in SBF for 36 hours) to 1.65 (immersed in SBF for 72 hours) [11]. The Ca/P ratio of newly mineralised tissue surrounding an HA coated Ti 64 rod implanted into a canine trabecular bone was 1.2 after an implantation time of 7 days, but increased to 1.7 after 14 days [12].

Crystal morphology

The morphology of synthetic HA varied a lot according to the production procedure, ranging from nano-flakes (Figure 9. 1b) [13], to small rods (Figure 9. 1c) [14] and crystal plates (Figure 9. 1d) [15]. *Serratia* HA is different from these examples. According to a previous study, the crystals formed by *Serratia* were described as needle-shaped [16]. In this work, higher resolution microscopy revealed plate-shaped structures of various sizes, usually nano-scale (Figures 6.5 and 6. 7). They appear to be needle-like at lower magnification (Figure 6.21a). The formation of nano-scale crystal is due to the reaction environment which was described as 'a confined reaction space bounded by the protective groups of the EPM polymers' which prevents the agglomeration of nano-particles [6].

As a summary, *Serratia* HA is calcium-deficient hydroxyapatite in the morphology of nano-scale curved plates. Foreign elements present in the solution can easily enter the crystal lattice during the mineralisation process.

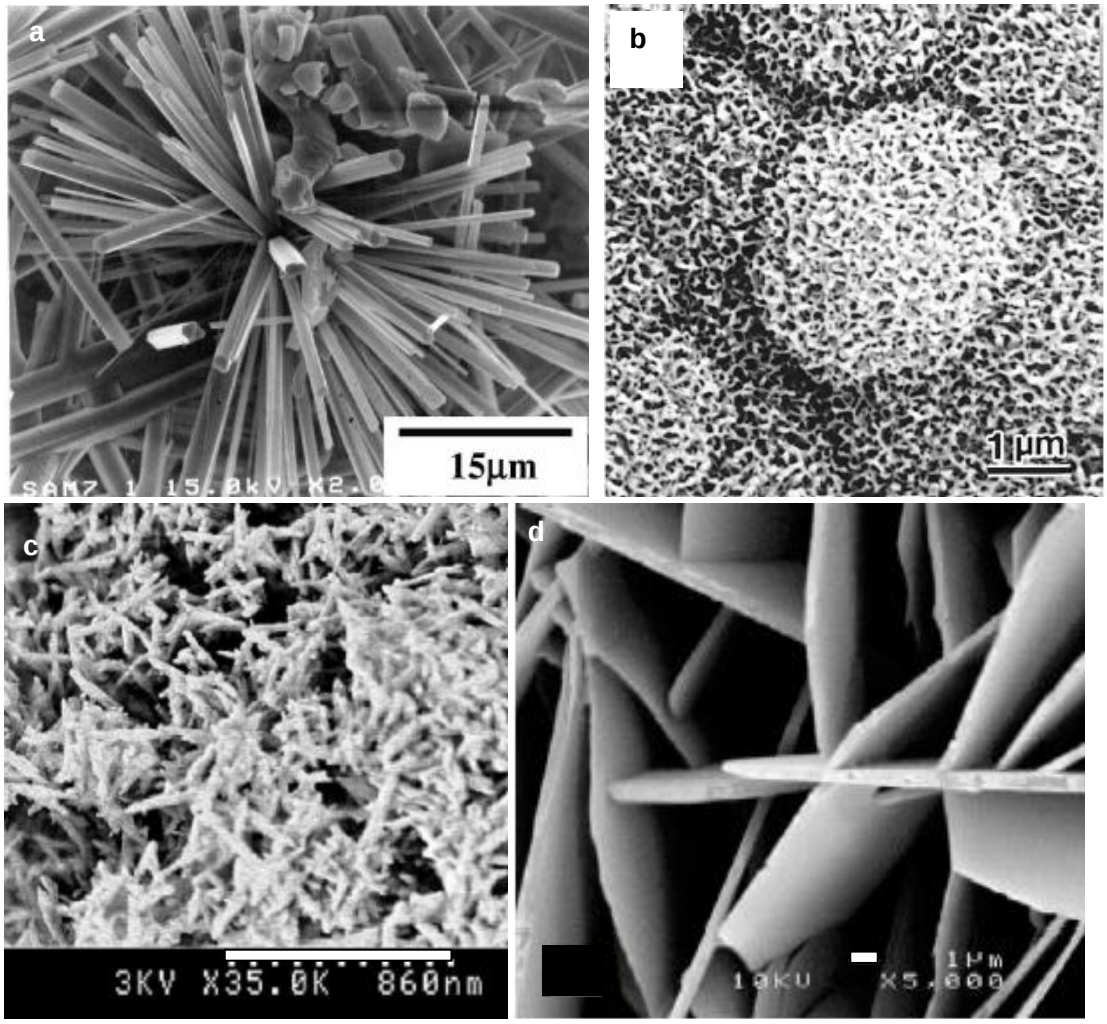

Figure 9. 1 Several examples of the morphology of the HA produced by different methods

a: Needle-shaped HA formed by the hydrothermal method (adapted from [17]).

b: Biomimetic HA formed on Ti-15Mo-5Zr-3Al alloy in SBF (adapted from [13]).

c: Rod-shaped HA formed by wet precipitation (adapted from [14]).

d: Biomimetic HA formed on acid etched titanium in a supersaturated solution (adapted from [15]).

9.1.2 The influence of ion concentration on HA crystal formation

It is difficult to study the influence of solution ion concentration on crystal size directly from the HA coated samples due to the complicated situation during mineralisation in the

bioreactor, which is explained as follows. To produce HA via *Serratia* biofilm, Ca^{2+} ions and β-GP molecules have to be able to diffuse into the biofilm structure to reach the bacteria. It has been demonstrated that both the cleavage of β-GP and the diffusion of metal ions are time-dependent and closely related to the ion concentration, solution pH and medium flow rate. After 57.1 hours, only 1.65 mM inorganic phosphate could be released by *Serratia* when the starting concentration of β-GP was 5 mM (pH=6.0, flow rate =11 ml/h) [18]. It took approximately 6.3 hours for Co^{2+} ions (4 mM solution at a speed of 12 ml/h) to complete the penetration of a *Serratia*-loaded foam (21 mm × 20 mm), but only half an hour if the starting concentration were increased to 10 mM and the flow rate controlled at 60 ml/h [19]. Thus, it is very possible that the ion concentration at different locations of the biofilm is different, due to its uneven thickness (bacterial clumps in Chapter 4) and porous structure [20]. Moreover, the biofilm-coated samples were arranged in the bioreactor in a vertical stack - as shown in Figure 2. 3. Fresh medium (mineralisation solution) was pumped through the bottom inlet and flowed up the column until it reached the outlet at the top. This arrangement itself may lead to an uneven distribution of ions, as samples at the bottom contact the fresh medium first while those further up only have access to the depleted solution that has passed through or by the lower samples. A previous study demonstrated that mineralisation happens faster on samples closer to the medium inlet [16].

For these reasons, parallel experiments (§ 6.8) were carried out to create artificial environments to mimic the calcium/phosphate excess conditions. It was found that both the chemical composition (Ca/P ratio) and the crystal size of the biosynthesised HA were closely associated with ion concentration, with the formation of smaller but thicker plates with lower Ca/P ratio when Ca^{2+} was scarce but larger and thinner curved plates with a higher Ca/P ratio when the β-GP (phosphate source) was scarce (Table 6. 1 and Figure 6. 23). However, this

experiment was carried out only once. Thus, further work will be necessary.

There are reports that the morphology of HA precipitated from an aqueous environment is sensitive to ions such as Cl^-, CO_3^{2-}, and to Tris and amino acids [21], alginate [22], proteins [23], and some other organic components such as monosaccharides [24]. Their reactions with the calcium ions at the surface of the HA precursor are important in determining the morphology of the ultimate crystal, as selective bonding of certain molecules to the primitive HA crystal can lead to preferential crystal growth in certain directions to form either plates or needles [21-24]. For example, Cl^- can promote a plate-like morphology of HA in a supersaturated solution [24], while small flake-like HA precipitates from calcium-rich simulated body fluid and a short rod-like structure is produced when more HPO_4^{2-} is present [25].

In this study, although HA crystals formed under both calcium excess and phosphate (β-GP) excess conditions are plate-like, the sizes and thicknesses of the curved plates are different. This may be caused by the low Ca^{2+} or Cl^- content in the phosphate excess solution which leads to an inhibition of the plate growth along certain directions and, thus, growth along the other direction is enhanced, resulting in thicker but smaller plates. The effect of Cl^- in promoting HA plate growth is attributed to its ability to incorporate into the surface at certain defect sites [25]. However, the difference of the crystal morphology in this study is not as distinct as observed by Li *et al.* (1993) of HA precipitated from solutions containing Ca^{2+} and HPO_4^{2-} [25].

What is worth noting is that β-GP-rich may not be HPO_4^{2-}-rich. HA cannot form directly from Ca^{2+} and β-GP. The organic phosphate has to be cleaved to release the inorganic HPO_4^{2-} first. The acid phosphatase enzyme involved in this process is not dysfunctioned by the

end-product, but rather can act as a phosphotransferase [26]. Nott *et al.* (2005) showed that the release of inorganic phosphate by *Serratia* was not instant but gradually increased until stabilising after a certain period of time [18]. They also observed that flow rate could affect the release rate: after challenging with 5 mM glycerol phosphate (pH=6.0) for 57.1 hours, the concentration of the inorganic phosphate in the outflow was 1.65 mM when the flow rate was controlled at 11 ml/h, but 0.69 mM at 128 ml/h [18]. It is a rather slow reaction when compared to the instant precipitation of HA (§ 6.9) and may be the rate controlling step during the production of *Serratia* HA.

9.1.3 Other potential influences of HA crystal formation

During one of the experiments, air failure occurred several times in fermentation, and the crystal morphologies in this situation are quite different, as shown in Figure 9. 2. They are mainly in the form of thick plates, but also in other shapes. It is possible that the reduced air and disturbance of the medium supply during fermentation might affect not only the biofilm structure, but also the individual bacterial activity, resulting indirectly in an abnormal condition during the following mineralisation where not only the ion concentration and the solution pH are affected, but also the production of certain crystal growth regulators or templates.

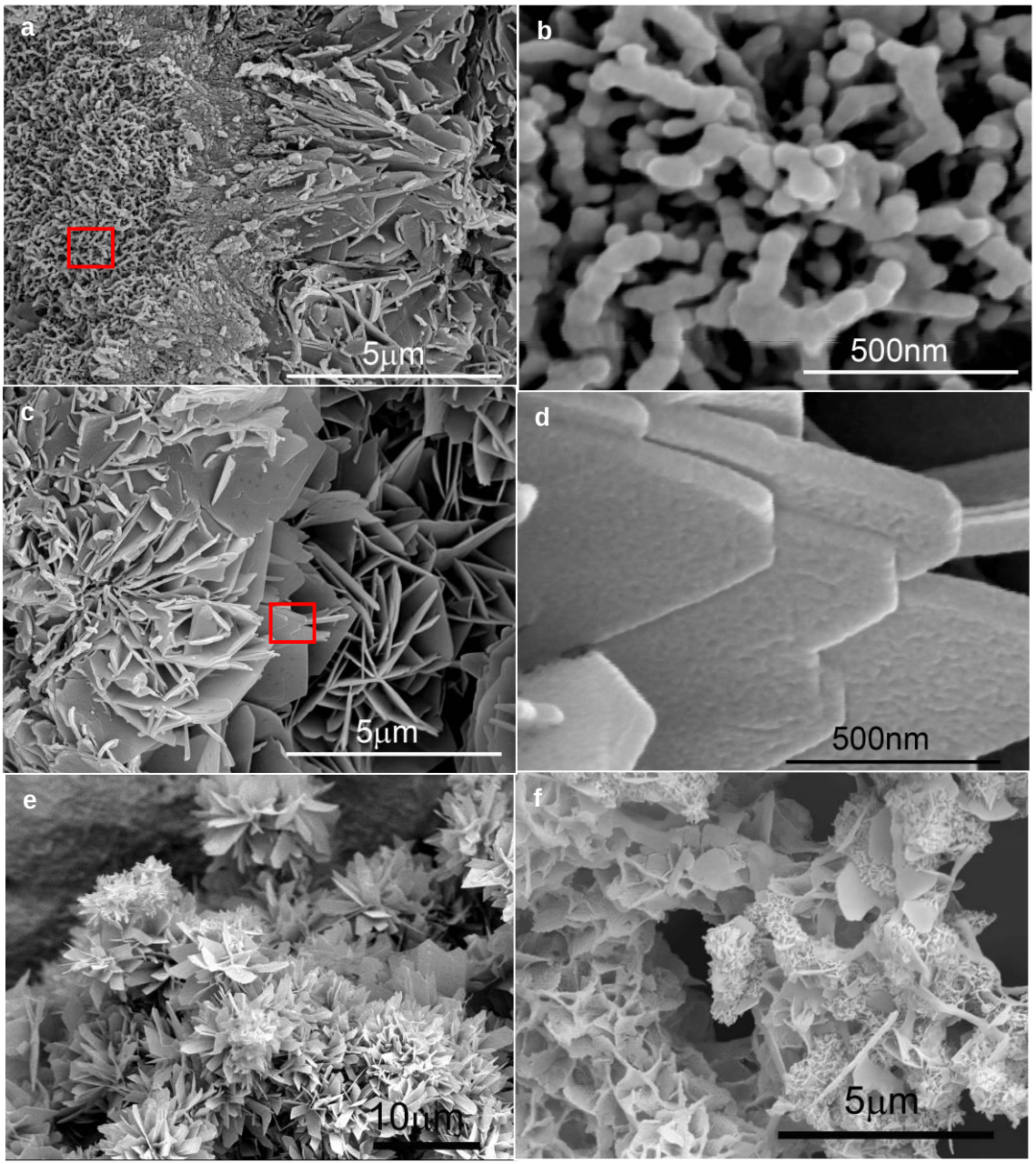

Figure 9. 2 Several examples of the abnormal crystal morphologies (SE imaging)

a: Transformation from nano-particles (b) to well developed plates (c) (on a Ti disc).

b: The square in (a) at higher magnification.

c: Well developed plate-shaped crystals.

d: The square in (c) at higher magnification demonstrating polygonal crystal plates.

e: Plate-shaped crystals in the form of flowers (on a Ti web).

f: A composite structure of plates and nano-particles (on a Ti web).

The role of solution pH to affect HA crystal size has been well accepted [25, 27, 28], and it is known that during the *Serratia* catalysed release of inorganic phosphate, the pH of the solution is not stable but varies at different stages and for different flow rates [18]. HA morphology is also closely associated with crystal growth templates, both *in vivo* and *in vitro*. It is well known that HA growth *in vivo* can be regulated by proteins such as matrix Gla protein [29, 30]. The morphology of HA precipitated from SBF was observed to differ significantly with and without the presence of poly(amidoamine) dendrimer which is considered as a template or crystal modifier [31]. Ferrous hydroxide crystals, mineralised by *Magnetospirillum magneticum* AMB-1, showed a huge difference in both crystal morphology and size with and without the presence of the acidic protein, Mms6 [32]. HA precipitation from HEPES-buffered mineralisation solutions was delayed by the presence of unbound lipoteichioc acid isolated from *Lactobacillus casei* and *Streptococcus sanguinis* [33, 34]. All these effects are attributed to the ability of the proteins or other components to bind to the metal ions during mineralisation. However, whether there is a similar compound in *Serratia* that leads to the significant difference of the crystal morphologies in Figure 9. 2 is yet unknown and merits further investigation, as it is not only helpful to better understand bacterial biomineralisation, but may also make the production of HA with controlled-morphology possible.

9.1.4 The role of *Serratia* in HA precipitation

The precipitation formed in the autoclaved solution in § 6.9 with the addition of fresh $CaCl_2$ was possibly a primitive form of HA. This observation suggests that with the presence of Ca^{2+} and bacteria freed HPO_4^{2-}, HA can form without the assistance of bacteria and enzyme. Thus, it can be deduced that the enzyme only functions to release HPO_4^{2-}, but may not be necessary

for any further reactions, which is in good agreement with Yong *et al*. [7]. Similar results were also reported by Hirschler *et al*., who found that during the precipitation of $CaCO_3$ by *E. coli*, the alkaline phosphatase was only involved in the release of inorganic phosphate into the medium but not in the subsequent precipitation [35].

The precipitates in § 6.9 may be very similar to the apatite nucleus formed during the biomineralisation of HA. Diffraction rings corresponding to HA (Figure 6.24a) suggest that these crystals might be a primitive form of HA. These crystals are nano-scale with regular dimensions (Figure 6. 24). The starting Ca/P ratio is unexpectedly low, approximately 0.16, comparing to 1.27 ± 0.11 of the samples after 10 days' mineralisation. If the above assumption is true, it can be deduced that maturation of the crystals occurs after nucleation with further incorporation of Ca^{2+} into the structure. However, the present techniques in this study are insufficient to define the phase and further analysis is necessary. Due to the sensitivity of the crystals to high energy electrons, cryo-techniques will be essential for any further microscopic analysis.

The precipitation in the autoclaved solution after the addition of fresh Ca^{2+} suggested the existence of HPO_4^{2-} in the solution, which indicates that the cleavage of β-GP maybe independent of the precipitation reaction. Otherwise, the excess phosphate would stay in their organic form, and thus no precipitation should occur, like in the control solution. To measure the inorganic phosphate content in these solutions will be essential for further investigation.

The formation of the nano-scale regular-shaped crystals in § 6.9 is notable for its instant speed. So far, any reactions to produce HA through precipitation are either time-consuming, such as the biomimetic methods [36], or yield amorphous calcium phosphate which only changes to HA if additional treatment is applied as in the sol-gel method [37]. Thus, further investigation

into this process may be of great interest. However, so far, researches into HA production via *Serratia* have focused on the complete process[1, 7]. That is to say, the cleavage of the organic phosphate is not separated from the deposition of metal phosphate salts. Observations in this work suggest that these two processes may be two independent reactions. By separating these two steps and sterilising the bacteria treated waste water in advance, nano-scale HA crystals are likely to be synthesised safely and easily at an amazing speed.

9.1.5 Possible nuclei and nucleation sites

Biomineralisation of HA via *Serratia* biofilm is a complicated process. Several possible locations may act as nucleation sites: bacterial cell walls, EPM layers and anywhere with free Ca^{2+} and HPO_4^{2-}.

1. *Serratia* cell walls

Macaskie *et al*. showed that LPS on *Serratia* cell walls was the major nucleation sites for the uranyl phosphate precipitation [38]. These groups may also serve as the nucleation sites for the production of *Serratia* HA: Ca^{2+} is bonded to the PO_4^{3-} functional part of LPS and nucleus is thus formed.

2. EPM layer

Jeong *et al.* reported two phosphatases in *Serratia*, CPI and CPII, possibly representing cell-bound and extracellular forms of the enzyme, respectively [26]. Thus, theoretically, HA can be produced both within and around the cell wall (CPI), and inside the extracellular polymer matrix (EPM) layer (CPII).

Cross-section study in this work reveals an extra crystal shell covering a group of crystal

spheres (Figure 6.4c & d). The gap found between the shell and the groups of spheres suggests two independent crystal formation reactions. It is possible that the bright circular shapes with 0.5 to 1 μm diameters (Figure 6. 4c) are the locations of *Serratia* cell walls, and the shell EPM. The contrast between the two is possibly caused by denser crystals around the cell walls, where most enzymes exist and thus the nucleation is most likely to happen, yielding a stronger signal when observed by SEM.

3. Where Ca^{2+} and free HPO_4^{2-} are available

What was discussed in § 9.1.4 indicates that the precipitation of HA is not necessarily cell-bound or enzyme-linked. Any sites where Ca^{2+} and free HPO_4^{2-} are available, nucleation could be initiated.

9.1.6 Advantages and disadvantages of *Serratia* biomineralisation

Bacteria *Serratia*, previously identified as *Citrobacter* sp., was first reported in the recycle of UO_2^{2+} [39]. This bacteria was later used to remove organic phosphate[7], cobalt, strontium and caesium[40]. After the bacterial treatment, the phosphate content in a contaminated solution decreased from ~ 0.27 mM (25 ppm) to ~ 0.02 mM (2 ppm) [7]; ^{137}Cs, ^{85}Sr and ^{60}Co were reported to be removed entirely from a simulated radioactive waste [40]. *Serratia* were also found to be able to produce calcium phosphate [6]. The simultaneous production of HA via bacteria *Serratia* and its ability to utilise and deplete organic phosphate are economically advantageous, but there are other advantages:

First of all, *Serratia* HA bear a resemblance to bone minerals, which are calcium deficient carbonated HA containing Na^+ and Cl^- [41]. Although not included in this work, previous studies by Thackray (2005) [16] and Ledo (2008) [5] have shown presence of carbonate

within the *Serratia* HA through FTIR analysis. Secondly, *Serratia* HA are superior when compared to HA obtained via traditional methods. The by-products such as TCP, OCP, CaO and TTCP which are often accompanying solid state reactions and hydrothermal reactions [42, 43] can be avoided. Thirdly, *Serratia* HA are nano-scale crystals, comparable to crystals formed by the biomimetic method [44] and much smaller than crystals formed by solid-state reactions or hydrothermal methods [17]. This aspect will be discussed further in § 9.2.1. Last but not the least, the reaction between Ca^{2+} and bacteria liberated HPO_4^{2-} is distinct. The formation of nano-scale crystalline minerals, possibly HA, is instant and the product benefit from having regular dimensions, whereas amorphous HA is the direct product in sol-gel method and only if heat treatment is applied can it transforms to a crystalline structure. The above discussions are summarised in Table 9. 1.

Table 9. 1 Biomineralisation of HA via *Serratia* in comparison with bone mineral and HA fabricated by other methods

Production method	***Reactions and products***			***Serratia HA before sintering***		
	Reaction conditions	***Main products***	***By products***	***Chemical composition***	***Crystal size***	**Crystal morphology**
Bone minerals [41, 45, 46]	—	—	—	Calcium-deficient HA with the incorporation of HPO_4^{2-}, CO_3^{2-}, Mg^{2+}, Na^+ and F^-…	Various in different bones	Usually plates with irregular edges
Solid-state reaction [42, 43]	High temperature	HA	α/β-TCP…	HA	—	—
Hydrothermal method [17]	High temperature, high pressure	HA	—	HA	Nano-scale to micro scale	Needles
Sol-gel method [37, 43, 47]	Strict pH control, heat treatment	HA	α/β-TCP, TTCP, CaO…	Crystalline HA only after heat treatment is applied	Nano-scale to micro-scale	—
Biomimetic method [44, 48, 49]	Often long reaction time (weeks) in SBF, but can be facilitated by increasing temperature or solution strength	HA	OCP	HA with the incorporation of CO_3^{2-}, Cl^-, Na^+, Mg^{2+}…	Nano-scale to micro-scale	Needles, rods, plates
Biomineralisation via *Serratia* [5, 16]	*Serratia*	HA	—	Carbonated calcium deficient HA with Na^- and Cl^-	Nano-crystals	Usually curved plates

9.2 Biomineralised HA as a coating on titanium substrates

Previous work was mainly focused on the *Serratia* biomineralisation process [7], characterisation of the mineral products [50] and production of porous crystal scaffolds [51], and its potential as a coating method is not totally understood, which was discussed in this section.

9.2.1 Coating structure

9.2.1.1 The *Serratia* HA coating structure

Serratia HA coating is a 3D porous structure with an extremely high surface area.

3D porous structure

Serratia HA coating structure is unique in its 3D porous architecture (Figure 6. 3 and Figure 6. 4) regardless of the solid substrate and comparative independence of the substrate topography (Figure 6. 4a). On the other hand, in almost all the other coating methods, the general morphology of the coating depends on the topography of the substrate. The biomimetic HA coating formed in SBF is an even HA layer several micrometres thick (Figure 9. 3d) consisting of crystal clusters (Figure 9. 3c) that are groups of nano-scale HA crystals [52, 53]. The coatings formed by plasma spraying are less even, thicker (Figure 9. 3b) but smoother at the micro-scale (Figure 9. 3a) than the biomimetic coating, and consist of both amorphous and crystalline HA with other decomposition phases [54, 55]. Either way, the coating itself is more solid rather than the *Serratia* HA coating, the structure of which is determined by the nature of the coating method. In traditional coating methods, the titanium substrate is the direct support for the HA film. In *Serratia* biomineralisation, it is the biofilm that is the skeleton for the

crystal growth, while titanium acts as the direct support of the biofilm and thus only has an indirect influence on the coating morphology. Biofilm usually adapts a 3D porous structure [20], which determines the porous architecture of the *Serratia* HA coating.

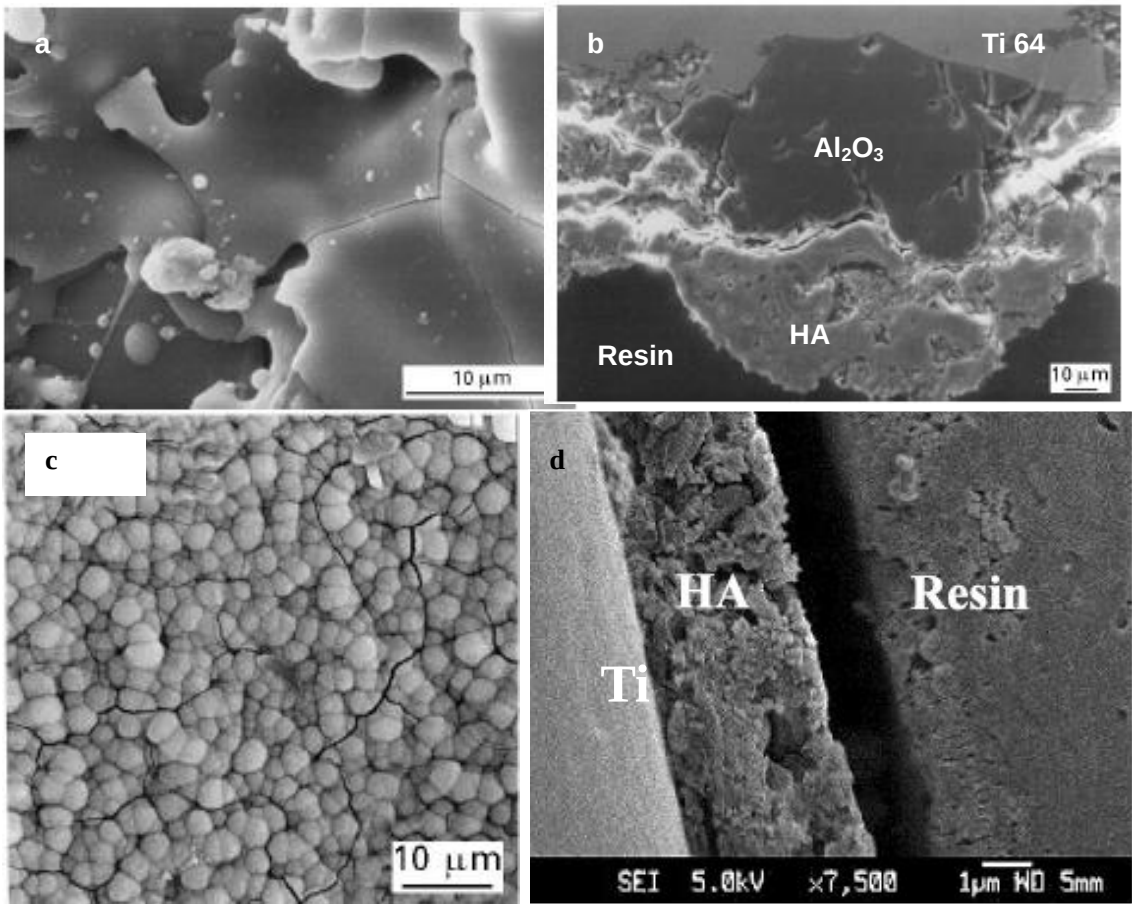

Figure 9. 3 Examples of HA coating formed on titanium by plasma spraying and the biomimetic method

a: The morphology of plasma sprayed HA coated alumina blasted Ti 64 (adapted from [54]).

b:Cross section through plasma sprayed HA coated alumina blasted Ti 64 (adapted from [54]).

c: The morphology of a biomimetic HA coating on CP Ti (adapted from [52]).

d: A cross section through a biomimetic HA coating on CP Ti (adapted from [53]).

High surface area

As in biomimetic coatings, the *Serratia* HA coating also consists of micro-spheres (Figure 6. 3b & c and Figure 6. 4c & d) which are usually composed of nano-scale HA crystals (Figure 6. 5 and Figure 6. 7). This hierarchy of architecture confers the coating with macro-, micro- and nano-scale roughness, thus ensuring an extremely high surface area. Mammalian cells are sensitive to discontinuities from the macro to the nano-scale [56-58]. The rate and quantity of new tissue formation is controlled by the surface roughness of the substrate and its topography, as they display a strong influence on protein adsorption, cell attachment, cell proliferation, contact guidance and cell differentiation [59]. Therefore, *Serratia* HA could be used as mammalian cell carriers to provide an appropriate environment where the cells can proliferate and produce the desired bone matrix, thus improving the osteoconductivity and osteointegration of the graft. Moreover, this coating may also have a wide market in water purification, as catalyst carriers, and for drug delivery *in vivo*. As far as the author is aware, *Serratia* biomineralisation is the only method to generate roughness at this wide range (from macro- to nano-scale), in comparison with other methods (in Figure 9. 4).

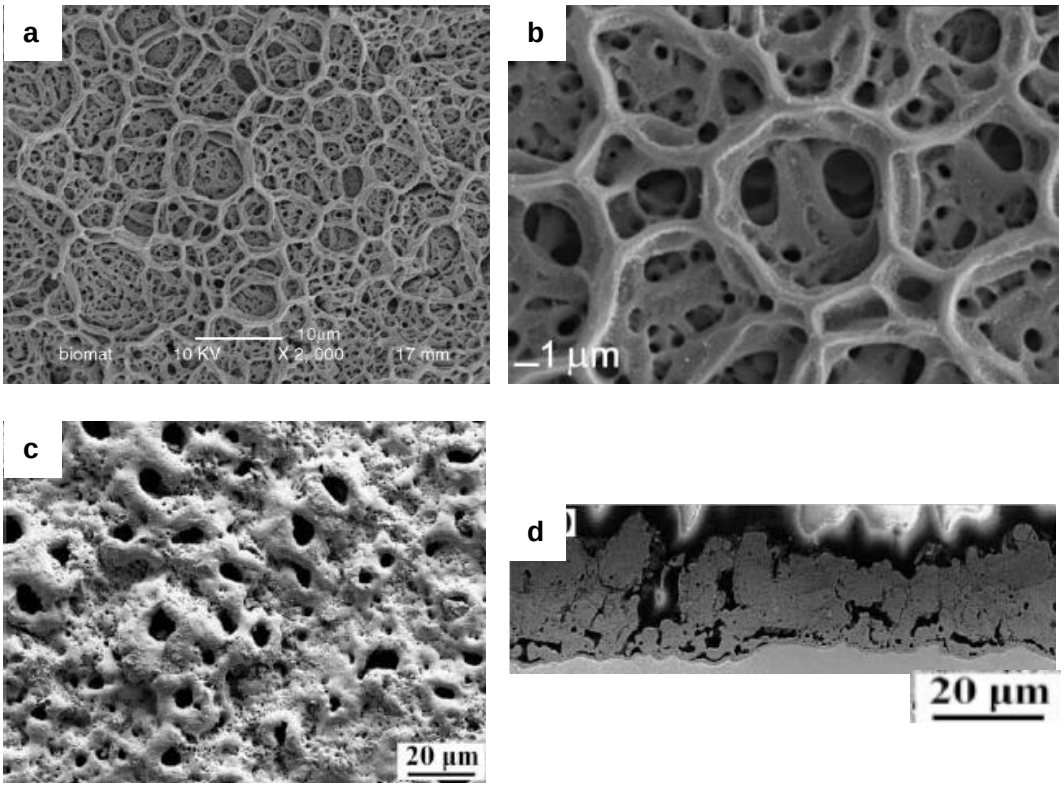

Figure 9. 4 Several examples of published porous coatings

a: An electrostatic spray deposited calcium phosphate coating on Al_2O_3 grit blasted titanium (adapted from [60]).

a: A detail of the coating in (a) (adapted from [61]).

c: HA-containing porous titania coating processed on ultrafine grained titanium by micro-arc oxidation (adapted from [62]).

d: Cross section through (c) (adapted from [62]).

Possible differently patterned structures

It was demonstrated in Chapter 4 that the morphology of the 7-day old biofilm differs on titanium discs with different surface treatments, when comparing Figures 4. 5 to 4. 10. Considering that this biofilm serves as a 'skeleton' for the subsequent crystal coating, it can be hypothesised that the morphology of the HA coating might be different on titanium

substrates with different surface treatments. Moreover, even on the same surface, the structure of the HA coating can be different as biofilm structure is sensitive to fermenter parameters during the biofilm formation, as has been shown with *Pseudomonas* biofilms, illustrated in Figure 9. 5 [63]. This suggests the possibility of developing a smart coating by adjusting either the substrate or the fermenter conditions. Such significant variation in coating structure may not be achieved using alternative methods and merits further investigation, as cells show guided growth on textured surfaces [57]

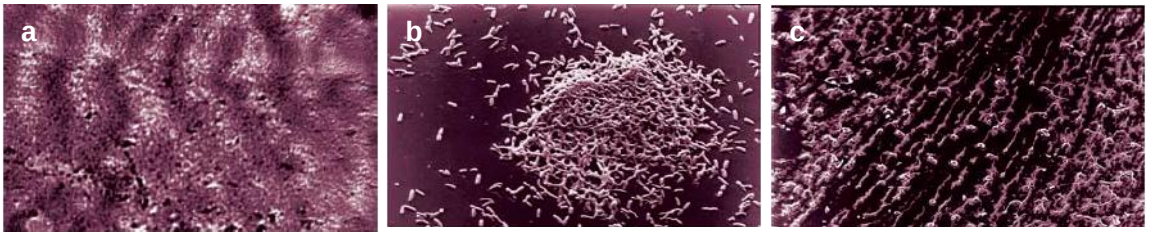

Figure 9. 5 Examples of different *Pseudomonas* biofilms obtained with different flow conditions (adapted from [63])

a: ripple-patterned biofilm

b: circular-shaped biofilm

c: biofilm streams

9.2.1.2 The sintered coating

Heat treatment was applied to burn off the biomass and to sinter the crystals coating. After sintering, the structure of the coating appears to be hardly changed at all at the macro/micro-scale (Figure 7. 2). However, the individual crystals changed not only in terms of morphology but also chemical composition.

Theoretically HA starts to decompose to β-TCP when heated to a temperature between 800 ºC to 900 ºC, according to the reaction in Equation 9. 1 [43]. It is possible that the decomposition

of the nascent HA in this study occurs in a similar route by losing OH^- to yield a structure ($Ca_{10}Na(PO_4)_7$) similar to that of β-TCP until it is completely transformed to β-TCP at 1200 ºC [16]. The formation of a calcium-deficient β-TCP structure with a Ca/P ratio of 1.16 ± 0.05, as compared to its stoichiometric state (Ca/P ratio = 1.5) is because of the low Ca/P ratio of the starting material (1.27 ± 0.11).

$$Ca_{10}(PO_4)_6(OH)_2 = 3Ca_3(PO_4)_2 + CaO + H_2O$$

Equation 9. 1

The phase transformations of the crystals during sintering are summarised in Table 9. 2, together with previous results by Thackray [16] and Medina-Ledo [64]. It can be seen that HA starts to decompose at 600 ºC and transforms entirely to β-TCP at 1200 ºC. Na and Cl originally incorporated within the lattice are retained within the crystals at lower temperatures (600 ºC and 800 ºC), but are removed at 1200 ºC. The formation of β-TCP can be beneficial, depending on the application. It is more soluble than HA *in vivo* and thus displays higher biodegradability [65].

Table 9. 2 The phases of the sintered crystals: comparison between this work and pulished studies

Sintering temprature	***Phases present***
Nascent crystals [16, 64, this work]	$Ca_{10}(PO_4)_6(OH)_2$ (HA)
600°C [16, 64]	$Ca_5(PO_4)_3Cl$ + NaCl+HA
800°C [this work]	$Ca_{10}Na(PO_4)_7$+ $Ca_5(PO_4)_3Cl$
1200°C [16]	Mainly β-$Ca_3(PO_4)_2$

After sintering, the transformation of the curved plates (Figure 6. 5c) to irregular particles (Figure 7. 3) but without significant crystal growth may lead to a smaller sphere, as illustrated in Figure 9. 6b. It can be seen from the cross section samples before (Figure 6.11) and after

(Figure 7.8) the heat treatment that the porosity of the coating was significantly increased. Sintering at higher temperatures such as 1100 ºC may result in further decrease in volume, possibly caused by crystal growth through a consolidation of the nano-particles and subsequent fusion of separate crystal clusters to form smooth grains, as illustrated in Figure 9. 6c. The morphologies of the bio-crystal coating sintered at 800 ºC and 1100 ºC [16] are compared in Figure 9. 7. Figure 9. 6b corresponds to Figure 9. 7a, while Figure 9. 6c corresponds to Figure 9. 7b. Judging by the similarity between the way the crystal spheres are positioned after sintering at 800 ºC (Figure 9. 7a) and the structure of the large grains after sintering at 1100 ºC (Figure 9. 7b), it may be assumed that the individual β-TCP grain in Figure 9. 7b is developed from a crystal cluster consisting of nano-particles as in Figure 9. 7a.

To obtain a coating with desirable strength, it should be a consolidated structure similar to that shown in Figure 9. 7b which means sacrificing the nano-scale roughness to form large grains which offer physical strength. To achieve this, the matrix should be sintered above 1000 ºC. With pure titanium as substrates, this is not practical since any heat treatment beyond its β-transus temperature (~882 ºC) will lead to rapid crystal growth and in turn a significant decrease in the substrate physical strength. However, at 800 ºC, the crystal clusters are still composed of nano-particles instead of consolidated grains as compared in Figure 9. 7. Thus, the strengthening effect may not be noticeable. The increased coating porosity after sintering (800 ºC) suggests that there will be hardly any significant improvement of the physical strength. Increasing the holding time at 800 ºC from 5 to 10 hours may not help either, as the crystal morphology is similar to the 5 hours (Figure 7.3).

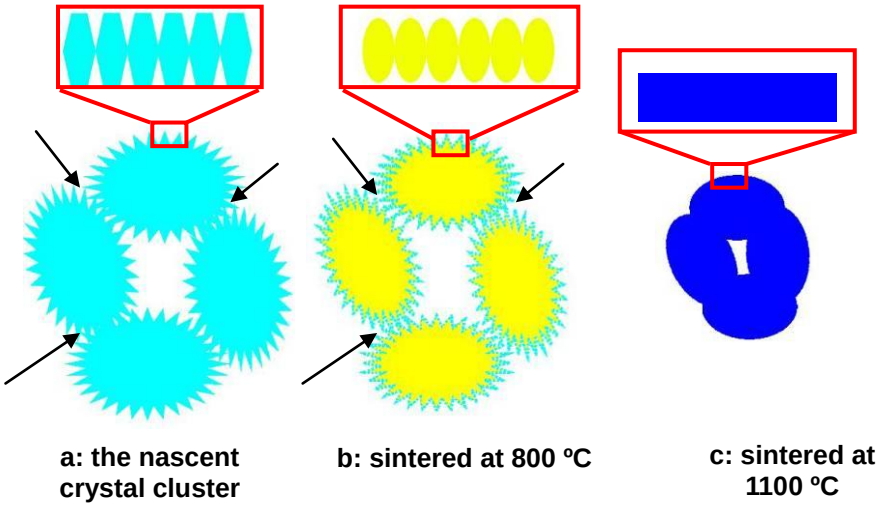

Figure 9. 6 Schematic drawing of the crystal morphology and volume change during heat treatment

a: The morphology of the nascent crystal clusters. Each cluster consists of plate-shaped crystals. Bacteria are not shown.

b: The morphology of the crystal clusters sintered at 800 ºC. Plate-shaped crystals change to nano-particles. Organic parts are burnt off. The volume of the crystal clusters in (a) is decreased from its original dimension (indicated by the green line) to a smaller sphere (the yellow part), leading to increased porosity between crystal clusters, as compared by the arrowed sites in (a) and (b).

c: Crystal fusion and growth result in a significant volume decrease and the formation of a smooth cluster surface.

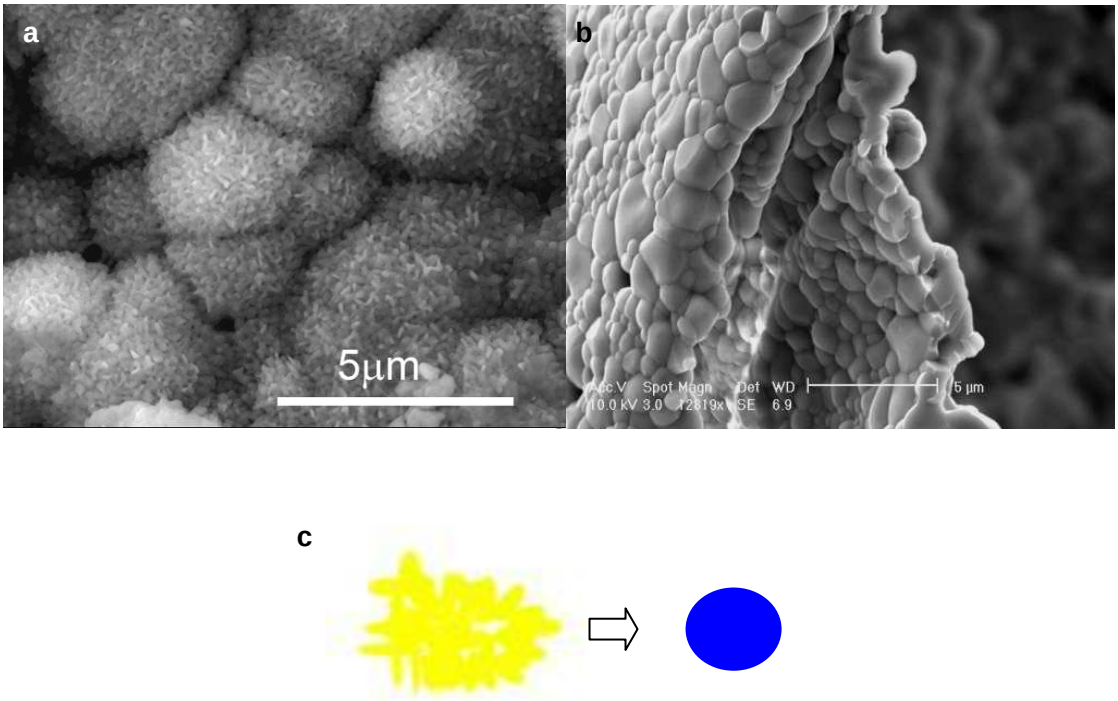

Figure 9. 7 The morphology of the crystal clusters sintered at 800 ºC and 1100 ºC

a: Crystal coating sintered at 800 ºC for 5 hours (heat treatment route 1)

b: Crystals sintered at 1100 ºC. (Ramp at 3°C/min to 550°C; hold at 550°C for 3 hours; ramp at 3°C/min to 1100°C; hold at 1100°C for 2 hours; cool.) [16].

c: Schematic drawing of the transformation from crystal clusters to a grain.

9.2.1.3 Advantages and disadvantages

Even today, the manufacture of an HA coating that can offer sufficient strength in load-bearing sites in the human body remains a huge challenge. So far, the most promising method in terms of coating strength is plasma spraying. However, this 'line-of-sight' method is not appropriate when porous titanium or titanium with complex structures is used as a substrate. Wet methods such as the biomimetic methods and electrochemical deposition are successful in coating porous structures, but they may not be able to withstand forces as the coating usually consists of loosely bound particles only. In spite of the weakness of such

coatings, they have proved to be successful after implantation for different periods [12, 15, 66], due to their advantage in promoting the mineralisation of bone tissues. The *Serratia* coating suffers from the same problem as it is also a network of loosely stacked crystal clusters even after sintering at 800 ^{o}C, and thus may not be used at load-bearing sites. It is extremely difficult to evaluate the coating strength for the following reasons. First of all, it is porous, containing crystal clumps with various sizes on a crystal matrix. Secondly, it is not solid even within the coating, but crystal clusters which are likely to be hollow spheres (Figure 6. 4c). Thus, traditional methods for coating strength may not give reliable results. Recently, Yong *et al.* used a micro-manipulation technique to measure the adhesion strength of fresh and mineralised *Serratia* biofilm on titanium surfaces [96]. This method may be explored in the future to compare the adhesion strength of *Serratia* HA coated titanium and HA coatings achieved via other methods.

However, enormous benefits can be achieved using this coating. It is superior for its 3D porous structure with an extremely high surface area and is independent of the substrate. Moreover, it is possible to obtain various patterned coating by adjusting the biofilm structure through fermenter conditions. Previous work has demonstrated that *Serratia* HA favoured mammalian cell adhesion, proliferation and differentiation [51]. Thus, the coating achieved in this work may promote cell growth (due to its nano- and micro-scale roughness) as well as a certain amount of bone ingrowth (due to micro- and macro-scale roughness) when compared with other coatings, which merits further investigation. Remarkable differences have been reported when the solid particles have nano-scale sizes, including changes in mechanical, electrical and magnetic properties to chemical properties such as solubility, reactivity and catalytic activity [67]. Cellular functions and tissue growth can be enhanced by nano-scale features, because of the ability of nano-roughness in promoting protein adsorption such as

fibronectin that is critical for mediating the adhesion of anchorage-dependent cells [68]. It was observed that cells react strongly to nano-scale roughness down to 10 nm [69]. Therefore the *in vivo* behaviour of *Serratia* coating could be outstanding. It will be of great interest to explore this aspect in the future.

9.2.2 The coating-substrate interface structure

The coating-substrate interface demonstrates how well the coating is bonded to the supporting material and therefore is an important component during the characterisation of the coating.

9.2.2.1 The interface between the crystal coating and the grit blasted titanium surface

The grit blasted titanium surface

Grit blasting is a common procedure used to increase the surface area of titanium implants, by producing a roughened surface (Figure 6. 1a) to improve bone interlocking. Aluminium oxide particles are still commonly used to bombard the surface. The presence of embedded Al_2O_3 particles (Figure 6. 1b & c) and their potential consequences have been reported by other researchers [70, 71]. The release of Al^{3+} from these particles into the physiological environment has aroused much concern, as it is recognised as an etiological factor in aluminosis, encephalopathy and osteodystrophy, and non-iron deficiency microcytic anaemia [72]. Thus, other grits such as SiO_2, TiO_2 or HA have been introduced to replace Al_2O_3 [73, 74].

In addition to the roughening effect, the grit blasting also produces a severely deformed surface composed of a nano-crystalline layer and a twinned region underneath (Figure 6. 1e & Figure 6. 11b). Similar effects, for example a nano-crystalline structure due to severe plastic deformation, have been reported for steels treated by air blast/ultrasonic shot peening [75, 76]

and in titanium processed by severe plastic deformation such as in equal channel angular pressing (ECAP) [77, 78]. This nano-crystalline structure not only improves the strength and hardness of the starting material, but may also lead to increased bacterial adhesion [77] and cell adhesion and proliferation [78-80], attributed to the increased surface roughness due to the nano-grained surface. The findings in this work demonstrate for the first time that simple grit blasting of CP Ti with Al_2O_3 can create a nano-crystalline surface which is very likely to promote both bacterial and cell adhesion, and will be interesting to investigate in the future.

The coating-substrate interface

The nascent crystals are sensitive to both ion beams (FIB/SEM) and high energy electrons (TEM), thus suffer severe beam damage during ion milling and when observed by TEM. The ion beam damage was so severe that when the specimen was thinned to around 90 nm, the entire crystalline structure of the coating was damaged and became amorphous with bubble-like features (Figure 6. 11c). Their original crystalline structure is only hinted by the weak diffraction rings (Figure 6. 11d). To solve the problem, a thicker specimen, approximately 150 nm, was prepared. However, this leads to a significant reduction in resolution, due to the super-fine crystals in comparison with the specimen thickness along the beam. In further studies, the introduction of cryo techniques for specimen preparation and characterisation (Cryo-FIB/SEM and Cryo-TEM) may solve the problem. In both cases, the specimen will be cooled to -196 ^{o}C in liquid nitrogen (freezing rate of the order of 10^6 K/sec) to prevent the formation of ice crystals before it is transferred to a cryo workstation, then into a cryo holder and finally the electron microscope [81].

In spite of the beam damage problem, it was possible to make a cross section showing that the coating layer remains in full contact with the substrate even before the heat treatment (Figures

6. 10 & 6. 11). However, cracks which extend to the substrate surface (Figure 6. 11a) and holes caused by the dehydration of bacteria can be observed within the deposited layer (Figures 6. 10b & 6. 11b). These would potentially lead to coating failures if force was applied. The diffraction pattern obtained near the titanium substrate suggests that the coating is crystalline (Figure 6. 11d). This is different and possibly advantageous in comparison with the amorphous calcium phosphate layer at the same location in a plasma sprayed coating [82], in which case the amorphous HA dissolves faster than the crystalline phase and may lead to coating failures [83], and is one of the major concerns in the successful application of plasma sprayed HA coatings [82, 84].

The influence of heat treatment on the interface structure

The increasing porosity of the coating after heat treatment has been discussed above. Although the crystals are no longer beam sensitive, this increase in porosity adds to the difficulty in producing a satisfactory TEM specimen. As shown in Figure 7. 8, curtaining was so severe that parallel artefacts were produced during ion milling. Moreover, the coating was almost entirely consumed, whilst the metal part was still too thick to be transparent to the electrons.

The transition layer at the interface, mainly consisting of Ti, P-rich Ti and Al-rich Ti due to the diffusion of P and Al during the heat treatment, as confirmed by both SEM and TEM (Figures 7. 7, 7. 9 and 7. 11), is of great interest. SEM EDX maps suggest complete diffusion of the embedded Al_2O_3, which is very surprising, as Al_2O_3 is very stable, and is reported to maintain its oxide form between 800 ^oC and 900 ^oC with the formation of $TiAl_3$ at the Al_2O_3-Ti interface [85]. Further work is necessary to investigate this phenomenon. The morphology of the TiP interface on the grit blasted titanium without alkali treatment is similar

to that described previously [86]. The complexity at the interface may be in part due to the roughened titanium surface prior to heat treatment because of the grit blasting, offering discontinuities as diffusion path during sintering. As a result, the interface structure appears to be a composite of Al-rich Ti, P-rich Ti and Ti (Figure 7. 7 to Figure 7. 9). $CaTiO_3$ was not observed in this work, but other researchers have reported this if the HA coated Ti was sintered at 1200 ºC [87], and occasionally at 800 ºC [88].

The P-rich titanium layer is potentially advantageous, due to its higher biocompatibility when compared with titanium. It has been reported that removal torque values were higher on a TiP surface than on an untreated CP Ti surface after 4 weeks' implantation [86]. Although HA coatings can significantly reduce the ion release of the metal substrate [89], cracks are a common defect in HA coatings no matter how they are made. There are concerns that the body fluid could penetrate these cracks and react with the underlying metal that may contain cytotoxic elements such as Al and Ni [90]. This additional TiP layer thus may provide an extra protection against the cytotoxic elements released by the metal substrate, even after the failure of the coating [86].

9.2.2.2 The interface between the crystal coating and the alkali treated grit blasted titanium surface

The introduction of alkali treatment was intended to improve the bonding strength of the HA coating to the titanium substrate. However, in *Serratia* HA coatings, the interface is no longer the weakest point as it is in the case of plasma sprayed HA, and thus no strengthening effect was anticipated. However, the interface structure of the alkali treated specimen turns to be of great interest.

The influence of alkali treatment on the grit blasted titanium surface

The morphology and chemical composition of the sodium titanate layer on the titanium surface is in good accordance with previous reports [91, 92]. This activated layer is also observed on the embedded Al_2O_3 (Figure 6. 22), but without the incorporation of Al (Figure 6. 20). This observation suggests that the small amount of entrapped alumina did not seem to affect the reaction between NaOH and Ti, in agreement with previous reports where the same sodium titanate was observed on Ti 64 and Ti-15Mo-5Zr-3Al as on pure titanium [13, 93]. Judging by the neat boundary between the sodium titanate Layer 1 (leaf-structure) and Layer 2 (random particles) and its similarity to that between Layer 2 and the titanium substrate in Figure 6. 22, it is possible that the boundary between Layer 1 and Layer 2 may be the original titanium surface before the alkali treatment. Ti in Layer 2 diffuses into the solution and reacts with Na^+ to form Layer 1; at the same time, Na^+ can diffuse into Layer 2 and reacts with titanium. Thus, the leaf-structure is observed to be the same on Al_2O_3 as on Ti. The lack of Layer 2 on Al_2O_3, combined with the absence of Al from the influenced layer, shows the stability of alumina when treated with NaOH.

The coating-substrate interface

The alkali treatment does not have any noticeable influence on the nascent coating in terms of structure and thickness. It is the interface that is different. HA is formed within and fills the gaps in the sodium titanate layer (Figures 6. 20 to 6. 22). This ingrowth may strengthen the adherence of the HA coating due to interlocking between the coating and the sodium titanate layer. The stability of the sodium titanate layer is consistent with a previous report [44]. In another research, although the sodium titanate layer could not be distinguished from the newly deposited HA, TEM/EDX indicated that the content of Ti in the same region was stable

[11]. The stability of sodium titanate would seem to suggest that its role was restricted in offering nucleation sites for HA only, but it is not involved in any further reactions.

The influence of heat treatment on the interface structure

Although the alkali treatment does not have any distinguishable influence on the nascent biomineralised crystal coating, its effect become visible after sintering, giving the appearance of a thicker and much more porous interface. Without the alkali treatment, the titanium substrate appears to be solid after sintering (Figure 7. 6b, plan view). It is only in cross section that the surface is found to be porous (Figure 7. 6d & Figure 7. 8). With alkali treatment, the substrate appears to be porous even in the plan view (Figure 7. 10a), consisting of randomly arranged rounded struts (Figure 7. 10b).

This layer itself can be an interesting feature, as it is not only porous but also rich in P. However, further structural analysis is needed in order to understand the formation mechanism.

9.2.3 Biosynthesis of HA on porous titanium webs

Compared with solid substrates, it is more difficult to apply coatings to porous scaffolds (Figure 9. 8). Traditional methods such as plasma/thermal spray will not be suitable due to their inability to coat the inside of the porous structure, or some hidden parts of a complex shape. So far, the successful methods include the sol-gel method, SBF biomimetic method and electrochemical deposition [15]. *Serratia* biomineralisation offers another approach to solve the problem.

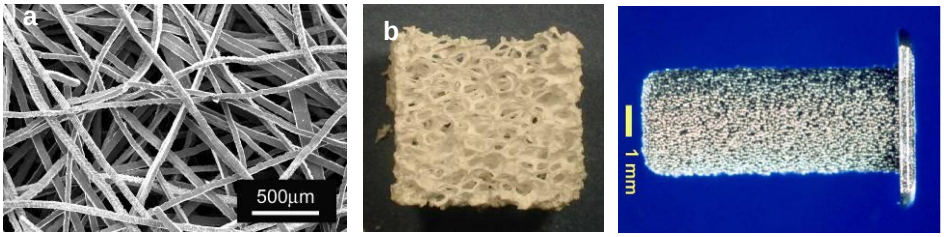

Figure 9. 8 Several examples of porous matrices and grafts with complex shapes

a: a porous titanium web (Hi-Lex. Ltd, Japan)

b: An HA coated porous polyurethane reticulated foam cubes [16]

c: A porous Ti implant [94]

The crystals formed within the porous titanium system are similar to those formed on the solid titanium discs, being calcium-deficient hydroxyapatite. The crystals are mainly nano-scale plates, although the crystal size tends to be larger inside the structure. The difference in ion concentration during mineralisation may contribute to the phenomenon, as discussed in § 9.1.2. The biofilm is anticipated to be thicker at the periphery of the porous matrix [95], and thus a crystal shell is likely to form during the early mineralisation of the outer biofilm, wrapping the entire matrix, making further transportation of medium into the scaffold even more difficult.

The X-Ray Micro-CT scanning indicates abundant crystal formation within the porous titanium matrix (the sample with biofilm pregrown in the fermenter), as shown in Figure 8. 2. Results also indicate that the crystals can develop well beyond the boundary of the titanium matrix (Figure 8. 2b). This may be caused by the thicker biofilm at the periphery of the matrix, as illustrated in Figure 5. 5. The easier access of the outer biofilm to the fresh mineralisation solution may also result in a faster crystal precipitation at the periphery of the structure. Actually, so many crystals were produced that spaces inside the metal scaffold were almost

entirely occupied, with only a few pores left (Figure 8. 2b, c & d). In other words, with a 5 day-old biofilm prepared in the fermenter, instead of an HA coated titanium web, what is obtained is more like a Ti reinforced porous HA composite. With decreased biofilm thickness, the amount of the mineralised crystals may be reduced. It was observed in this work that biofilm prepared by simply incubating the titanium meshes in a secondary bacterial culture for three days (Figure 8. 5) was much thinner than the 5-day-old specimen processed in a fermenter (Figure 4. 13). As a result, the subsequent HA coating was thinner as well, if Figure 8. 6a and Figure 8. 1a are compared.

However, the challenge remains to form a smooth and even coating on the porous 3D scaffold through bacterial biomineralisation. Even on the thin HA coated specimen (3-day old biofilm), the coating thickness ranged from 1 μm to above 10 μm. In fact, the crystal coating is directly supported by the bacterial colonies rather than the metal matrix. Therefore, it is natural to anticipate such a coating structure with a wide thickness distribution and a large amount of crystal clusters suspended between the titanium wires, as the biofilm thickness varied on different titanium wires and bacteria formed hanging bridges across different wires (Figure 8.5). To form an even and smooth coating, the biomimetic method might be more suitable (Figure 9. 9). However, bacterial biomineralisation is still a better solution for applications when a high surface area is a priority.

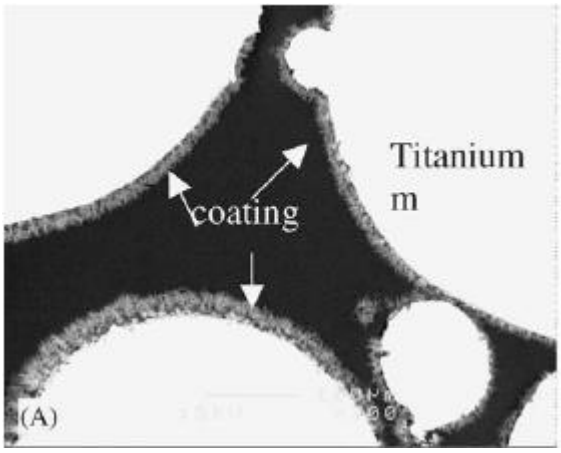

Figure 9. 9 Biomimetic HA coating on a porous titanium substrate [15]

9.3 Bacterial biomineralisation as a coating method: advantages and major limitations

There are several disadvantages of *Serratia* HA coatings. First of all, the complex structure of the biofilm makes the ion concentration differ from site to site, possibly leading to an unevenness in crystal size within the structure. Secondly, strict controls are required for both the fermentation and biomineralisation processes. Moreover, not only is the average thickness of the biofilm dependent on the position of the support within the fermenter body, but also, during mineralisation, samples closer to the 'medium inlet' are quicker to form HA and the amount of the crystals formed is higher than at the far end. Thus, both the fermenter and bioreactor need to be adjusted to achieve even coatings. Due to its structure, a *Serratia* HA coating may not be successful on pure titanium if used at load bearing sites. Sintering at higher temperatures (>1000 ^{o}C) may solve the problem, but the nano-roughness will be lost and the choice of metal substrates will be very limited.

However, more benefits can be obtained. First of all, like the apatite found in bone *in vivo*, HA formed in this way is calcium deficient with the presence of Na^{+} and Cl^{-}. Secondly, it is theoretically very easy to substitute Ca^{2+} with other elements such as Mg^{2+} and Sr^{2+}, and to

incorporate F^-, simply by modifying the composition of the mineralisation solution. Thirdly, a porous substrate can be coated due to the motility of bacteria in an aqueous environment. Last, but not least, the macro-, micro- and nano-roughness of the coating conveys an extremely high surface area into the system. This method is the first to introduce roughness over this wide range. This kind of structure is independent of the substrate and may show different patterns according to the biofilm structure.

References

1. Macaskie LE, Bonthrone KM, Yong P, Goddard DT. Enzymically mediated bioprecipitation of uranium by a *Citrobacter* sp.: a concerted role for exocellular lipopolysaccharide and associated phosphatase in biomineral formation Microbiology 2000;146:1855-1867.
2. Rabaey K, Verstraete W. Microbial fuel cells: novel biotechnology for energy generation. Trends in Biotechnology 2005;23(6):291-298.
3. Mandal D, Bolander M, Mukhopadhyay D, Sarkar G, Mukherjee P. The use of microorganisms for the formation of metal nanoparticles and their application. Applied Microbiology and Biotechnology 2006;69(5):485-492.
4. L.Sammons R, Thackray AC, Ledo HM, Marquis PM, Jones IP, Yong P, Macaskie LE. Characterisation and sintering of nanophase hydroxyapatite synthesised by a species of *Serratia*. Journal of Physics: Confrence Series 2007;93:1-7.
5. Ledo HM, Thackray AC, Jones IP, Marquis PM, Macaskie LE, Sammons RL. Microstructure and composition of biosynthetically synthesised hydroxyapatite. Journal of Materials Science: Materials in Medicine 2008;19(11):3419-3427.
6. Macaskie LE, Yong P, Paterson-Beedle M, Thackray AC, Marquis PM, Sammons RL, Nott KP, Hall LD. A novel non line-of-sight method for coating hydroxyapatite onto the surfaces of support materials by biomineralization. Journal of Biotechnology 2005;118(2):187-200.
7. Yong P, Macaskie LE, Sammons RL, Marquis PM. Synthesis of nanophase hydroxyapatite by a *Serratia* sp. from waste-water containing inorganic phosphate. Biotechnology Letters 2004;26(22):1723-1730.
8. Cai Y, Zhang S, Zeng X, Wang Y, Qian M, Weng W. Improvement of bioactivity with magnesium and fluorine ions incorporated hydroxyapatite coatings via sol-gel deposition on Ti6Al4V alloys. Thin Solid Films 2009;517(17):5347-5351.
9. Pan HB, Li ZY, Lam WM, Wong JC, Darvell BW, Luk KDK, Lu WW. Solubility of strontium-substituted apatite by solid titration. Acta Biomaterialia 2009;5(5):1678-1685.
10. Gonda Y, Ioku K, Shibata Y, Okuda T, Kawachi G, Kamitakahara M, Murayama H, Hideshima K, Kamihira S, Yonezawa I, Kurosawa H, Ikeda T. Stimulatory effect of hydrothermally synthesized biodegradable hydroxyapatite granules on osteogenesis and direct association with osteoclasts. Biomaterials 2009;30(26):4390-4400.
11. Takadama H, Kim H, Kokubo T, Nakamura T. TEM-EDX study of mechanism of bonelike apatite formation on bioactive titanium metal in simulated body fluid. Journal of Biomedical Materials Research Part B: Applied Biomaterials 2001;57(3):441-448.
12. Wang H, Eliza N, Xiang Z, Hsu H, Spector M, Hobbs L. Early bone apposition *in vivo* on plasma-sprayed and electrochemically deposited hydroxyapatite coatings on titanium alloy. Biomaterials 2006;27(23):4192-4230.
13. Kim H-M, Takadama H, Kokubo T, Nishiguchi S, Nakamura T. Formation of a bioactive graded surface structure on Ti-15Mo-5Zr-3Al alloy by chemical treatment. Biomaterials 2000;21(4):353-358.
14. Afshar A, Ghorbani M, Ehsani N, Saeri MR, Sorrell CC. Some important factors in the wet precipitation process of hydroxyapatite. Materials and Design 2003;24(3):197-202.
15. Zhang Q, Leng Y, Xin R. A comparative study of electrochemical deposition and biomimetic deposition of

calcium phosphate on porous titanium. Biomaterials 2005;26(16):2857-2865.
16. Thackray AC. Bacterial biosynthesis of a bone substitute material. PhD Thesis. University of Birmingham; 2005.
17. Jinawath S, Pongkao D, Suchanek W, Yoshimura M. Hydrothermal synthesis of monetite and hydroxyapatite from monocalcium phosphate monohydrate. International Journal of Inorganic Materials 2001;3(7):997-1001.
18. Nott KP, Heese FP, Hall LD, Macaskie LE, Paterson-Beedle M. Measurement of flow field in biofilm reactors by 3-D magnetic resonance imaging. AIChE Journal 2005;51(11):3072-3079.
19. Graf von der Schulenburg DA, Holland DJ, Paterson-Beedle M, Macaskie LE, Gladden LF, Johns ML. Spatially resolved quantification of metal ion concentration in a biofilm-mediated ion exchanger. Biotechnology and Bioengineering 2008;99(4):821-829.
20. Stoodley P, Sauer K, Davies DG, Costerton JW. Biofilms as complex differentiated communities. Annual Review of Microbiology 2002;56(1):187-209.
21. Eiden-Aβann S, Viertelhaus M, Heiβ A, Hoetzer KA, Felsche J. The influence of amino acids on the biomineralization of hydroxyapatite in gelatin. Journal of Inorganic Biochemistry 2002;91(3):481-486.
22. Teng S, Shi J, Peng B, Chen L. The effect of alginate addition on the structure and morphology of hydroxyapatite/gelatin nanocomposites. Composites Science and Technology 2006;66(11-12):1532-1538.
23. Romberg RW, Werness PG, Riggs BL, Mann KG. Inhibition of hydroxyapatite-crystal growth by bone-specific and other calcium-binding proteins. Biochemistry 1986;25(5):1176-1180.
24. Walsh D, Kingston JL, Heywood BR, Mann S. Influence of monosaccharides and related molecules on the morphology of hydroxyapatite. Journal of Crystal Growth 1993;133(1-2):1-12.
25. Li P, Nakanishi K, Kokubo T, de Groot K. Induction and morphology of hydroxyapatite, precipitated from metastable simulated body fluids on sol-gel prepared silica. Biomaterials 1993;14(13):963-968.
26. Jeong BC, Kim HW, Macaskie LE. Phosphotransferase activity of acid phosphatases of a *Citrobacter* sp. FEMS Microbiology Letters 1997;147(1):103-108.
27. Liu J, Ye X, Wang H, Zhu M, Wang B, Yan H. The influence of pH and temperature on the morphology of hydroxyapatite synthesized by hydrothermal method. Ceramics International 2003;29(6):629-633.
28. Tanahashi M, Kamiya K, Suzuki T, Nasu H. Fibrous hydroxyapatite grown in the gel system: effects of pH of the solution on the growth rate and morphology. Journal of Materials Science: Materials in Medicine 1992;3(1):48-53.
29. Roy ME, Nishimoto SK. Matrix Gla protein binding to hydroxyapatite is dependent on the ionic environment: calcium enhances binding affinity but phosphate and magnesium decrease affinity. Bone 2002;31(2):296-302.
30. Zhu W, Robey PG, Boskey AL, Robert M, David F, Dorothy AN, Clifford JR. The regulatory pole of matrix proteins in mineralization of bone. Osteoporosis (Third Edition). San Diego: Academic Press, 2008. p. 191-240.
31. Khopade AJ, Khopade S, Jain NK. Development of hemoglobin aquasomes from spherical hydroxyapatite cores precipitated in the presence of half-generation poly(amidoamine) dendrimer. International Journal of Pharmaceutics 2002;241(1):145-154.
32. Amemiya Y, Arakaki A, Staniland SS, Tanaka T, Matsunaga T. Controlled formation of magnetite crystal by partial oxidation of ferrous hydroxide in the presence of recombinant magnetotactic bacterial protein Mms6. Biomaterials 2007;28(35):5381-5389.
33. Damen JJM, de Soet JJ, ten Cate JM. Adsorption of [^{3}H]-lipoteichoic acid to hydroxyapatite and its effect on crystal growth. Archives of Oral Biology 1994;39(9):753-757.
34. Damen JJM, ten Cate JM. Inhibition of hydroxyapatite crystal growth by lipoteichoic acid. Archives of Oral Biology 1994;39(2):141-146.
35. Hirschler A, Lucas J, Hubert J-C. Bacterial involvement in apatite genesis. FEMS Microbiology Letters 1990;73(3):211-220.
36. Kokubo T. Apatite formation on surfaces of ceramics, metals and polymers in body environment. Acta Materialia 1998;46(7):2519-2527.
37. Layrolle P, Ito A, Tateishi T. Sol-gel synthesis of amorphous calcium phosphate and sintering into microporous hydroxyapatite bioceramics. Journal of the American Ceramic Society 1998;81(6):1421-1428.
38. Macaskie LE, Bonthrone KM, Yong P, Goddard DT. Enzymically mediated bioprecipitation of uranium by a *Citrobacter* sp.: a concerted role for exocellular lipopolysaccharide and associated phosphatase in biomineral formation. Microbiology 2000;146(8):1855-1867.
39. Macaskie LE, Empson RM, Cheetham AK, Grey CP, Skarnulis AJ. Uranium bioaccumulation by a *Citrobacter* sp. as a result of enzymically mediated growth of polycrystalline HUO_2PO_4. Science 1992;257(5071):782-784.

40. Paterson-Beedle M, Macaskie LE, Lee CH, Hriljac JA, Jee KY, Kim WH. Utilisation of a hydrogen uranyl phosphate-based ion exchanger supported on a biofilm for the removal of cobalt, strontium and caesium from aqueous solutions. Hydrometallurgy 2006;83(1-4):141-145.
41. Simmer JP, Fincham AG. Molecular mechanisms of dental enamel formation. Critical Reviews in Oral Biology and Medicine 1995;6(2):84-108.
42. Rao RR, Roopa HN, Kannan TS. Solid state synthesis and thermal stability of HAP and HAP – β-TCP composite ceramic powders. Journal of Materials Science: Materials in Medicine 1997;8(8):511-518.
43. Feng W, Mu-sen L, Yu-peng L, Yong-xin Q. A simple sol-gel technique for preparing hydroxyapatite nanopowders. Materials Letters 2005;59(8-9):916-919.
44. Muler FA, Muler L, Caillard D, Conforto E. Preferred growth orientation of biomimetic apatite crystals. Journal of Crystal Growth 2007;304(2):464-471.
45. Rubin MA, Jasiuk I, Taylor J, Rubin J, Ganey T, Apkarian RP. TEM analysis of the nanostructure of normal and osteoporotic human trabecular bone. Bone 2003;33(3):270-282.
46. Hong S, Hong S, Kohn D. Nanostructural analysis of trabecular bone. Journal of Materials Science: Materials in Medicine 2009;20(7):1419-1426.
47. Milev A, Kannangara GSK, Ben-Nissan B. Morphological stability of hydroxyapatite precursor. Materials Letters 2003;57(13-14):1960-1965.
48. Feng QL, Wang H, Cui FZ, Kim TN. Controlled crystal growth of calcium phosphate on titanium surface by NaOH-treatment. Journal of Crystal Growth 1999;200(3-4):550-557.
49. Yas AC, Bhaduri SB. Rapid coating of Ti6Al4V at room temprature with a calcium phosphate solution similar to 10x simulated body fluid. Journal of Materials Research 2004;19(9):2732-2749.
50. Sammons R, Thackray AC, Ledo HM, Marquis PM, Jones IP, Yong P, Macaskie LE. Characterisation and sintering of nanophase hydroxyapatite synthesised by a species of *Serratia*. Journal of Physics: Conference Series 2007;93:1-7.
51. Thackray AC, Sammons RL, Macaskie LE, Yong P, Lugg H, Marquis PM. Bacterial biosynthesis of a calcium phosphate bone-substitute material. Journal of Materials Science: Materials in Medicine 2004;15(4):403-406.
52. Kim HM, Miyaji F, Kokubo T. Effect of heat treatment on apatite-forming ability of Ti metal induced by alkali treatment. Journal of Materials Science: Materials in Medicine 1997;8(6):341-347.
53. Lee PS, Loo J, Lee P, Ma J. Biomimetic processing of bioactive interface on silicon substrates. Journal of Biomedical Materials Research Part B Applied Biomaterials 2007;85(2):368-377.
54. Park E, Condrate RA, Hoelzer DT, Fischman GS. Interfacial characterization of plasma-spray coated calcium phosphate on Ti–6Al–4V. Journal of Materials Science: Materials in Medicine 1998;9(11):643-649.
55. Ji H, Marquis PM. Effect of heat treatment on the microstructure of plasma-sprayed hydroxyapatite coating. Biomaterials 1993;14(1):64-68.
56. Kunzler TP, Drobek T, Schuler M, Spencer ND. Systematic study of osteoblast and fibroblast response to roughness by means of surface-morphology gradients. Biomaterials 2007;28(13):2175-2182.
57. Anselme K, Bigerelle M. Topography effects of pure titanium substrates on human osteoblast long-term adhesion. Acta Biomaterialia 2005;1(2):211-222.
58. Ranella A, Barberoglou M, Bakogianni S, Fotakis C, Stratakis E. Tuning cell adhesion by controlling the roughness and wettability of 3D micro/nano silicon structures. Acta Biomaterialia 2010;6(7):2711-2720.
59. Paital SR, Dahotre NB. Calcium phosphate coatings for bio-implant applications: Materials, performance factors, and methodologies. Materials Science and Engineering: R: Reports 2009;66(1-3):1-70.
60. Leeuwenburgh SCG, Wolke JGC, Siebers MC, Schoonman J, Jansen JA. *In vitro* and *in vivo* reactivity of porous, electrosprayed calcium phosphate coatings. Biomaterials 2006;27(18):3368-3378.
61. Leeuwenburgh SCG, Heine MC, Wolke JGC, Pratsinis SE, Schoonman J, Jansen JA. Morphology of calcium phosphate coatings for biomedical applications deposited using Electrostatic Spray Deposition. Thin Solid Films 2006;503(1-2):69-78.
62. Chen J-z, Shi Y-l, Wang L, Yan F-y, Zhang F-q. Preparation and properties of hydroxyapatite-containing titania coating by micro-arc oxidation. Materials Letters 2006;60(20):2538-2543.
63. Hall-Stoodley L, Costerton JW, Stoodley P. Bacterial biofilms: from the natural environment to infectious diseases. Nature Review Microbiology 2004;2(2):95-108.
64. Ledo HJM. Microstructure and composition of bacterially synthesised hydroxyapatite Birmingham: University of Birmingham; 2006.
65. Kasten P, Luginbühl R, van Griensven M, Barkhausen T, Krettek C, Bohner M, Bosch U. Comparison of human bone marrow stromal cells seeded on calcium-deficient hydroxyapatite, beta-tricalcium phosphate and demineralized bone matrix. Biomaterials 2003;24(15):2593-2603.
66. Rigo ECS, Boschi AO, Yoshimoto M, Allegrini JS, Konig JB, Carbonari MJ. Evaluation *in vitro* and *in vivo*

of biomimetic hydroxyapatite coated on titanium dental implants. Materials Science and Engineering: C 2004;24(5):647-651.
67. Lloyd JR, Pearce CI, Coker VS, Pattrick RAD, Van Der Laan G, Cutting R, Vaughan DJ, Paterson-Beedle M, Mikheenko IP, Yong P, Macaskie LE. Biomineralization: linking the fossil record to the production of high value functional materials. Geobiology 2008;6(3):285-297.
68. Khang D, Kim SY, Liu-Snyder P, Palmore GTR, Durbin SM, Webster TJ. Enhanced fibronectin adsorption on carbon nanotube/poly(carbonate) urethane: Independent role of surface nano-roughness and associated surface energy. Biomaterials 2007;28(32):4756-4768.
69. Dalby M, Pasqui D, Affrossman S. Cell response to nano-islands produced by polymer demixing: a brief review. IEE proceedings - Nanobiotechnology 2004;151(2):53-62.
70. Ruer M, Gensior TJ, Herren C, Walter Mv, Ocklenburg C, Marx R, Erli H-J. The removal of Al_2O_3 particles from grit-blasted titanium implant surfaces: Effects on biocompatibility, osseointegration and interface strength in vivo. Acta Biomaterialia 2010;6(7):2852-2861.
71. Aparicio C, Gil FJ, Planell JA, engel E. Human-osteoblast proliferation and differentiation on grit-blasted and bioactive titanium for dental applications. Journal of Materials Science: Materials in Medicine 2002;13(12):1105-1111.
72. Corain B, Nicolini M, Zatta P. Aspects of the bioinorganic chemistry of aluminium(III) relevant to the metal toxicity. Coordination Chemistry Reviews 1992;112:33-45.
73. Gotfredson K, Wennerberg A, Johansson C, Skovgaard LT, Hjørting-Hansen E. Anchorage of TiO_2-blasted, HA-coated, and machined implants: An experimental study with rabbits. Journal of Biomedical Materials Research 1995;29(10):1223-1231.
74. Degasne I, Baslé MF, Demais V, Huré G, Lesourd M, Grolleau B, Mercier L, Chappard D. Effects of roughness, fibronectin and vitronectin on attachment, spreading, and proliferation of human osteoblast-like cells (Saos-2) on titanium surfaces. Calcified Tissue International 1999;64(6):499-507.
75. Liu JL, Umemoto M, Todaka Y, Tsuchiya K. Formation of a nanocrystalline surface layer on steels by air blast shot peening. Journal of Materials Science 2007;42(18):7716-7720.
76. Todaka Y, Umemoto M, Tsuchiya K. Comparison of nanocrystalline surface layer in steels formed by air blast and ultrasomic shot blasting. Materials Transactions 2004;45(2):367-379.
77. Truong VK, Lapovok R, Estrin YS, Rundell S, Wang JY, Fluke CJ, Crawford RJ, Ivanova EP. The influence of nano-scale surface roughness on bacterial adhesion to ultrafine-grained titanium. Biomaterials 2009;31(13):3674-3683.
78. Valiev RZ, Semenova IP, Latysh VV, Rack H, Lowe TC, Petruzelka J, Dluhos L, Hrusak D, Sochova J. Nanostructured titanium for biomedical applications. Advanced Materials 2008;10(8):B15-B17.
79. Kim TN, Balakrishnan A, Lee BC, Kim WS, Dvorankova B, Smetana K, Park KK, Panigrahi BB. *In vitro* fibroblast response to ultra fine grained titanium produced by a severe plastic deformation process. Journal of Materials Science: Materials in Medicine 2008;19(2):553-557.
80. Estrin Y, Kasper C, Diederichs S, Lapovok P. Accelerated growth of preosteoblastic cells on ultragine grained titanium. Journal of Biomedical Materials Research Part A 2008;90A(4):1239–1294.
81. Koning RI, Koster AJ. Cryo-electron tomography in biology and medicine. Annals of Anatomy - Anatomischer Anzeiger 2009;191(5):427-445.
82. Yan L, Leng Y, Weng L-T. Characterization of chemical inhomogeneity in plasma-sprayed hydroxyapatite coatings. Biomaterials 2003;24(15):2585-2592.
83. Blind O, Klein LH, Dailey B, Jordan L. Characterization of hydroxyapatite films obtained by pulsed-laser deposition on Ti and Ti-6Al-4V substrates. Dental Materials 2005;21(11):1017-1024.
84. Balani K, Anderson R, Laha T, Andara M, Tercero J, Crumpler E, Agarwal A. Plasma-sprayed carbon nanotube reinforced hydroxyapatite coatings and their interaction with human osteoblasts in vitro. Biomaterials 2007;28(4):618-624.
85. Kliauga AM, Ferrante M. Interface compounds formed during the diffusion bonding of Al_2O_3 to Ti. Journal of Materials Science 2000;35(17):4243-4249.
86. Kim CS, Hwang KE, Hwo SJ. Hard tissue conmpatibility of titanium phosphide layers obtained by diffusion in Ti-Ha interface. Annals of transplantation 2004;9(1):82-87.
87. Wei M, Ruys AJ, Swain MV, Milthorpe BK, Correll CC. Hydroxyaoatite-coated metals: interfacial reactions during sintering. Journal of Materials Science Materials in Medicine 2005;16(2):101-106.
88. Stoch A, Brozek A, Kmita G, Stoch J, Jastrzebski W. Electrophoretic coating of hydroxyapatite on titanium implants. Journal of Molecular Structure 2001;596(1-3):191-200.
89. Sousa SR, Barbosa MA. Effect of hydroxyapatite thickness on metal ion release from Ti6Al4V substrates. Biomaterials 1996;17(4):397-404.
90. Eisenbarth E, Velten D, Muller M, Thull R, Breme J. Biocompatibility of beta-stabilizing elements of

titanium alloys. Biomaterials 2004;25(26):5705-5713.
91. Faure J, Balamurugan A, Benhayoune H, Torres P, Balossier G, Ferreira JMF. Morphological and chemical characterisation of biomimetic bone like apatite formation on alkali treated Ti6Al4V titanium alloy. Materials Science and Engineering: C 2009;29(4):1252-1257.
92. Liang F, Zhou L, Wang K. Apatite formation on porous titanium by alkali and heat-treatment. Surface and Coatings Technology 2003;165(2):133-139.
93. Takadama H, Kim H-M, Kokubo T, Nakamura T. XPS study of the process of apatite formation on bioactive Ti-6Al-4V alloy in simulated body fluid. Science and Technology of Advanced Materials 2001;2(2):389-396.
94. Nguyen HQ, Deporter DA, Pilliar RM, Valiquette N, Yakubovich R. The effect of sol-gel-formed calcium phosphate coatings on bone ingrowth and osteoconductivity of porous-surfaced Ti alloy implants. Biomaterials 2004;25(5):865-876.
95. Gutierrez MC, Carcia-Carvajal ZY, Hortiguela MJ, Yuste L, Rojo F, Ferrer ML, Monte Fd. Biocompatible MWCNT scaffolds for immobilization and proliferation of *E. coli*. Journal of Materials Chemistry 2007;7(29):2992-2995.
96. Yong P, Paterson-Beedle M, Liu W, Zhang Z, Beauregard DA, Johns ML, Maacaskie LE. A study of biofilm and non-line-of sight bio-hydroxyapatite coatings using a *Serratia* sp. Advanced Materials Research 2009;71(73):741-744.

Chapter 10 Conclusions

10.1 Biofilms on titanium

This study is clinically important, as it offers information concerning bacterial interaction with titanium surfaces, which are widely used as dental and orthopaedic implants. The influence of titanium surface properties, including microstructure, alloy phase, chemical composition and surface treatments, on bacterial adhesion, proliferation and biofilm formation were considered.

10.1.1 Bacterial adhesion and proliferation

The combination of direct electron microscope imaging by SE, BSE and EBSD and the image processing techniques used in this work provides a novel approach to study bacterial distribution on metal surface directly and statistically. Not only are the artefacts due to etching avoided entirely, but also more information is extracted without additional specimen treatment such as coating, further polishing and etching. What is even more significant is the fact that using this method, bacterial distribution can be easily related to nearly all the microstructural components. Thus, a thorough statistical analysis is easier, more accurate and more informative.

The Gram-positive bacteria *S. epidermidis* and *S. sanguinis*, and the Gram-negative *E. coli* and *Serratia* attached randomly on CP Ti, regardless of GBs and grain orientation, in both adhesion and the early proliferation stage (*Serratia* alone). This suggests that bacteria may not be sensitive to the energy and morphological changes due to the presence of GBs or different orientations on pure titanium with an equiaxial structure as used this work. Neither did the

Gram-positive bacteria (*S. epidermidis* and *S. sanguinis*) distinguish between the two phases of Ti 64, suggesting they may not be sensitive to minor chemical difference during adhesion.

Although all the four bacteria showed equivalent adhesion on CP Ti and Ti 64 with similar surface wettabilities in terms of WCAs, the Gram-positive bacteria and the Gram-negative bacteria showed opposite adhesion patterns on CP Ti, Ti 64 and V: whilst *S. epidermidis* and *S. sanguinis* preferred the less hydrophilic V, the Gram-negative *E. coli* and *Serratia* tended to show better adhesion on the more hydrophobic CP Ti and Ti 64. However, further studies are required to draw any general conclusion here, as will be discussed in Chapter 11. Al may be a potential bacterial adhesion/proliferation inhibitor as indicated by the low number of adhered bacteria.

In the adhesion stage, the bacteria may not be able to detect the minor differences of the chemical composition between the two phases of Ti 64, judging by the random adhesion patterns of the two *cocci* on Ti 64, and between CP Ti and Ti 64, considering the equal numbers of adherent bacteria. However, the effect of chemical composition may start to play a role during the early proliferation, as the number of *Serratia* was slightly higher on CP Ti than on Ti 64, although the difference is not significant. Studying the proliferation for a longer time and with other bacteria may help to better understand the problem.

10.1. 2 *Serratia* biofilm formation

The importance of this section lies in a comparative study of the mature biofilm formation on different titanium surfaces, which has been rarely reported before. It was observed in this work that rather than being surface roughness-related, the number of bacteria associated in a 7-day old *Serratia* biofilm on titanium discs showed a weak dependence on the substrate surface wettability. Generally speaking, biofilm formation appears to be better on the

hydrophilic surfaces than on the hydrophobic ones. However, there were exceptions – for example the biofilm formed well on the plasma sprayed surface, possibly due to its high surface area. The quantitative analysis of the biofilm was carried out using bicinchoninic protein assay. More accurate methods will be required in the future.

It was also observed that the topography of the substrates is important during biofilm formation, as the colony shapes and bacterial orientation appeared to be quite different on various substrates. On the mirror polished surface, flattened colonies with highly oriented bacteria were common, whereas on the Al_2O_3 grit blasted surface they were more outstanding and the cells were randomly arranged. Bacterial colonies were often observed to be in the shape of bridges extending from the extruding titanium granules to the substrate on the plasma sprayed surface. The embedded Al_2O_3 particles may not affect the biofilm morphology as biofilms appeared to be the same on both titanium and Al_2O_3 surface on the alumina grit blasted deep profile surface.

The porous titanium webs used in this study are suitable as carriers for biofilm development. *Serratia* biofilm was observed to form at the periphery of the porous substrate and deep inside the matrix. Not only did bacteria attach to the solid surface (on the titanium wire), they were also capable of extending between far separated features through ‘bacterial hanging bridges’, which could lead to bacterial colonial growth filling the pores in the matrix.

The 3D examination using X ray Micro-CT is based on a different X-ray absorption rate of samples with different density. It has never been involved in the characterisation of biofilm on metal substrates. In this study, it was found that Micro X ray-CT (Skyscan) can distinguish the large bacterial colonies and the solid titanium wires. However, it is inadequate for the analysis of thin biofilms and smaller colonies, either due to the resolution limit or the insufficient

contrast of the above features.

Fixed and dehydrated samples were used for the study of biofilm morphology and distribution using SEM and Micro X ray-CT. These techniques can be used to characterise the biofilm development, not only on solid titanium discs, but also on porous substrates. However, there may be artefacts due to fixation and dehydration during sample preparation, especially in the characterisation of biofilm distribution within a porous structure.

10.2 Biomineralisation on titanium discs

Bacterial biomineralisation is a well-known phenomenon, and is suggested to have applications in metal accumulation [1], bionanomineral production [2] and wastewater treatment [3]. It may also be used as a coating method [4]. This work evaluated in detail the biomineralised HA coatings on titanium and the potential applications.

10.2.1 *Serratia* HA

The nascent biomineralised crystals are nano-scale hydroxyapatite. They are calcium-deficient, but mature with prolonged mineralisation time. The crystals are usually curved plate-shaped, but occasionally can be in the form of flat plates. Results in this work suggest that the ion concentration of the mineralisation solution can influence the crystal size and morphology, with the formation of larger and thinner HA plates when β-GP was scarce. Further studies are required to investigate other possible influence of crystal formation during bacterial biomineralisation.

The cleavage of β-GP is suggested to be the rate controlling step in this biomineralisation process. Although the cleavage of β-GP to liberate HPO_4^{2-} is undoubtedly bacteria-related, results in this work indicate that the further reaction between HPO_4^{2-} and Ca^{2+} to form HA

may not be dependent on the *Serratia* cells. Thus, spontaneous deposition of HA is possible where both Ca^{2+} and the free HPO_4^{2-} are available and not necessarily bacteria-bound. Therefore, there are three possible locations for HA deposition during bacterial biomineralisation, around/inside the *Serratia* cells, within the EPM layer, and where both Ca^{2+} and HPO_4^{2-} are free.

10.2.2 Biomineralisation for coatings on solid titanium substrates

The HA coating formed on titanium by *Serratia* biofilm is calcium-deficient hydroxyapatite and forms a structure with an extremely high surface area due to its macro-, micro- and nano-roughness. This structure resembled, but differed from, the structure of the biofilm prior to mineralisation, containing bacterial towers on a bacterial matrix. No noticeable difference was observed between crystals formed on the surface of titanium, the embedded Al_2O_3, the sodium titanate layer and on the surface layer of the coating.

Sintering is necessary to demolish the biomass and to calcify the crystal coating, and it significantly changed the properties of both the coating and the substrate. After sintering at 800 ^oC for 5 hours, the HA crystals changed to a phase that closely resembled β-TCP. Although the coating structure was preserved, most of the nano-plates transformed to irregular-shaped nano-particles. Bacteria-shaped crystals and holes of approximately the size of the *Serratia* cells were observed. Due to the migration of P from the crystal coating to the metal surface, a diffusion zone was formed at the coating-substrate interface, consisting of P-deficient calcium phosphate and P-rich titanium. The grain size of the titanium substrate was increased from around 40 to 50 μm to above 100 to 200 μm.

Coating titanium discs with HA using bacterial biomineralisation is superior to other methods when surface area is essential but physical strength is not so important, such as implants in the

non-load bearing sites and as catalyst carriers. The coating structure is not determined by the topography of the substrate, but the structure of the biofilm, yielding an extremely high surface area with nano-, micro- and macro-scale roughness. This unique structure and the nano-scale calcium-deficient HA may be beneficial *in vivo* to facilitate tissue mineralisation and bone ingrowth. Its high surface area may find applications for drug release. This study is the first to report calcium phosphate coatings with such structures. The disadvantage of the coating is its strength. Sintering at higher temperature (above 1000 ^{o}C) may solve the problem, but titanium may not be suitable as the supporting material (due to its low β-transus temperature) and the mismatch of the thermal expansions between the crystal coating and the substrate may become another challenge.

Due to the nature of biomineralisation itself, it can be hypothesised that all coatings obtained from biofilms may resemble those found in this study, being a system of loosely bound crystals with a potential porous structure which is not dependent on the topography of the substrate. Similarly, the coating strength may be a universal challenge. Although it may be solved by sintering at a higher temperature, the choice of substrates will then be very limited, as only those that can stand heat treatment at approximately 1000^{o}C (in the case of HA) or even better above, can be used. Moreover, the nano-scale roughness may be lost.

10.3 Biomineralisation on porous titanium meshes

Serratia biomineralisation is a successful method of coating porous titanium with HA. The coating thickness is closely associated with the thickness of the biofilm. Using porous titanium meshes with biofilm pregrown in a fermenter lead to the formation of a very thick layer of HA. Thus, the product was in fact a porous HA/Ti composite. The crystal layer was thicker at the periphery of the Ti web, forming a crystal shell covering the entire structure.

The crystals were nano-scale HA, the same as those formed on the Ti discs. However, the crystals deep inside the porous Ti scaffold were larger than those on the surface. The coating thickness was significantly reduced when the biofilm was prepared by simply cultivating the titanium web in secondary *Serratia* culture for three days. However, the coating achieved was not even, ranging from 1 μm to more than 10 μm, due to the un-even formation of biofilm. In both situations, the coating itself is porous with a high surface area, similar to that on the titanium discs. This HA coated Ti system may have applications as implants at non-load bearing sites, for drug release *in* vivo, in water purification industry and as catalyst carriers. However, it must be noted that this method may fail when an even coating of the porous scaffold is required.

Significant crystal loss of both systems was observed after sintering, especially for the HA/Ti composite. The entire crystal shell was destroyed. However, the remaining crystals were still thick enough to coat the titanium wires, although there were cracks throughout the coating.

References

1. Macaskie LE, Empson RM, Cheetham AK, Grey CP, Skarnulis AJ. Uranium bioaccumulation by a *Citrobacter* sp. as a result of enzymically mediated growth of polycrystalline HUO_2PO_4. Science 1992;257(5071):782-784.
2. Lloyd JR, Pearce CI, Coker VS, Pattrick RAD, Van Der Laan G, Cutting R, et al. Biomineralization: linking the fossil record to the production of high value functional materials. Geobiology 2008;6(3):285-297.
3. Yong P, Macaskie LE, Sammons RL, Marquis PM. Synthesis of nanophase hydroxyapatite by a *Serratia* sp. from waste-water containing inorganic phosphate. Biotechnology Letters 2004;26(22):1723-1730.
4. Macaskie LE, Yong P, Paterson-Beedle M, Thackray AC, Marquis PM, Sammons RL, et al. A novel non line-of-sight method for coating hydroxyapatite onto the surfaces of support materials by biomineralization. Journal of Biotechnology 2005;118(2):187-200.

Chapter 11 Future work

11.1 Biofilms on titanium

11.1.1 Bacterial adhesion and proliferation

It will be interesting to continue the study of microbial adhesion on metals using the present methods. Other Gram-positive and Gram-negative bacterial strains and mammalian cells and other metal systems such as steels and magnesium alloys may be included in future work. It is premature to draw the conclusion that bacterial adhesion on metal surfaces is Gram-property-related, based on the present results. A wider choice of both Gram-positive and Gram-negative bacteria and their adhesions should be examined in the future.

Although bacteria cannot distinguish grain orientations at the micro-scale, to study their behaviour on highly textured titanium substrates with different preferential orientations may be fruitful, as certain orientations have shown different affinities for mammalian cells. For example, MC3T3 pre-osteoblast cells attached better on a Ti 64 specimen with the predominant orientation of $(10\bar{1}0)$ than on a $(11\bar{2}0)$-domain surface, attributed to a difference in surface wettability of the two specimens [1].

Although Gram-positive *S. epidermidis* and *S. sanguinis* attached randomly on Ti 64, regardless of the different phase structures, it would be worthwhile to study further the adhesion of Gram-negative bacteria on Ti 64, with a proper choice of the substrate: its grain size should be much larger than the size of the Gram-negative bacteria used.

This study focuses on the influence of substrate microstructure and chemical composition, but other factors may be equally important and should be included in further analysis, such as the

surface charge of both the substrates and the bacteria, and the local pH environment.

11.1.2 *Serratia* biofilm formation

To estimate the amount of bacterial associated within the biofilm using protein assay is not accurate and offered only a rough estimation. Thus, other techniques should be involved in the future for a more accurate quantitative investigation.

Further experiments are necessary to confirm the influence of the embedded Al_2O_3 particles on biofilm growth. It will be helpful to replace alumina with other grits such as TiO_2 and HA, and to compare the biofilm development on these substrates. It will also be interesting to study the adhesion strength of biofilm formed on titanium with different surface treatment which can be directly related to the cleaning of medical devices.

One deficiency of this work was that all the studies of biofilm structure were done using dehydrated samples where biofilms deformed and shrank. Cryo and environmental techniques will be used in the future to investigate the live biofilm structure. It will be of great interest to analyse the structure of the biofilm using environmental SEM, and to build up 3D profiles of the biofilm development on various titanium surfaces as well as on porous scaffolds with different structures and porosities in environmental conditions using techniques such as confocal microscopy [2] and high frequency ultrasound imaging [3]. To monitor the biofilm development in real time using confocal microscopy on different matrices will be of major importance, as it will lead to a thorough knowledge on the conditions of the biofilm at different stages and the influence of the substrate properties. Furthermore, a study of stained biofilms to investigate the distribution of EPM [4], polysaccharides [5] and the activity of the bacteria [4] would reveal more information about the biofilm growth and possibly the influence of the substrate surface properties. Last but not the least, a cryo-FIB/SEM/TEM

study may provide information such as the arrangement of bacteria at different locations within a biofilm, the distributions of water channels and maybe even the elemental distribution down to nano-scale which will be difficult to obtain using other techniques.

11.2 Biomineralisation on titanium

11.2.1 Biosynthesis of hydroxyapatite

Due to the sensitivity of the crystals to the high energy electron beam, it is difficult to further describe the crystal morphology. The use of cryo-TEM may solve the problem.

Further information is required to explain the exact mechanism of the precipitation of HA by *Serratia*. Although observations in this work indicated the solution ion strength could affect the crystal size, there are other possible factors that may influence the crystal morphology. It is possible that bacteria can secrete crystal growth templates or regulators in certain environments, just like during bone healing *in vivo*. There is evidence that bacteria can produce crystal regulators as discussed in § 9.1.3. Observations in this work indicate that it is not entirely impossible, especially in the cases illustrated in Figure 9. 2, which merit further investigations.

It will be interesting to continue the study of the reactions between the bacteria-liberated HPO_4^{2-} and fresh Ca^{2+} (§ 6.9). Not only is the reaction immediate, the products are nano-scale crystals with a very narrow size distribution. A more precise description of these products is required, possibly also by cryo-techniques. Even if they are HA, these crystals are possibly in a very primitive form, judged by the low Ca/P ratio. It may be beneficial to adjust the chemical composition of the solution and the reaction time to study the crystal formation in different solutions.

11.2.2 Biomineralisation of hydroxyapatite for coatings

The most fascinating aspect of the coating is its unique structure, which may be beneficial to promote cell adhesion, *in vivo* mineralization and bone ingrowth. Although to study its biocompatibility is not included in this work, the adhesion, proliferation and differentiation of mammalian cells on the biosynthesised HA coated Ti will be evaluated in the future. Biofilm structures are different on different substrates, as demonstrated in this project. Thus, HA coatings with different patterns may be formed. To examine cell adhesion on these coatings with different architectures will be interesting as the cells show different distribution patterns on substrates with different topographies [6].

The shortcoming of the coating is its strength. By choosing a substrate that can stand higher temperatures than Ti 64 (T_β = 995 ^oC), the problem may be solved. However, the mismatch between the thermal expansions of calcium phosphate and metals may lead to significant crystal loss. *Serratia* are also known to produce polyhydroxybutyrate [7], which raises the possibility of a polyhydroxybutyrate-reinforced HA coating which may solve the problem of the physical strength. However, to eliminate the bacteria effectively afterwards remains a challenge. The coating may also be strengthened by filling the cracks and pores with HA sol, such as described by Thackray in 2005 [8].

By adjusting the thickness of the biofilm, it may be possible to achieve composites with different HA/Ti ratios, or rather, HA coatings with different thicknesses on porous titanium. To compare cell adhesion on the HA coated porous Ti webs with different HA/Ti ratio may be interesting. There have been a few reports concerning this aspect: for example, Webster *et al.* (2003) reported cells behaved differently on carbon nanofiber (CN) reinforced polycarbonate urethane (PU) according to the CN/PU ratio: with the increased CNs in PU, osteoblast cell

density was significantly increased, although astrocyte and fibroblast cell adhesions were slightly decreased [9]. To investigate the biofilm and the subsequent crystal coating formation on titanium with different porosity will also be important. It is very possible that there exists a critical value for the pore size below which it will be difficult for biofilm to penetrate inside the scaffold and thus crystal coating will only exist at the periphery of the structure.

References

1. Faghihi S, Azari F, Li H, Bateni MR, Szpunar JA, Vali H, Tabrizian M. The significance of crystallographic texture of titanium alloy substrates on pre-osteoblast responses. Biomaterials 2006;27(19):3532-3539.
2. Rieu Al, Briandet R, Habimana O, Garmyn D, Guzz J, Piveteau P. *Listeria monocytogenes* EGD-e biofilms: no mushrooms but a network of knitted chains. Applied and Environmental Microbiology 2008;74(14):4491-4497.
3. Shemesh H, Goertz DE, Sluis LWMvd, Jong Nd, Wu MK, Wesselink PR. High frequency ultrasound imaging of a single-species biofilm. Journal of Dentistry 2007;35:673-678.
4. Ma L, Conover M, Lu H, Parsek MR, Bayles K, Wozniak DJ. Assembly and development of the *Pseudomonas aeruginosa* biofilm matrix. PLoS Pathog 2009;5(3):1000354-1000365.
5. Dongari-Bagtzoglou A, Kashleva H, Dwivedi P, Diaz P, Vasilakos J. Characterization of mucosal *Candida albicans* biofilms. PLoS One 2009;4(11):7967-7976.
6. Anselme K, Bigerelle M. Topography effects of pure titanium substrates on human osteoblast long-term adhesion. Acta Biomaterialia 2005;1(2):211-222.
7. Lugg H, Sammons R, Marquis P, Hewitt C, Yong P, Paterson-Beedle M, Redwood M, Stamboulis A, Kashani M, Jenkins M, Macaskie L. Polyhydroxybutyrate accumulation by a *Serratia* sp. Biotechnology Letters 2008;30(3):481-491.
8. Thackray AC. Bacterial biosynthesis of a bone substitute material. PhD Thesis. University of Birmingham; 2005.
9. Webster T, Waid M, McKenzie J, Price R, Ejiofor J. Nano-technology:carbon nanofobres as improved neural and orthopaedic implants. Nanotechnology 2004;15(1):48-54.